Southern Regional Center for Lightweight Innovative Design

Phase III

Final Scientific & Technical Report

October 1, 2009-September 30, 2011

For compliance with contract requirements of Award DE-EE0002323

Submitted December 27, 2011

SOUTHERN REGIONAL CENTER FOR LIGHTWEIGHT INNOVATIVE DESIGN

Field Technical Monitors: Dr. Mark F. Horstemeyer; Dr. Paul Wang
Center for Advanced Vehicular Systems
Mississippi State University
Box 5405
Mississippi State, MS 39762
(662)325-5449; e-mail: mfhorst@me.msstate.edu
(662)325-2890; e-mail: pwang@cavs.msstate.edu

Technology Area Development Manager: William Joost
U.S. Department of Energy
1000 Independence Ave., S.W., Washington, DC 20585
(202) 287-6020; e-mail: william.joost@ee.doe.gov

Contractor: Mississippi State University (MSST)
Contract No.: DE-FC-26-06NT42755 and DE-EE0002323

EXECUTIVE SUMMARY

Objectives

Lightweighting materials are critical to reducing emissions and the United States' reliance on foreign oil. Understanding how lightweighting materials utilized in vehicles perform in crash scenarios is paramount as well, for passenger safety as well as energy efficiency are primary design challenges facing today's automotive industry. The Southern Regional Center for Lightweight Innovative Design (SRCLID) plans to develop an experimentally validated cradle-to-grave modeling and simulation effort to optimize automotive and truck components in order to decrease weight and cost, yet increase performance and safety in crash scenarios.

SRCLID's end-to-end ("Atoms to Autos") modeling effort quantifies the microstructure-property relations of lightweight materials by evaluating them at various length scales, starting at the atomic level, for each step of the manufacturing process. Utilizing theory development, experimental characterization, and large scale computing, we have developed multiscale physics-based material models that are experimentally validated and account for uncertainty. Our design methodologies then guide design optimization of components, systems, and materials in engineering practice throughout the southern automotive corridor of the US. Both the new, lightweight materials and the math-based tools developed through SRCLID are being implemented in development of next-generation vehicles, with particular consideration given to their performance under various crash and high-speed impact environments.

In summary, the three major objectives of this Phase III project are:

- To develop experimentally validated cradle-to-grave modeling and simulation tools to optimize automotive and truck components for lightweighting materials (aluminum, steel, and Mg alloys and polymer-based composites) with consideration of uncertainty to decrease weight and cost, yet increase the performance and safety in impact scenarios;
- To develop multiscale computational models that quantify microstructure-property relations by evaluating various length scales, from the atomic through component levels, for each step of the manufacturing process for vehicles; and
- To develop an integrated K-12 educational program to educate students on lightweighting designs and impact scenarios.

Accomplishments

We are generating process-structure-property (PSP) relationships for aluminum, steel and magnesium alloys, and we have developed a physics-based multiscale internal state variable (ISV) model that includes uncertainty. We validated the model for aluminum and steel alloys and have begun to validate it for magnesium alloys. We developed a material database, ISV material models, and process models for extruded (AM30 and AZ61) and warm formed (AZ31) magnesium alloys. The database includes results from the mechanical and microstructure characterization studies performed using current experimental equipment at CAVS. The material model being developed is based on a multiscale modeling approach, where information from crystal plasticity, dislocation dynamics, and molecular dynamics simulations provide insights into the functional form of the ISV's evolution equations and corresponding material parameters. The extrusion and forming process models being constructed are finite element codes that are suitable for problems with large mesh distortions (e.g., extrusion using flat dies). The MultiStage Fatigue (MSF) Model has been correlated with different magnesium alloy strain-life curves and will be extended to describe joint behavior.

In conjunction with the multiscale internal state variable model, we have initiated optimization methods, including ISV and PSP with finite element analysis and design. With uncertainty under low strain rate, variable temperature, and high strain rate tension-compression-torsion tests, we characterized several structural materials for lightweighting (i.e., aluminum, steel, and Mg alloys) throughout their manufacturing and life cycle history. We then tested these materials in crash simulations and safety performance evaluations.

Six of our twelve tasks are directly related to the USAMP Front-End Magnesium Project. In strong support of the Integrated Computational Material Engineering program, we established several focused research teams with USAMP members and 10-year draft roadmaps for magnesium, steel and polymers with the DOE.

At the atomic scale, we established a number of atomistic potentials (i.e., Fe, C, Si, Al, Mg) that will be used in development of high strength steel alloys. We showed in the dislocation scale that the standard procedure of using just the elastic modulus and cohesive energy is not robust enough to capture the appropriate dislocation behavior. Instead, optimizing both the atomistic potential (MEAM) to the generalized stacking fault (GSF) energy curve and the Peierls stress is the key, as is illustrated in this report. In the absence of experimental data, one can use *ab initio* modeling results to complete the material database. In our research, the improved magnesium MEAM model was correlated with both experiments and *ab initio* results. Physical properties such as the lattice parameter, the vacancy formation energy, the GSF energy curves for basal slip, and mechanical properties such as elastic constants and Peierls stress for basal slip were all well captured.

Our cyberinfrastructure (CI) integrates our software and experimental information in Wiki and has garnered high recognition from TMS and USAMP. The CI has become the foundation of a virtual organization (VO), known as the Engineering Virtual Organization for Cyber Design (EVOCD). EVOCD has been developed with the primary goal of accumulating and protecting the intellectual property generated by the participants of the organization. The portal provides powerful passage for accruing and exchanging community knowledge as well as access to repositories of experimental data, material models and computational tools at different length scales, which together exploit the integrative nature of the Integrated Computational Material Engineering (ICME). To achieve this goal, EVOCD is comprised of four primary functional components that are the foundation of the VO: (i) Knowledge Management; (ii) Repository of Codes; (iii) Repository of Data; (iv) Online Calibration Tools. The implementation is primarily based on third-party, open-source software packages (such as Apache's Tomcat, Apache's ServiceMix, View VC, SVN) customized to the particular needs of EVOCD and the principles of the Service-Oriented Architectures (SOA). All of the computational and experimental databases can be found for the MSST cyberinfrastructure at https://icme.hpc.msstate.edu.

The composites effort is developing process/product concepts by employing multiscale material models. The natural fiber program is now able to produce good samples for evaluation. The biomechanics

program has been advanced to incorporating polymeric ISV models for tissues and evaluating damage phenomena for brain subject to high rate impact using finite element analyses. The biomechanics projects are included in order to incorporate the human effects into the multi-objective design of metal and composite materials as objectives.

We have graduated 12 students with MS and PhD degrees. For the K-12 program, we have developed crash kits and run K-2 and 3-6 grade "Mission Eggcellence" competitions in multiple counties throughout Mississippi in an effort to inspire their interest in science and engineering.

In our industrial partnership development, we have created strong ties with companies from various sectors (i.e., automotive, software, and local manufacturers), and they have embraced the technology being developed in this program. As the result of extensive interaction with MSC, Alpha Star, SAC, POSCO, and Mitsubishi Motors, we received $1,100,000 in additional cost sharing support from these companies.

We will continue developing the structure-property relationships and multiscale models for magnesium alloys with a focus on demonstrating the technology through the USAMP Mg Front-End Project sponsored by DOE. Composite, biomechanics and natural fiber research teams will move forward to develop material-specific multiscale models validated by critical experiments. We will employ these materials in crash simulations with new data generated. We will then update the cyberinfrastructure to expand the national and an international user base.

MISSISSIPPI STATE UNIVERSITY

Southern Regional Center for Lightweight Innovative Design

Phase III

Final Scientific & Technical Report

October 1, 2009-September 30, 2011

For compliance with contract requirements of Award DE-EE0002323

Task 1

MULTISCALE MICROSTRUCTURE-PROPERTY PLASTICITY CONSIDERING UNCERTAINTY

Submitted December 27, 2011

TASK 1: MULTISCALE MICROSTRUCTURE-PROPERTY PLASTICITY CONSIDERING UNCERTAINTY

Table of Contents

TASK 1: MULTISCALE MICROSTRUCTURE-PROPERTY PLASTICITY CONSIDERING UNCERTAINTY

Principal Investigator: Kiran Solanki
Co-Principal Investigator: Mark F. Horstemeyer
Chair Professor, Computational Manufacturing & Design
Center for Advanced Vehicle Systems
Mississippi State University
PO Box 5405, Mississippi State, MS 39762-5405
(662) 325-5449; fax: (662) 325 5433; *e-mail: mfhorst@cavs.msstate.edu*

Participants: P.T. Wang, D.J. Bammann, E.B. Marin, M.F. Horstemeyer, H. El Kadiri, Y. Hammi, A. Oppedal, Q. Ma, B. Li, C. Bouvard, S. Horstemeyer, A. Parkar

William Joost: Technology Area Development Manager
e-mail: william.joost@ee.doe.gov

Magda Rivera: Project Manager
e-mail: magda.rivera@netl.doe.gov

Contractor: *Mississippi State University (MSST)*
Contract No.: *DE-EE0002323*

Objective

- Develop physically-based and experimental-validated material models, extrusion and sheet process models, and corresponding design methodologies to enhance the workability of Mg alloys (extrusion: AM30, AZ61; sheet: AZ31).
- In particular, the work involves establishing material anisotropy relationships to understand the effect of material state (microstructure), product geometry and processing parameters on the mechanical properties, and final geometry (distortion) of formed Mg components.

Approach

We develop a material database, ISV material models, and process models for extruded (AM30 and AZ61) and warm formed (AZ31) magnesium alloys. The database includes results from the mechanical and microstructure characterization studies performed using current experimental equipment at CAVS. The material model being developed is based on a multiscale modeling approach, where information from crystal plasticity, dislocation dynamics, and molecular dynamics simulations are to be used to provide insights into the functional form of the ISV's evolution equations and corresponding material parameters. The extrusion and forming process models being constructed are finite element codes that are suitable for problems with large mesh distortions (e.g., extrusion using flat dies). Specific sub-tasks to be performed are as follows:

- Quantify structure-property relations with consideration of uncertainty for AZ31 sheet metal.
- Quantify structure-property relations with consideration of uncertainty for pre-extruded and extruded AM30 and AZ61.
- Perform lab-scale extrusion experiments on Mg alloys AM30 and AZ61 to generate data for validation of simulation tools.
- Develop crystal plasticity and ISV macroscopic models to model microstructure evolution during extrusion processes.

- Construct finite element models and performing analysis of stamping for Mg alloys.
- Develop robust process models for lab-scale and industrial extrusion processes using Eulerian-ALE finite element formulations.
- Develop methodologies for the optimum design of extrusion/stamping processes considering uncertainty.

Accomplishments

- Designed lab-scale indirect extrusion fixture with dies of different geometry, performed extrusion experiments on Mg alloys AZ61 and AM30 billets with conical and flat dies, respectively, and characterized deformed microstructure of material. Data generated is being used for validation of numerical simulation tools.
- Performed dynamic recrystallization (DRX) studies using interrupted tests for uniaxial compression experiments on Mg alloy AZ61 and channel die compression (CDC) experiments on Mg alloy AM30. The mechanical tests were performed for a range of temperatures and strain rates. Experimental data showed the strong effect that DRX has on the mechanical response of the alloy during hot deformation. Some of the experimental data is being processed to obtain the fraction of recrystallized grains and grain size evolution for ISV material modeling purposes.
- Studied twinning activation upon compression of an extruded AM30 alloy along two perpendicular directions. Some important twinning activation and sequence of twinning has been revealed through this analysis. Also, studies on the effect of twinning on the stress-strain response of the extruded AM30 were also carried out.
- Performed numerical simulations of the lab-scale extrusion experiments using the Eulerian finite element code HyperXtrude. Both the conical die experiments on AZ61 and flat die experiments on AM30 were modeled and simulated using the sine hyperbolic inverse material model with parameters fitted to experimental data from the literature. Predicted results of load-displacement and temperature histories captured well the experimental values.
- Predicted evolution of microstructure (texture) using streamline information extracted from HypeXtrude and the Visco-Plastic Self Consistent (VPSC) crystal plasticity model. The simulations exercised the Voce's and the dislocation-based hardening laws embedded in the code and whose material parameters were computed from in-house generated data obtained from high-temperature compression tests. The predicted textures for both the conical and flat die experiments agree well with the experimental ones.
- Developed preliminary version of internal state variable (ISV) material model that accounts for recrystallization and grain growth. Initial calibration of the model to one temperature and strain rate shows that it predicts well the stress softening behavior as well as the fraction of recrystallized grains. Current work is focused on fine tuning the model to fit the mechanical response for a range of strain rates and temperatures.
- Developed meso-scale capability for materials modeling based on the coupling of crystal plasticity and finite element methods (crystal plasticity finite element method, CPFEM) as well as Voronoi tessellation as a basis to repented synthetic microstructures.. The capability allows studying the behavior of crystal aggregates where each crystal is discretized with hundreds of finite elements. Current application of the capability is focusing on studying texture evolution and mechanical response of channel die compresses specimens.
- Performed sheet metal forming simulations at various temperatures and binding pressures with GM researchers.

- Performed sheet metal forming simulations at various temperatures and binding pressures with GM researchers.
- Performed tensile tests on specimen cut from the 12 mm, 9mm and 4mm sheet along different directions. Response seems to be isotropic.
- Developed a phenomenological model for DRX of AZ31. Experimental stress-strain response and grain size data from the literature were used to calibrate model.
- Completed implementation of plane stress case of the MSU DMG 1.0 Plasticity-Damage material model in the user material subroutine Vumat of Abaqus/Explicit. The model implementation includes the kinematic and isotropic hardenings, isotropic damage, and adiabatic conditions.
- Completed implementation of the Sellars-Tegart model (Abaqus/Vumat).
- Wrote 13 peer reviewed journal publications.

Future Directions

- Complete lab-scale extrusion experiments using other die geometries (dog-bone die and porthole die).
- Complete finite element simulations of lab-scale experiments.
- Model extrusion processes for industry-type profiles (double hat and dog-house profiles).
- Perform post-forming predictions for profiles used in structural applications.
- Finish development of ISV model with recrystallization and grain growth.
- Work with Altair (developers of HX) to enhance code for the use of ISV material models.
- Complete tool design and machining to perform sheet bending experiments.
- Complete analysis of lab-scale bending problems (validation of tools).
- Simulate the sheet bending process using DMG-Umat and compare with experimental results.
- Use the Visco-Plasticity Self Consistent (VPSC) material point simulator to predict the texture using the deformation history from finite element analysis.

Introduction

This final report presents the progress made in the SRCLID program - Task 1 during the period October 1, 2009 – September 31, 2011 (Phase 3). The main focus of the work was on material modeling, extrusion, and sheet metal forming. The ultimate goals of Task 1 are twofold: (1) an experimentally validated cradle-to-grave modeling and simulation effort to optimize automotive components (i.e., front end) for magnesium alloys with consideration of uncertainty in order to decrease weight and cost, and, yet, to increase the performance and safety in impact scenarios; (2) the multiscale ("From Atoms to Autos") modeling approach in which we quantify the microstructure-property relations by evaluating various length scales, starting at the atomic level for each step of the manufacturing process (i.e., extrusion, sheet) for vehicles.

Extrusion Process Modeling and Simulations of Magnesium Alloys

Modeling the extrusion process of magnesium alloys is a key component of the cradle-to-grave modeling approach used at CAVS to promote the use of magnesium extrusions in the automotive industry. Our research in this area relies on a combined experimental-modeling methodology where data

from lab-scale extrusion experiments are being generated to validate the prediction of selected numerical tools to model the extrusion process, i.e. the coupled thermo-mechanical (T-M) Eulerian finite element code HyperXtrude (HX) and constitutive frameworks based on macroscopic and crystal plasticity models. In addition, microstructural characterization of uniaxial and channel die compressed specimens were performed to study particular features of the microstructure evolution of Mg alloys that affect importantly their mechanical response: dynamic recrystallization and twinning. The specific materials used in this work are magnesium alloys AZ61 and AM30, although the bulk of the study has been focused on the latter.

Due to the strong connection of our work to the USAMP-MFERD project, the research activities of this task have been centered on developing and applying the above experimental-modeling methodology to predict the post-forming structural performance of extruded automotive components considering the deformation history of the material from the extrusion process. This aspect of our research is summarized in Figure 1, where the research activities have been grouped in five main topics marked as I to V. In this report we present mainly the activities that have been performed in topics I to IV in the context of Phase 3. Complementary activities on these topics as well as the post-forming experiments and modeling (topic V) have been presented in the quarterly reports and will be summarized in the final report of Phase 4.

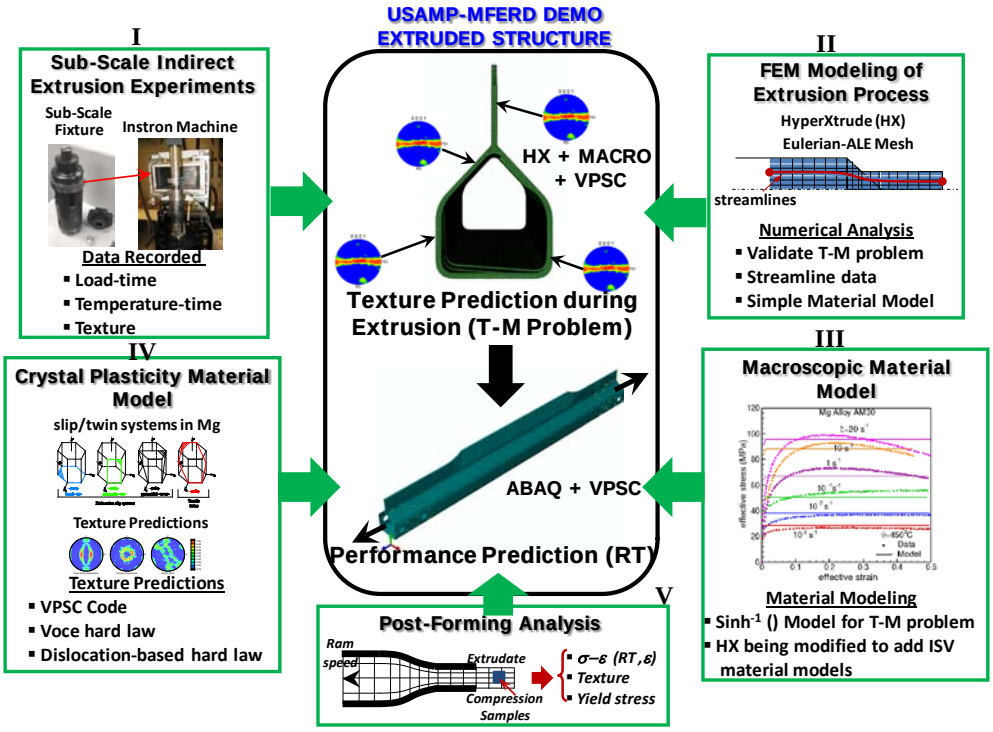

Figure 1: Research activities on the extrusion process as related to the post-forming analysis of extruded structural parts.

Sub-Scale Indirect Extrusion Experiments: Fixture and Experimental Studies/Results

A Fixture for Lab-Scale Extrusion Experiments

A lab-scale indirect extrusion fixture has been designed and built to study details of the extrusion process of Mg alloys as well as to generate experimental data for validation of the simulation tools. In essence, the fixture consists of (i) a chamber, (ii) a replaceable die, and (iii) a base. The chamber consists of two parts (top – bottom), each having an internal sleeve. A clamp holds these two parts together. Billets of 1 1/4" diameter and 1" length can be extruded using different die geometries (e.g. conical and flat dies) with extrusion ratios in the range of 6.25 to 125. Processing parameters that can be controlled are billet temperature and ram speed, and processing variables that can be recorded are extrusion load

versus displacement and temperature histories at particular points in the die. Besides, microstructure information (texture, grain morphology) as well as material flow patterns can be characterized on the extruded sample using microscopy techniques. Details of the fixture and its set-up on the testing machine for the extrusion experiments are shown in Figure 2.

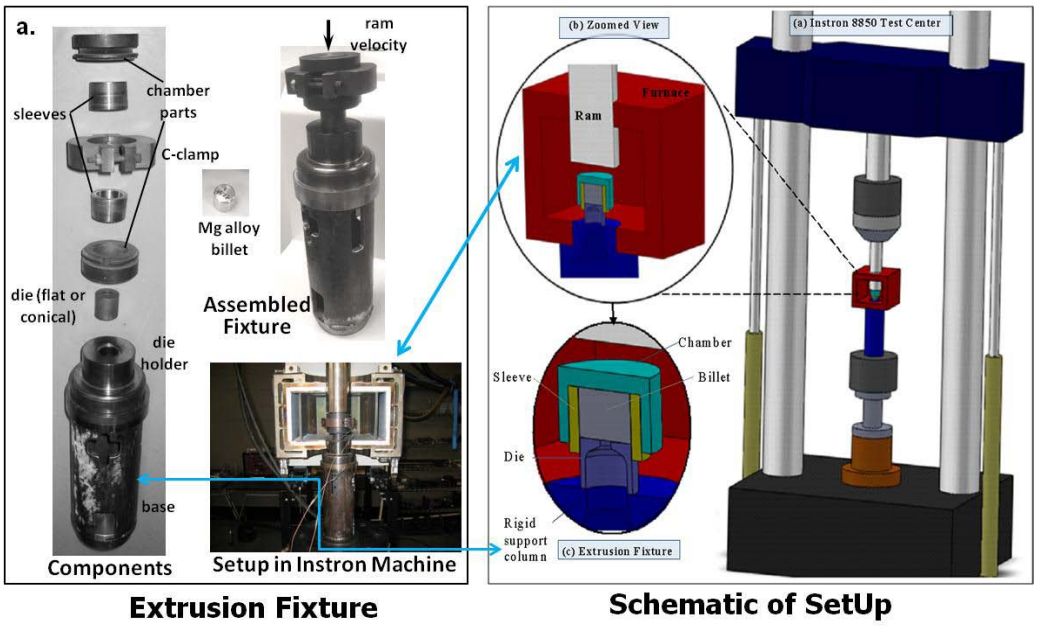

Figure 2: Details of the Lab-Scale Fixture for Indirect Extrusion and set-up on the Instron machine.

The lab-scale fixture has been designed to accommodate different die geometries as shown in Figure 3. Three different profiles can be generated with these dies: circular cross section, dog-bone cross section and thin-walled circular tube. Up to know we have performed experiments using the conical and flat die for circular profiles, results that are reported below, while experiments using the other die geometries are in progress.

Lab-Scale Extrusion Experimental Results

The end goal of these experiments is to build an experimental database for extrusion of Mg alloys that can be used to validate numerical models of the process, which include finite element models and robust internal state variable and polycrystal plasticity material models. Figure 4 presents the thermo-mechanical data (load and temperature histories) recorded from the extrusion experiments using the conical and flat dies to extrude solid circular cross section profiles. The conical die experiments were performed on Mg alloy AZ61 with a billet temperature of 454^{o}C, a ram speed of 5 mm/min and an extrusion ratio of 6.25 (1/2” profile diameter). As shown in Figure 4 these experiments used two sample geometries (billet and billet-pocket) and were designed to compare the predictive capabilities of Lagrangian (ABAQUS) and Eulerian (HyperXtrude) finite element codes. On other hand, the flat die tests used Mg alloy AM30 and were performed at a billet temperature of 454^{o}C, ram speeds of 5 and 10 mm/min, and an extrusion ratio of 25 (1/4” profile diameter). Note that, although not reported here, flat-die experiments with other ram speeds (15, 20, 30, 40 mm/min) have also being carried out.

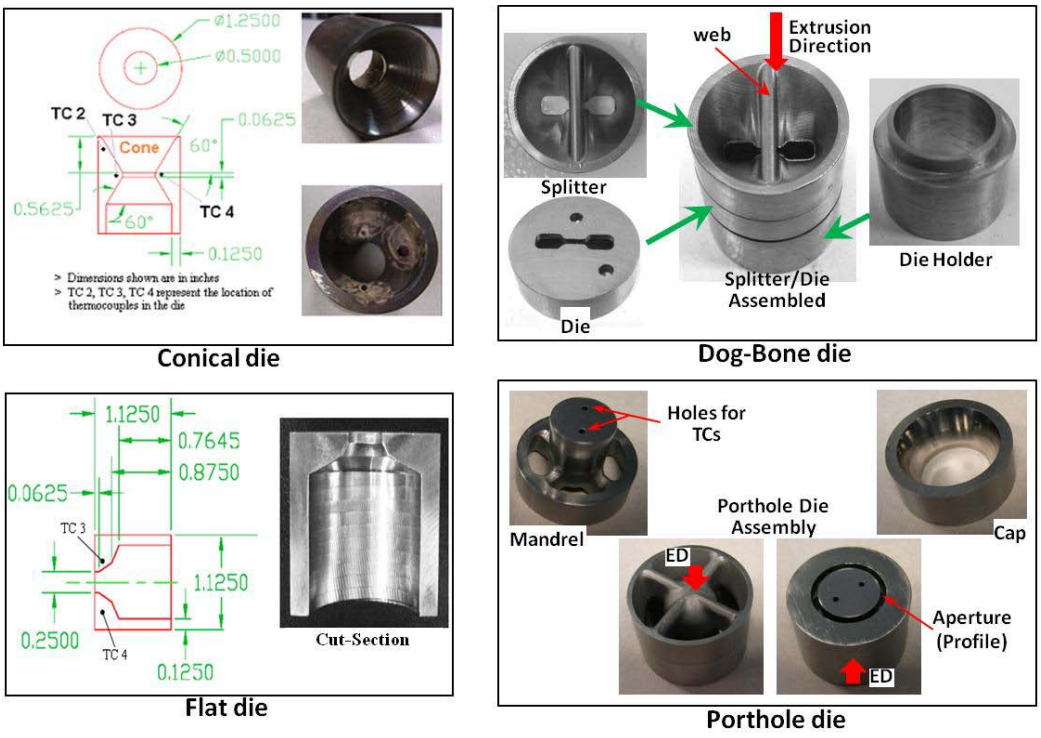

Figure 3: Different die geometries designed for the lab-scale extrusion experiments.

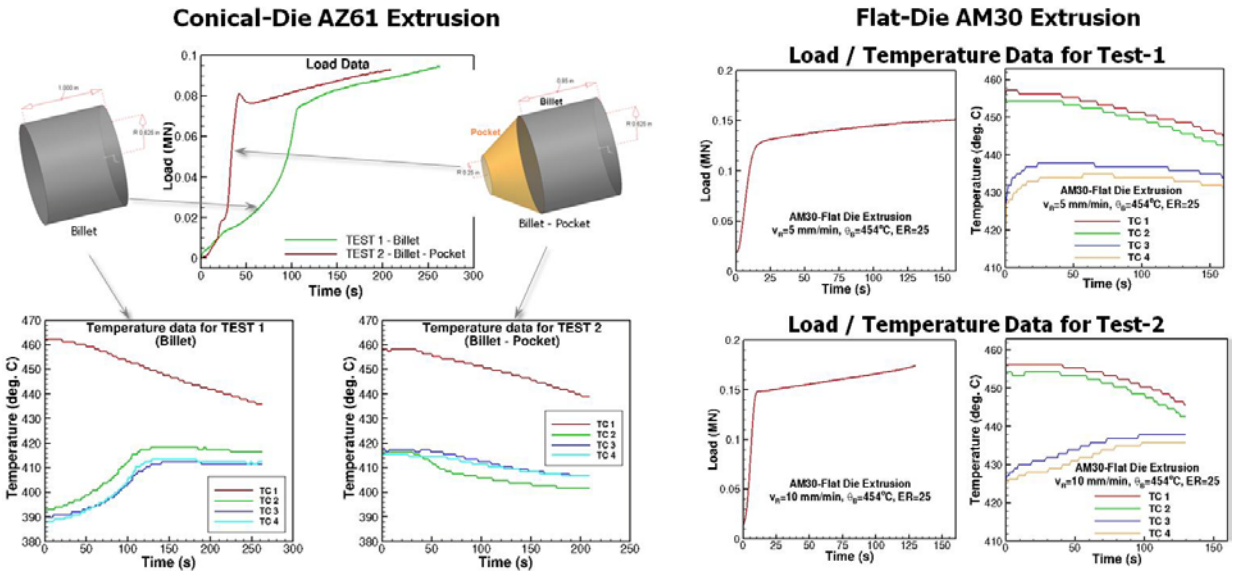

Figure 4: Lab-scale experimental results using the conical die for AZ61 extrusion and the flat die for AM30 extrusion.

Figure 5 shows the flow patterns, texture and grain morphology at the exit of the bearing area, along the axis of the billet (center), for both the conical and the flat dies. Clearly, at the selected material point for both cases, the initial texture of the pre-extruded billet evolves towards a rod-type texture typical of extrusion. Also not shown here, shearing effects due to the die wall, which usually tend to weaken this texture, are not predominant at these points because indirect extrusion minimizes the frictional effect as

compared to direct extrusion. Also, the grain morphology depicted by the micrographs from Optical Microscopy (OM) and Scanning Electron Microcopy (SEM) shows a refined grain structure typical of a dynamic recrystallization process, a phenomenon usually occurring during hot extrusion of Mg alloys.

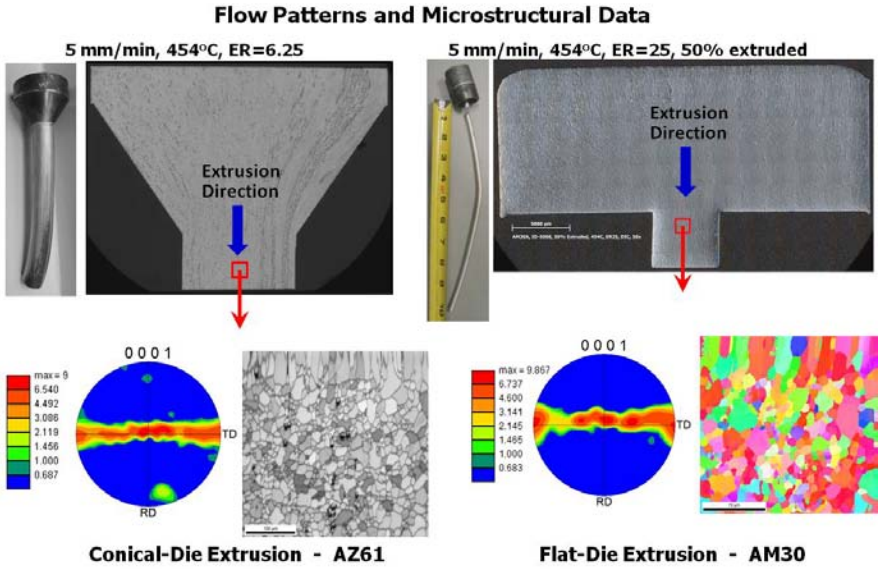

Figure 5: Material flow lines and microstructure of partially extruded billets using OM and SEM.

Dynamic Recrystallization Studies in Mg Alloy AZ61 during Extrusion

Due to the low workability of magnesium and its alloys, thermo-mechanical processing of Mg alloys, such as extrusion, rolling, sheet forming, and severe plastic deformation (SPD), is normally performed at elevated temperatures at which dynamic recrystallization (DRX) dominates the microstructure evolution. The resulting microstructure (texture) from DRX strongly influences the mechanical properties of the processed Mg alloys; hence, investigating DRX mechanisms in Mg and its alloys is extremely important for the design and optimization of lightweight structural components.

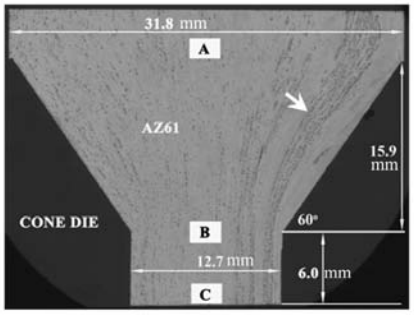

Figure 6: The 60° conical die section of the AZ61 Mg alloy extruded at 450°C with a ram speed of 5 mm/min and extrusion ration of 6.25. EBSD scans on the partially extruded billet were obtained at locations labeled A, B, and C. The gray lines indicated by the arrow are the extrusion flow lines.

In this study, an AZ61 Mg alloy (mass %, Al 5.86%, Zn 0.81%, Mn 0.29% and Mg in balance) has been extruded using the lab-scale fixture with a 60° conical die and processing parameters: billet temperature of 450°C, ram speed of 5 mm/min and extrusion ratio of 6.25. The AZ61 billet of 31 mm in diameter and 25.4 mm in length was heated to 450°C in the furnace that houses the extrusion fixture built on the sample stage of an INSTRON 8850 machine and then was extruded. A high temperature graphite

paste GPL-420 was used as lubricant during extrusion. The experiment was terminated after 80% of the initial billet was extruded and the extruded AZ61 alloy embedded in the cone die was taken out to investigate the microstructure evolution using Electron Back Scattering Diffraction (EBSD), see Figure 6.

Figure 7 displays the EBSD inverse pole figure (IPF) maps of locations A, B and C in the extruded AZ61 alloy. In Figure 7(a), dynamically recrystallized grains can be seen with a fine grain size, as shown in the magnified view of a rectangular area. The grain size and the grain morphology progressively change as the extrusion proceeds. A misorientation profile along the line EF substantiates that some grain boundaries satisfy the ~86° boundary misorientation. Thermally driven grain coarsening can be seen in Figure 7(b) and (c).

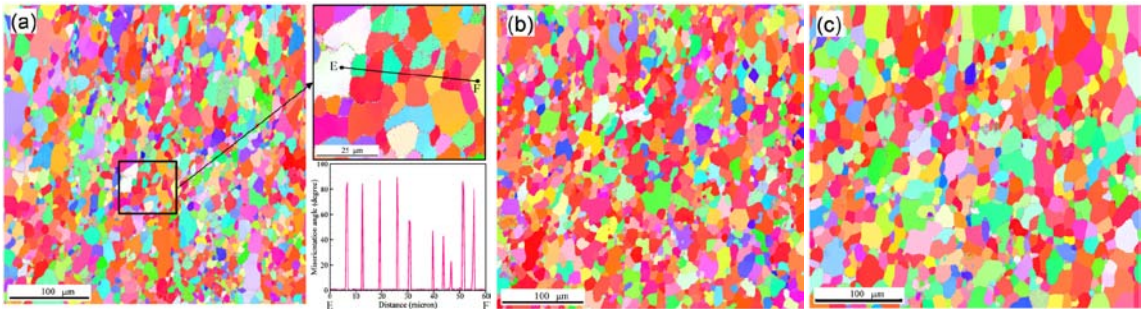

Figure 7: EBSD inverse pole figure (IPF) maps of locations A (a), B (b) and C (c) in the extruded AZ61 alloy. The grain size and morphology vary from location A to C corresponding to the extrusion timeline. The fine grains in (a) are the dynamically recrystallized grains during extrusion, and the fine DRX grains can be better seen in the highlight area in (a). The point-to-point misorientation profile along the line EF in the highlighted area substantiates the ~86° boundary relationship. As the extrusion proceeds, grain growth can be clearly seen in (b) and (c).

Figure 8 shows the EBSD Image Quality (IQ) maps of the dynamically recrystallized grains. In these maps, grain boundaries with a misorientation of 86.3±5° $\{1\bar{2}10\}$, which are actually $\{1\bar{2}10\}<10\bar{1}\bar{1}>$ twin interfaces, were plotted in yellow. A tolerance of 5° is reasonable for the large plastic deformation of the material. Those grain boundaries with a misorientation greater than 15° were plotted as thin, black lines. In the EBSD IQ map of location A (Figure 8(a)), many fine grains with a size below 10 μm are

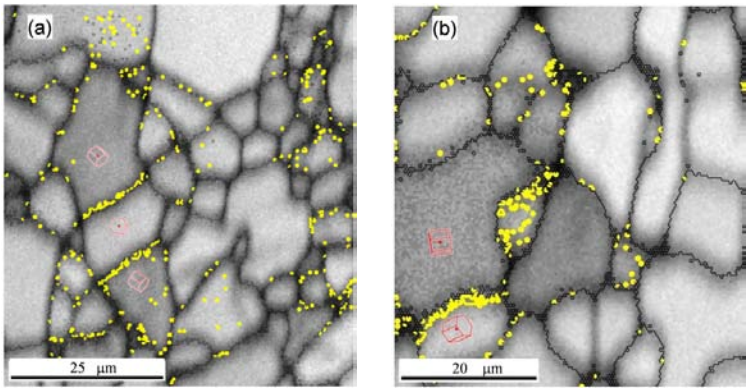

Figure 8: $\{1\bar{2}10\}<10\bar{1}\bar{1}>$ twins in the EBSD image quality (IQ) maps at location A (a) and C (b) in the extruded AZ61 alloy. The yellow lines correspond to the 86.3±5°$\{1\bar{2}10\}$ orientation relationship which are the $\{1\bar{2}10\}<10\bar{1}\bar{1}>$ twin boundaries. The 5° tolerance is reasonable for the large plastic deformation. The thin black lines represent the boundaries with misorientations greater than 15°.

shown. Those grains separated by the yellow lines satisfy the $\{1\bar{2}10\}<10\bar{1}\bar{1}>$ twin orientation relationship. Three of these grains are marked with a red hexagon to show their orientations in 3D. Similar pattern can be seen in Figure 8(b). After the grains coarsen during extrusion, fine grains coalesce

via the migration of the grain boundaries (actually twin boundaries; we call them twin boundaries because the grains on both sides satisfy the twin orientation relationship). This can be seen from the bulging of the twin boundaries in Figure 8(b). Grains in dark gray have a high density of dislocations, whereas those in bright gray are with a low density of dislocations. The grains in dark gray are being consumed by the migration of the twin boundaries, as a result of DRX.

Recrystallization Studies of Magnesium Alloy AM30

Channel die compression tests were continued at 300 and 400 °C at strain rates of 10^{-1}, 10^{-2} and $10^{-3}s^{-1}$ and at strain levels of 30%, 80%, 130%, and 180%. During the experiments at 400 °C, there was a brief set back due to the channel-die apparatus cracking. A new channel-die was fabricated and testing continued. Then all the compressed samples were examined by optical microscopy and generated the features supporting twinning activity and recrystallization behavior (Figures 10and 11). Electron back scattering diffraction (EBSD) experiments were also continued to gather the information about the texture, new grains, and recrystallized grains, and their orientations to culminate the deformation mechanism. Figure 9 shows the summary of EBSD analysis that was accomplished (marked as green) and ongoing (marked as red), along with the twinning activity observed on the 3% compressed samples. At quick stroke rates, twinning was very dominant in the samples

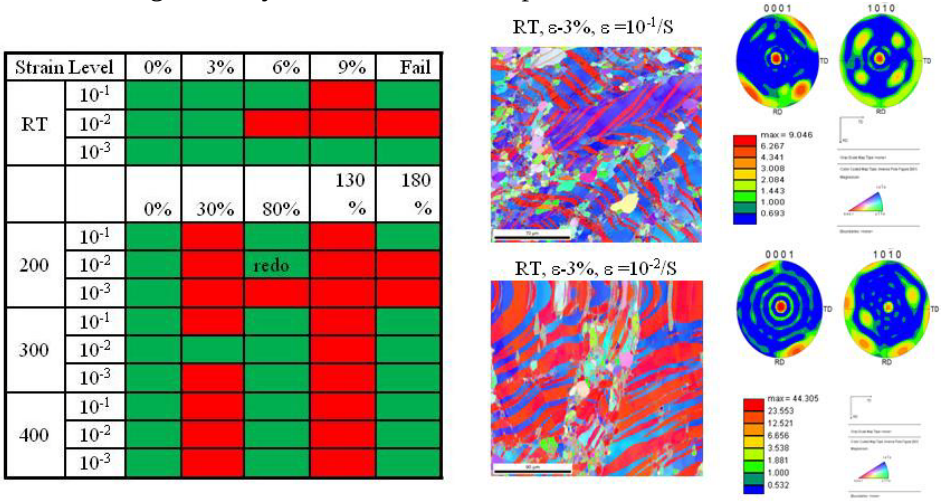

Figure 9: Ongoing and accomplished EBSD experiments along with twinning morphology

For all samples the EBSD data shows a change in orientation from initial texture to that of the compressed samples, see Figure 10. This change typically goes from mostly prismatic to basal, which agrees with work reported in the literature. Twinning activity has also being observed in the deformed samples, Figure 11. From 300˚C to 400˚C one can observe an increase in grain size, Figure 12. Optical Microscopy was performed using a Zeiss Axiovert optical microscope. Microstructure analysis of samples deformed at room temperature, 200˚C, 300˚C, and 400˚C was performed to determine grain size evolution. Grain size analysis is currently under progress. Optical images have also been used to determine the recrystallized fraction of grains using the Image Analyzer software, Figure 12. The EBSD data from the undeformed sample was used as reference. Measurements revealed an increase in misorientation angle with increases in deformation temperature.

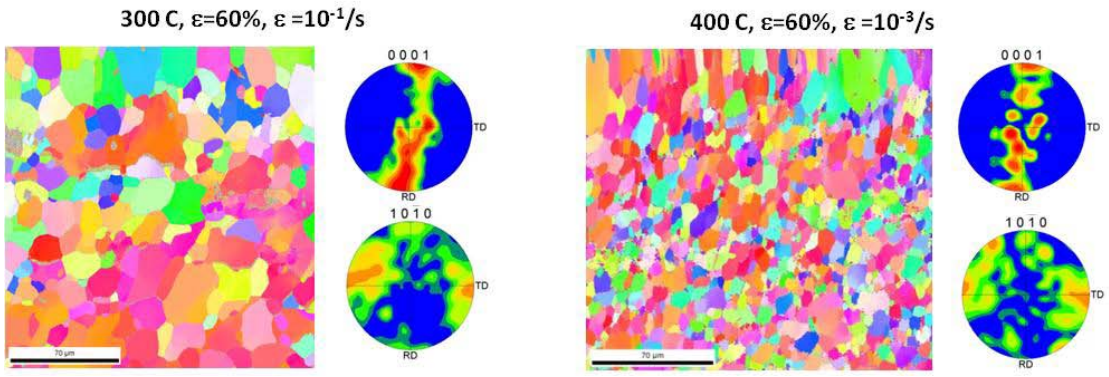

Figure 10: EBSD pattern at 300°C and 400°C

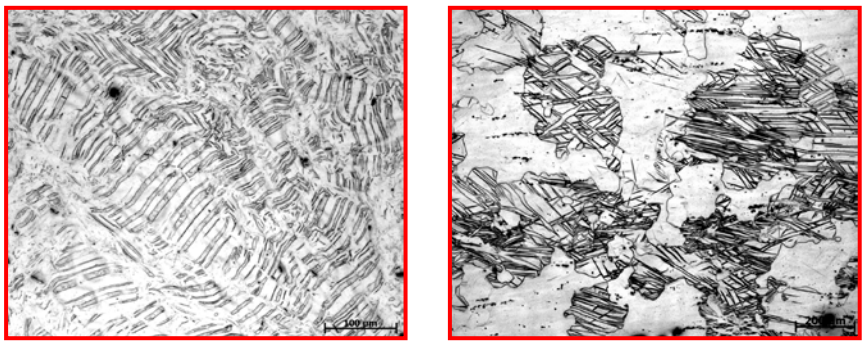

Figure 11: Twinning at room temperature (ε=0.03) and 450°C (ε=0.6). Strain rate of 10^{-1} s^{-1}.

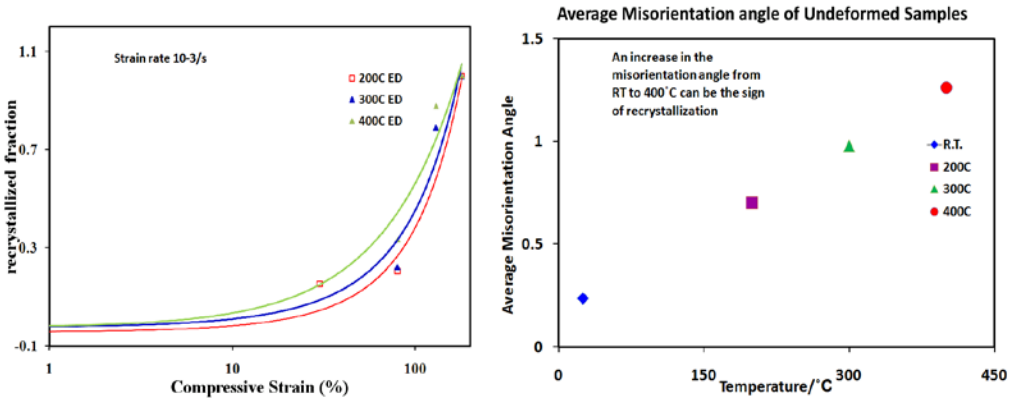

Figure 12: Changes of recrystallized fraction and misorientiation angle with strain and temperature

Twinning and double-twinning upon compression of an extruded AM30 alloy

Due to the crucial effect of twinning on the mechanical response and texture evolution of magnesium, we continue to study twinning activation upon compression of an extruded AM30 alloy along two perpendicular directions. Although there are results reported in literature for twinning related issues, no detailed twinning activations from compression along two perpendicular directions has been reported previously. Some important twinning activation and sequence of twinning has been revealed through our extensive study on extruded AM30 alloy.

Figure 13a shows the two loading directions of samples from the ED (extrusion direction) and ERD (extrusion radial direction) in the original AM30 billet. Figure 13b presents the initial texture of the AM30 based on x-ray diffraction (XRD). Figures 13c, 13d and 13e present the EBSD inverse pole figure

(IPF) maps of the ED samples before deformation, and at -0.036, and -0.088 true plastic strains, respectively. As shown in Figure 13d, profuse $\{10\bar{1}2\}\langle 10\bar{1}1\rangle$ twinning activated within both the elongated parent grains and small, equiaxed recrystallized grains. These zonal shape twins crossing the matrix grain boundaries from grain to grain are typical of residual twins. Figure 13e reveals that at strain -0.088, nearly all parent grains were totally twinned by the primary $\{10\bar{1}2\}$ twins, except for a portion of the small recrystallized grains.

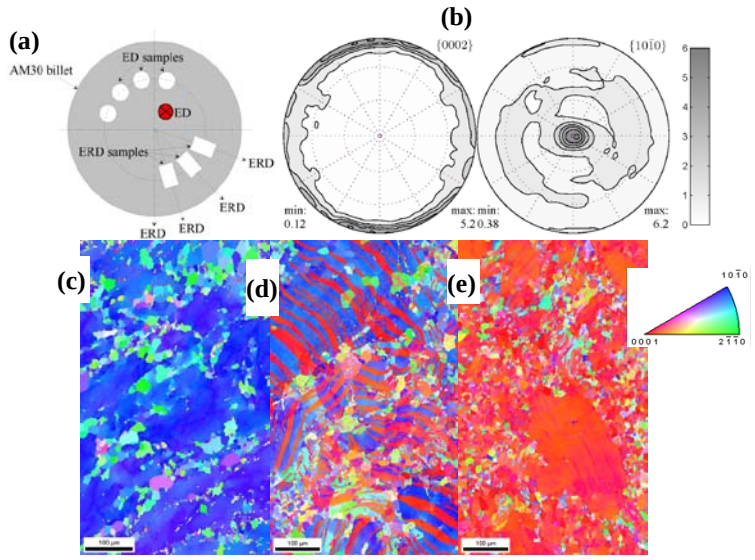

Figure 13: (a) The ED and ERD samples in the AM30 billet; (b) the initial texture of AM30 alloy based on XRD, typical of the prismatic texture from extrusion; and EBSD IPF maps of ED samples at strain (c) 0; (d) -0.036; (e) -0.088 showing $\{10\bar{1}2\}\langle 10\bar{1}1\rangle$ twin development. (The loading direction is out of the paper. IPFs represents the ED direction.)

The third-order twinning of $\{10\bar{1}2\}-\{10\bar{1}1\}-\{10\bar{1}2\}$ and $\{10\bar{1}2\}-\{10\bar{1}3\}-\{10\bar{1}2\}$ also initiated under compression along ED and the $\{10\bar{1}1\}-\{10\bar{1}2\}$ and $\{10\bar{1}3\}-\{10\bar{1}2\}$ double twinning coexisted in the matrix grain of ERD as shown in Figure 14a and 14b, respectively.

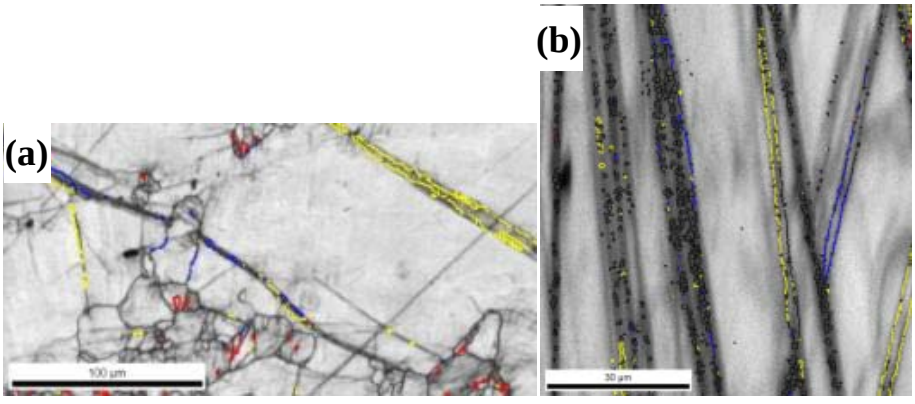

Figure 14: (a) The $\{10\bar{1}2\}-\{10\bar{1}1\}$ double twin and the $\{10\bar{1}3\}-\{10\bar{1}2\}$ double twin evolved in the completely twinned matrix grain in the ED rupture sample; (b) the $\{10\bar{1}2\}-\{10\bar{1}1\}$ and $\{10\bar{1}3\}-\{1021\}$ double twins in the ERD rupture sample. Fine black lines refer to grains boundary >15°.

Another time-sequence double twinning is also originated in the matrix grain as shown in Figure 15. This figure shows that the primary $\{10\bar{1}1\}$ twins were followed by $\{10\bar{1}2\}$ twins involved/contained within the $\{10\bar{1}1\}$ twin.

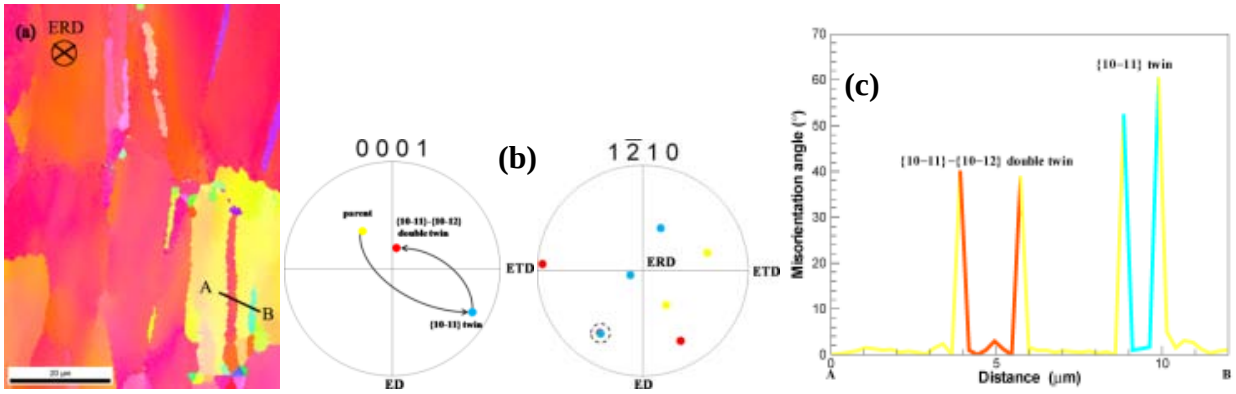

Figure 15: (a) Primary contraction $\{10\bar{1}1\}$ twin and $\{10\bar{1}2\} - \{10\bar{1}1\}$ double twin in ERD sample at plastic strain -0.088. The twinning sequence was proved by (b) the common rotation axis $\langle 1\bar{2}10 \rangle$ and (c) the characteristic misorientation ~56° for $\{10\bar{1}1\}$ twinning and ~38° for $\{10\bar{1}2\} - \{10\bar{1}1\}$ twinning. The colors used here correspond to the colors of the IPF map in (a). The single $\{10\bar{1}1\}$ twin in (a) verified the time-sequence of $\{10\bar{1}1\} - \{10\bar{1}2\}$ double twinning in ERD samples.

Effect of Twinning on the Mechanical Response of Extruded AM30 Alloy

Uniaxial compression along two perpendicular directions of AM30 was conducted to obtain stress-strain curves. The quasi-static compression true stress-strain behavior and corresponding strain hardening rates at room temperature and at a strain rate of 0.001 /s along the ED and ERD are presented in Figure 16. The true plastic stress-strain behavior along the ED exhibits a sigmoidal-shaped flow curve in which four stages corresponding to four hardening rates arises: i) an initial decreasing hardening rate up to approximately 0.5% plastic strain (~140 MPa); ii) a very low concave increasing hardening rate, from approximately 0.5% to ~2.5% plastic strains, termed Regime I; iii) a very high hardening rate between approximately 2.5% and 7.5% plastic strains termed Regime II; and iv) a decreasing hardening rate from approximately 7.5% plastic strain to rupture termed Regime III. These four stages are better appreciated in a strain hardening rate vs. stress (theta-sigma) curve, which corresponds to the evolution of hardening rate as a function of stress. Note that Regime II in the hardening-stress behavior has an increasing rate.

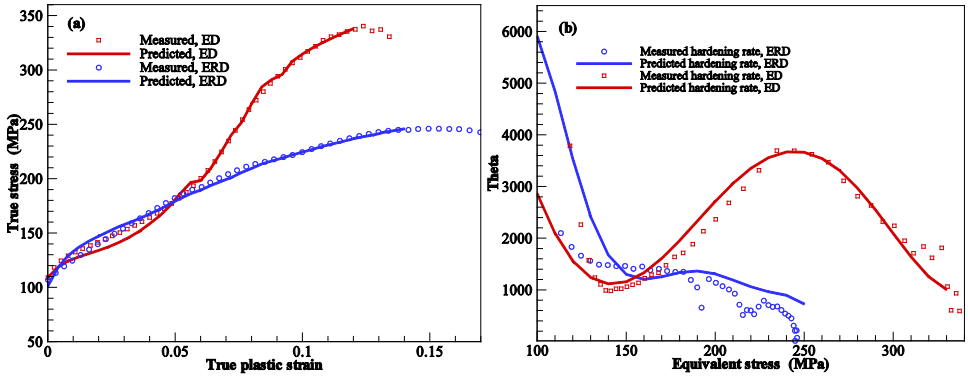

Figure 16: Measured and predicted flow behavior for an extruded AM30 Magnesium alloy loaded in compression along the extrusion direction (ED) and along extrusion radial (ERD) direction showing results for (a) the stress-strain behaviors and (b) the strain hardening rates versus stress calculated from the ED and ERD stress-strain behaviors.

The stress-strain behavior obtained under simple compression along the ERD seems to show exclusive concavity typical of slip predominance. However, the hardening rate curves reveal a peculiar regime of constant slope up to 4% plastic strain, termed as Regime IIR, which followed an early slip regime up to 1.7% plastic strain. This regime is followed by a regime of parabolic decrease with a transition marked with load drops in the hardening rate. Ductility seems to be higher under the ERD compared to the ED. The saturation stress is remarkably higher under ED than under ERD, although the last stages under both orientations are marked by pyramidal slip activities. This is indicative of a peculiar hardening behavior brought about by twinning.

The typical "S" shape of ED true stress-strain curve shown in Figure 16a resulted from profuse $\{10\bar{1}2\}$ extension twinning. The high increasing strain hardening rate was indeed caused by the twinning transmutation effect upon profuse twinning growth into the matrix. With respect to ERD, however, extension twinning was suppressed due to twin multivariants and twin interaction resulting in a parabolic stress-strain curve and the decreasing strain hardening rate as shown in Figure 16. The Hall-Petch effect, in which twin interfaces were considered as grain boundaries, was non-reasonable, otherwise, the ERD hardening rate should be very high due to the tin primary compression twin and/or double twins had the more effective Hall-Petch effect on hardening rate.

Finite Element Modeling of the Lab-Scale Extrusion Experiments

Extrusion is a metal forming process used to produce long complex profiles with high tolerance and surface quality. Unlike other material forming processes, such as forging and rolling, profile extrusion process usually has complex material flow patterns accompanied with extremely large and severe plastic deformation. Such a feature puts rigorous requirements on the numerical tools used to simulate the extrusion process. As Lagrangian codes have important limitations to simulate general 3-D material flows trough complex die geometries (e.g. porthole dies) unless intensive re-meshing is employed, in this work we rely on Eulerian finite element formulations to perform the extrusion simulations. One such software is HyperXtrude, a code developed by Altair Engineering, Inc.

HyperXtrude is a finite-element based code designed to model/simulate the non-isothermal material flow during metal extrusion. The code uses an Eulerian formulation of the fundamental differential equations that govern flow and heat transfer of non-Newtonian incompressible viscous fluids. As such, the code uses a fixed-space control volume representation of the problem domain through which the material flows as it is extruded through the tooling. Figure 17 presents the HyperXtrude finite element models constructed to simulate the lab-scale experiments with the conical and flat dies, respectively. Due to symmetry, only a quarter model has been used. Note that the models include the tooling to have more flexibility when specifying the boundary conditions, in particular the thermal ones, an important aspect when validating the models.

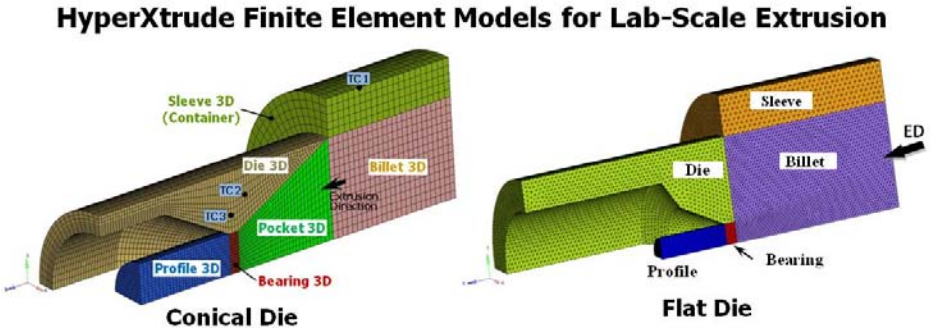

Figure 17: HyperXtrude finite element models for extrusion simulations using the conical and the flat dies.

Particle tracing (streamlines) is a capability offered by HyperXtrude to determine the trajectory and corresponding deformation histories of individual material particles as they traverse the fixed control

volume that defines the extrusion deformation domain. This capability is important when performing an uncoupled analysis (post-processing) to evolve the material state and microstructure during extrusion, i.e. when using stand alone codes for complex constitutive models which are driven by the deformation path history provided by HyperXtrude. Figure 18 provides an example of the streamline analysis performed for the conical die extrusion. Three material particles have been selected and the deformation histories along the corresponding streamlines at three different times (transient problem) have been obtained, although only the history of strain and pressure for the AXIS streamline has been plotted in this figure. In this work, the uncoupled approach is being used to determine texture evolution using crystal plasticity models.

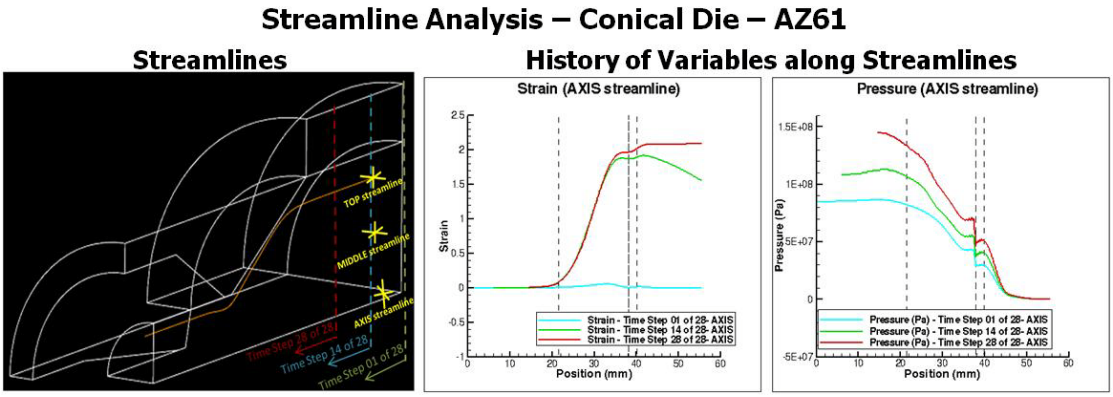

Figure 18: History of variables along particular streamlines of the material flow in conical die extrusion.

Modeling of Lab-Scale Experiments Using Macroscopic Material Models

The material library in the current version of the HyperXtrude mainly considers flow-stress type models, with general constitutive equation: $\sigma = \hat{\sigma}(\epsilon, \dot{\epsilon}, \theta)$, where σ is the flow (effective) stress, ϵ is the effective strain, $\dot{\epsilon}$ is the effective strain rate, and θ is the temperature. No provision for internal state variable (ISV) models is presently available in the code even though HyperXtrude's developers are currently working on extending the material capabilities of the code to include ISV material models. For this reason, the extrusion simulations presented here have been performed using flow-stress models. In particular, we are using the sine hyperbolic inverse model which is given by:

$$\bar{\sigma} = \frac{1}{\alpha}\sinh^{-1}\left[\left(\frac{Z}{A}\right)^{1/n}\right], \qquad Z = \dot{\epsilon}\exp\left(\frac{Q}{R\theta}\right) \tag{1}$$

where: n, Q, A, R and α are material parameters. Note that this model with constant material properties typically predicts a steady state response which may not capture well the mechanical response of Mg alloys, materials that usually exhibits a stress softening behavior due to dynamic recrystallization. However, some simple modifications of the model could be introduced to approximately describe such feature as indicated below for the case of Mg alloy AZ61.

Conical Die Extrusion Simulations – AZ61

Figure 19 presents experimental stress-strain curves under different temperatures and strain rates obtained from the literature [1] for Mg alloy AZ61. As shown in this figure, the softening behavior observed in the experimental mechanical response is due to dynamic recrystallization, a phenomenon typically displayed by Mg alloys during hot working. This behavior cannot be captured by the above material model unless some of the parameters are made function of strain. In this respect, following [1], we have used the sine hyperbolic inverse model with the parameter A being strain dependent. The functional form for $A = \hat{A}(\epsilon)$ has been obtained by fitting experimental data reported in [1], see Figure

19. The use of $\hat{A}(\epsilon)$ in this material model captures the stress softening response displayed by the experimental stress-strain curves, as shown also in Figure 19.

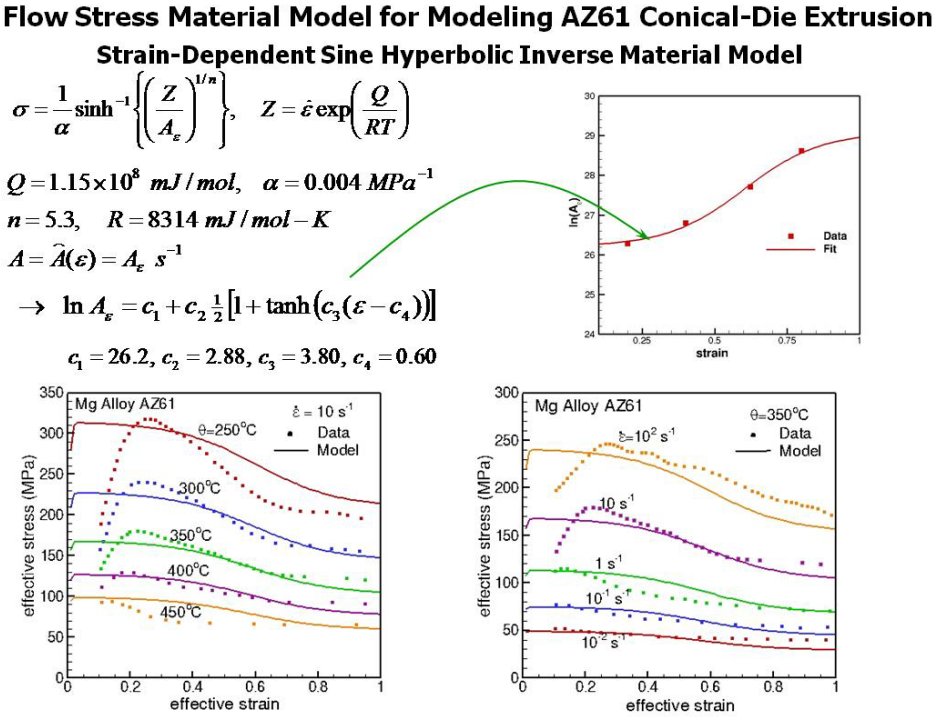

Figure 19: The use of a strain-dependent sine hyperbolic inverse material model captures well the stress softening response exhibited by the experimental data for Mg alloy AZ61.

This version of the sine hyperbolic inverse model has been implemented in HyperXtrude by means of a User Defined Function (UDF) to model the extrusion process of AZ61. The extrusion of this alloy is modeled as a transient process using the finite element model shown in Figure 17 together with adequate thermo-mechanical boundary conditions suggested by the experimental scenario. The predicted load and temperature as a function of time are shown in Figure 20. Note that the simulation predicts well the bump observed at the breakthrough load.

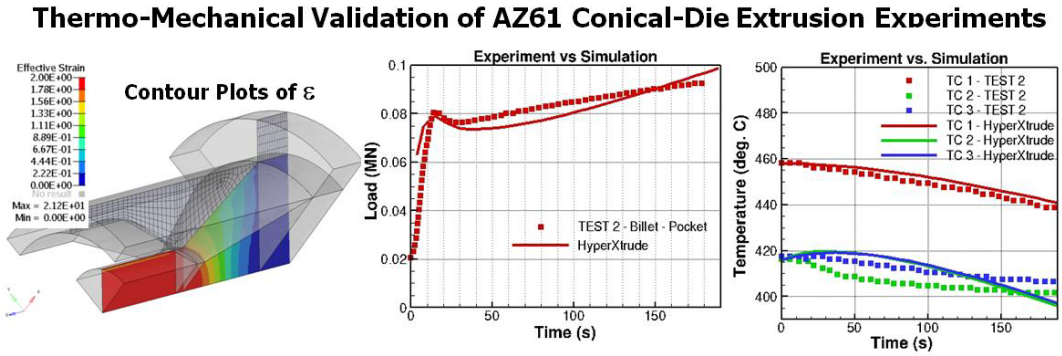

Figure 20: HyperXtrude simulation results using a strain-dependent sine hyperbolic inverse model. Note that the bump in the load-time response is captured by the simulations

Flat Die Extrusion Simulations – AM30

HyperXtrude simulations of the lab-scale experiments performed with a flat die were also carried out using a sine hyperbolic inverse material model. In this case, however, the model used constant material

parameters as not enough experimental data were available to characterize the parameter *A* as a function of strain, see Figure 21. The simulations for the different processing parameters have been performed using the finite element model (control volume) displayed in Figure 17.

Simulation results are presented in Figure 21. For now, only two ram speeds has been simulated: 5 mm/min and 10 mm/min, both run with an initial billet temperature of 450°C and an extrusion ratio of 25. Note that the load and temperature evolution are predicted reasonably well. On-going work is focused on simulating the rest of the experiments performed with the flat die.

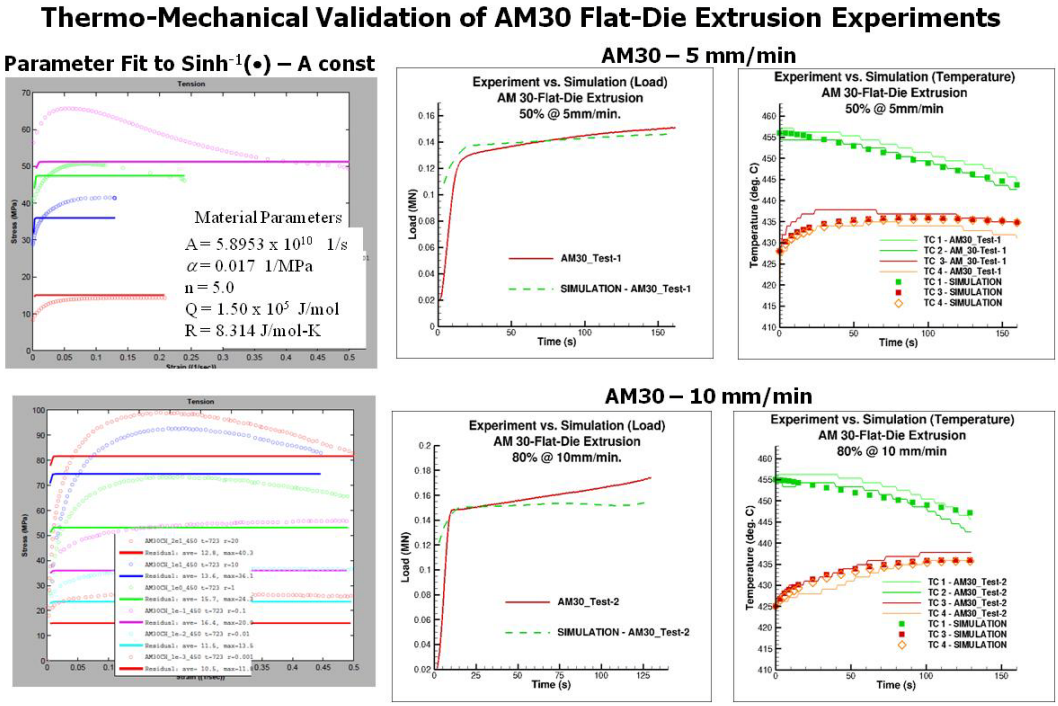

Figure 21: Material model fitting and HyperXtrude simulations versus experiments for the flat-die extrusion of Mg alloy AM30.

Internal State Variable Constitutive Model for Extrusion Modeling

The research version of CAVS's macroscopic constitutive framework will be used to model the extrusion process using HyperXtrude, once this code has the user interface needed to implement complex material models. Meanwhile, some work has been performed to extend the ISV model to account for recrystalization and grain growth, phenomena typically present during hot extrusion. A summary of the ISV model equations without recrystallization is presented in Figure 22. The same figure presents the experimental data for AZ61 used to fit the material constants of the model. Note that the stress softening observed in the experimental data is due to recrystallization. As this version does not account for this phenomenon, the fitting was mainly performed using the hardening part of the curve. This version of the model with the computed constants is being used to model the lab-scale conical die extrusion experiments of AZ61 using ABAQUS and a UMAT that implements the numerical integration of the model.

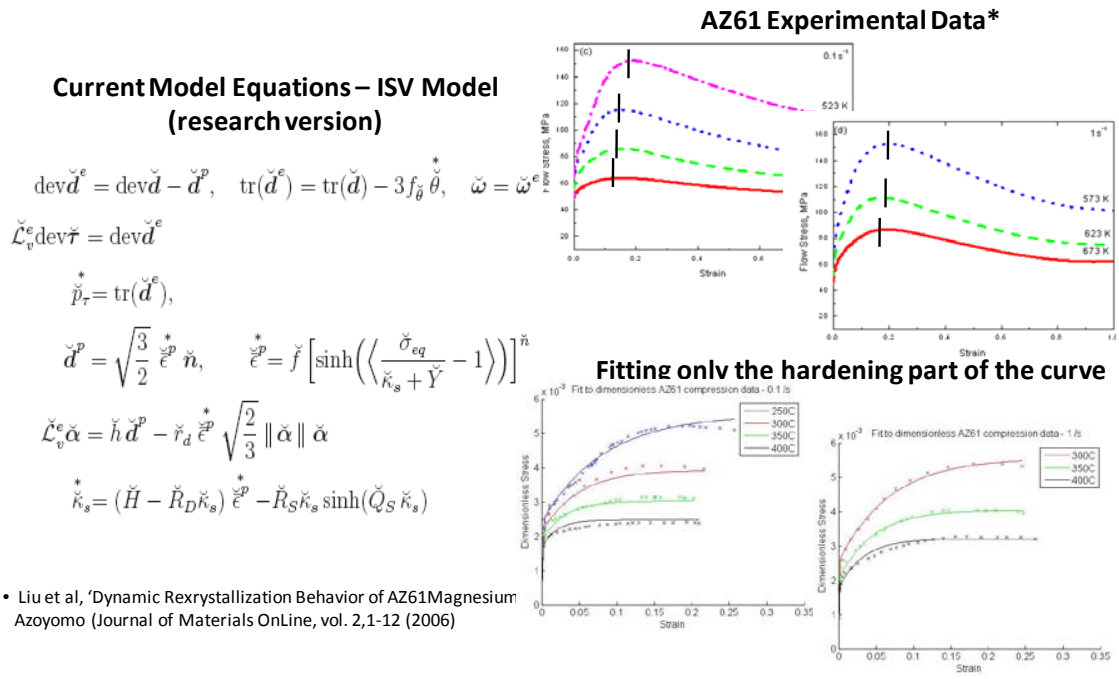

Figure 22: Current research version of ISV material model fitted to AZ61 experimental data. Fitting was limited to the hardening part of the curves.

Recrystallization is a complex inhomogeneous process in which nucleation and growth of new strain--free grains replaced the worked microstructure of a strained material. It is mainly due to the motion of grain and sub-grain boundaries. As the boundaries move, they sweep away the dislocation structure, leaving a strain-free material with a very low dislocation density. When the expanding grain reaches a critical size, it becomes a stable recrystallized grain that can continue growing due to grain growth processes. The driving force for recrystallization is the energy stored in the dislocation structures. In this work we attempt to model recrystallization using the ISV material modeling framework, see Figure 22. For this purpose, we have extended the above constitutive equations with features to capture these phenomena. The specific changes that have been introduced are:

- Add the effect of grain size to both the initial mechanical strength Y and the evolution of the isotropic hardening variable, κ, a variable that physically represents the evolution of statistically stored dislocation.
- Add a recovery or softening term to the evolution of κ whose effect is triggered when the energy stored in the material during deformation reaches a critical value,
- Develop physically–based evolution equations for the fraction of recrystallized grains and grain size,
- Incorporate a model for geometrically necessary dislocations through a stress–like variable (mis-orientation variable) which effectively accounts for the stored energy due to misorientations of the deformation-induced dislocation boundaries.

The extended model is presented in Figure 23. The same figure also presents the fitting of the model to AZ61 stress-strain data at 300°C and 1.0 s^{-1}. As displayed by the figure, the model is able to capture the stress softening due to recrystallization. Current work is underway to fit the model to other deformation conditions.

Model Equations for Recrystallization Model

$$\mathrm{dev}\,\breve{\tau}^{\nabla} = \mathrm{dev}\,\breve{\boldsymbol{d}}^{e} = \mathrm{dev}\,\breve{\boldsymbol{d}} - \breve{\boldsymbol{d}}^{p}$$

$$\breve{\boldsymbol{d}}^{p} = \sqrt{\frac{3}{2}}\,\overset{*}{\breve{\varepsilon}}^{p}\,\boldsymbol{N}, \qquad \overset{*}{\breve{\varepsilon}}^{p} = \breve{f}\,\sinh^{n}\left[\left\langle \frac{\breve{\bar{\sigma}}}{\breve{\kappa}+\breve{Y}(\breve{D})} - 1 \right\rangle\right]$$

$$\overset{*}{\breve{\kappa}}_{u} = \left(\breve{H}_1 + \frac{\breve{H}_2}{\breve{\kappa}_u\,\breve{D}} + \frac{\breve{H}_3\breve{\zeta}_u}{\breve{\kappa}_u}\right)\overset{*}{\breve{\varepsilon}}^{p} - \left(\breve{R}_d\,\overset{*}{\breve{\varepsilon}}^{p} + \breve{R}_s\sinh(\breve{Q}_s\breve{\kappa}_u)\right)\breve{\kappa}_u$$

$$\overset{*}{\breve{\kappa}}_{r} = \left(\breve{H}_1 + \frac{\breve{H}_2}{\breve{\kappa}_r\,\breve{D}} + \frac{\breve{H}_3\breve{\zeta}_r}{\breve{\kappa}_r}\right)\overset{*}{\breve{\varepsilon}}^{p} - \left(\breve{R}_d\,\overset{*}{\breve{\varepsilon}}^{p} + \breve{R}_s\sinh(\breve{Q}_s\breve{\kappa}_r)\right)\breve{\kappa}_r - \breve{\kappa}_r\frac{\overset{*}{X}}{1-X}$$

$$\overset{*}{\breve{\zeta}}_{u} = \frac{\breve{H}_4}{\breve{D}}\,\breve{\zeta}_u^{\,1-1/r}\,\overset{*}{\breve{\varepsilon}}^{p}$$

$$\overset{*}{\breve{\zeta}}_{r} = \frac{\breve{H}_4}{\breve{D}}\,\breve{\zeta}_r^{\,1-1/r}\,\overset{*}{\breve{\varepsilon}}^{p} - \breve{\zeta}_r\frac{\overset{*}{X}}{1-X}$$

$$\overset{*}{X} = \frac{\mu(\theta)}{\mu_0}\frac{\exp(-\breve{Q}_6/\breve{\theta})}{\breve{\theta}}\left[1-\exp(-\breve{C}\breve{\zeta}_u^{\,m})\right]\left(\breve{C}_\kappa\breve{\kappa}_u^{\,2} + \breve{C}_\zeta\breve{\zeta}_u^{\,2}\right)X^{A}(1-X)^{B}$$

$$\overset{*}{\breve{D}} = \underbrace{G(\breve{\kappa},\breve{\zeta},\breve{D},\breve{\theta})}_{\substack{\text{grain refinement \&}\\ \text{G.G. during rex.}}} + \underbrace{\frac{\breve{B}(\breve{\theta})}{\breve{D}^{m}}}_{\text{normal G.G.}}$$

- Liu et al, 'Dynamic Rexrystallization Behavior of AZ61Magnesium Alloys', Azoyomo (Journal of Materials OnLine, vol. 2,1-12 (2006)

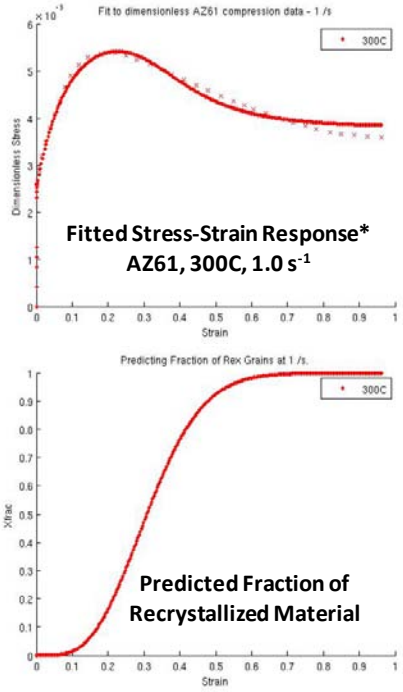

Figure 23: Internal State Variable material model extended to account for recrystallization.

Texture Predictions during Extrusion using Crystal Plasticity

At present Hyperxtrude has no interface to couple the solver with complex materials models. For this reason, an uncouple approach was used to predict of microstructure (texture evolution) at material points during extrusion using the Visco-Plastic Self Consistence (VPSC) crystal plasticity formulation. In this approach, deformation histories along streamlines are obtained from the HyperXtude post-processor and use as input to the VPSC code to compute texture and get a detailed account of the slip/twinning activity in the material. Material constants for the hardening laws in the crystal plasticity model have been obtained by fitting the mechanical response to experimental data.

Conical Die Extrusion of AZ61

The VPSC code was used to predict texture evolution during the conical die extrusion of AZ61. Input data to the code are the deformation path, represented by the velocity gradient, the time step and temperature history. Additional input for the code is the initial texture and the material parameter of the crystal plasticity model, represented in this case by the hardening parameters. For these simulations, Voce's hardening law was used. Figure 24 depicts the initial texture determined by XRD and the fitting of the Voce's law parameters to the stress-strain response of AZ61 at 1 s^{-1} and 300^{o}C. The fitting considered the following deformation modes: basal <a> {0001}<11-20>, prismatic <a>, {10-10}<11-20>, second order pyramidal <c+a>, {11-22}<11-2-3> and the extension twinning {10-12}<10-1-1>.

The predicted stress-strain response and texture along three streamlined are presented in Figure 25. No much difference in stress levels is predicted among the material particles traversing the trajectories defined by the streamlines. Recall that the implementation of Voce's law in the VPSC code does not account for rate and temperature effects. On the other hand, the texture patterns produced by extrusion (rod type texture) seem to be rotated as the material particle gets closer to the boundary, as aspect due to the effect of friction. Note that the texture along the axis streamline seems to reproduce trends observed in the experiments.

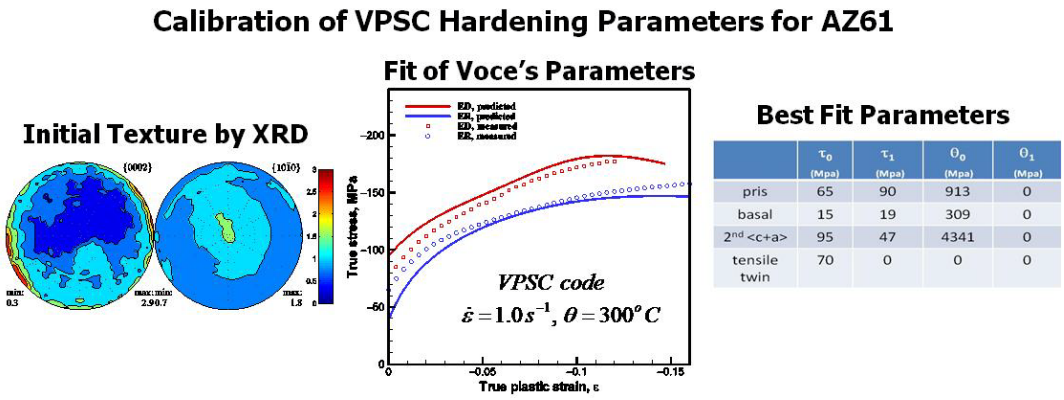

	τ_0 (Mpa)	τ_1 (Mpa)	θ_0 (Mpa)	θ_1 (Mpa)
pris	65	90	913	0
basal	15	19	309	0
2nd <c+a>	95	47	4341	0
tensile twin	70	0	0	0

Figure 24: Experimental data (texture and stress-strain response) for AZ61 and fitting of material parameters of Voce's hardening used in the VPSC code.

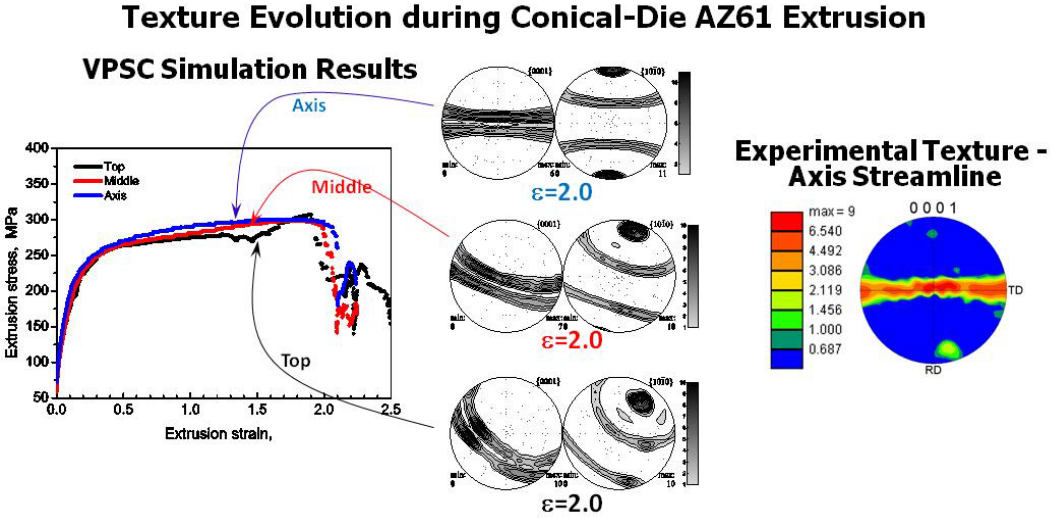

Figure 25: Extrusion stress-strain curves along three streamlines and corresponding VPSC predicted texture during extrusion. The EBSD measured texture along the axis streamline is also presented.

Flat Die Extrusion of AM30

Simple compression tests were performed on specimens obtained from a pre-extruded billet. The specimens were cut along two different directions: the extrusion (ED) and the extrusion radial (ER) directions. The tests were carried out at 450°C and various strain rates: 0.001 s^{-1}, 0.1 s^{-1}, 0.5 s^{-1}, 0.8 s^{-1} while the initial texture was measured by EBSD, see Figures 26. The recorded stress-strain response was used to obtain the material parameters of a dislocation-based hardening law used in the VPSC code. The calibrated response is presented in Figure 26. One can note that the quality of the fitting is reasonable although a different set of parameters was used for each curve.

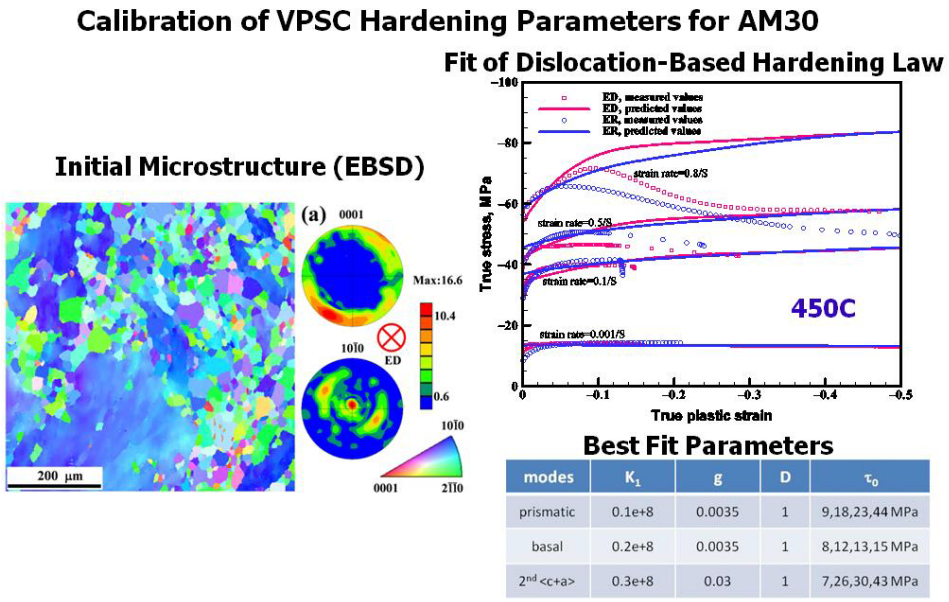

Figure 26: Experimental data (texture and stress-strain response) for AM30 and fitting of material parameters of a dislocation-based hardening used in the VPSC code.

The evolution of texture was predicted using the VPSC code and the streamline information (velocity gradient and time steps) obtained from the HyperXtrude simulations of the flat die extrusion of AM30. This prediction assume a constant temperature of 450°C and used the initial texture given in Figure 26 as well as the parameters for the dislocation-based hardening law calibrated from the above fitting at 0.8 s^{-1}. This hardening law accounts for rate and temperature dependence. The hardening parameters were determined for the four deformation modes: basal <a> {0001}<11-20>, prismatic <a>, {10-10}<11-20>, second order pyramidal <c+a>, {11-22}<11-2-3> and the extension twinning {10-12}<10-1-1>. The center streamline, shown in Figure 27, was selected for the VPSC simulations for the two ram speeds mentioned above (5 and 10 mm/min).

Figure 27 presents the computed stress-strain response along the center streamline and the corresponding texture prediction for the case of a ram speed of 5 mm/min. Note that the predicted texture follows the trends observed in the experiments.

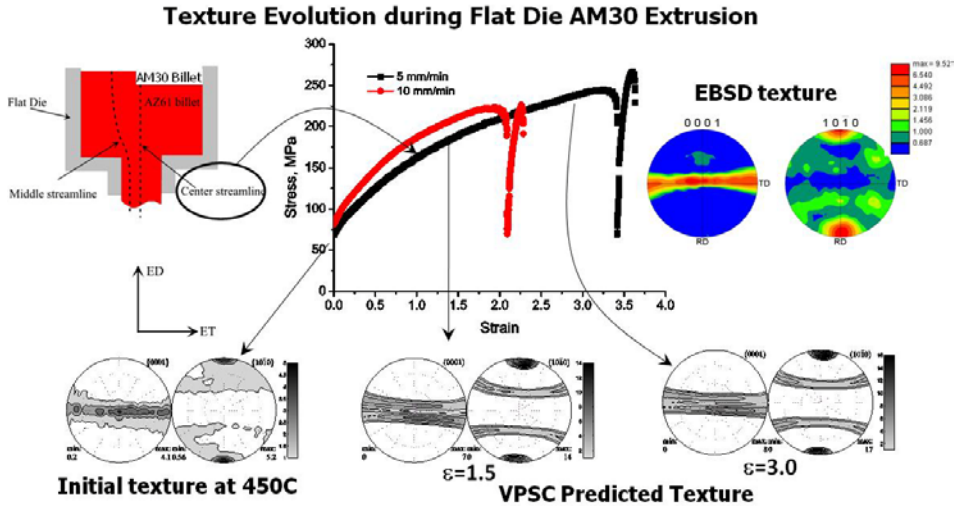

Figure 27: Extrusion stress-strain curves along the center streamline and VPSC predicted and EBSD measured local texture at different positions during extrusion of AM30 at 450°C.

Limitation of Current Hardening Models in Predicting Anisotropy by Twinning in HCP Metals: Application to a Rod-Textured AM30 Magnesium Alloy

When a strongly textured hexagonal close packed (HCP) metal is loaded under an orientation causing profuse twinning or de-twinning, the stress-strain curve is sigmoidal in shape and inflects at some threshold. Authors have largely attributed the dramatic stress increase in the lower-bound vicinity of the inflection point to a combined effect of a Hall-Petch mechanism correlated to grain refinement by twinning, and twinning-induced reorientation requiring activation of hard slip modes. These two mechanisms drove the correlation approaches of crystal plasticity hardening models to the macroscopic mechanical response. In this work, we experimentally and numerically demonstrate that these two mechanisms alone are unable to consistently reproduce the stress-strain behaviors obtained under intermediate loading orientations correlated to in-between profuse twinning and nominal twinning. We argue based on adopting various mechanistic approaches in hardening model correlations from the literature. We used both a physics dislocation based model and a phenomenological Voce hardening model. The HCP material is exemplified by an extruded AM30 magnesium alloy with a $\langle 10\bar{1}0\rangle$-fiber parallel to the extrusion direction. The intermediate loading orientations corresponded to obtuse angles with the extrusion direction and gave rise to curve inflections progressively vanishing toward the extrusion radial direction. We demonstrate that this behavior could only be captured when Hall-Petch is disregarded and the twin is considered to harden by slip at least three times more than the parent. This consideration was stimulated by the dislocation transmutation effects by the interfacial twinning shear.

In this research, by using a $\langle 10\bar{1}1\rangle$ fiber texture and adopting the same correlation approaches used in the literature, we derive an important discrepancy in the prediction of the stress-strain behaviors measured under loading orientations with intermediate volume fractions of twins. Only the stress-strain behaviors under orientations completely prohibiting twinning and maximizing twinning could be acceptably reproduced. In between, the models do not provide enough precision to capture the hardening trend. We demonstrate that the reason lies behind a misunderstanding of the nature of twin-slip interactions.

The material used in this research is an AM30 Magnesium alloy received from Timminco in the form of a 200 mm diameter billet extruded from a 450 mm diameter as-cast ingot. Samples for uniaxial mechanical testing were prepared using EDM (electrical discharge machining) to extract right cylinders 10 mm dia. x 10 mm length, see Figure 28. The materials in this study were tested in the “as received” state. The tests were conducted at room temperature and a strain rate of 0.001 ss^{-1}. Uniaxial compression tests were conducted to several different strain levels so that the experimental macro- and micro- texture analysis could be conducted on the samples.

Samples were prepared for testing along four different loading paths. Conventionally, previous investigators chose orthogonal loading paths to maximize and minimize the effect of twinning on the mechanical behavior. In this study, additional intermediate loading paths were desired, and were obtained by extracting samples at intermediate orientations. Samples were prepared allowing loading along the Extrusion Direction (ED), 30 degrees from the extrusion direction (ED30), 60 degrees from the extrusion direction (ED60), and perpendicular to the extrusion direction, i.e. extrusion radial direction (ERD).

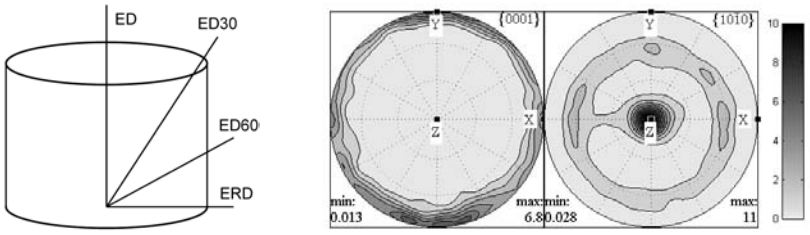

Figure 28: a) Schematic of sample orientations prepared from billet and b) {0001} and {10$\bar{1}$0} pole figures obtained by neutron diffraction on an untested specimen. Z corresponds to extrusion direction; X and Y correspond to the extrusion tangent and extrusion radial directions, respectively. A pronounced ED ∥ {10$\bar{1}$0} fiber from the extrusion process is evident.

The macrotexture information in this study was collected by x-ray diffraction (XRD) and neutron diffraction (ND) using a Rigaku Smartlab X-Ray Diffractometer and also by neutron diffraction using the facilities of LANSCE (Los Alamos Neutron Science) at Los Alamos National Laboratory. Details of the LANSCE facility can be found in Von Dreel [2] and Wenk et al. [3]. Texture analyses and pole figure plots of XRD and ND were done using the popLA [4] and pole8 [5] software from Los Alamos National Laboratory and MTEX [6].

The mechanical tests corresponded to simple compression at room temperature and at a rate of 0.001/s. The intermediate loading directions (30ED and 60ED) were performed in an effort to tests the hardening models and correlation approaches used in the literature to fit the entire yield surface domain corresponding to various levels of twin activity, see Figure 29. This is of great importance to metal forming modeling since real world conditions correspond exactly to intermediate twin activities in between profuse and nominal.

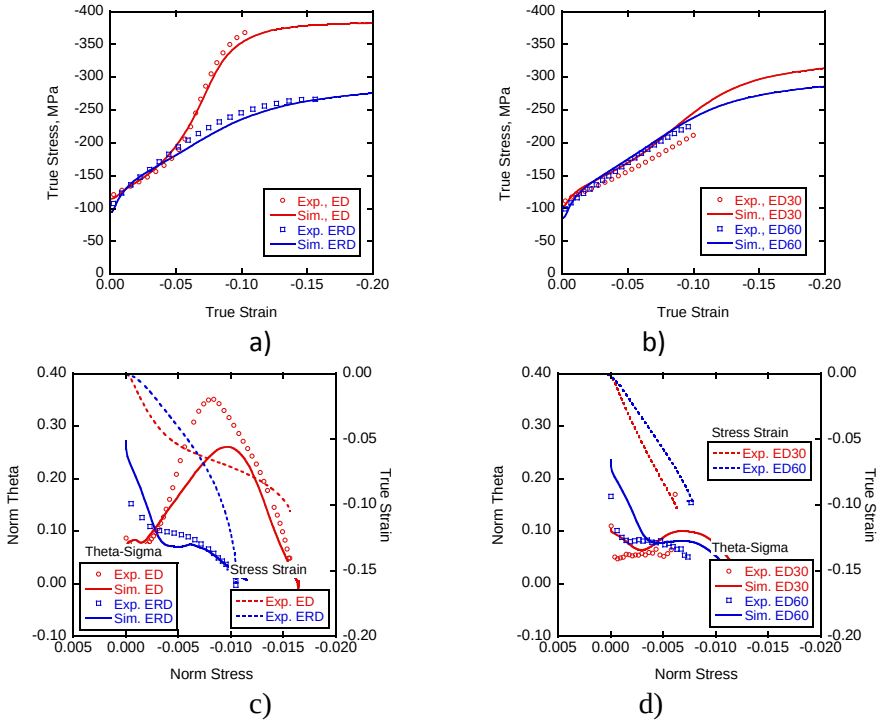

Figure 29: Stress- strain curves of the (a) extrusion and extrusion radial direction and (b) 30 degrees and 60 degrees from the extrusion direction, and strain hardening rate versus stress curves for the (c) extrusion and extrusion radial direction and (d) 30 degrees and 60 degrees from the extrusion direction for simulations using the dislocation density hardening rule. A twin storage factor equal to 3 was used.

The simulations are consistent with the idea of an increased hardening in the twin during profuse twinning caused by the dislocation transmutation idea put forward by El Kadiri and Oppedal [7]. Details of the model and more extensive description of the experiment can be found in the paper by Oppedal et al. [8]. In the simulations using the dislocation density hardening model, it was not possible to achieve a good model correlation to the experimental data without using a twin storage factor of three. This also gave the desirable effect of correlating fairly well the strain hardening rate versus stress behavior as well. With a twin storage factor of three, the simulations could reach the proper saturation stress levels that the experimental test data showed. The simulations also predicted well the experimentally observed stress-strain and texture behavior without utilizing a Hall-Petch type effect that has been attributed to the grain refinement by twinning. Also, the Hall Petch effect for magnesium twin boundaries has been experimentally observed to be quite low [9].

The use of the VPSC simulations with the dislocation density based hardening rule allowed a coupling between slip, twinning, texture, and stress state behavior analysis that has not fully explained by the use of empirical latent hardening parameters such as used in the Voce hardening models. Furthermore, the quantification of the slip activity, twin activity, texture evolution, and hardening as a function of strain allows for macroscale internal state variable.

Channel Die Compression Simulations of AM30 Magnesium Alloy using **CPFEM**

The crystal plasticity finite element model (CPFEM) combined the single crystal plasticity constitutive law with finite elements to compute the macroscale response of crystal aggregates. In CPFEM, the equilibrium of forces (stresses) and the compatibility of displacements are implicitly satisfied by the finite element formulation. This technique can be used to model two dimensional (2D) or three dimensional (3D) microstructures to investigate many aspects of the heterogeneous plastic response of a local grain within a polycrystal under various boundary conditions. At present, 3D CPFEM deformation simulations attract more attention as 3D microstructure deformation resembles the realistic deformation of polycrystals. In this context, the use of a fine meshed regular polyhedron representing a grain with a particular orientation has been widely used to investigate intragranular orientation gradient and grain interaction effects during deformation. Many CPFEM studies have used brick-shape grains, rhombic dodecahedron grains, and tetradecahedron grains to investigate grain interaction effects on texture evolution, grain subdivision and strain localization. However, as suggested by Mika and Dawson, crystal shape could also play a large role on texture scatter, and hence, the use of uniform and regular grain shapes can still produce a discrepancy between experimental textures and simulations.

We investigate the plane strain deformation of a polycrystal aggregate using the CPFEM and 3D Voronoi grains. The focus is on revealing the effect of grain interaction on global texture evolution, intergranular heterogeneous plasticity, and intragranular orientation spread. The material studied is HCP AM30 magnesium alloy. As twinning is usually suppressed at high temperature, we select three deformation modes as shown in Figure 30 in the channel die compression simulation of AM30 at 200°C.

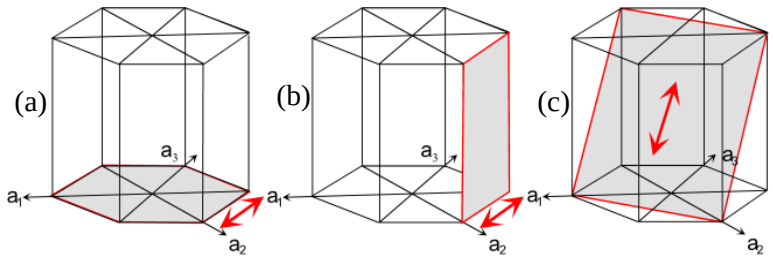

Figure 30: Typical slip deformation modes in magnesium: (a) basal <a>-{0002}<11$\bar{2}$0> slip, (b) prismatic <a>-{10$\bar{1}$0}<11$\bar{2}$0> slip, and (c) second order pyramidal <c+a>-{11$\bar{2}$2}<11$\bar{2}$3> slip.

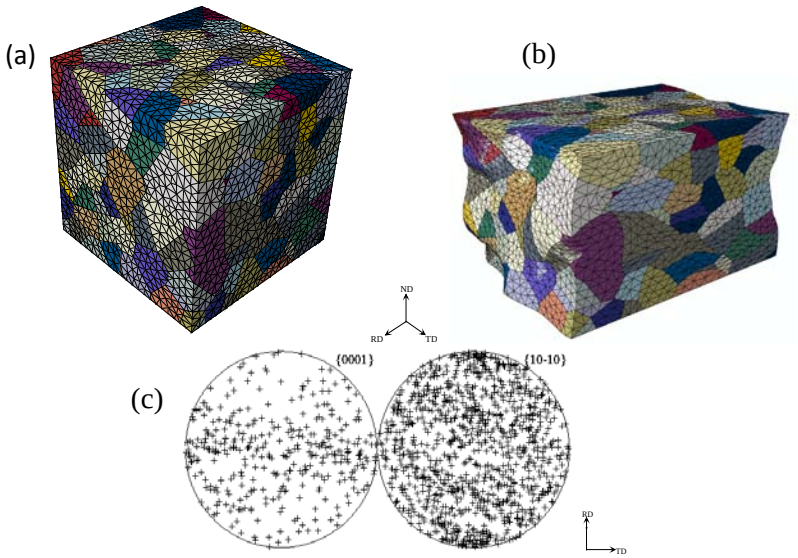

Figure 31: (a) The undeformed 343 3D Voronoi grains and (b) deformed 343 Voronoi grains and (c) the initial 343 discrete orientations representing the initial texture of AM30 magnesium alloy.

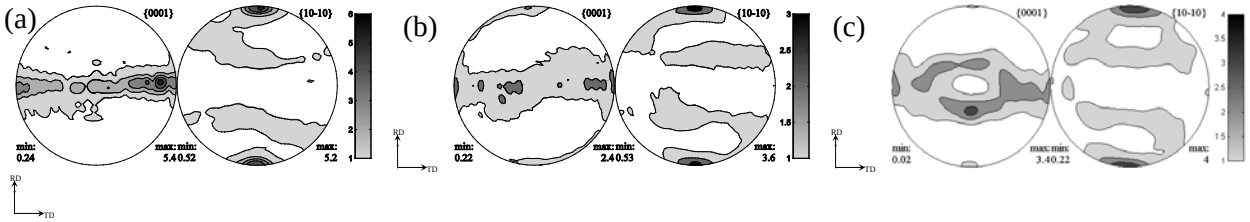

Figure 32: Pole figures for an AM30 magnesium alloy showing (a) the experimental initial texture and (b) the experimental channel die compression at a strain of 30% and (c) the finite element crystal plasticity simulation result at a strain of 30%.

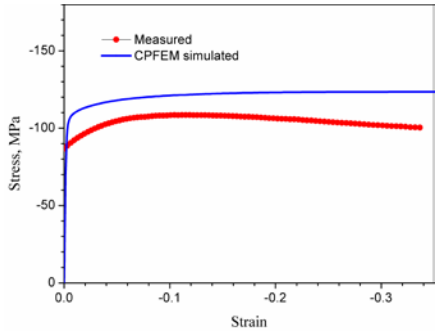

Figure 33: The finite element simulation stress-strain curve based on crystal plasticity model and the experimental stress-strain curve under channel die compression for AM30 magnesium alloy at 200°C.

The initial 343 3D Voronoi grains and the channel die compressed grains and the starting 343 orientations are presented in Figure 31(a), 31(b) and 31(c), respectively. The measured initial texture and the channel die compression texture at strain of 30% by XRD of the AM30 and the CPFEM simulation texture are presented in Figure 32. Figure 33 displays the measured and predicted stress-strain curves of channel die compression of the AM30 at 200°C and strain of 30%.

As a summary, plane strain compression simulations of a three dimensional microstructure of hcp magnesium AM30 were performed using an elastic-plastic crystal plasticity model and the finite element

method. The mechanical response and global texture evolution were captured by the 3D Voronoi microstructure channel die compression simulation. Simulation results showed that the effect of grain interaction could play an important role on global texture evolution, the orientation spread and the local heterogeneity deformation of one grain.

Material Modeling and Sheet Forming Simulations of Magnesium Alloys

Sheet metal stamping is a manufacturing process that is widely used in several industries to form auto-body panels and a variety of appliance parts. The principle consists of a punch, and draw ring and blank-holder assembly, or binder. During the sheet metal stamping process, a sheet of metal (the blank) is placed between the upper die and lower die, which are designed into the form of the desired part. The upper die (or punch) is driven into the lower die which high force using a press and the sheet of metal is stamped into the desired shape by the press. In this process, tensile forces that cause the deformation and the contact stress between the punch and the sheet, generating stresses that are much lower than the yield stress of the sheet. These mentioned features are common in many sheet processes, namely that forming is not caused by the direct contact stresses, but by tensile forces transmitted through the sheet and there will be a balance between tensile forces over the punch and compressive forces in the outer flange material [10].

However, the tooling design and fabrication to make these parts without defects, such as wrinkles and splits, is a time consuming and cost effective process, even today. Tooling design is a complex task, as forming dynamics involve interactions between the sheet-metal blank, the press, the blank-holder, and the die. In addition, operating conditions such as die lubrication and temperature significantly affect the forming process. Typical defects that occur due to incorrect flow of material into the die during the stamping process are wrinkling (caused by excessive compression). Moreover, operational variations such as lubricant build-up in the dies, small changes in the material properties and thicknesses of the sheet metal blanks as well as temperature effects can result in parts being formed with defects, thus resulting in material scrapping costs of millions of dollars. Therefore, die design requires the combination of skill and extensive computer-aided engineering simulations.

MsSt's objective of the sheet forming work is to develop a physically-based material model and an experimental-validated sheet forming model with corresponding design methodologies to enhance the formability of Mg alloys (AZ31). The current work involves establishing material anisotropy relationships to understand the effects of microstructure state, product geometry and processing parameters on the resulting mechanical properties and distortion of Mg sheets.

Plasticity-Damage Material Model

To predict the thickness distribution in sheet metal forming simulation, we use an ISV plasticity-damage model called DMG microstructure-plasticity model, which includes kinematics, damage progression equations, and the elastic-plastic framework. Standard notation is used throughout. All tensor components are written with respect to a fixed Cartesian coordinate system, and the summation convention is used for repeated Latin indices, unless otherwise indicated.

Kinematics

The formulation of the kinematics follows closely that of Davison et al. [11], Bammann and Aifantis [12], Bammann et al. [13], and Horstemeyer et al. [14]. The kinematics of motion combine elastic straining, inelastic flow, and formation and growth of damage and is illustrated by the multiplicative decomposition of the deformation gradient as shown in Figure 34. The deformation gradient, $\boldsymbol{F}$, is decomposed into the isochoric inelastic, or plastic, $(\boldsymbol{F}_d^p)$, dilational inelastic $(\boldsymbol{F}_v^p)$, and elastic parts $(\boldsymbol{F}^e)$ given by

$$\boldsymbol{F} = \boldsymbol{F}^e \boldsymbol{F}_v^p \boldsymbol{F}_d^p. \tag{2}$$

Eq. (2) assumes that the motion of the body is described by a smooth displacement function. This precludes the initiation of discrete failure surfaces but still allows a continuum description of damage. The elastic deformation gradient, $\boldsymbol{F}^e$, represents lattice displacements from equilibrium. The inelastic deformation gradient, $\boldsymbol{F}_d^p$, represents a continuous distribution of dislocations whose volume preserving motion produces permanent shape changes. The volumetric inelastic deformation gradient, $\boldsymbol{F}_v^p$, represents a continuous distribution of voids causing the volume change of the material from that arises from inelastic deformation. It is assumed to have the form $\boldsymbol{F}_v^p = \phi \boldsymbol{I}$, where ϕ is a function to be determined from kinematics (or conservation of mass).

The Jacobian of Eq. (2) is related to the change in volume or change in density for constant mass as

$$J = \det \boldsymbol{F}_v^p = \frac{V_2}{V} = \frac{\rho_0}{\rho_2} \tag{3}$$

and must be positive. The change in volume from the reference configuration (State 0) to the intermediate configuration (State 2) is $V_2 = V_0 + V_v$ assuming that the volume in State 0 equals that in State 1 because of inelastic incompressibility. The volume and density in the reference configuration are given by V_0 and ρ_0, respectively. In transforming the configuration from State 0 to State 2, an added volume from the voids, V_v, is introduced to the total volume, but the volume of the solid matter remains unchanged at its reference value, because the material is unstressed in this configuration. The intermediate configuration in State 2 then designates when elastic unloading has occurred.

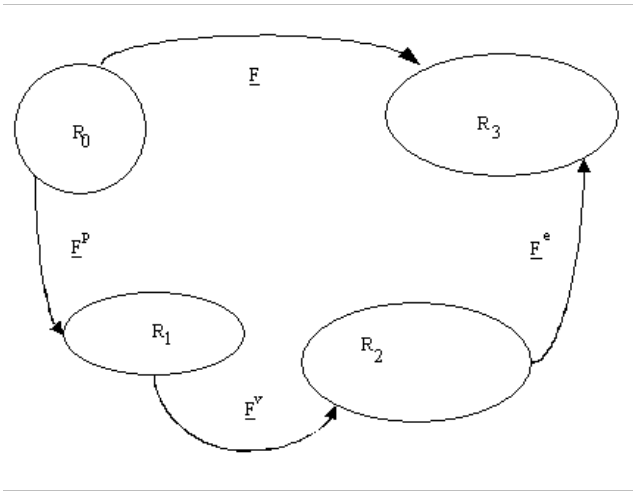

Figure 34: Multiplicative decomposition of the deformation gradient into deviatoric, dilatational plastic, and elastic parts.

Damage, ϕ can be defined as the ratio of the change in volume of an element in the elastically unloaded state (State 2) from its volume in the initial reference state to its volume in the elastically unloaded state,

$$\phi = \frac{V_v}{V_2} \tag{4}$$

From this definition, we get

$$V_0 = (1 - \phi)V_2 \tag{5}$$

where now the Jacobian is determined by the damage parameter, ϕ, as

$$J = \det \boldsymbol{F}_v^p = \frac{1}{1 - \phi} \tag{6}$$

Consequently, the restriction that damage is assumed to produce isotropic dilatation gives the volumetric part of the deformation gradient as

$$\boldsymbol{F}_v^p = \frac{1}{(1-\phi)^{1/3}}\boldsymbol{I} \tag{7}$$

where $\phi = (1-\phi)^{-1/3}$. The velocity gradient associated with the deformation gradient, $\boldsymbol{L} = \dot{\boldsymbol{F}}\boldsymbol{F}^{-1}$, from Eq. (2) is given by

$$\boldsymbol{L} = \boldsymbol{L}^e + \boldsymbol{L}_v^p + \boldsymbol{L}_d^p \tag{8}$$

where $\boldsymbol{D} = \frac{1}{2}(\boldsymbol{L} + \boldsymbol{L}^T)$ and $\boldsymbol{W} = \frac{1}{2}(\boldsymbol{L} - \boldsymbol{L}^T)$ with analogous formulas holding for the elastic, volumetric plastic, and deviatoric plastic parts of the velocity gradients expressed as $\boldsymbol{L} = \dot{\boldsymbol{F}}\boldsymbol{F}^{-1}$. The volumetric part of the velocity gradient is then given by

$$\dot{\boldsymbol{F}}_v^p \boldsymbol{F}_v^{p-1} = \frac{\dot{\phi}}{3(1-\phi)^{1/3}}\boldsymbol{I} \tag{9}$$

which defines the plastic volumetric rate of deformation as

$$\boldsymbol{D}_v^p = \frac{\dot{\phi}}{3(1-\phi)^{1/3}}\boldsymbol{I} \tag{10}$$

Also note here that $\boldsymbol{W}_v^p$ vanishes. The trace of the volumetric part (Eq. (10)) is given as

$$\mathrm{tr}\left(\boldsymbol{D}_v^p\right) = \frac{\dot{\phi}}{(1-\phi)^{1/3}} \tag{11}$$

Therefore the damage parameter, ϕ, directly relates to the volumetric rate of deformation. The elastic rate of deformation relates to the volumetric rate of deformation by the additive decomposition of the deformation rates similar to Eq. (8),

$$\boldsymbol{D}^e = \boldsymbol{D} - \boldsymbol{D}_v^p - \boldsymbol{D}_d^p \tag{12}$$

Similarly, the elastic velocity gradient can be decomposed into components like Eq. (8) and Eq. (12), where the elastic spin equals the total spin when no plastic spin is prescribed. Recall that no volumetric component exists for the spin tensor, that is $\boldsymbol{W}_v^p = 0$.

Now that the rate of deformation related to the damaged state is defined, we can describe damage in terms of void nucleation and void growth in the unstressed intermediate configuration. First, we let N equal the total number of voids in a representative continuum volume V_0 of material in the reference configuration (State 0) and let η^* be the number of voids per unit volume in the reference configuration; hence, $\eta^* = N/V_0$. The average void volume is $v_v = 1/N \sum_{i=1}^{N} v_i$, where v_i is the void volume from each particle that has nucleated a void. As such the volume of voids is given by

$$V_v = \eta^* V_0 v_v \tag{13}$$

By combining this definition and inserting them into Eq. (4), the damage parameter, ϕ, can be written as

$$\phi = \frac{\eta^* V_0 v_v}{V_0 + \eta^* V_0 v_v} = \frac{\eta^* v_v}{1 + \eta^* v_v} \tag{14}$$

This formulation for damage was employed by Davison et al. [11]. If the number of voids per unit volume is defined in the intermediate configuration, we can write

$$\phi = \frac{V_v}{V_2} = \frac{V_v}{N}\frac{N}{V_2} = \eta v_v \tag{15}$$

where

$$\eta = \frac{N}{V_2} = \frac{N}{V_0}\frac{V_0}{V_2} = \eta^* \frac{V_0}{V_2}. \tag{16}$$

Recalling that the unstressed intermediate configuration has the volume $V_2 = V_0 - V_v$ and employing Eq. (4), we get the relation

$$\eta^* = \eta/(1-\phi). \tag{17}$$

The density of voids is counted after the specimen is loaded to a certain strain level and then unloaded. From this point, the specimen is machined and the number counting of voids nucleated is performed representing the elastically unloaded intermediate configuration; hence, η is experimentally determined.

Void Nucleation, Growth, and Coalescence Aspects

The process of ductile fracture of most metals and alloys occurs mainly due to the void nucleation, growth and finally coalescence into a micro-crack (Figure 35). If the extent of void growth up to fracture is small, it is possible to ignore its effects on the constitutive equations. However, a realistic model on ductile fracture prediction must include void nucleation, void growth and a condition for void coalescence.

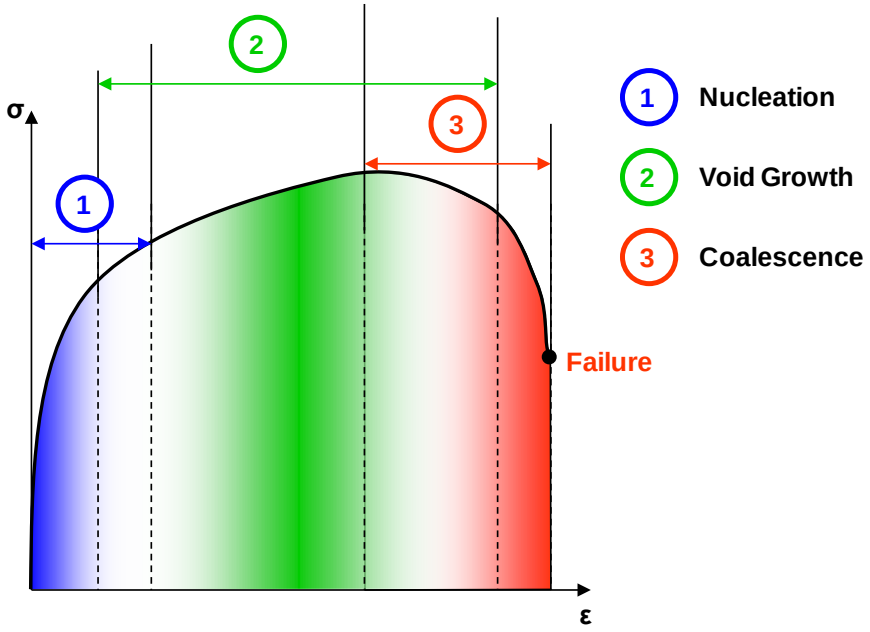

Figure 35: Sequences in a ductile fracture mechanism.

The damage formulation is shown conceptually in Figure 36. The number density of voids can change and growth of voids can occur independently or simultaneously. This framework is illustrated by the schematic in Figure 37 when examining the limiting cases. One void growing can exist or many voids can nucleate without void growth. A typical void growth model is assumed to have an initial void embryo of a size determined by optical micrographs or some other method. As such, the growth rule applies to both voids that are already present and those that are nucleating. These two types of voids would experience the same void growth rule in the damage analysis. Because the void growth rule is initialized with a positive volume, the nucleated void volume is assumed to incur this same initialization volume. Perhaps

the most realistic embryo size for the newly nucleated site is the size of the second phase particle. The framework conceivably allows for this initialization as well. For materials with second phases and pre-existing voids, one would anticipate that the average size of the second phase and average size of the pre-existing voids would be different owing to solidification mechanisms. Finally, nucleation is assumed to occur by decohesion of the particle/matrix interface or by particle fracture, and more than one void can be nucleated at a given particle at different sides of the particle.

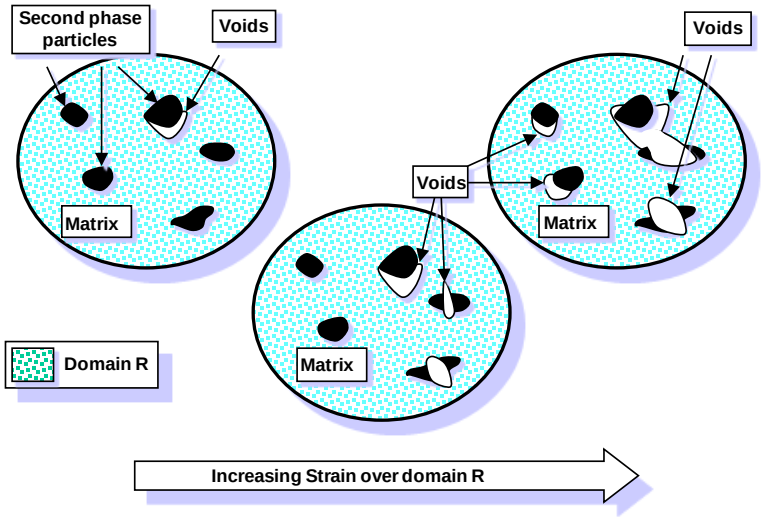

Figure 36: Schematic of fictitious material with increasing void nucleation density and void growth in which the model conceptually comprises.

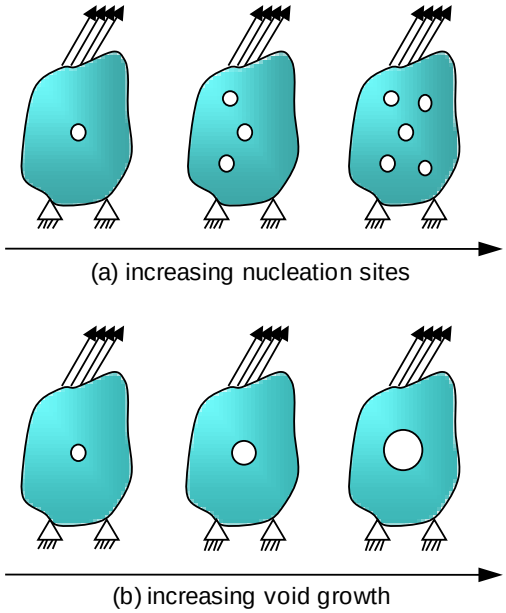

Figure 37: The damage model encompasses the limiting cases shown by (a) just void nucleation and (b) a single void growth.

The void nucleation rule of Horstemeyer and Gokhale [15] is used to model the results from the experimental data under compression, tension, and torsion. The integrated form of the void nucleation rate equation is given by

$$\eta(t) = C_{coeff}\, exp\left[\frac{\varepsilon(t) d^{1/2}}{K_{IC} f^{1/3}}\left\{a\left(\frac{4}{27} - \frac{J_3^2}{J_2^3}\right) + b\frac{J_3}{J_2^{3/2}} + c\left\|\frac{I_1}{\sqrt{J_2}}\right\|\right\}\right] exp\left(\frac{C_{T\eta}}{T}\right) \tag{18}$$

where $\eta(t)$ is the void nucleation density, $\varepsilon(t)$ is the strain at time t, C_{coeff} is a material constant. T is temperature in the absolute scale, and $C_{T\eta}$ is the temperature dependent material constant determined from experiments. The material parameters *a*, *b*, and *c* relate to the volume fraction of nucleation events arising from local microstresses in the material. These constants are determined experimentally from tension, compression, and torsion tests in which the number density of void sites is measured at different strain levels. The stress state dependence on damage evolution is captured in Eq. (18) by using the stress invariants denoted by I_1, J_2, and J_3, respectively. I_1 is the first invariant of stress ($I_1 = \sigma_{kk}$). J_2 is the second invariant of deviatoric stress ($J_2 = \frac{1}{2}S_{ij}S_{ij}$), where $S_{ij} = \sigma_{ij} - \frac{1}{3}\sigma_{kk}\delta_{ij}$. J_3 is the third invariant of deviatoric stress ($J_3 = S_{ij}S_{jk}S_{ki}$). The rationale and motivation for using these three invariants of stress is discussed in Horstemeyer and Gokhale [15]. The volume fraction of the second phase material is f, the average silicon particle size is d, and the bulk fracture toughness is K_{IC}.

A crucial feature in determining the damage state, besides nucleation of voids, is void growth. Many void growth rules have been developed and studied [16; 17] but none can comprehensively capture different levels of stress triaxialities, different hardening rates, different strain rates, and different temperature regimes. The damage framework allows for different void growth rules to be included and evaluated. We considered several void growth models. The first one by McClintock [18] is given in terms of the void radius as

$$\dot{r} = \frac{\sqrt{3}R_0}{2(1-n)}\left[\sinh\left(\sqrt{3}(1-n)\frac{\sqrt{2}I_1}{3\sqrt{J_2}}\right)\right]\dot{\varepsilon} \tag{19}$$

In Eq. (19) the void volume grows as the strain and/or stress triaxiality increases. The material constant n is related to the strain hardening exponent and is determined from the tension tests. R_0 is taken to be the initial radius of the voids. As with most void growth models, the McClintock model allows voids to grow in tension, but not in compression or torsion. This complies with physical observations from measurements from these Mg alloys. Another void growth model in terms of void radius is given by Rice and Tracey [19] is given by,

$$\dot{r} = 0.283R_0 \exp\left(\frac{3}{2}\frac{\sqrt{2}I_1}{3\sqrt{J_2}}\right)\dot{\varepsilon} \tag{20}$$

Another void growth model by Budiansky et al. [20] in terms of void volume rate is given by,

$$\dot{v} = \frac{3v}{2}\left[\frac{3m}{2}\frac{\sqrt{2}I_1}{3\sqrt{J_2}} + (1+m)(1+0.4319m)\right]^{1/m}\dot{\varepsilon} \tag{21}$$

The last one worth mentioning in this context is that by Cocks and Ashby [21] given in terms of the void volume fraction rate,

$$\dot{\phi} = \left[\frac{1}{(1-\phi)^{1/m}} - (1-\phi)\right]\sinh\left[\frac{2(2-m)}{2+m}\frac{\sqrt{2}I_1}{3\sqrt{J_2}}\right]\dot{\varepsilon} \tag{22}$$

As it turns out, all of these void growth rules give very similar results as will demonstrated later. In practice, the McCintock [18] model was used for the silicon particles and the Cocks and Ashby [21] model was used for the casting pores.

Another item related to damage is the phenomenon of void coalescence. Coalescence is the joining of voids either at the microscale or macroscale and has been observed to occur by two main mechanisms.

The first mechanism [22] occurs when two neighboring voids grow together until they join as one, that is, as the ligament between them necks down to a point as illustrated in Figure 38. Another mechanism occurs when a localized shear band occurs between neighboring voids [23, 24], often referred to as the "void sheet" mechanism also shown in Figure 38.

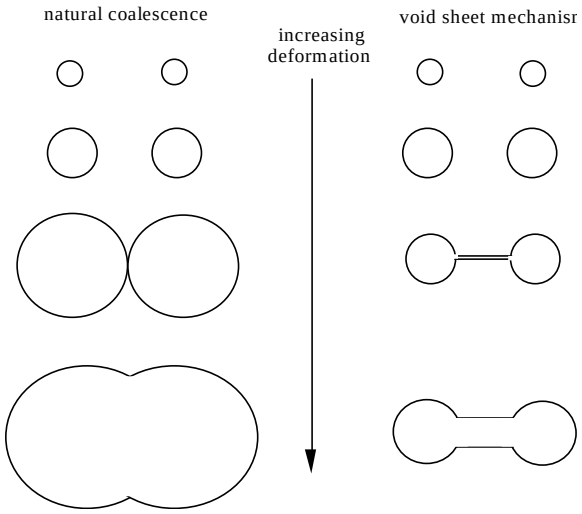

Figure 38: Two different coalescence mechanisms observed in various materials.

Coalescence can be added to the damage framework described in Eq. (15). It arises naturally with the multiplicative relation between the nucleation and growth terms. As Figure 38 demonstrates, we start with two voids that are nucleated and each independently grows until they join together. Then, one void emerges as they coalesce together. The coalescence event causes a discontinuous jump in the nucleation evolution and growth evolution but allows for continuous growth of total damage evolution, ϕ. Although discontinuities occur in discrete regions for the nucleation and growth rules, the rate equations evolve as internal state variables at a higher length scale in the continuum where their effects are observed on macroscale effective quantities and thus are continuous functions.

In a phenomenological manner, we include the coalescence term

$$C = (C_{D1} + C_{D2}\eta v)\left(\frac{DCS_0}{DCS}\right)^z (TC_{TC}) \tag{23}$$

which gives

$$\phi = (\eta v + \phi_{pore})C \tag{24}$$

In the limiting case when the function $C_{D2} = 0$ in Eq. (23) equals zero, simple coalescence occurs. In this case, the model reflects the growing of two voids into one. When $C_{D2} \neq 0$, microvoid linking is reflected and the rate of damage is increased. Garrison and Moody [16] and Magnusen et al. [25] observed that the microvoid sheet mechanism is related to particles initiating small voids in between two larger voids as the larger voids impose their influence on the surrounding region. As such, coalescence is a function of both nucleation and void growth. Actually, both forms of coalescence occur in this material and hence both constants C_{D1} and C_{D2} are nonzero.

From Eq. (24), we observed that the void nucleation and growth arise from the η and v, which relate to the silicon particles. The ϕ_{pore} term is related to the casting porosity and its growth is given by the Cocks and Ashby [21] void growth form (Eq. (22)). Here, the coalescence operates on the both the silicon fracturing/debonding into voids and the initial porosity that grows. Results from the mesomechanical finite element simulations motivated this phenomenological form.

The dependence on grain size for wrought and powder metals and dendrite cell size (DCS) from castings comes in based on the work of Major et al. [26], who noted a dependence of the elongation to failure with DCS. Because the elongation to failure is directly a result of the damage progression, we can assert that the DCS influences the damage progression. The parameter z comes in to normalize the effect of the DCS and also plays a role in the work hardening rate as shown in the next section. The effect of the DCS is minor compared to the other features in the model.

The temperature dependence of the coalescence term was determined from the multitude of mesomechanical simulations [27, 28], which are a powerful tool for modeling heterogeneous materials at the mesoscopic scale (at the grain structure scale). Mesomechanical simulations can either be used for virtual material characterization and establish the basis for new continuum models or within a multi-scale simulation approach A general trend was determined from the mesomechanical simulations, and the constant C_{TC} was determined. More work related to the coalescence needs to be done, however this first order form captures most of the features observed from microstructure/inclusion behavior.

DMG Microcrosture-Plasticity Model

The viscoplasticity model formulated by Bammann et al. [13], called DMG-plasticity model, is used in this work to describe the nonlinear response of the material behavior. The thermo-viscoplastic constitutive equations are developed in the framework of the classical thermodynamics of irreversible processes with internal state variables (ISVs). Based upon a multiplicative decomposition of the deformation gradient into elastic and plastics parts, and assuming linear isotropic elasticity with respect to the natural configuration associated with this decomposition, the assumption of linear elasticity can be written:

$$\widehat{\boldsymbol{\sigma}} = \boldsymbol{C}\colon \boldsymbol{D^e} = \lambda\, tr(\boldsymbol{D^e})\mathbf{1} + 2\mu \boldsymbol{D^e} \tag{25}$$

where, $\boldsymbol{D}$ is the elastic strain rate tensor, $\boldsymbol{C}$ is the elastic stiffness, and λ and μ the elastic Lame constants, and the Cauchy stress tensor $\boldsymbol{\sigma}$ is convected with the elasctic spin $\boldsymbol{W^e}$ as:

$$\widehat{\boldsymbol{\sigma}} = \dot{\boldsymbol{\sigma}} - \boldsymbol{W^e}\boldsymbol{\sigma} + \boldsymbol{\sigma}\,\boldsymbol{W^e}. \tag{26}$$

Decomposing the total strain rate $\boldsymbol{D}$ into elastic and plastic parts, the elastic relation can also be written

$$\dot{\boldsymbol{\sigma}} = \boldsymbol{C}\colon (\boldsymbol{D} - \boldsymbol{D^p}). \tag{27}$$

The plastic flow rule is defined by the hyperbolic sine functional form

$$\boldsymbol{D^p} = \begin{cases} f(T)\sinh\left[\dfrac{|\boldsymbol{s}-\boldsymbol{\alpha}| - \kappa - Y(T)}{V(T)}\right]\boldsymbol{n} & if\ |\boldsymbol{s}-\boldsymbol{\alpha}| - \kappa - Y(T) \geq 0 \\ 0 & if\ |\boldsymbol{s}-\boldsymbol{\alpha}| - \kappa - Y(T) < 0 \end{cases}, \tag{28}$$

where $\boldsymbol{n}$ the plastic normal tensor defined by

$$\boldsymbol{n} = \frac{3}{2}\frac{\boldsymbol{s}-\boldsymbol{\alpha}}{|\boldsymbol{s}-\boldsymbol{\alpha}|}. \tag{29}$$

$Y(T)$, $f(T)$ and $V(T)$ are temperature dependent functions and are related to yielding with an Arrhenius-type temperature dependence. The function $Y(T)$ is the rate-independent yield stress, the function $f(T)$ determines when the rate-dependence affects initial yielding, and the function $V(T)$ determines the magnitude of rate-dependence on yielding.

Table 1: Material parameters C_i for the viscoplasticity model.

Mechanism	Description	Term Definition
Yield Stress	Rate-Independent Yield Stress	$Y(T) = \frac{C_3(1+\tanh[C_{19}(C_{20}-T)])}{2(C_{21}+\exp[-C_4/T])}$
	Magnitude of Rate-Dependence on yielding	$V(T) = C_1 \exp[-C_2/T]$
	Rate-Dependence on Initial Yielding	$f(T) = C_5 \exp[-C_6/T]$
Kinematic Hardening	Modulus	$h(T) = C_9 - C_{10}T$
	Dynamic Recovery	$r_d(T) = C_7 \exp[-C_8/T]$
	Static Recovery	$r_s(T) = C_{11} \exp[-C_{12}/T]$
Isotropic Hardening	Modulus	$H(T) = C_{15} - C_{16}T$
	Dynamic Recovery	$R_d(T) = C_{13} \exp[-C_{14}/T]$
	Static Recovery	$R_s(T) = C_{17} \exp[-C_{18}/T]$

The definition of this plastic flow rule leads to a Mises type yield function defined by

$$f = |\boldsymbol{s} - \boldsymbol{\alpha}| - \kappa - Y(T) - V(T)\sinh^{-1}\left[\frac{\dot{\lambda}_p}{f(T)}\right] = 0\,. \tag{30}$$

The evolution of the plasticity internal state variables is prescribed in the hardening-minus recovery format. The hardening may be defined as the increase in yield stress due to plastic deformation. For hardening materials, the yield surface will evolve in space in one of three ways:

- The first form of yield surface evolution is called isotropic hardening, κ, which reflects the effect of the global dislocation density. For isotropic hardening, the yield surface grows in size while the center remains at a fixed point in stress space.
- The second form of yield surface evolution is called kinematic hardening, $\boldsymbol{\alpha}$, also called Bauschinger effect, which reflects the effect of anisotropic dislocation density. For kinematic hardening, the center of the yield surface translates in stress space, while the size remains fixed. For both isotropic and kinematic hardening, the orientation of the yield surface remains fixed.
- The third type of yield surface evolution is called mixed hardening where both isotropic and kinematic hardening characteristics are evident. For mixed hardening, the orientation (not considered here) of the yield surface may also change as well.

Although isotropic hardening is the most common form of yield surface evolution assumed in finite element models for metal forming simulation, it is not necessarily the most accurate. The mixed hardening model is most likely the most accurate of the three models. The kinematic hardening internal state variable $\boldsymbol{\alpha}$, representing the directional hardening, is define by the evolution equation

$$\dot{\boldsymbol{\alpha}} = h(T)\boldsymbol{D}^p - \left[r_d(T)\bar{d}_p + r_s(T)\right]\|\boldsymbol{\alpha}\|\boldsymbol{\alpha} \tag{31}$$

and the isotropic hardening κ by

$$\dot{\kappa} = H(T)\bar{d}_p - \left[R_d(T)\,\bar{d}_p + R_s(T)\right]\kappa^2 \tag{32}$$

where

$$\bar{d}_p = \sqrt{\frac{2}{3}\boldsymbol{D}^p : \boldsymbol{D}^p} \quad \text{and} \quad \|\boldsymbol{\alpha}\| = \sqrt{\frac{3}{2}\boldsymbol{\alpha} : \boldsymbol{\alpha}}\,. \tag{33}$$

The temperature dependence of the hardening functions $H(T)$ and $h(T)$ should in general be proportional to the temperature dependence of shear modulus. The terms $r_s(T)$ and $R_s(T)$ are scalar functions describing the diffusion-controlled static or thermal recovery, and $r_d(T)$ and $R_d(T)$ are the functions describing the dynamic recovery. The temperature-dependent functions are defined in Table 1.

Numerical Integration of the Constitutive Equations

In the context of finite element analysis the integration of the constitutive equations of the viscoplasticity model described in the previous section is carried out at the integration points. A stress integration algorithm was developed to solve the constitutive equations of the viscoplasticity model described in the previous section. Although the model was implemented in a finite element code with an explicit solver (Abaqus/Explicit), equations are fully implicitly integrated. The Eqs. (30–33) can be reduced to the following system:

$$q - \kappa - \sqrt{1-\phi}\,Y(T) - \sqrt{1-\phi}\,V(T)\sinh^{-1}\left[\frac{\Delta\lambda}{f(T)\Delta t}\right] = 0 \tag{34}$$

$$\omega_\alpha - \frac{(1-\phi)h}{1+\left(r_d\Delta\lambda + r_s\Delta t\right)\omega_\alpha}\left\|\underline{\beta}_n + \Delta\lambda\underline{n}\right\| = 0 \tag{35}$$

$$\omega_\kappa - \frac{(1-\phi)H}{1+\left(R_d\Delta\lambda + R_s\Delta t\right)\omega_\kappa}\left[\varepsilon_{ss}^n + \Delta\lambda\right] = 0 \tag{36}$$

$$\Delta\gamma - \frac{\Delta\phi}{\sqrt{1-\phi}} = 0 \tag{37}$$

These equations are solved using the Newton's method. The unknowns of the system are the plastic equivalent strain increment $\Delta\lambda$, the plastic volumetric strain increment $\Delta\gamma$, the norm of the back stress $\left|\underline{\alpha}\right|$, the isotropic hardening κ, and the strain increment component $\Delta\varepsilon_{33}$.

The Mises equivalent stress is discretized as

$$q = (1-\phi)q_e - \sqrt{1-\phi}\Delta\lambda\left[3G + \frac{h}{1+\left(r_d\Delta\lambda + r_s\Delta t\right)\omega_\alpha}\right] \tag{38}$$

and the pressure as

$$p = (1-\phi)\,p_e - K\sqrt{1-\phi}\Delta\gamma \tag{39}$$

Where G and K are respectively the shear and bulk moduli. The plastic normal tensor n is defined by

$$\underline{n} = \frac{3}{2}\frac{\underline{Z}^d}{q_e} \tag{40}$$

Where Z is the tensor difference

$$\underline{Z}^d = \underline{s}^e - \frac{2}{3}\frac{h}{1+\left(r_d\Delta\lambda + r_s\Delta t\right)\omega_\alpha}\underline{\beta}_n \tag{41}$$

and its norm is defined by

$$q_e = \sqrt{\frac{3}{2}\underline{Z}^d : \underline{Z}^d} \tag{42}$$

The tensor $\underline{s}^e$ is the deviatoric part of the trial stress tensor $\underline{\sigma}^e$ and it is written as

$$\underline{s}^e = \underline{\sigma}^e + p_e\underline{1} \tag{34}$$

In plane stress condition, the out-of-plane strain components are not defined kinematically but using the plane stress condition. The variable $\Delta\varepsilon_{33}$ is treated as an extra unknown of the problem, with the extra plane-stress equation for its determination being the constraint

$$\sigma_{33} = s_{33} - p = 0 \tag{43}$$

which can be written as

$$2G\left(-p + (1-\phi)s_{33}^e\right)q_e - 6G^2\sqrt{1-\phi}\Delta\lambda Z_{33}^d = 0 \tag{44}$$

The plastic strain is composed of a volumetric and a deviatoric part, and is written as

$$\underline{D}^p = \frac{1}{3}\frac{\Delta\gamma}{\sqrt{1-\phi}}\underline{1} + \frac{\Delta\lambda}{\sqrt{1-\phi}}\underline{n} \tag{45}$$

Finite Element Modeling of Warm Pan Forming Experiments

The forming limit diagram (FLD) depicts the maximum strains that can be sustained by sheet materials prior to the onset of localized necking, which is a common failure mode in metal forming. Generally, this failure process is controlled not only by external loading but also by internal microstructures. The major mechanical material properties controlling the formability (i.e. the FLD) of sheet metals are the work hardening, the rate sensitivity, and the plastic anisotropy of the sheet material.

Warm Pan Forming Experiments

To evaluate the mechanical properties of Mg AZ31 magnesium alloys and study their formability, warm forming experiments of five different magnesium sheet materials (Figures 39 and 40) were performed at various conditions (temperature, tool speed, friction, binding pressure, etc.) by P. Krajewski, P. Friedman, J. Singh (GM) at Troy Tooling, NY (Figure 39). The minimum thickness was measured for all 250 pans and detailed thickness profiles were produced for O-temper state, typically obtained after hot blow forming (e.g. quick plastic forming [29]) are investigated to match FE analysis work. Warm forming experiments were performed at various temperature and binding pressure conditions. Successful pans without any split and wrinkles were noted in green, pans with wrinkles in yellow, and pans with splits in red (Figure 40 and 41).

Figure 39: Pan forming press at Troy Tooling, NY.

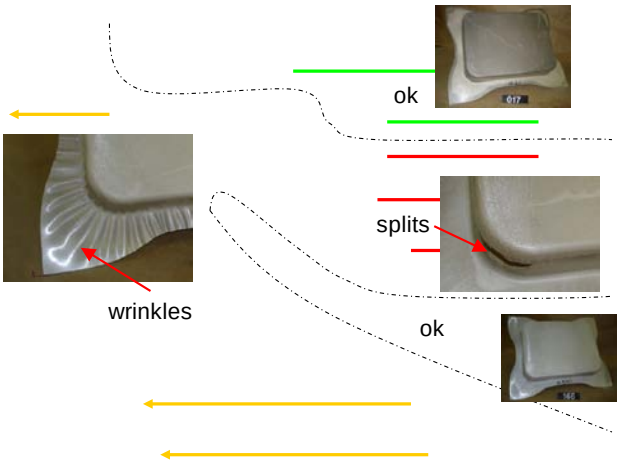

Figure 40: Warm pan forming results as function of temperature and binder pressure.

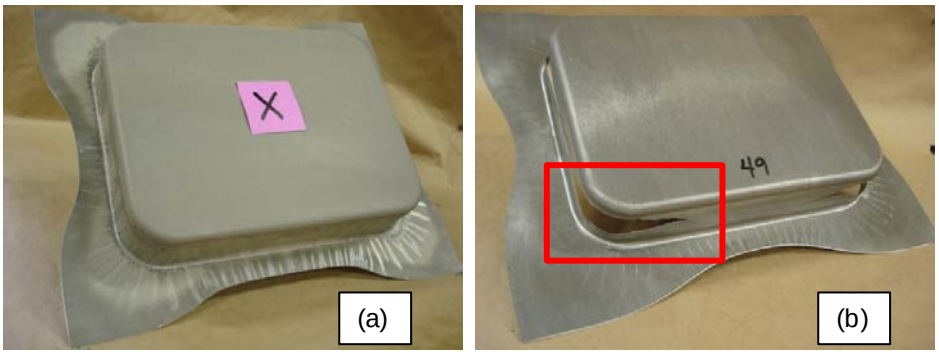

Figure 41: (a) No splitting: successfully stamped, but with some wrinkling. (b) Split: unsuccessfully stamped.

Warm Forming Simulations

In collaboration with Dr. Hector at GM Research and Development Center (Warren, MI), several pan forming simulations were performed to correlate experimental tests (Figures 39 and 40) and evaluate the mechanical properties of MgAZ31 magnesium alloys and study their formability. The simulation were performed at various conditions (temperature, tool speed, friction, binding pressure, etc.) using the current version of the DMG plasticity model material subroutine Vumat (Abaqus/Explicit) developed and implemented at Center for Advanced Vehicular Systems (distributed to GM under the Software Licence Agreement Version 4.21.09). The goal of these simulations was to correlate the new batch of pan forming experimental tests that were conducted at Troy Tooling, NY by Dr. Krajewski (GM). The pan forming simulations were performed at the same temperatures and binding pressures that were applied during experimental tests.

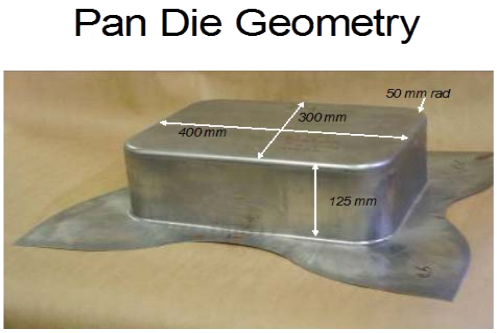

Figure 42: MgAZ31 Warm Forming Pan Geometry for FE Simulations.

The Mg metal sheet was described by quadrilateral finite-membrane-strain and arbitrarily large rotations elements. In ABAQUS/Explicit, these shell elements are only available under the coded name S4R. The thickness of this shell element is updated with deformation and calculated from the membrane strain and Poisson's ratio. Since the S4R element uses reduced integration with one integration point, the strain is uniform within the element. The first order transverse shear stiffness is defined by the user as a fraction of the shear modulus to match the shear response for the shell to that of a three-dimensional solid for the case of bending about one axis. The default option of hourglass control is chosen for this shell element.

The die, punch and binder are considered rigid bodies and modeled using rigid elements (4-node, bilinear quadrilateral). A pure master-slave relationship is used the contact surface interaction between the Mg sheet metal and rigid bodies, in which a tangential friction coefficient is defined to describe the frictional behavior.

Boundary conditions were applied such that all rigid body translations and rotations were eliminated. The die was piloted with a velocity at its reference node, and a concentrated force was applied on reference node of the binder rigid surface to reproduce the binder pressure in experiments. The analysis was decomposed into two steps. A pre-stamping step analysis corresponded to the application of the initial binding pressure on the magnesium sheets, while the die and the punch were completely constrained. The second step analysis corresponded to the stamping process, in which the binding pressure was ramping up to its final value. Tthe punch was assumed stationary, while the die moves down after the sheet is clamped with a given binder force and the sheet is then formed around the stationary punch to obtain the same final shape as in experiment (Figure 42).

The ABAQUS/Explicit time integration procedure requires very small stable time increments, which are automatically calculated based on the material density, element size and velocity. In this analysis where the material response is strain rate sensitive. Therefore, to increase the stable time increment and computationally speed up the process, the die speed was not changed and only the mass of the whole model was to artificially increased by defining a mass scaling factor of 100. This was equivalent to the increase 10 times the die speed without mass scaling.

Table 2: Temperature and binding pressure conditions.

Temperature (°C)	Binding Pressure (Psi)
200	2500
	2750
	3000
225	2000
	2250
250	1500
275	1500
300	1500
	3000
325	3000
350	1000
	1250
	1500

To expedite the modifications of the ABAQUS input file, several variables were defined as parameters:

- Period;
- Displacement;
- Friction;
- Die velocity (=Displacement/Period);
- Initial binding force (before stamping);
- Final binding force (at the beginning and during stamping);
- Fictive binder mass defined as a rigid body in the analysis.

Different series of pan forming simulations were performed using the temperature and binding pressure conditions in Table 2 with either the DMG plasticity model or the Sellars-Tegart creep plasticity model. Because the coefficient of friction in the pan forming experimental tests is unknown, three series of pan forming simulation were performed to numerically determine the friction coefficient using the inverse fitting procedure. Using the DMG plasticity model and friction coefficients of 0.1, 0.2 and 0.3 (assumed uniform at any point and throughout the forming process) and, the simulation results were post-processed in order to compare the numerical draw dimensions to the measured ones (Figure 43).

The comparison of draw dimensions between several numerical results and experimental data concluded that the value of the friction coefficient is near 0.06.

New series of simulation were performed with the friction coefficient of 0.06 and using both DMG plasticity model and Dr. Agnew creep plasticity model. The numerical results of draw dimensions from both simulation series showed that both plasticity models give very similar results. The simulations compared quite well with experimental data for the draw dimensions d_2 and d_3 (2-3% error), but compared relatively poorly for the draw dimension d_1 (2-10% error), which lead to the conclusion that adding anisotropic texture effect to the material model is a necessity.

In the pan forming simulations, no wrinkling was observed in the numerical results as it was the case during experimental tests. The binding mass was chosen as a numerical parameter to virtually increase the binder's kinetic energy and cause wrinkling. Wrinkling up to 8 mm was observed for binder masses larger

than 0.66 tons (previous simulations were run with a binding mass of 0.01 tons), while no wrinkling occurred for binding mass of 0.65 tons.

The nodal paths to output the formed thickness profiles from ABAQUS pan forming calculations are shown on Figure 44. Numerical thickness profiles will be compared after measurement of thickness from experimental tests.

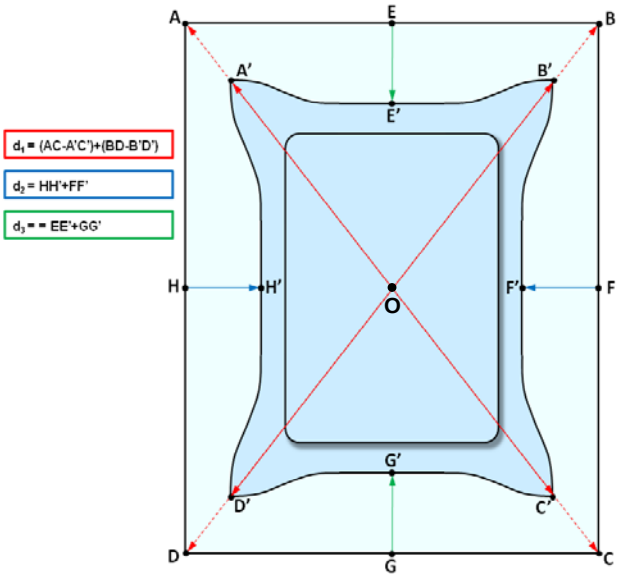

Figure 43: Draw Dimensions d_1, d_2 and d_3 used for comparing numerical and experimental pan forming results.

New series of simulation were performed with the friction coefficient of 0.06 and using both MG plasticity model and Dr. Agnew creep plasticity model. The numerical results of draw dimensions from both simulation series showed that both plasticity models give very similar results. The simulations compared quite well with experimental data for the draw dimensions d2 and d3 (2-3% error), but compared relatively poorly for the draw dimension d1 (2-10% error), which lead to the conclusion that adding anisotropic texture effect to the material model is a necessity.

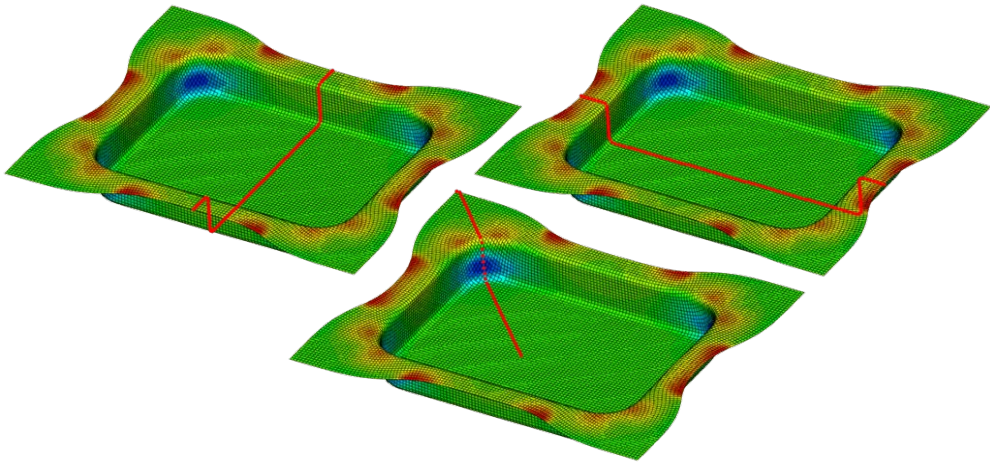

Figure 44: Different nodal paths for outputting thickness profiles.

In the pan forming simulations, no wrinkling was observed in the numerical results as it was the case during experimental tests. The mass of the binder was chosen as a numerical parameter to virtually increase the binder's kinetic energy and cause wrinkling. Wrinkling up to 8 mm was observed for binder

masses larger than 0.66 tons (previous simulations were run with a binding mass of 0.01 tons), while no wrinkling occurred for binding mass of 0.65 tons or less.

Warm pan forming simulations with a damage-plasticity coupling were also performed. The damage addition in the material response showed that the thickness is thinner at the split location, which leads to the conclusion that the warm forming finite element analysis must be conducted with damage-plasticity coupling in order to capture any split mode (Figure 45).

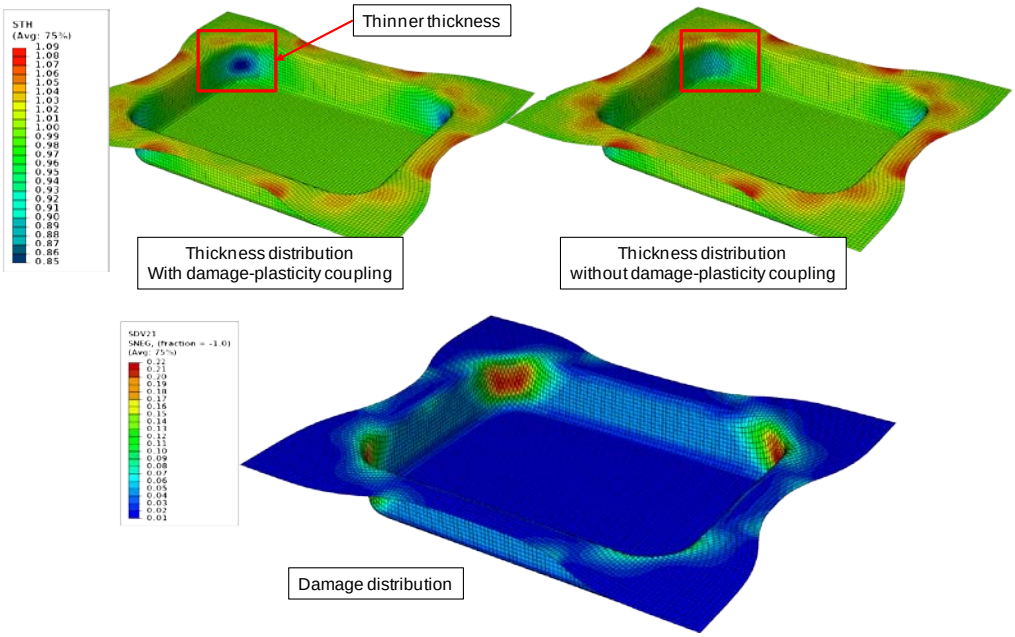

Figure 45: Damage and thickness distributions for pan forming simulations with and without damage-plasticity coupling.

Effect of Friction

In sheet metal forming, the workpiece and tool and lubricant at the interface form a complex, multivariable, and time-dependent tribological system. The lubrication mechanism is determined by the surface topography and mechanical properties of workpiece and tool, the lubricant, and their interactions under conditions of pressure, velocity, and temperature. The friction influences the deformation pattern of the workpiece and surface finish of the products. Therefore, lubrication and friction at the workpiece-tool interface play an important role in product quality control of metal forming process. In simulation, it is most of the times assumed to be constant, and is described by the coefficient of friction μ. In reality, it depends on:

- The surface fineness of the sheet metal material (Figure 46);
- The surface fineness of the tool surface;
- The actual local surface pressure;
- The actual relative speed between the sheet segment concerned and the tool surface;
- The temperature in the active interface;
- The type of lubricant (Figure 47);
- The topology of the sheet surface is highly dependent on its manufacturing method (Figure 48).

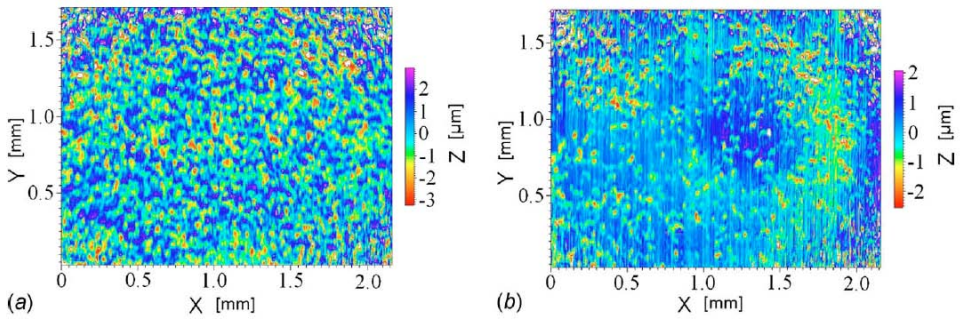

Figure 46: Surface image of aluminum alloy sheet AA6016 T4, EDT surface before and after strip drawing test [30].

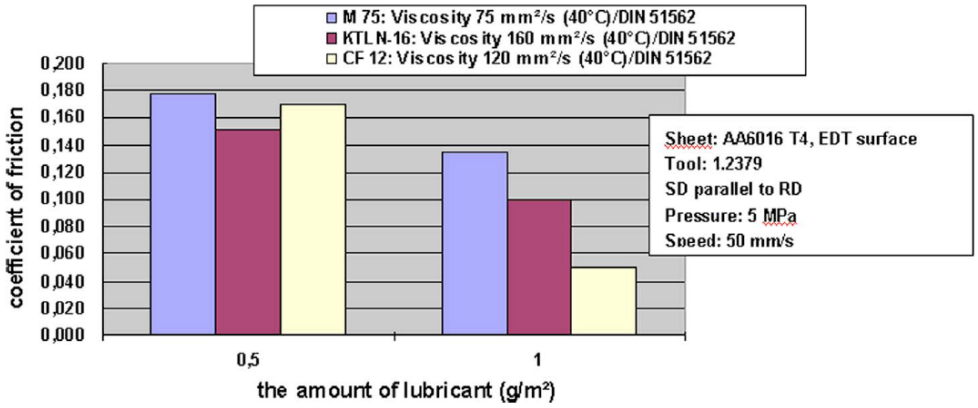

Figure 47: The coefficient of friction tested with lubricants M75, KTLN-16, and CF12 [30].

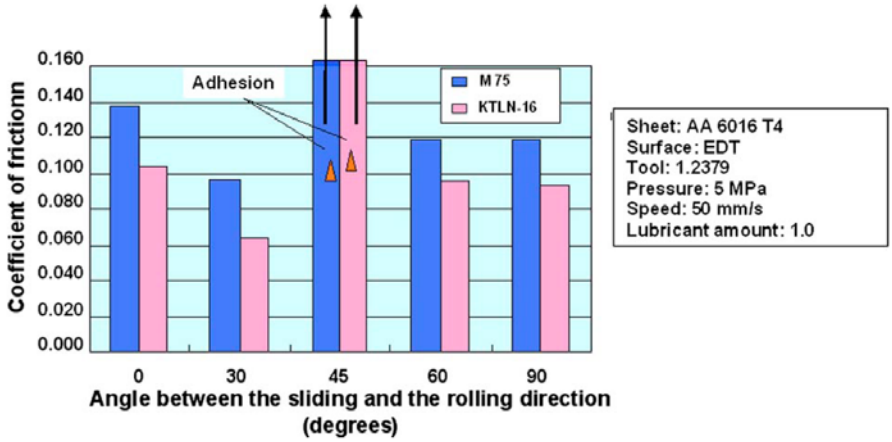

Figure 48: Coefficient of friction over the angle between the sliding and rolling directions [30].

The effect of the friction coefficient on the thickness profile was measured by running several warm pan forming simulations with adiabatic heating for five different values of the friction coefficient. Experimental results of two pans (26 and 134) formed without splits at different temperatures and binding pressures were chosen to be compared with simulation results. We can observe on Figure 49 that the frictional behavior has a very significant effect on the thickness profile of the formed pan. The variation of the thickness strain can reach 5% for a 0.04 change in the value of the friction coefficient in the pan 132. The friction coefficient induces more significant change in the simulation of the pan 132 than in the

one of the pan 26 because of a higher binding pressure per cylinder, respectively 1500 lbs·ft and 1250 lbs·ft.

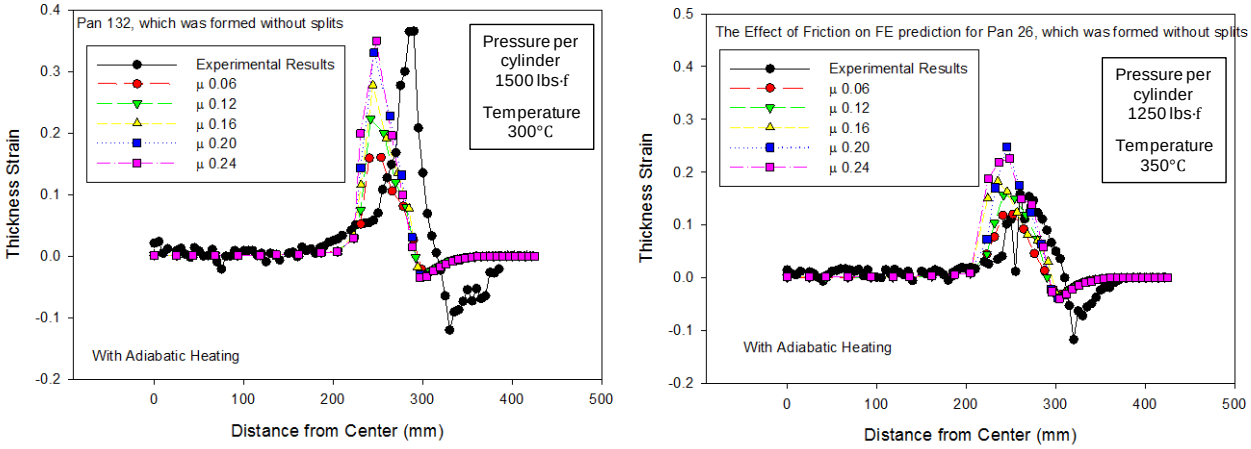

Figure 49: Comparison with experimental results of numerical thickness strains from the center to the corner of the pan for different friction coefficients.

Therefore, it can be concluded that the friction coefficient is at least as important as the material model in the prediction of the thickness distribution. To improve warm forming simulations, a more realistic frictional behavior should be developed in addition of improving the material model.

Publications

1. Solanki KN, Horstemeyer MF, Steele GW, Hammi Y, Jordon JB. Calibration, validation, and verification including uncertainty of a physically motivated internal state variable plasticity and damage model. IJSS 2010;47(2),186-203.
2. Bammann. D.J., & Solanki, K.N. (2010). On Kinematic, Thermodynamic and Coupling of a Damage Theory for Polycrystalline Material, International Journal of Plasticity. 26(6), 775–793.
3. Solanki, K.N., & Bammann, D.J. (2010). A Thermodynamic Framework for a Gradient Theory of Continuum Damage. Acta Mechanica, 213, 27–38.
4. Acar, E., Solanki, K.N., Rais-Rohani, M., & Horstemeyer, M. (Mar 2010). Stochastic Uncertainty Analysis of Damage Evolution Computed through Microstructure-Property Relations. Probabilistic Engineering Mechanics Elsevier, 25(2), 198-205
5. Ma, Q., Li, B., Marin, E.B., et al., "Twinning induced dynamic recyrstallization in a magnesium alloy extruded at 450 C," Scripta Materialia, 2011, 65: 823-826.
6. Ma, Q., Marin, E.B., et al., "On predicting the channel die compression behavior of HCP magnesium AM30 using crystal plasticity FEM," Magnesium Technology 2011, 583-587.
7. Ma,Q., El Kadiri, H., Oppedal, A.L., et al., “Twinning and double twinning upon compression of prismatic textures in an AM30 magnesium alloy,” Scripta Materialia, 2011, 64: 813-816.
8. Ma,Q., El Kadiri, H., Oppedal, A.L., et al., “Twinning effects in a rod-textured AM30 magnesium alloy,” International Journal of Plasticity, 2011,doi:10.1016/j.ijplas.2011.08.001.
9. Ma, Q., El Kadiri,H., Oppedal, A.L., et al., “Twinning multiplicity in an AM30 magnesium alloy under uniaxial compression,” Magnesium Technology 2011, 301-305.
10. Parkar, A.A., Bouvard, C., Marin, E.B., Horstemeyer, S.J., Wang, P.T., Horstemeyer, M.F.,“Comprehensive Thermo-Mechanical Validation of Extrusion Simulation Cycle for Al 1100 Using HyperXtrude,” TMS 2011.

11. Parkar, A. A., Bouvard, C., Horstemeyer, S. J., Marin, E. B., Wang, P. T., "Experiments and Simulation of AZ61 Extrusion through Conical Dies with Eulerian and Lagrangian Codes," ESAFORM 2011.
12. H. El Kadiri, A.L. Oppedal, A crystal plasticity theory for latent hardening by glide twinning through dislocation transmutation and twin accommodation effects, Journal of the Mechanics and Physics of Solids. 58 (2010) 613–624.
13. H. El Kadiri and A. L. Oppedal. Transmutation and accommodation effects by glide twinning. In S. R. Agnew, N. R. Neelameggham, E. A. Nyberg, and W. Sillekens, editors, *Magnesium Technology 2010*. The Minerals, Metals & Materials Society, 2010.
14. A.L. Oppedal, H. El Kadiri, C.N. Tomé, J.C. Baird, S.C. Vogel, M.F. Horstemeyer, Limitation of current hardening models in predicting anisotropy by twinning in hcp metals: Application to a rod-textured AM30 magnesium alloy, Magnesium Technology. (2011) 313 - 320.
15. A. L. Oppedal, H. El Kadiri, C. N. Tomé, G. C. Kaschner, S. C. Vogel, J. C. Baird, and M. F. Horstemeyer. Effect of dislocation transmutation on modeling hardening mechanisms by twinning in magnesium. *International Journal of Plasticity*, doi:10.1016/j.ijplas.2011.09.002, 2011.
16. A. L. Oppedal, H. El Kadiri, C. N. Tomé, J. C. Baird, S. C. Vogel, and M. F. Horstemeyer. Anisotropy in hexagonal close packed structures: improvements to crystal plasticity approaches applied to magnesium alloy. Submitted, 2011.

References

[1] F.A. Slooff, J. Zhou, J. Duszczyk, L. Katgerman, "Strain-dependent constitutive analysis of three wrought Mg-Al-Zn alloys", J. Mater. Sci. (2008) 43:7165-7170.

[2] R.B. Von Dreele, Quantitative texture analysis by Rietveld refinement, Journal of Applied Crystallography. 30 (1997) 517–525.

[3] H.R. Wenk, L. Lutterotti, S. Vogel, Texture analysis with the new HIPPO TOF diffractometer, Nuclear Instruments and Methods in Physics Research Section A: Accelerators, Spectrometers, Detectors and Associated Equipment. 515 (2003) 575–588.

[4] U.F. Kocks, J.S. Kallend, H.R. Wenk, A.D. Rollett, S. I., popLA Preferred Orientation Package - Los Alamos Report LA-CC-89-18, (1995).

[5] Tomé, Program Pole (version 8b), (2008).

[6] R. Hielscher, H. Schaeben, A novel pole figure inversion method: specification of the MTEX algorithm, Journal of Applied Crystallography. 41 (2008) 1024–1037.

[7] H. El Kadiri, A.L. Oppedal, A crystal plasticity theory for latent hardening by glide twinning through dislocation transmutation and twin accommodation effects, Journal of the Mechanics and Physics of Solids. 58 (2010) 613–624.

[8] A.L. Oppedal, H. El Kadiri, C.N. Tomé, J.C. Baird, S.C. Vogel, M.F. Horstemeyer, Limitation of current hardening models in predicting anisotropy by twinning in hcp metals: Application to a rod-textured AM30 magnesium alloy, Magnesium Technology. (2011) 313 - 320.

[9] C.H. Cáceres, P. Lukáč, A. Blake, Strain hardening due to {10-12} twinning in pure magnesium, Philosophical Magazine. 88 (2008) 991-1003.

[10] Z. Marciniak., J.L. Duncan., S.J. Hu, Mechanics of Sheet Metal Forming, Butterworth Heinemann, (2002).

[11] Davison L., Stevens A.L., Kipp M.E., "Theory of Spall Damage Accumulation in Ductile Metals," *Journal of the Mechanics and Physics of Solids*, Vol. **25**, pp. 11–28, 1977.

[12] Bammann, D.J. and Aifantis, E.C., “A Damage Model for Ductile Metals", *Nuclear Engineering and Design*, Vol. 116, pp. 355–362, 1989.

[13] Bammann, D. J., Chiesa, M. L., Horstemeyer, M. F., Weingarten, L. I., "Failure in Ductile Materials Using Finite Element Methods," *Structural Crashworthiness and Failure*, eds. T. Wierzbicki and N. Jones, Elsevier Applied Science, The Universities Press (Belfast) Ltd, 1993.

[14] Horstemeyer, M.F., Lathrop, J., Gokhale, A.M., and Dighe, M., “Modeling Stress State Dependent Damage Evolution in a Cast Al-Si-Mg Aluminum Alloy,” *Theoretical and Applied Fracture Mechanics*, Vol. 33, pp. 31-47, 2000.

[15] Horstemeyer, M.F. and Gokhale, A.M., “A Void Nucleation Model for Ductile Materials,” *International Journal of Solids and Structures*, Vol. 36, pp. 5029-5055, 1999.

[16] Garrison, W.M. Jr., and Moody, N.R., “Ductile Fracture,” *Journal of Physics and Chemistry of Solids*, Vol. 48, pp. 1035–1074, 1987.

[17] Tvergaard, V., “Material Failure by Void Growth to Coalescence,” *Advances in Applied Mechanics*, Eds. J.W. Hutchinson and T. Y. Wu, Vol. 27, pp. 83-151, 1990.

[18] McClintock, F.A., “A Criterion for Ductile Fracture by the Growth of Holes,” *Journal of Applied Mechanics*, Vol. 35, pp. 363–371, 1968.

[19] Rice J.R., and Tracey, D.M., “On the Ductile Enlargement of Voids in Triaxial Stress Fields," *Journal of the Mechanics and Physics of Solids*, Vol. 17, p. 201–217, 1969.

[20] Budiansky et al., 1982 B. Budiansky, J.W. Hutchinson and S. Slutsky, Void growth and collapse in viscous solids. In: H.G. Hopkins and M.J. Sewell, Editors, *Mechanics of Solids*, Pergamon Press, Oxford, pp. 13–45, 1982.

[21] Cocks, A.C.F. and Ashby, M.F., “On Creep Fracture by Void Growth,” *Progress in Material Sciences*, Vol. 27, pp. 189–244, 1981.

[22] Garber, R., Bernstein, I.M., and Thompson, A.W., “Effect of Hydrogen on Ductile Fracture of Spheroidized Steel,” *Scripta Metallurgica*, Vol. 10, pp. 341–345, 1976.

[23] Cox T. B. and Low J. R., “An Investigation of the Plastic Fracture of AISI 4340 and 18 Nickel– 200 Grade Maraging Steels,” *Metallurgical Transitions*, Vol. 5, pp. 1457–1470, 1974.

[24] Rogers H C., “The Tensile Fracture of Ductile Metals,” *Transactions of the Metallurgical Society of AIME*, Vol. 218, pp. 498–506, 1960.

[25] Magnusen, P.E., Dubensky, E.M., and Koss, D.A., “The Effect of Void Arrays on Void Linking During Ductile Fracture,” *Acta Metallurgica*, Vol. 36, No. 6, pp. 1503-1509, 1998.

[26] Major, J.F., Makinde, A., Lee, P.D., Chamberlain, B., Scappaticci, T., and Richman, D., “The Lincoln Mark VIII Cast Aluminum Suspension Control Arm (Parallel Development),” *SAE 1994 Transactions*, (1994), pp. 635-646.

[27] Horstemeyer, M.F. “From Atoms to Autos: Part 1 Microstructure-Property Modeling,” Sandia National Laboratories Report, SAND2001-8662, (2001).

[28] Horstemeyer, M.F., Fan, J., and McDowell, D.L., “From Atoms to Autos: Part 2 Fatigue Modeling,” Sandia National Laboratories Report, SAND2001-8661, (2001).

[29] Schroth, J.G., in: Taleff, E.M., Friedman, P.A., Krajewski, P.E., and R.S., Mishra, J.G. Schroth (Eds.), Advances in Superplasticity and Superplastic Forming, TMS, (2004), pp. 9–20.

[30] Liu, X., Liewald, M., and Becker, D., “Effects of Rolling Direction and Lubricant on Friction in Sheet Metal Forming,” *Journal of Tribology*, (2009), Vol. 131, pp. 1–8.

Key Words

Finite-strain; Extrusion; Sheet Forming; Thermodynamics; Void Growth; Anisotropic Damage; Material Length Scale; Model Verification and Validation; Internal State Variable; Uncertainty; Kinematics.

Brief Description of Report

This final report for Phase 3 of the SRCLID program describes the research activities performed to model the extrusion and sheet forming on Mg alloys, as well as the work on constitutive modeling and corresponding numerical implementation. The end goals of this effort are twofold: (1) an experimentally validated cradle-to-grave modeling and simulation effort to optimize automotive components (i.e., front end) for magnesium alloys with consideration of uncertainty in order to decrease weight and cost, and yet increase the performance and safety in impact scenarios; (2) the multiscale ("From Atoms to Autos") material modeling approach in which we quantify the microstructure-property relations by evaluating various length scales, starting at the atomic level for each step of the manufacturing process (i.e., extrusion, sheet) for vehicles.

MISSISSIPPI STATE UNIVERSITY

Southern Regional Center for Lightweight Innovative Design

Phase III

Final Scientific & Technical Report

October 1, 2009-September 30, 2011

For compliance with contract requirements of Award DE-EE0002323

Task 2

CYBERINFRASTRUCTURE

Submitted December 27, 2011

TASK 2: CYBERINFRASTRUCTURE

Table of Contents

TASK 2: CYBERINFRASTRUCTURE

Principal Investigator: Tomasz Haupt
Associate Research Professor
Center for Advanced Vehicular Systems
Mississippi State University
PO Box 5405, Mississippi State, MS 39762-5405
(662)325-4524; fax: (662)325-5433; email: haupt@cavs.msstate.edu

Participants: R. Carino, F.M. Ciorba

William Joost: Technology Area Development Manager
e-mail: william.joost@ee.doe.gov

Magda Rivera: Project Manager
e-mail: magda.rivera@netl.doe.gov

Contractor: *Mississippi State University (MSST)*
Contract No.: *DE-EE0002323*

Overview

The objective of this effort was to design and develop a cyberinfrastructure (CI) to exploit the recent transformative research in material science involving multiscale physics-based predictive modeling, multiscale experiments, and design. The CI has become the foundation of a virtual organization, known as the Engineering Virtual Organization for Cyber Design (EVOCD). EVOCD has been developed with the primary goal of accumulating and protecting the intellectual property generated by the participants of the organization. The portal provides powerful passage for accruing and exchanging community knowledge as well as access to repositories of experimental data, material models and computational tools at different length scales, which together exploit the integrative nature of the Integrated Computational Material Engineering (ICME). To achieve this goal, EVOCD is comprised of four primary functional components that are the foundation of the VO: (i) Knowledge Management; (ii) Repository of Codes; (iii) Repository of Data; (iv) Online Calibration Tools. The implementation is primarily based on third-party, open-source software packages (such as Apache's Tomcat, Apache's ServiceMix, View VC, SVN) customized to particular need of EVOCD, and the principles of the Service-Oriented Architectures (SOA).

Creating a Virtual Organization

Cyberinfrastructure is widely recognized for facilitating system-level science through formation of Virtual Organizations (VOs). To construct the VO, the underlying cyberinfrastructure must enable collaborative research by supporting the creation of virtual workgroups and teams, facilitate access to resources, and enhance problem-solving processes. The literature describes many attempts to create effective VOs by capitalizing on dramatic advances in IT. Among the most notable examples of VOs are Southern California Earthquake Center (SCEC), cancer Biomedical Informatics Grid (caBIG™), Earth System Grid (ESG), nanoHUB, GEON, CAMERA, CHOIS, LEAD and others.

While it is not possible to create a VO without cyberinfrastructure, the cyberinfrastructure alone is insufficient to establish an effective VO: organizational, human, and social factors are also important aspects of VO creation and operation. For example, the participants must reorient their research methods to work together as a community while still protecting their competitive advantages. Moreover, standardizing patterns of interactions in organizations (e.g., fostering a "corporate culture" for accumulating and sharing the intellectual property) - developing a signature rather than a mere Web site—is critical for the initialization of a successful VO. Having this in mind we have developed a VO

aimed toward satisfying the specific needs of ICME: the Engineering Virtual Organization for CyberDesign (EVOCD).

The primary focus of the ICME vision is establishing a knowledge base accessible to the community-at-large for solving a plethora of disparate issues in material science, applied mechanics, and engineering. This knowledge base requires collection of experimental data describing phenomena at different scales (exploratory experiments, calibration of material models, and validation of models), performing simulations at different scales (atomic, molecular, dislocation, crystal-plasticity, macro-scale FEA), and linking all this information together to determine structure-properties relationships, thereby leading to new concepts and design of new materials. In addition to pushing the edge of material science and solid mechanics by supporting the development and validation of new methods, particularly in the area of multiscale modeling which requires multidisciplinary expertise, the knowledge base is further expected to be used for engineering design optimization and to support workforce training, including enhancing academic curricula at the graduate level.

It follows that managing the ICME knowledge base directs the principal rationale and objective for establishing a VO. Management entails gathering, developing, integrating, and disseminating experimental data, material models, and computational tools, as well as their use for material and product design. Consequently, the Engineering Virtual Organization for CyberDesign (EVOCD, http://icme.hpc.msstate.edu) is dedicated to the accumulation of the "intellectual capital" pertaining to ICME. It is the organization's capital that attracts community participation in the organization. There are three critical aspects to the process of accumulating capital in order to create a relevant organization: (1) protection of intellectual property, (2) quality assurance of information, and (3) the management of complexity.

In a competitive environment in which materials research and development is performed, protection of the intellectual property is imperative. While the information meant for public consumption must be clearly attributed to its creators, the innovative research may require a restriction of information (e.g., pre-publication or proprietary data) exchange to only a narrow group of collaborators. The VO must support the former, and enforce the latter. Quality assurance of the information must include its pedigree and then its validation, followed with approval by either a curator or a peer-review process. The management of complexity implies that the information must be easily navigable through intuitive interfaces, yet all complexity of the underlying infrastructure must be hidden from the end user. Furthermore, the information must be understandable to students and directly and efficiently accessible to practitioners.

Notably, many other currently established VOs facilitate wide-spread collaborative efforts to process huge datasets (petabytes of satellite images, collider data, astronomical observations, etc.) and require a network of petaflop-range supercomputers to solve specific grand-challenge problems. In this sense, EVOCD is different: it is a cyberspace where the participants can solve their own scientific and engineering problems. On the other hand, EVOCD complements the efforts of nanoHub, 3D Material Atlas, MatDL, NIST Data Gateway, and when linked together with these portals, it will become part of the global ICME cyberinfrastructure.

Functionality of EVOCD

EVOCD has been developed with the primary goal of accumulating and protecting the intellectual property generated by the participants of the organization. The portal provides powerful passage for accruing and exchanging community knowledge as well as access to repositories of experimental data, material models and computational tools at different length scales, which together exploit the integrative

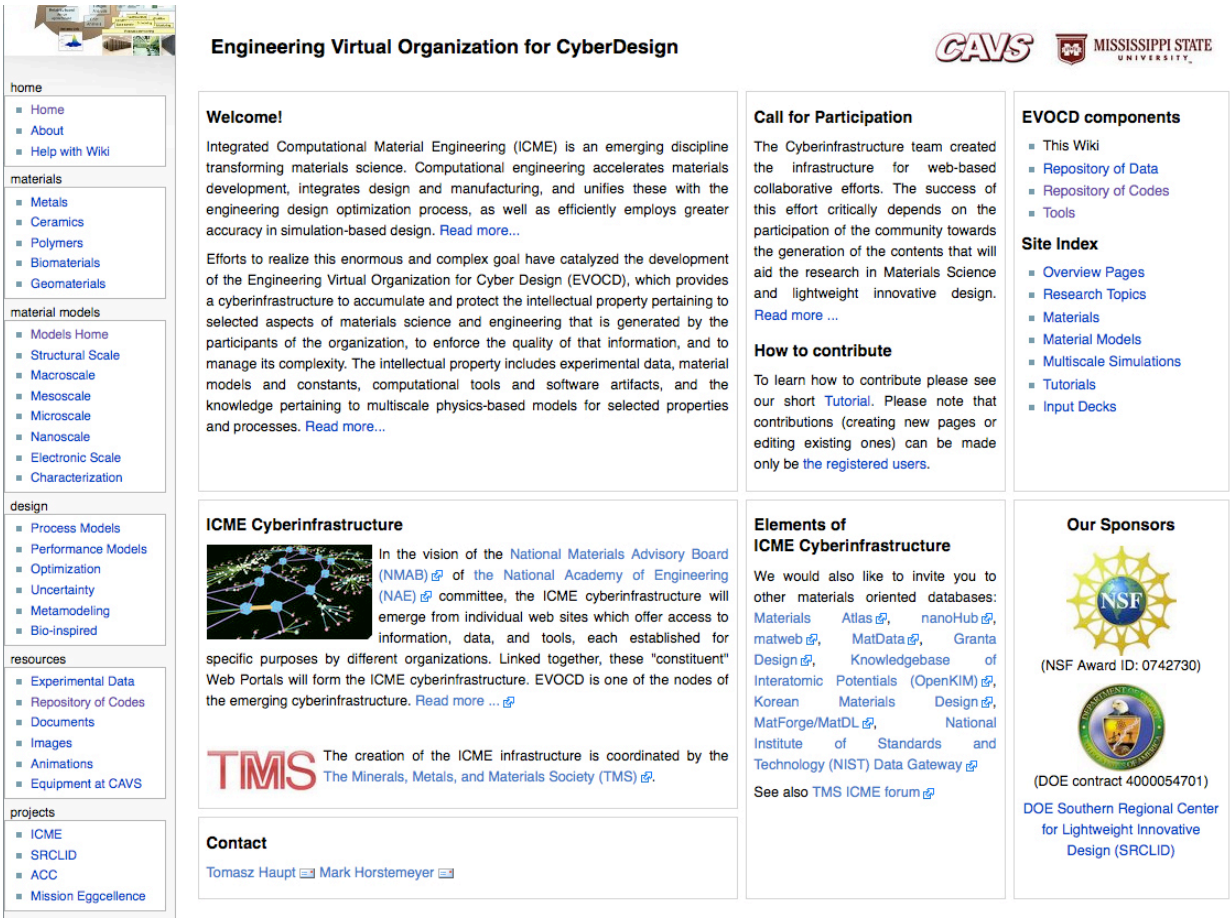

Figure 1: The home page of EVOCD Wiki

nature of ICME. To achieve this goal, EVOCD is comprised of four primary functional components that are the foundation of the VO: (i) Knowledge Management; (ii) Repository of Codes; (iii) Repository of Data; (iv) Online Calibration Tools.

Knowledge Management: Wiki

Knowledge management has been achieved by applying an "architecture of participation" as advocated and implemented by Web 2.0 concepts and technologies. Tools like Wiki lead to the creation of a collective (read: peer-reviewed) knowledge database that is always up-to-date with a structure that spontaneously evolves to reflect the current state of the art. Therefore, we have chosen Wiki as the mechanism for community-driven knowledge management.

The Wiki has become the façade for the EVOCD portal to accumulate the knowledge pertaining to ICME. The Wiki captures the knowledge about different classes of materials (metals, ceramics, polymers, and others), material models at various length scales, and design issues, from process and performance models, to optimization under uncertainty, to bio-inspired design. In addition, the Wiki provides direct access to resources, such as data and code repositories.

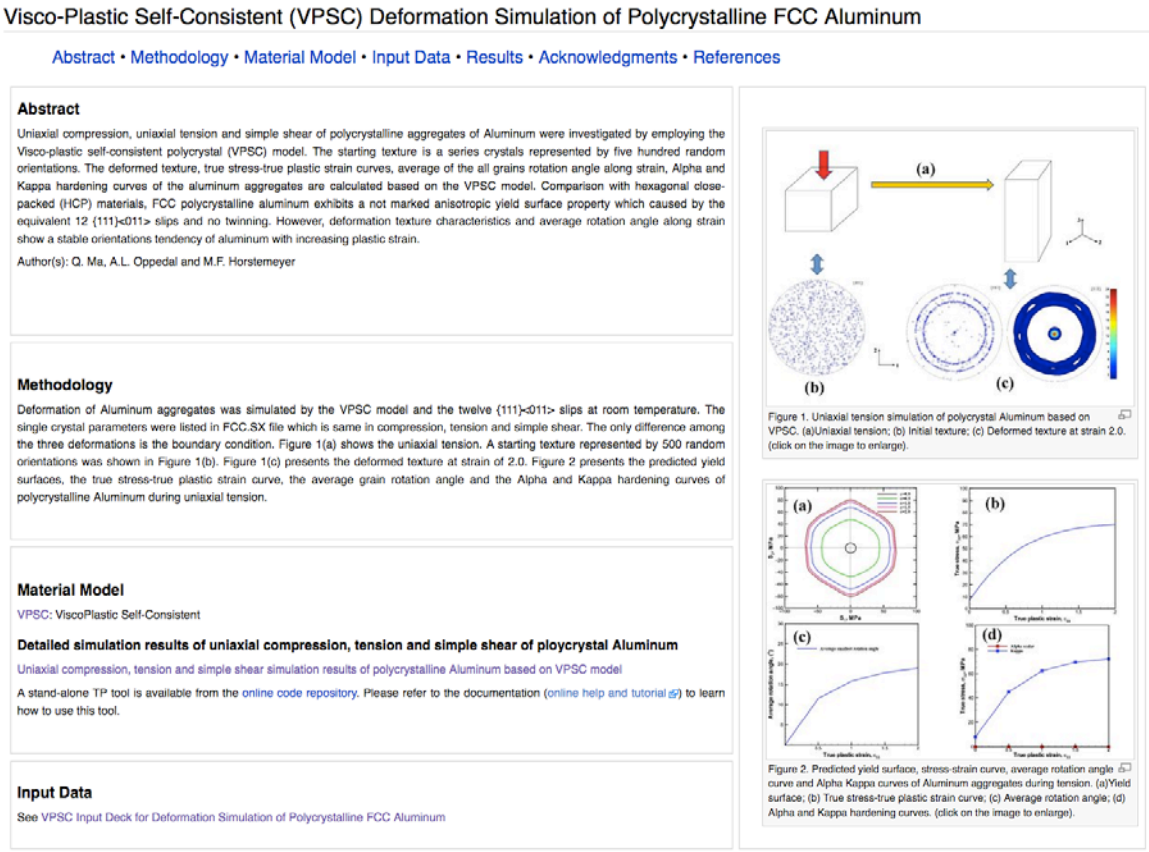

Figure 2: Example page in EVOCD Wiki

The intellectual property is protected by configuring the Wiki server to restrict creation and editing of pages to only registered users verified by their email addresses. As a result, all contributions are uniquely attributed to their authors. Following the model introduced by Wikipedia, the quality of contributions is guaranteed by the Web 2.0 process but further monitored by the Wiki editors.

The home page of the EVOCD Wiki (http://icme.hpc.msstate.edu) is shown in Figure 1, and example of knowledge captured by the Wiki is shown in Figure 2.

Repository of Codes

ICME applies computational methods to material science, applied mechanics, and engineering. A significant part of the knowledge is therefore captured as software artifacts from implementing material models, as well as simulation, modeling and optimization codes. Realization of ICME thus critically depends upon providing the capability to gather and disseminate the information about these software components, which is, in turn, an imperative part of the VO's intellectual capital. Consequently, EVOCD serves as the repository of open-source codes contributed by the EVOCD participants. Each code is accompanied with documentation (installation instructions, user manual, theoretical background, and examples). In addition to the open-source material models, the repository provides tutorials and examples for popular commercial or otherwise proprietary codes (such as ABAQUS and LAMMPS).

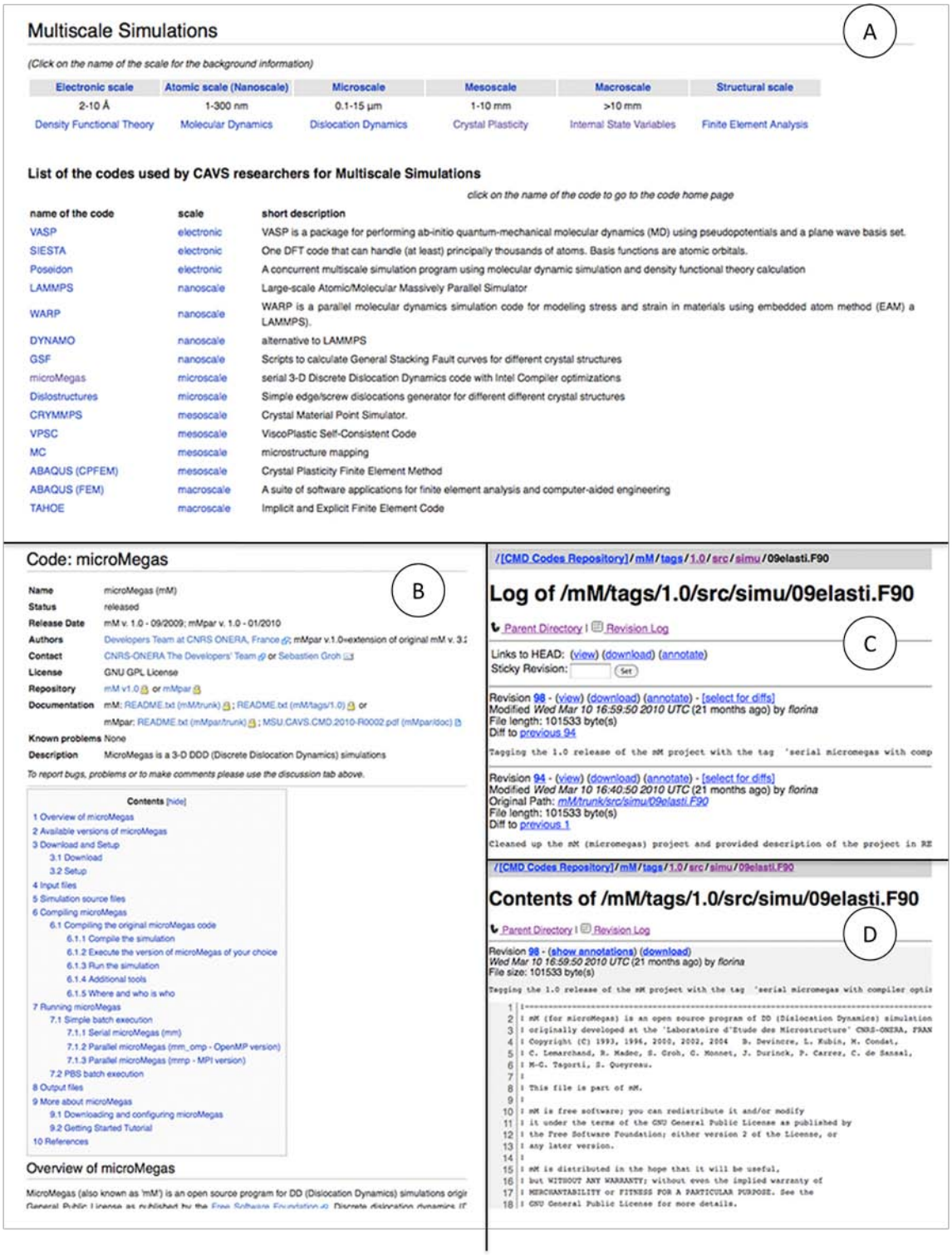

Figure 3: Snapshots of the code repository interface. (A): EVOCD Wiki page serving as the entry point to the code repository; (B): EVOCD Wiki page describing microMegas code (C): Example snapshot of the ViewVC interface showing the history of modifications; (D): Example snapshot of the ViewVC showing the actual source code of selected routine.

The repository of codes complements the knowledge captured in Wiki, enabling the EVOCD user to reproduce the results reported there. Figures 3 shows the snapshots of the code repository user interface.

The intellectual property is further protected by restricting access to the actual SVN repository. Only individually-approved contributors have the privilege to offer new revisions. The contributed codes are made available to the general public through a read-only SVN mirror that serves as the back-end for the Web SVN client (open source ViewVC). All codes downloaded through the ViewVC client are subject to Mississippi State University (MSU) policies and disclaimers. Because of these arguably restrictive policies, many codes listed and documented in the EVOCD repository are available from other locations specified in the repository, typically web sites of their developers or vendors' web sites. This is the beginning of the "supply chain" envisioned as being the foundation of the global cyberinfrastructure for ICME. The quality of the codes is assured by the fact that they have been used to generate results described in the EVOCD Wiki.

Repository of Data

Experimental data is another critical component of the intellectual capital captured by EVOCD. At this time, EVOCD focuses on force-displacement, stress-strain, strain-life (fatigue), and materials characterization data, such as images of microstructure (c.f. Figure 4), all of which complement the data repositories offered by other ICME cyberinfrastructure participants, e.g., 3D Material Atlas. The significance of the data types supported by EVOCD is that they are necessary for the development of Internal State Variable (ISV) material models used in hierarchical multiscale modeling. The ISV-based models are described in detail in the Wiki pages, and the codes that implement them are available from the repository.

This time, the intellectual property is protected at two levels. At the first level, similarly to the protection of Wiki and repository of codes, only registered users are allowed to contribute. At the second level, the data repository is under access control. To this end, each data request is augmented with SAML-based credentials that are checked against the custom-developed Community Authorization Server (CAS). This authorization mechanism allows each user to create a group and invite a selected group of users to participate in the group. Only the members of this group are permitted (subject to CAS authorization) to upload data to the group folder. The group moderator (the group creator, or a group member appointed by the group creator) makes the decision to keep the data private, i.e., visible only to the group members, or to make the data "public" by granting read-only access to all users. This group-based access control mechanism is used to exchange restricted-access data, an essential tool for collaborations within EVOCD.The issue of data quality is addressed in several ways. First, metadata is provided to reveal the pedigree of the data. The information included in a metadata record and pertaining to the data quality is generated automatically from the user session and the mandatory header of the data file. The data is automatically rejected by the system if any critical information is missing (e.g., initial temperature or strain rate for stress-strain data). Most of the publicly available data in the repository have been published in professional journals, thus verified by a peer-review process, and described in the Wiki pages. Non-published data are typically hidden from the general public (group data) and require verification by the group members. Finally, data generated by students are subjected to approval by a curator, most often an academic advisor, and therefore are stored in private group folder. The assurance of the data quality is an example of standardizing the organizational patterns of interactions between the participants defining the organization.

Online Calibration Tools

The derivation of the material constants from the experimental data to be used by a particular material model is referred to as model calibration, and the capability of model calibration is yet another distinguished feature of EVOCD. Currently, the EVOCD provides three online models for calibration:

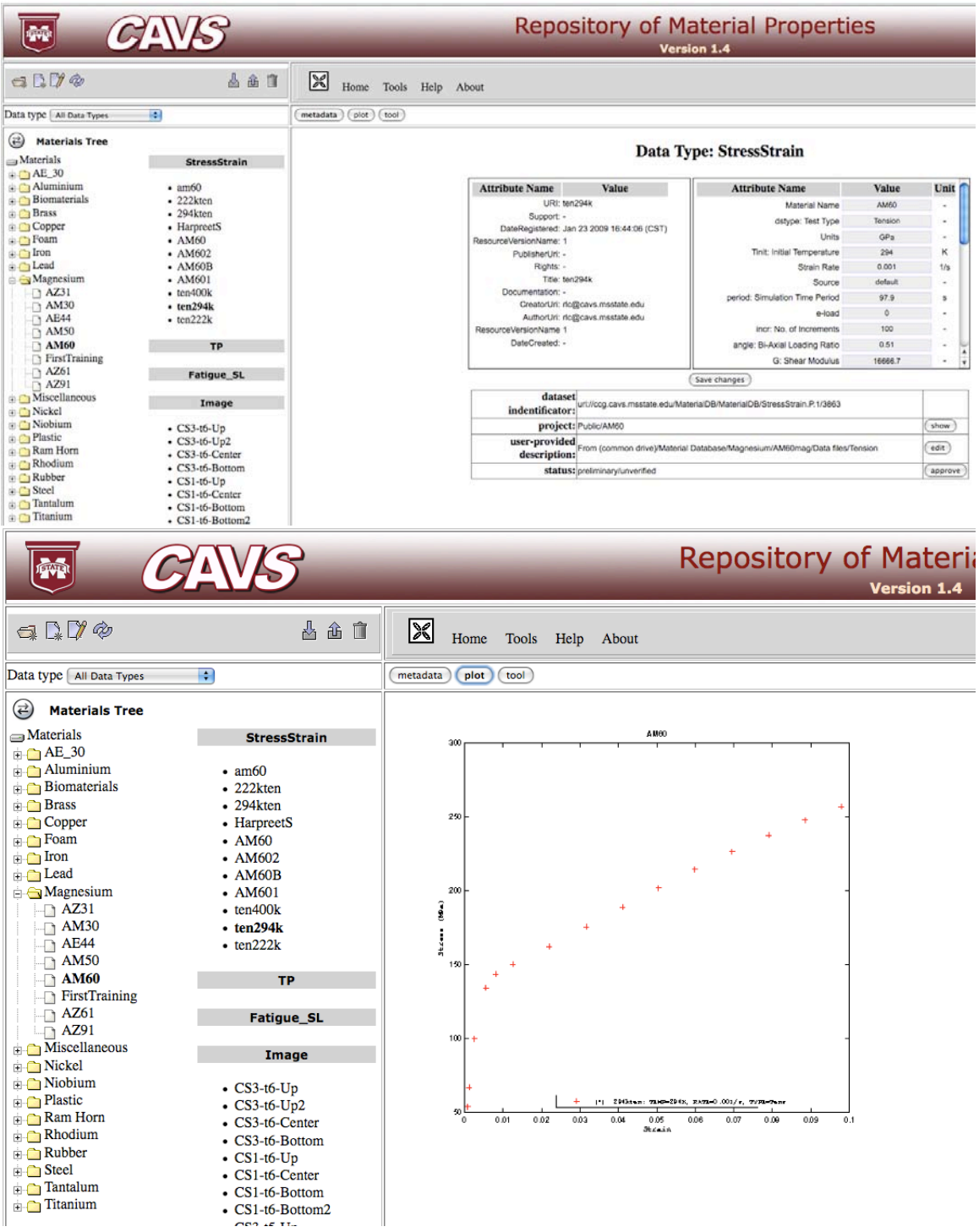

Figure 4: Example snapshots of the data repository displaying metadata associated with the selected data item (upper) and plot (stress-stain curve) generated on the fly visualizing the selected dataset.

Plasticity-Damage (c.f. Figure 5), Multistage Fatigue, and Thermoplastic; there is also an Image Analysis tool for material characterization. The models are contributed to EVOCD by MSU researchers, available to all users, and their quality scrutinized by the community-at-large. In addition to an intuitive user interface, the tools are functionally integrated with the data repository to facilitate their use; therefore, a selected data set can be seamlessly loaded into the tool, even if it requires data format translation. This defines two important patterns of use possible with EVOCD: (1) the user uploads experimental data, performs model calibration, and saves the material constants in the data repository; (2) the user searches for the constants of a particular model of a particular material and retrieves the constants for further analysis, typically to use them in numerical simulations, such as finite element analysis using ABAQUS, LS-Dyna, or other software.

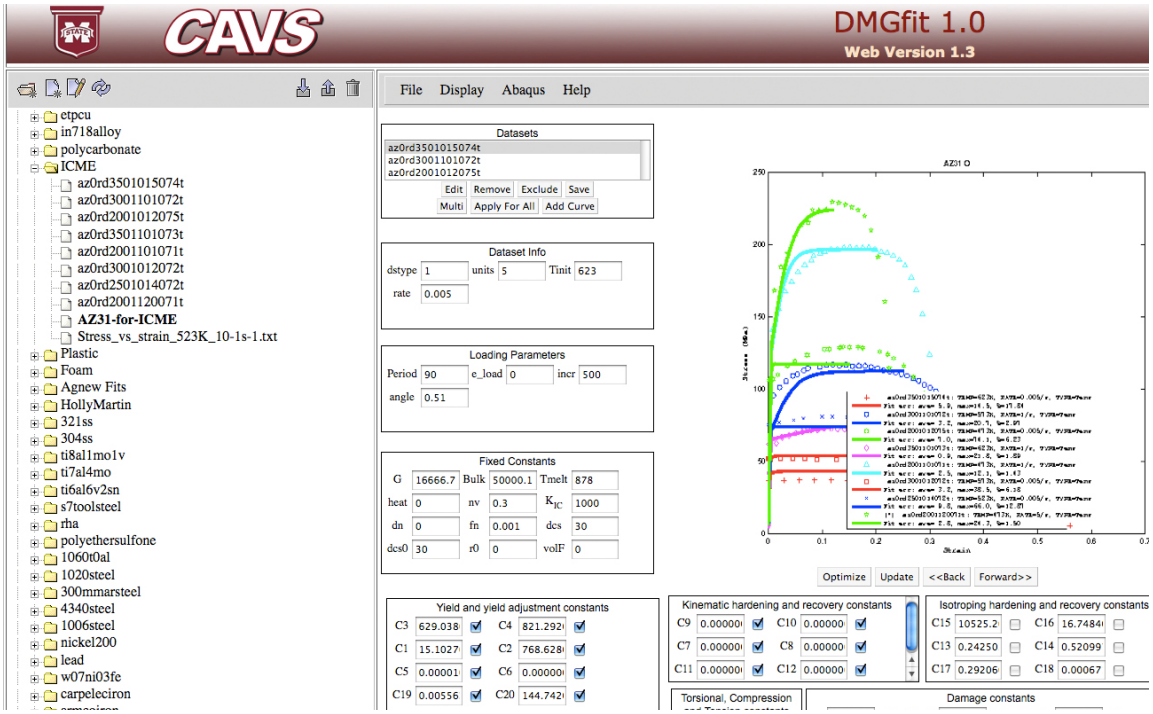

Figure 5: A snapshot of the Web-based interface to the DMGfit calibration tool.

Cyberinfrastructure for EVOCD

The third characteristic of an efficient VO is the management of complexity, which relates to the implementation of the VO and its supporting cyberinfrastructure. One aspect of the management of complexity is the ease of use, which involves, among others features, clarity of presentation, ability to find all relevant information, availability and accessibility of the information for the user's purpose, and hiding from the end-user the intricacies of the underlying infrastructure. Ease of use is realized by the design and implementation of the user interface. Another aspect of complexity management involves maintainability of the VO, including its extensibility, scalability, and most importantly, horizontal integration agility (to avoid messy stow-pipes) to coordinate disparate, autonomous software components into a self-consistent, and perhaps self-healing, unified system.

User Interface

To achieve the simplicity and consistency of the Web browser-based graphical user interface (GUI), EVOCD follows Representational State Transfer (REST) architectural style. The EVOCD's data repository GUI serves as a good example of this approach. Each file in the data repository is assigned a unique Unified Resource Identifier (URI) as its primary database key. Furthermore, the data files are organized into two types of collections: materials and groups. There is a hierarchy of these collections: materials types (e.g., metals, polymers, bio-materials, etc.) and materials classes (e.g., alloys of the same base metal), and independently, folders and subfolders of each collection group. These collections, each identified by its own URI, allow the user to easily find the data of interest, and, in the case of the group hierarchy, to specify the access privileges. The collections are represented in the GUI as nodes of an expandable tree so that the user may browse the contents of the repository by navigating either the material or group tree. The leaves of the tree correspond to individual data sets. The user may request one of four representations of the data set: the metadata record, the data file itself, a plot visualizing the data, and/or the data opened in a corresponding model calibration tool. Consequently, the search and retrieval of the data is implemented as a sequence of GET requests specifying the URI of the resource and the requested representation of the selected resource. The requests are dynamically created using JavaScript, depending on the state of the widgets on the page. Thanks to AJAX, only relevant parts of the page are refreshed upon receiving the response thereby preserving the state of page and making the GUI more intuitive for the end user. Thus, using REST not only adequately hides the server-side implementation details from the end user, but also from the GUI developer.

EVOCD Services

The cyberinfrastructure for EVOCD is a collection of interoperable, autonomous, and platform-independent services to manage and streamline the process of gathering and disseminating knowledge, including computational codes, experimental data, and derived material properties. The Service-Oriented Architecture (SOA) enables the EVOCD portal to hide the details of the heterogeneous platforms and allows integration of services on demand, promoting agility and dynamism to distributed applications in the system. The SOA, which is defined by the Organization for the Advancement of Structured Information Standards (OASIS) as a paradigm for organizing and utilizing distributed capabilities that may be under the control of different ownership domains, empowers the EVOCD cyberinfrastructure to separate functions into distinct services which can be accessed, combined and reused over the network, providing flexibility to adapt to new business prospects and challenges.

EVOCD cyberinfrastructure is comprised of a number of services, notably data, transformation, plotting, computing and authorization services. The data service is an aggregation of three independent "sub-services": metadata, storage, and replica locator services. Each experimental data set in the repository is stored in a file system. The storage service manages the part of the file system designated to store the data sets. When a file is submitted to the storage service, the service determines the location at which the file is to be stored, then returns its URI to the caller. GridFTP is used as the transport mechanism for moving the files to and from storage. The metadata service collects the information about data sets maintained by the storage service. The information is comprised of the file identification (a name assigned by the user, project, material, etc.), the data provenance (owner, date submitted, etc.), tags which enable querying of the metadata repository to find data sets matching particular search criteria, and some additional information necessary to process the data (such as transformation from raw force-displacement measurement to stress-strain relationship). When a new metadata record is created, the service returns its URI so that it can be referred to at a later time. The metadata repository is implemented as a DBMS application. The replica locator provides mappings between the metadata records and data files. There are two significant advantages to this approach. First, the decoupling of the metadata and data storage services permits geographical distribution of the repository to accommodate different storage and access control mechanisms, thus allowing for aggregation of data services maintained by different organizations. Second, the CAS authorization service can be used to control access to metadata and data

separately: the user may be made aware of the existence of the data without being granted automatic access to it.

The data services are augmented with independently developed and maintained transformation services, such as format translations (e.g., force-displacement to true stress-strain) and data visualization services.

The computing service provides the capability of performing model calibration on selected data sets. The model calibration tools were originally prototyped as the standalone MATLAB applications. However, the implementation of this service required the conversion of an interactive application into a stateless service with actual computations delegated to a back-end computational server. Therefore, to accommodate EVOCD's multi-user environment, a pool of computational engines is scheduled in round-robin fashion. This approach has proven very successful: during a training session, 30 simultaneous users were served by a pool of just four computational engines without any noticeable latencies.

Service Integration

The final step in developing the cyberinfrastructure for EVOCD is the integration of the disparate autonomous software components (services) into a single unified system capable of processing REST-based requests from the front end. This is achieved by the employment of the Enterprise Service Bus (ESB). With ESB, requestors and service providers are no longer interacting directly with each other; rather they exchange messages through the bus, and the messages can then be processed by mediations (e.g., message transformation, routing, monitoring). Mediations implement the integration and communication logic, and they are the means by which ESB can ensure that services interconnect successfully. As a result, the ESB acts as the intermediary layer between a portal server and the back-end data sources with which the data portal interacts.

EVOCD uses an open-source Apache ServiceMix implementation of ESB. An HTTP-binding component receives REST requests (for security reasons, forwarded by the Apache Tomcat server). A custom router then directs them to the corresponding service provider through the mediation process that involves orchestration of services and message transformations. For example, a simple GET request for a selected data set is processed as a sequence of service invocations: request to the replica locator to convert the data URI to a physical file location followed by GridFTP file transfer. Similarly, to produce a plot visualizing a data set, the GET request parameter must be transformed from the data URI to the location of the local copy of the data retrieved from the repository. Note that this ESB-based mediation process removes all the dependencies of the visualization service on the actual data location. Finally, the model calibration tools require data in a strictly defined format. In the case of format mismatch, the ESB automatically forces format translation. In general, ESB provides the necessary mechanisms for agile and robust service integration on the one hand, and the bridge between REST and SOA architectures on the other.

The EVOCD portal is up and running (it has been accessed more than 16,000 times by about 8,000 visitors and contributors form over 80 nation around the world since September 1, 2010). And becomes a node of the global ICME cyberinfrastructure – an effort coordinated by the Minerals, Metals, and Materials Society (TMS).

In Phase IV of this effort we will continue the development of Wiki capturing the knowledge about material models and manufacturing processes at different length-scales, as well as the development of databases to store the materials properties and multiscale models of lightweight metals, polymers, steel, and bio-inspired materials. In addition, we initiated the research towards the development of autonomic (i.e., self-managing, self-optimizing, self-healing, and self-protecting) environment for execution hierarchical multiscale simulation and multilevel design optimizations.

Publications

The research conducted within this task resulted in the following scholarly publications:

1. Haupt, T., “Using Service Mashups to Implement e-Science Portals,” The 2010 IRAST International Congress on Computer Applications and Computer Science (CACS 2010), Singapore, December 4-6, 2010.
2. Haupt, T., “Cyberinfrastructure for Integrated Computational Material Engineering,” in Magnesium Technology 2010: Proceedings of a Symposium Sponsored by the Magnesium Committee of the Light Metals Division of TMS, S. Agnew, N. Neelameggham, E. Nyberg, and W. Sillekens (eds.), John Wiley and Sons, 2010.
3. Haupt, T., “Cyberinfrastructure Support for Integrated Materials Engineering,” in the Proceedings of the 1st World Congress on Integrated Computational Materials Engineering (ICME), J. Allison, P. Collins, G. Spanos (eds.), Willey, 2011, pp. 229-234.
4. Haupt, T., Sukhija, N., Horstemeyer, M.F., “Cyberinfrastructure Support for Engineering Virtual Organization for CyberDesign,” 2nd Workshop on Scalable Computing in Distributed Systems (SCoDiS’11), Torun, Poland, September 11-14, 2011.
5. Haupt, T., Sukhija, N., Zhuk, I., " Autonomic Execution of Computational Workflows," in the proceeding of the Federated Conference on Computer Science and Information Systems (FedCSIS'11), Szczecin, Poland, September 18-12, 2011, pp 965-972.

MISSISSIPPI STATE UNIVERSITY

Southern Regional Center for Lightweight Innovative Design

Phase III

Final Scientific & Technical Report

October 1, 2009-September 30, 2011

For compliance with contract requirements of Award DE-EE0002323

Task 3

FATIGUE OF LIGHTWEIGHT AUTOMOTIVE MATERIALS

Submitted December 27, 2011

TASK 3: FATIGUE OF LIGHTWEIGHT AUTOMOTIVE MATERIALS

Table of Contents

TASK 3: FATIGUE OF LIGHTWEIGHT AUTOMOTIVE MATERIALS

Principal Investigator: J. Brian Jordon

Co-Principal Investigator: Mark. F. Horstemeyer
Chair Professor, Computational Manufacturing & Design
Center for Advanced Vehicular Systems
Mississippi State University
PO Box 5405, Mississippi State, MS 39762-5405
(662) 325-5449; fax: (662) 325-7223; mfhorst@me.msstate.edu

Participants: M. Lugo, J. Bernard, A. Yeldell, D. Rayborn

William Joost: Technology Area Development Manager
e-mail: william.joost@ee.doe.gov

Magda Rivera: Project Manager
e-mail: magda.rivera@netl.doe.gov

Contractor: *Mississippi State University (MSST)*
Contract No.: *DE-EE0002323*

Objective

- Develop design and prognostic tools for fatigue of lightweight automotive components.

Approach

Strain-life fatigue tests of selected magnesium alloys (AZ31, AZ61, and AM30) will be conducted to investigate the fatigue behavior of magnesium alloys and automotive components. A structure-property analysis will be conducted to determine relations between microstructural features and fatigue life. In addition, scanning electron microscope (SEM) experiments will be conducted to determine fatigue crack incubation and microstructurally/physically small fatigue crack stages. Experiments will also be performed to determine the fatigue performance of several different types of joints.

Fatigue performance of magnesium alloys will be characterized and will be developed a structure-property modeling framework for fatigue life using the Multistage Fatigue (MSF) modeling approach. We will use a microstructure-sensitive fatigue model which decomposes total fatigue lifetimes into crack incubation, microstructurally small crack (MSC) and physically small crack (PSC), and long crack growth, to correlate the differences in fatigue behavior of magnesium alloys. The model proposed has the capabilities to capture competing structure-property relations, including grain size, inclusions size, and texture, and their consequential impact on fatigue lifetimes. While the model was originally developed for a cast A356 Al alloy by McDowell et al., [1], it has been modified to extend its application to wrought materials [2]. The total fatigue life N_{Total} is given by equation (3-1).

$$N_{Total} = N_{Inc} + N_{MSC/PSC} + N_{LC} \tag{3-1}$$

where, N_{Total} is the total fatigue life. N_{Inc} is the number of cycles to incubate a crack at a micronotch formed by an inclusion, which can be a relatively large constituent particle, a large pore, or a cluster of each or both. The incubated crack extends from the inclusion into the matrix and propagates through a region of the micronotch root influence. $N_{\text{MSC/PSC}}$ is the number of cycles required for propagation of a microstructurally small/ physically small crack. Finally, N_{LC} is number of cycles required for long crack

(LC) propagation to final failure, which depends on the amplitude of loading and the corresponding extent of microplasticity ahead of the crack tip. This multistage framework will be evaluated for the prediction of fatigue damage in magnesium alloys and magnesium welded joints. The MSF will also be implemented into commercial FEA codes and validated by solving specific problems concerning the mechanical response and reliability/safety aspects of magnesium alloys used in automotive applications.

Milestones, Metrics and Accomplishments

Sub-Task 3.1 – Perform strain-life tests for AM30 Ford Rail in the extruded and transverse direction.

- Performed tensile testing on Mg AM30 alloy in the extruded and transverse directions.
- Conducted strain-life tests of Mg AM30 in the extruded and transverse directions.

Sub-Task 3.2 – Perform strain-life tests for AZ61 Ford Rail in the extruded and transverse direction.

- Performed tensile testing on Mg AZ61 alloy in the extruded and transverse directions.
- Conducted strain-life tests of Mg AZ61 alloy in the extruded and transverse directions.

Sub-Task 3.3 – Perform strain-life tests and SEM fractography on four different casting methods of Mg AZ91 and AM60 cast alloys (HIMAC).

- Performed tensile testing and strain-life tests of cast Mg AZ91 alloy produced by 4 different casting methods.
- Conducted SEM fractography of cast Mg AZ91 alloy produced by 4 different casting processes.

Sub-Task 3.4 – Perform long crack growth tests of the Mg AZ31 sheet alloy.

- Conducted long crack test via compact tension specimens for Mg AZ31 alloy.

Sub-Task 3.5 – Perform multi-axial fatigue of AZ31 plate.

- Performed uniaxial fatigue tests for AZ31 plate.
- Conducted multi-axial fatigue tests for AZ31 plate.

Sub-Task 3.6 – Conduct in-situ SEM experiments of the alloys selected.

- Performed fractography studies for AM30,AZ31 and AZ61 magnesium alloys.

Sub-Task 3.7 – Conduct atomistic fatigue simulations of crack growth in magnesium alloys.

- The influences of the stress evolution near the fatigue crack tip on the fatigue crack growth behavior in magnesium crystals was investigated.
- The plastic deformation mode at the crack tip was investigated. The size effects on fracture toughness at the nanoscale were analyzed.

Sub-Task 3.8 – Develop structure-property fatigue relations for extruded Mg AM30, AZ61, and AZ31 alloys via SEM fractography.

- Determined structure-property relationships between microstructure features and fatigue life for AM30 alloy.
- Performed structure-property relationships between microstructure features and fatigue life for AZ61 alloy.
- Conducting structure-property relationships between microstructure features and fatigue life for AZ31 alloy.

Sub-Task 3.9 – Develop a higher order MultiStage fatigue models for the AZ31, AM30 and AZ61 extruded Mg alloys.

- Developed multistage fatigue model for AM30, AZ31 and AZ61 alloys.
- Incorporated structure-property relationships into the MultiStage Fatigue model to predict the scatter in the fatigue life.

Sub-Task 3.10 – Validate the models with components specified by sponsors.

- Currently conducting monotonic tests for the shock tower.
- Conducting finite element simulations for the shock tower to validate the MSF models.

Sub-Task 3.11 – Fatigue experiments for friction stir spot welds.

- Conducted monotonic and cyclic lap-joint testing on Mg friction stir spot welds.
- Characterized fracture mode and path of Mg friction stir spot welds.

Sub-Task 3.12 -- Develop higher-order fatigue model for friction stir spot welds based on fatigue experiments and joint simulations.

- Implemented crack growth model for predicting fatigue life of lap-joint of Mg friction stir spot welds.

Sub-Task 3.13 – Integrate Multistage Fatigue model with plasticity/damage model (DMG 1.0).

- Conducting finite element simulations for the shock tower to validate the MSF models.

Sub-Task 3.14- Integrate fatigue models and codes with Task 2 (Cyberinfrastructure)

- Implementing integration of fatigue models and codes with Task 2.

Introduction

Industry and government have recently had an elevated interest in lightweight materials as part of the solution to reduce green house emissions and improve fuel economies in transportation vehicles. This heightened interest in lightweight materials has pushed the materials community to investigate not only cast magnesium but also wrought magnesium products for their high strength-to-weight ratio and better fatigue resistance. While studies of cyclic performance of magnesium alloys exist in the literature most of these are associated with cast formed materials. In fact, wrought magnesium alloys generally have higher mechanical strength and fatigue resistance than cast magnesium alloys due to their ability to limit inclusion sizes and for precipitation hardening after the severe deformation during processing. Thus, a need arises for a predictive tool that can capture the fatigue damage in wrought magnesium alloys with the intent of determining/designing the best alloy for use in a range of automotive applications. Therefore, the overarching goal of this task is the development of a physically-motivated microstructurally-based fatigue model.

In order to reach the goal of using more light weight metals in automobiles, understanding and modeling the fatigue damage of welded joints is of great importance. As with the base materials, research is needed to determine the reliability and performance of potential welding techniques and develop microstructurally-based modeling approaches. While research in the area of fatigue in friction stir spot welds is not unique, recent work has been exclusively focused FCC alloys and not HCP alloys such as magnesium.

Finally, the investigation of fatigue behavior of nanoscale materials has been of significant interest to many researchers due to the development of technologies of nano-materials. As such, understanding how fatigue damage initiates and grows at the nanoscale for magnesium alloys will lead to better modeling approaches at the higher length scales.

Effect of Twinning, Slip, and Inclusions on the Fatigue Anisotropy of Extrusion-Textured Magnesium AZ61 Alloy

Using a MultiStage Fatigue (MSF) model, experiments were conducted with extruded magnesium AZ61 alloy to quantify structure-property relations with respect to fatigue. These experiments were conducted in the extruded and transverse directions under low and high cycle strain control fatigue conditions. Structure-property relations were quantified by examining the fracture surfaces of the fatigued specimens using a scanning electron microscope (SEM). In terms of crack incubation, fatigue cracks were found to initiate from intermetallic particles (inclusions) that were typically larger than the mean

size. Quantified sources of fatigue crack incubation, microstructurally small cracks, and cyclic stress-strain behavior were correlated to the MSF model. Based on the specific material parameters, the MSF model was able to predict the difference in the strain-life results of the magnesium AZ61alloy in the extruded (ED) and extruded transverse directions (ETD), including the scatter of the experimental results. Finally, the MSF revealed that the inclusion size was more important in determining the fatigue life than the anisotropic effects from the texture, yield, and work hardening.

SEM fractography conducted in this study (typical SEM images shown in Figure 1) resulted in the characterization of the different stages of fatigue damage: incubation, microstructurally small crack (MSC)/ physically small crack (PSC), and long crack (LC). For low cycle fatigue, the first few hundred cycles of fatigue loading resulted in particle fracture, and incubation of the fatigue crack in the magnesium arose shortly afterward, indicating that approximately 30% of the life was incubation. SEM analysis of the fracture surfaces showed that intermetallic particles near the surface fractured without significant debonding.

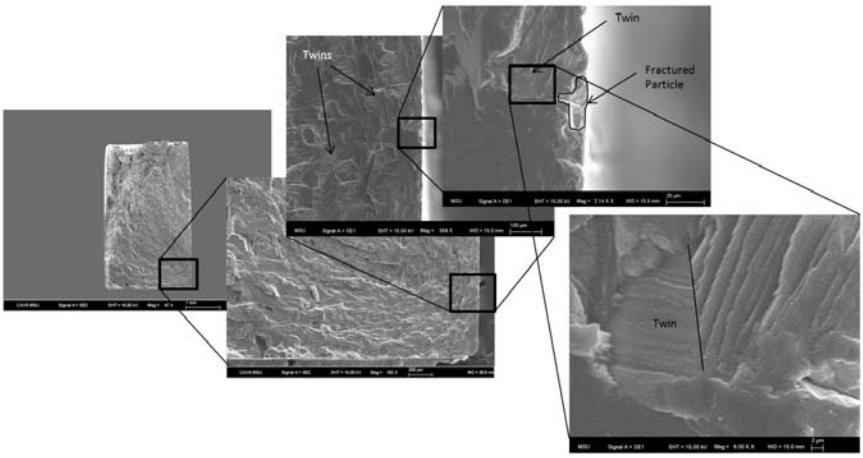

Figure 1: Fracture surface of Mg AZ61 alloy in the extrusion direction (ED). The scale bar magnitudes from left to right are 1 mm, 200 µm, 100 µm, 20 µm, and 2 µm. Note the twinning on the surface and the intermetallic particle that initiated the fatigue crack (90µm). This specimen was fatigue tested at 0.3% strain amplitude.

Fatigue Model

The Multistage Fatigue (MSF) model, first proposed by McDowell *et al.* [1], comprises three distinct regimes of fatigue damage: crack incubation, microstructurally small crack (MSC) and physically small crack (PSC) growth, and long crack (LC) growth, as shown in Equation (2).

$$N_{Total} = N_{Inc} + N_{MSC} + N_{PSC} + N_{LC} = N_{Inc} + N_{MSC/PSC} + N_{LC}, \quad (3\text{-}2)$$

where N_{Total} is the total fatigue life. N_{Inc} is the number of cycles to incubate a crack at an inclusion, which can be a relatively large constituent particle, a large pore, or a cluster of each or both. While the MSF model has been correlated to magnesium alloys prior to this study, this modeling effort was focused on wrought magnesium whereas past work focused on cast alloys. As such, the driving forces in cast alloys are primarly the casting pores [1]. However, the material of interest is an extruded magnesium alloy that does not contain casting pores or oxide films. Thus, based on experimental results in this study, the primary source of fatigue damage is intermetallic particles. Figure 2 shows the correlations of the MSF model to experimental data for both extruded direction (ED) and the extruded transverse direction (ETD).

For validation purposes, components were made by cutting through the cross-section of the extruded Ford rail. These components were 25.4 mm wide and were the same magnesium AZ61 alloy presented earlier. These components were tested under fully-reversed displacement control at a frequency of 3Hz. A total of four components were tested at two different displacement amplitudes: 2 mm; 3 mm. The

specimens tested at 2 mm were switched from displacement control mode to load control mode at 10,000 cycles and continued until failure at 30 Hz.

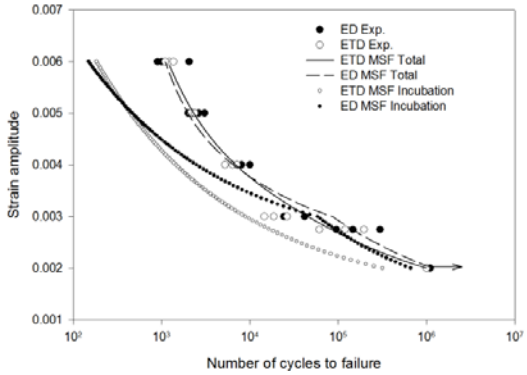

Figure 2: A comparison of the Multistage Fatigue (MSF) model of total and incubation life with experimental data for extruded AZ61 magnesium alloy in both the extrusion direction and the extrusion transverse direction.

In order to make MSF predictions of the component, finite element simulations were performed to determine the local stress/strain state due to the presence of stress concentrations. The material model employed in this present study is the internal state variable (ISV) plasticity/damage model. Three-dimensional finite element simulations were performed with the aforementioned constitutive model and a mesh refinement study was employed to determine the appropriate element size. The maximum principal strain amplitude from the finite element results was used as an equivalent uniaxial strain amplitude for the input to the MSF model. Figure 3b shows the comparison of the component fatigue specimens to the MSF prediction. The MSF showed good correlation to the fatigue life at the lower amplitude but showed a more conservative prediction for the higher amplitude. Also shown in the Figure 3b is the incubation and MSC/PSC crack growth predictions. The slightly conservative predictions are likely due to the lack of a long crack growth model, especially for the higher amplitude. At higher amplitudes, the long crack growth will dominate the fatigue damage at a greater percentage than at lower amplitudes where MSC/PSC is more dominant.

a) b)

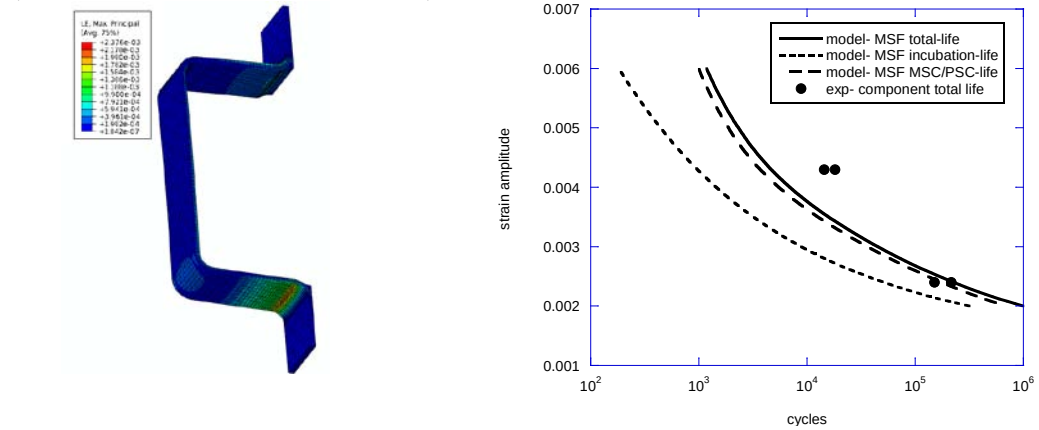

Figure 3: (a) Maximum principal strain contour plot of the finite element analysis of the Mg AZ61 components. Analysis of the half-plane symmetry of the component was performed based on a displacement of 2mm and 3mm applied at the boundaries. The material model employed was an internal state variable plasticity model for Mg AZ61 alloy in the transverse directions. (b) Comparison of the MSF model to the experimental fatigue results of the AZ61 component test. The components tests were conducted under displacement amplitudes of 2 mm and 3mm. Using an internal state variable plasticity finite element analysis, the local multi-axial strain amplitude was estimated. Maximum Principle strain theory was used as input to the MultiStage Fatigue model.

Atomistic Simulations of Fatigue Crack Growth and the Associated Fatigue Crack Tip Stress Evolution in Magnesium Single Crystals

Using Large-scale Atomic Molecular Massively Parallel Simulator (LAMMPS), a classical molecular dynamics code, atomistic simulations were performed to investigate the fatigue crack growth rate and the evolution of the associated atomic stress fields near the crack tip during fatigue crack growth in magnesium single crystals. The interatomic bonds of atoms were described using the EAM potential. The specimens with initial edge cracks were subjected to uniaxial Mode I cyclic loading. For the sake of revealing the influence of the initial cracks' crystal orientations, three different orientations were considered. The fatigue growth rate can be expressed by da/dN = cCTOD, where the values of constant c are determined by the atomistic simulations. Notably, the values of the constant c are much larger for magnesium single crystals than for FCC single crystals and vary widely from one orientation to another. The simulation results show that the evolution of atomic stress fields was highly dependent on the crystal orientations due to anisotropy and magnesium single crystals' HCP structure. Interestingly, the von Mises stress or normal stress around the crack tip controlled the fatigue crack growth behaviors.

Fig. 4 illustrates the edge crack specimen adopted for the present study. The initial crack was introduced by removing the atoms from the perfect crystal.

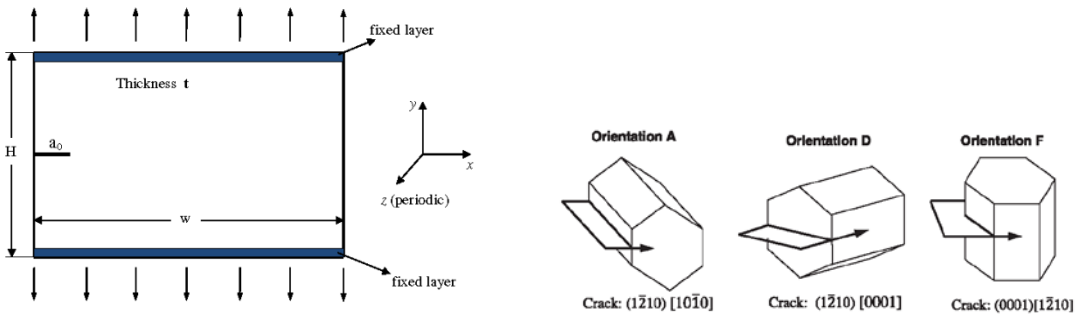

Figure 4: Edge crack specimen used for the simulation of fatigue crack growth and crystallographic orientations of the initial cracks

Results shown that fatigue crack tip stress evolution is strongly dependent on the crystal orientations. The most substantial differences in fatigue crack growth behaviors of different crystal orientations are essentially caused by the detailed atomic stress evolution around the crack tip due to the Schmid Factor. Figure 5 presents the contour plots of the stress component σ_{yy} for Orientation A $(1\bar{2}10)[10\bar{1}0]$. Stress evolution around the crack tip is shown in Figure 6.

Small Fatigue Crack Growth Observations in an Extruded Magnesium Alloy

Fully-reversed, interrupted load control tests were conducted on notched specimens that were taken from an extruded Mg AZ61 alloy. In order to measure crack growth, replicas of the notch surface were made using a two-part silicon-rubber compound at periodic cyclic intervals. Scanning electron microscopy (SEM) analysis of the replica surfaces revealed multi site crack initiation and subsequent crack coalescence. The crack growth behavior of the small fatigue cracks was shown to have a strong dependence on the material microstructure, as the crack was submitted to a tortuous growth path along grain boundaries and crystallographic slip planes. A microstructurally dependent crack growth model that was previously developed for FCC metals was further extended here to HCP metals. Figure 7 shows model comparison to crack growth rate for Mg AZ61 alloy.

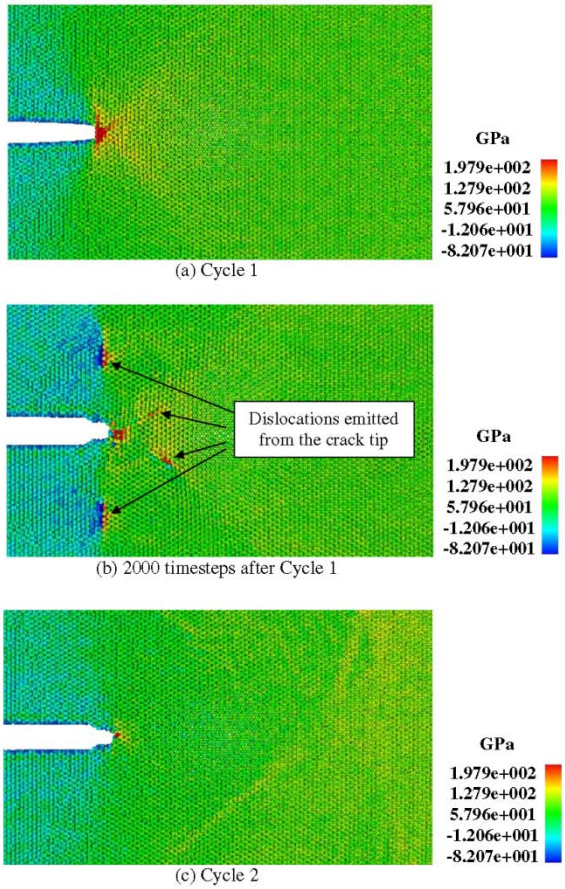

Figure 5: Contour plots of stress component σ_{yy} of Orientation A $(1\bar{2}10)[10\bar{1}0]$ at (a) the maximum loading of Cycle 1; (b) 2000 time steps after the maximum loading of Cycle 1; (c) the maximum loading of Cycle 2.

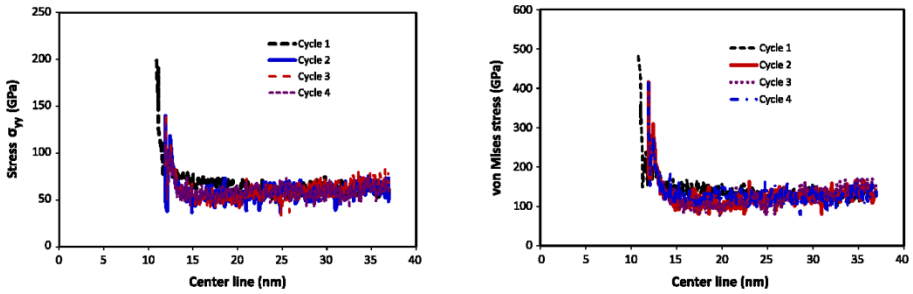

Figure 6: Variations of stress component s_{yy} and von Mises stress along the crack line in Orientation A $(1\bar{2}10)[10\bar{1}0]$ at the maximum strain points of Cycles 1–4.

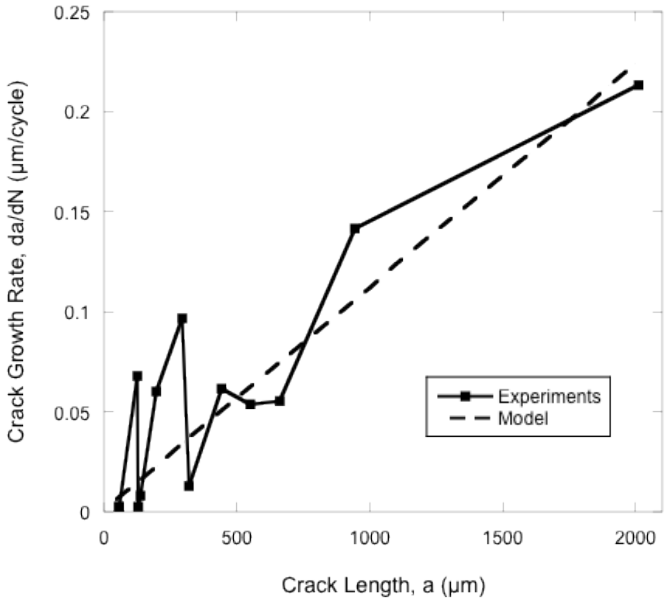

Figure 7: Crack growth rate versus crack length for a stress amplitude of 105 MPa with the model approximations also shown.

Monotonic and Cyclic behavior of Cast Magnesium Alloys

Monotonic and cyclic testing was performed on five different casting processes: LPPM, Ablation, Squeese Cast, T-Mag, and LPPM (EM-P). In addition, inclusion quantification was performed on the fracture surfaces on the failed specimens. Figure 8 displays the strain-life results for the five casting groups for all of the fatigue tests and the arrow represents test run-outs (all tests were stopped at 10^6 cycles).

The scanning electron microscopy (SEM) analysis of the fracture surfaces confirmed that, compared to the LPPM and Squeeze Cast processes, the Ablation and T-mag processes contained very few fatigue failures resulting from large casting defects. SEM analysis of the fatigue fracture surfaces revealed that the cracked, debonded particles and small casting pores were the source of fatigue crack initiation for the Ablation process. For the least fatigue-resistant process, SEM analysis of the LPPM fracture surfaces revealed that the main source of fatigue crack initiation was due to large pore shrinkage clusters. Some of the pore shrinkage clusters were observed to be as large as the cross-section of the specimen. The Squeeze cast specimens also experienced fatigue crack initiation from pore shrinkage clusters. However, these pore shrinkage clusters were typically smaller than those generated during the LPPM process. In the Squeese Cast process the fatigue cracks were also observed to initiate from oxide films. Several of the T-Mag specimens had fatigue cracks that initiated from large pores and oxide films on the order of a couple hundred microns. The large oxide films and pores greatly reduced the fatigue-life of the T-Mag process specimens as compared to the Ablation process specimens.

Microstructure and Damage Evolution during Tensile Loading in a Wrought Magnesium Alloy

The damage evolution in a wrought magnesium alloy under uniaxial tensile deformation was investigated. Sectioned specimens subjected to interrupted tensile deformation were examined under optical microscopy to quantify the number density of cracked intermetallic particles as a function of applied strain. Digital image analysis of the optical images was employed to quantify damage by separating cracked from non-cracked particles. Finally, an internal state variable damage model was shown to adequately capture the experimentally observed damage progression due to the intermetallics.

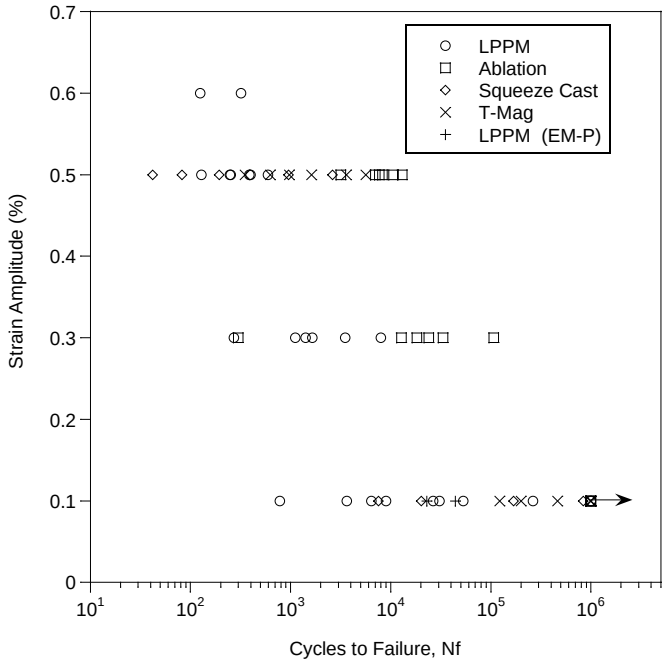

Figure 8: Applied strain amplitude (R=-1) versus the number of cycles to failure for the LPPM, Ablation, Squeeze Cast, T-Mag, and LPPM electromagnetic (EM-P) process. Arrow indicates run-out.

Horstemeyer and Gokhale [3] proposed a model capable of capturing in ductile materials damage nucleation associated with inclusions or second phase particles. The void nucleation parameters in this model are two main microstructural quantities: length scale parameter *d*, which oftentimes represents the particle size, and particle volume fraction *f*. They developed the following equation for the number of voids per area:

$$\eta = C_{coeff} exp\left(\frac{\varepsilon(t) d^{1/2}}{K_{IC} f^{1/3}}\left\{a\left[\frac{4}{27} - \frac{J_3^2}{J_2^3}\right] + b\frac{J_3}{J_2^{3/2}} + c\left|\frac{I_1}{\sqrt{J_2}}\right|\right\}\right). \quad (3\text{-}3)$$

Figure 6 shows the number of cracked particles per volume versus applied tensile strain. Damage in this type of alloy is due mainly to slip and twinning occurring in the matrix magnesium adjacent to the particles. However, Figure 9 shows a strong correlation between progression of cracking particles and damage. The constants used in (Equation 3-2) are the following: *a=0*, *b=55000*, *c=50000*, C_{coeff}*=1.9*, *f*=0.004, *d* =2.4 μm, and K_{IC}=20 MPa·m$^{1/2}$. Constants C_{coeff}, *a*, *b*, and *c* were determined from the interrupted tension tests using a best correlation method. The damage nucleation model predicted results that are in good agreement with the observed damage progression of the AZ61 magnesium alloy.

In regards to the microstructural properties, the following can be concluded: (1) under uniaxial tension the area fraction of cracked particles composed of (Mn-Al) and (Mg-Al) varies in an exponential pattern as function of strain, (2) the number density (1/mm^2) of cracks follows a shallow nonlinear pattern, (3) three types of particles were identified: Oxide/intermetallic, Mn-Al, and Mg-Al phases, and (4) cracks were observed in the (Mn-Al) and (Mg-Al) based particles.

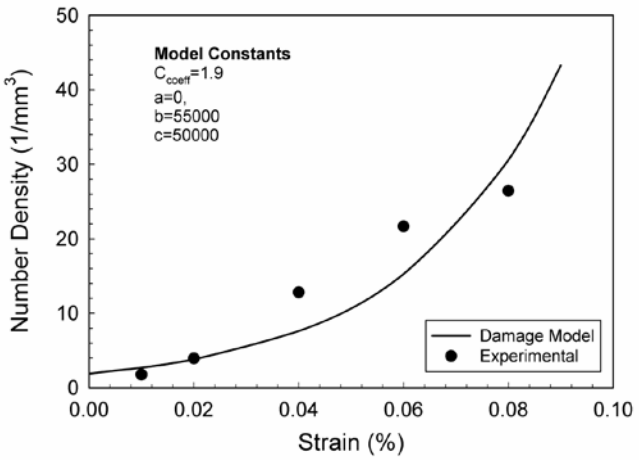

Figure 9: Number density versus strain of an AZ61 magnesium alloy showing a comparison of the Horstemeyer-Gokhale [3] void nucleation model with experimental data.

Finite Element Analysis of the Mechanical Behavior and Local Stress Intensity Factor Solutions for Friction Stir Spot Welds in Lap-Shear Specimen

The purpose of this study was to investigate the mechanical behavior and to calculate the local stress intensity factors for friction stir spot welds (FSSW) of Mg AZ31 alloy in lap-shear specimens using finite element method. Three dimensional finite element models were constructed to thoroughly analyze the stress field in spot welds and the distribution of local stress intensity factors. For the local stress intensity factors, two cases were considered, namely an infinitesimal kinked crack and a finite length kinked crack. The local stress intensity factors at the critical points of the infinitesimal length kinked crack were determined using the global stress intensity factors and analytical expressions of Cotterell and Rice [4].

A detailed investigation of the stress field in FSSW on lap-shear specimens was performed using three dimensional finite element models in order to understand their influences on the structural performance and failure behavior of Mg AZ31(see Figure 10). The following conclusions were obtained from this study: a) for the specimen with no kinked crack, the asymmetrical geometry of the weld nugget has strong effects on the stress state in the base plate close to the weld nugget, but its influence diminishes as distance from the weld nugget increases, b) because the stress concentration occurs in a very small region around the interception of the nugget boundary with the faying interface in the specimen with no kinked crack, the step hole in the weld nugget should not influence the values of global stress intensity factor (SIF) solutions. However, the asymmetrical geometry of the weld nugget due to the step hole will cause the distribution of global SIF to deviate from the distributions of the model having a solid nugget. The local SIF solutions obtained via Cotterell and Rice relations demonstrate that the values of local k_I and k_{II} at the critical point are the highest, which implies that the fatigue crack will initiate from this point.

Cyclic Behavior and Microstructure Properties of an Extruded AM30Magnesium Alloy

Strain controlled experiments were conducted to study the cyclic behavior of an AM30 magnesium alloy. The material used in this research was in the form of an automotive crash rail profile with a thickness of approximately 2.5 mm (Figure 11). Anisotropy and asymmetric behavior were identified in both directions the extrusion and transverse directions. Formation of cracks occurred for most of the samples at inclusions of second particles which were identified as Al-Mn rich. In addition, other initiation crack sites were observed to occur due to profuse twinning.

Figure 11 shows the strain-life for extruded AM30 magnesium alloy in the extrusion and transverse directions, for strain controlled, constant strain amplitude and completely reversed loading conditions.

The strain-life curve in the log-log domain show a linear pattern from 0.6 to close to 0.3 %, then the slope changes drastically below of a strain amplitude of 0.3%.

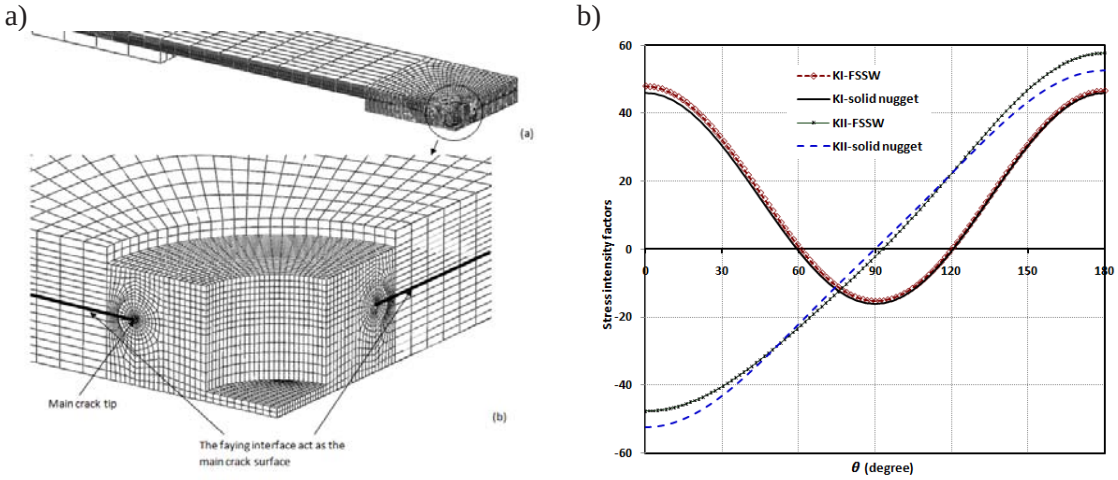

Figure 10: (a) A mesh for the left half finite element model with a close-up view of the mesh near the main crack tip. (b) The global SIF K_I and K_{II} of FSSW and the model with solid nugget as functions of the angle θ.

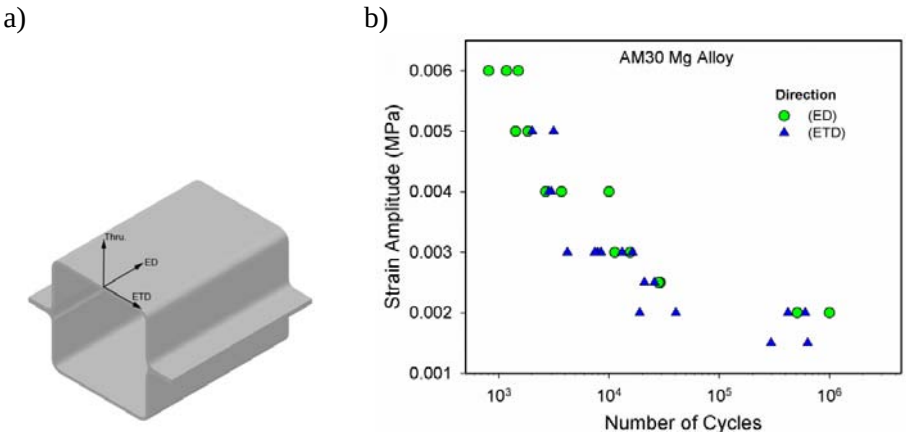

Figure 11: a) Automotive crash rail profile used in this research, and b) Total strain life of an AM30 magnesium alloy in the extrusion and transverse directions.

Cyclic Deformation Response

Figure 12 shows the hysteresis curves for several strain amplitude levels. These curves include the first cycle and the mid-life cycle. An asymmetric pattern in the cyclic deformation is observed for the first and mid-life cycles for all the strain amplitudes. This asymmetry is more pronounced for the first cycle, and at higher strain levels. The hysteresis loops show that hardening take place at lower strain amplitudes under tensile loading, and hardening under compressive loading. For lower strain amplitudes the tensile and compressive stress was almost the same. The asymmetry from tensile to compressive is larger as the strain amplitude increases. Both tensile and compressive stresses are greater than the corresponding yield strength of the alloy.

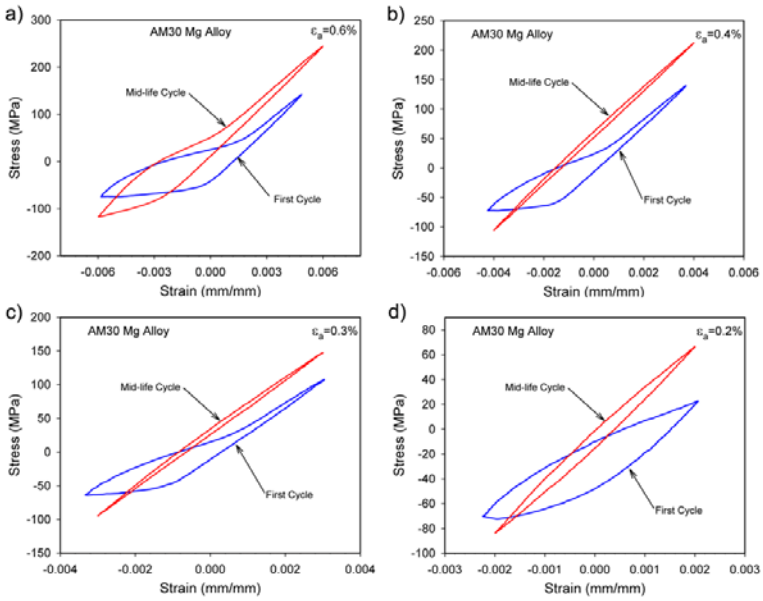

Figure 12: Hysteresis curves of AM30 extruded Mg alloy in the extruded direction at the strain amplitude of a) 0.6%, b) 0.5%, c) 0.3% and d) 0.2%.

Figure 13 shows the evolution of stress amplitude as a function of number of cycles at the strain amplitudes of 0.6%, 0.5%, 0.3%, and 0.2%. The strain amplitudes ranging from 0.3% to 0.6% showed a greater hardening effect than the other strain amplitude levels. The cyclic hardening appears strongly in the initial cycles at about 10% of the total fatigue life and a small amount of hardening continued to the point of the final failure. This hardening effect is most likely related to twinning in compression and detwinning in tension that occurs at high strain amplitudes [5].

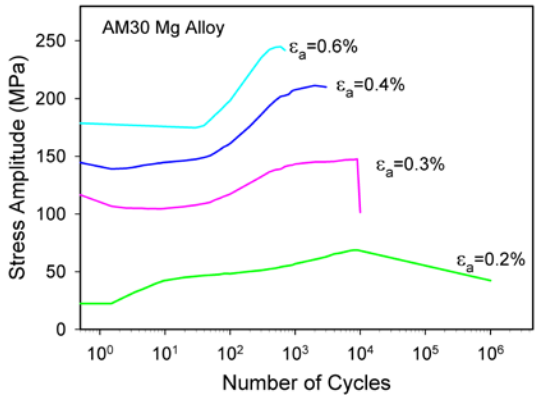

Figure 13: Stress amplitude response of AM30 magnesium Alloy

Fatigue Fractured Surfaces

All the fracture surfaces of the fatigued specimens were examined. The crack initiation site for all the specimens occurred near surface, and for most of the specimens at inclusion particles. For a few specimens crack initiated near regions with profuse twining. Figure 14 shows a typical fracture surface.

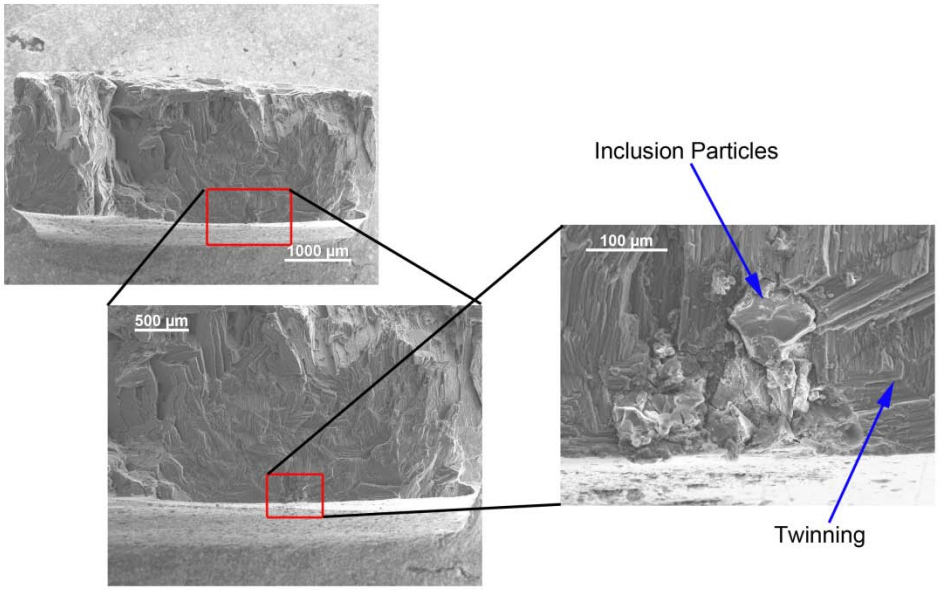

Figure 14: Typical fracture surface of AM30 magnesium Alloy. Crack initiated at inclusion second phase particles. Twinning was also observed near crack initiation site.

Fatigue Performance of an AZ31 Sheet Magnesium Alloy

A strain-life fatigue test program was conducted to quantify and to evaluate the mechanisms of fatigue and the fatigue life in an AZ31 sheet magnesium alloy. Fatigue specimens were designed in conformity with ASTM standard E-647. These tests were performed under strain control mode, constant strain amplitude, and fully reversed. A 50% drop of the peak stress load was used to determine failure of the sample.

Strain-Life

The strain-life curve for the AZ31sheet magnesium alloy for strain controlled, constant strain amplitude and completely reversed loading conditions is shown in Figure 15. The strain-life curve in the log-log domain shows a pattern from 0.5 to close to 0.3 %, then the slope changes drastically below of a strain amplitude of 0.3%.

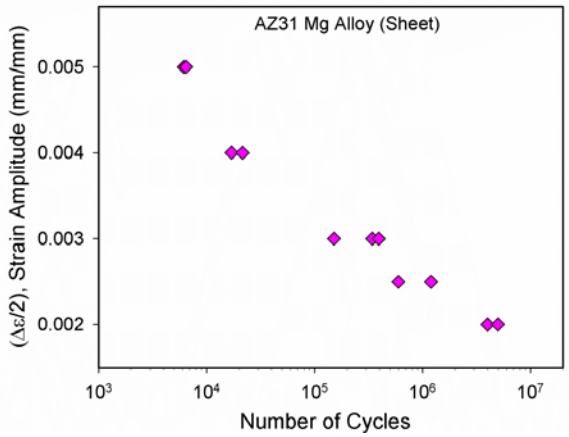

Figure 15: Total strain-life for an AZ31 sheet magnesium alloy

Cyclic Deformation Response

Figure 16 shows the hysteresis curves for several strain amplitude levels. These curves include the first cycle and the mid-life cycle, and show a little difference between the initial and mid-life cycle.

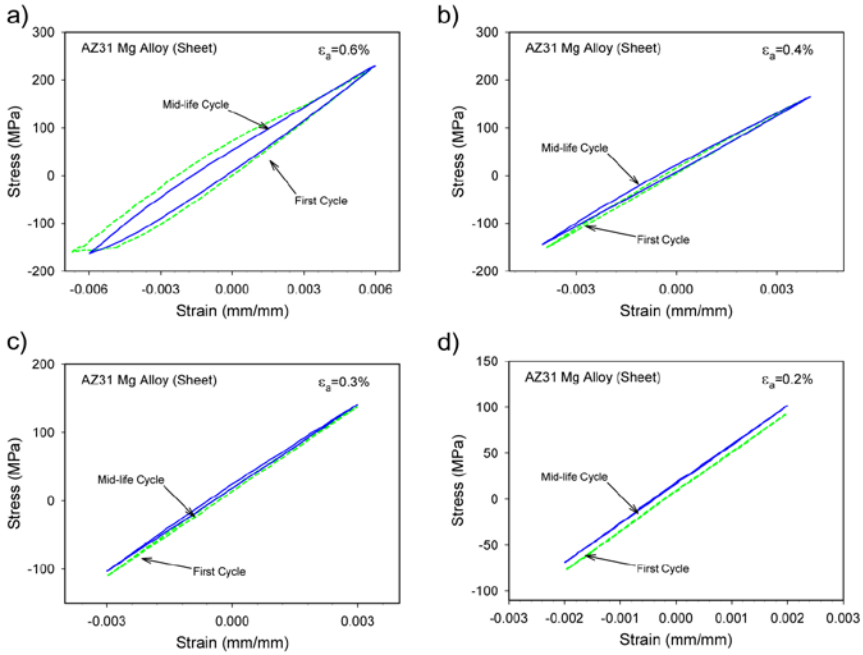

Figure 16: Hysteresis curves of AZ31 sheet Mg alloy at the strain amplitude of a) 0.6%, b) 0.4%, c) 0.3% and d) 0.2%.

Cyclic Stress-strain Response

Figure 17 shows the evolution of stress amplitude as a function of number of cycles at strain amplitudes ranging from 0.2 to 0.5 percent. The stress amplitude experiences a slight softening effect at the first cycles, followed by a slight hardening, and then remains almost constant.

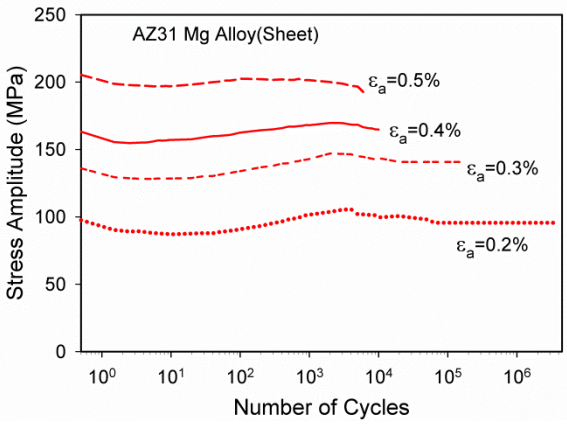

Figure 17: Stress amplitude response of AZ31 magnesium alloy

Multiscale Fatigue Modeling of AZ91 and AM60 Magnesium Alloys

In order to construct physically-motivated and microstructurally-sensitive fatigue estimations of the AZ91 and AM60 cast magnesium alloys presented in this study, the Multistage Fatigue (MSF) model was employed. The MSF model first proposed by McDowell *et al.* [1], comprises three distinct regimes of fatigue damage: crack incubation, microstructurally small crack (MSC) and physically small crack (PSC) growth, and long crack (LC) growth as shown in Eq. (3-4).

$$N_{Total} = N_{Inc} + N_{MSC/PSC} + N_{LC}. \tag{3-4}$$

Incubation Regime

For the incubation life, N_{inc} for a given material, a damage parameter, β, is equated to a modified Coffin-Manson law at the microscale

$$C_{\text{inc}} N_{\text{inc}}^{\alpha} = \beta, \tag{3-5}$$

where β is the nonlocal damage parameter around an inclusion, and C_{inc} and α are the linear and exponential coefficients in the modified Coffin-Manson law for incubation. The physical representation of the damage parameter is related to the local average maximum plastic shear strain amplitude at an inclusion and is estimated by the following:

$$\beta = \frac{\Delta\gamma^{P*}_{\max}}{2} = \Psi Y\left(\varepsilon_a - \varepsilon_{th}\right)^q, \quad \frac{l}{D} < \eta_{\lim} \tag{3-6}$$

$$\beta = \frac{\Delta\gamma^{P*}_{\max}}{2} = \Psi Y\left(1+\xi\frac{l}{D}\right)\left(\varepsilon_a - \varepsilon_{th}\right)^q, \quad \frac{l}{D} > \eta_{\lim} \tag{3-7}$$

where, ε_a is the remote applied strain amplitude, and ε_{th} and ε_{per} were introduced by McDowell *et al.* [1] and employed by Xue *et al.* [2, 6-7] to represent the strain threshold for damage incubation and the percolation limits for microplasticity, respectively. Both the strain threshold and the percolation limits for microplasticity can be determined through micromechanical simulations. However, Xue et al. [2] showed that the strain threshold is easily estimated by using the standard methods for estimating the endurance limit, where $\varepsilon_{th} = \frac{0.29Sut}{E}$. Furthermore, the percolation limit can also be estimated, where $\varepsilon_{per} = \frac{0.7\sigma_y^{cyclic}}{E}$. The parameter Y is correlated as $Y = y_1 + 0.1(1+R)y_2$, where y_1 and y_2 are material constants. For completely reversed loading cases, $Y = y_1$. An experimentally observed structure-property relationship term was recently added [8] to the incubation damage parameter. This structure-property term, $\Psi = \left[\frac{(MPS^2)}{(NND)(DCS)}\right]^{\gamma}$, is a function of maximum pore size (*MPS*), nearest neighbor distance (*NND*), dendrite cell size (*DCS*), and sensitivity exponent, γ, where the above parameters are microstructural parameters determined from fractographic and metallographic analysis.

Microstructually Small Crack Growth Regime

For the combined MSC/PSC growth regime, The growth for the fatigue crack is governed by the range of crack tip displacement, ΔCTD, which is proportional to the crack length, and the nth power of the applied stress amplitude in the HCF regime and to the macroscopic plastic shear strain range in the LCF regime; i.e.,

$$\left(\frac{da}{dN}\right)_{MSC/PSC} = \chi(\Delta CTD - \Delta CTD_{th}), \quad a_i = 0.625D \tag{3-8}$$

$$\Delta CTD = C_{II}\Psi\left(\frac{DCS}{DCS_0}\right)^{\varphi} f(\phi)\left[\frac{U\Delta\hat{\sigma}}{S_{ut}}\right]^{\zeta} a_i + C_I\Psi\left(\frac{DCS}{DCS_0}\right)^{\varphi}\left(\frac{\Delta\gamma^P_{max}}{2}\right)^2 \tag{3-9}$$

Here, χ is a constant for a given microstructure and C_I and C_{II} are material dependent parameters that capture the microstructural effects on MSC/PSC growth. A porosity related term is included in the high cycle fatigue regime, where $f(\phi) = 1 + \omega\left\{1 - exp\left(-\frac{\phi}{2\bar{\phi}}\right)\right\}$ and the porosity threshold, $\bar{\phi}$ is assumed as 0.0001. The effect of variation of dendrite cell size on crack growth is explicitly addressed relative to a reference size, DCS_0, and the sensitivity exponent, φ, is unity. The threshold value for crack tip displacement was set equal to the Burger's vector for the magnesium rich matrix [9], $\Delta CTD_{th} = 3.2 * 10^{-4}\mu m$.

A long crack growth stage of the MSF model is based on linear elastic fracture mechanics [1, 6]. However, in this study the modeling efforts focused on incubation and MSC/PSC growth regimes after Jordon *et al.* [8, 10]. This approach is consistent with the experimental evidence that the formulation for MSC/PSC can characterize fatigue cracks up to several millimeters in length [11].

Model Correlations and Fatigue Estimations

Figures 1a-c show the MSF model correlations for the AZ91 as-cast, AZ91-T6, and AM60 as-cast alloys, respectively. The incubation life in cast alloys are typically a larger percentage of total fatigue life compare to wrought alloys. For the mean life prediction, an incubation life of 36%, 43%, and 48% for total life was found suitable for the AM60 as-cast, AZ91 as-cast, and AZ91-T6 alloys, respectively. In addition, the mean fit for each of the fatigue data sets were based on mean microstructure values along with the corresponding cyclic mechanical properties. The mean pore size responsible for incubating the fatigue crack determined through the 3-D fractograghy analysis were used in the mean fits for each of the data sets.

To show the robustness of the MSF model and to capture the effect of microstructure on fatigue lifetimes, estimations for the upper and lower bounds of the strain-life data sets are also presented. These model predictions were determined by using the extreme pores sizes and DCS's for each data set. The model showed good correlation to both the upper and lower bounds as compared to the experimental results as shown in Fig. 18. As such, the MSF model was generally able to bound the scatter of each fatigue data set considering only the microstructure variation observed between locations L1 and L2. The model showed more sensitivity to pore size as compared to DCS. This is not unexpected considering there was not much variation of the DCS from locations L1 and L2. As such, the defect size was the primary factor determining number of cycles to failure for both the AM60 and the AZ91 alloys.

a)

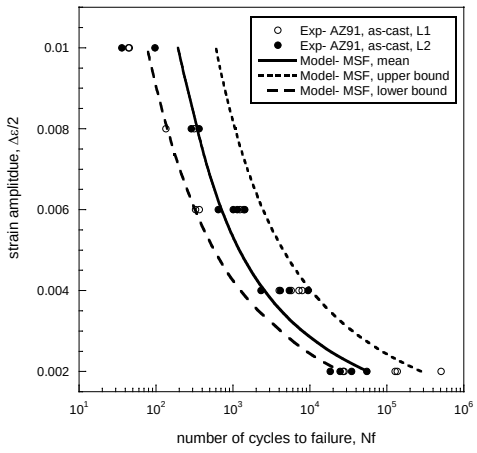

b)

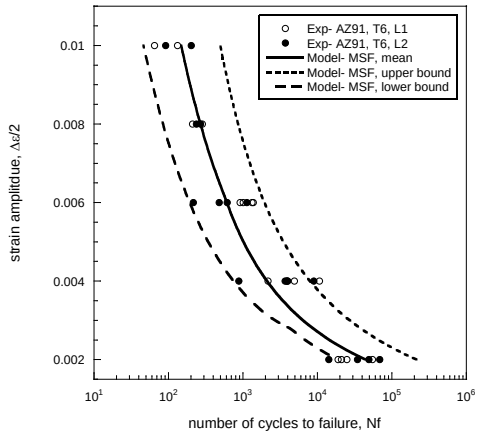

c)

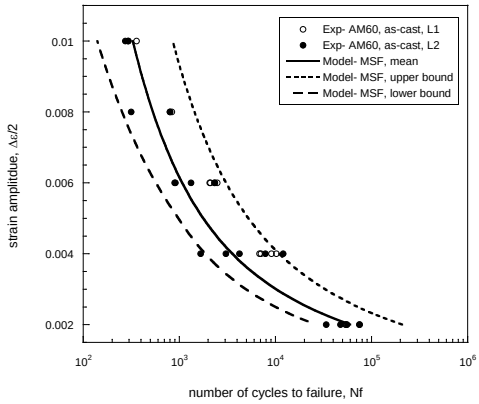

Figure 18: Comparison of the Strain-life experimental results for locations L1 and L2 to the mean, upper, and lower bound estimations of the Multistage fatigue model: a) AZ91 as-cast; b) AZ91-T6; c) AM60 as-cast.

The percentage of incubation to MSC/PSC growth of the MSF model varied considerably from the lower to the upper bounds. For the large pore sizes (lower bound), the average incubation life increased to approximately 60% of total life for all three data sets. Whereas, for the smallest pore sizes employed (upper bounds), the average incubation life consisted of approximately 12% of total life for all three data sets. This variation in the ratio of percentage of incubation life seems reasonable considering that a larger pore size will have a greater plastic zone around the inclusion resulting in more incubation life. As such, a smaller inclusion will result in a smaller plastic zone and therefore, less incubation life. The capability of the MSF model to capture the scatter typically observed in fatigue data based on microstructure variation alone is directly related to it's ability to vary the contribution of incubation and MSC/PSC growth for a given material. Table 1 lists the microstructure related MSF parameters for the mean, upper, and lower bounds estimations for the AM60 and the AZ91 alloys.

Table 1: Microstructure related MSF Parameters for AZ91 and AM60 magnesium alloys

	AZ91 As-Cast			AZ91-T6			AM60 As-Cast		
	Lower bound	Mean	Upper bound	Lower bound	Mean	Upper bound	Lower bound	Mean	Upper bound
Pore Size (μm)	495	293	119	554	290	116	600	274	107
DCS (μm)	19.6	16.7	13.7	19.6	16.7	13.7	19.6	16.6	13.5

Microstructure-Sensitive Fatigue Modeling of AZ31 Magnesium Alloy in Extrusion, Plate and Sheet Form

The strain-life fatigue behavior of AZ31 magnesium alloy in the extrusion, plate, and sheet formation were examined and structure-property relations were quantified. Samples for this study were taken from various locations as shown in Figure 19. Nearly identical asymmetric cyclic stress-strain behavior was observed in the extrusion and plate materials compared to the sheet material which exhibited more symmetric hysteresis loops. Twinning was observed on fracture surfaces of the extrusion material, while no evidence of twinning was observed on fracture surfaces of the plate and sheet materials. However, intermetallic particles at or near the surface were identified as sources of fatigue crack initiation all three materials. A multistage fatigue model was employed to predict the fatigue damage in the three differently processed materials. The multistage model comprises three scales of fatigue damage: crack incubation, microstructurally small crack and physically small crack, and long crack growth. In addition, the fatigue model incorporates microstructure influences resulting from crystallographic orientation, grain size, and inclusion size in the incubation and growth stages.

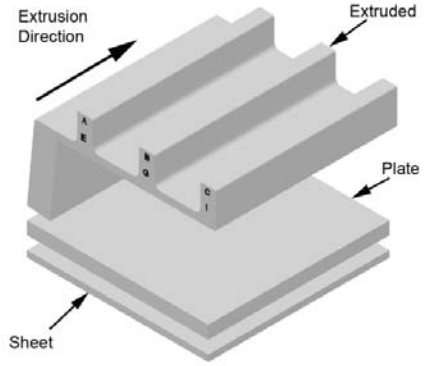

Figure 19: Sampling location of specimens in the extruded, plate and sheet materials

Microstructure of the AZ31 Alloys

The microstructural features of each material were quantified in order to provide understanding of the anisotropic behavior associated with fatigue. Figure 20 exhibits the grain morphologies and sizes of the AZ31alloys. For the extrusion, sectioned material parallel to the extrusion direction was found to have grains averaging 28.8 µm (Figure 20a), however, grains as large as 140 µm were seen. Regarding the intermetallic particles present in the material, the particles had an average particle size of 5.77 µm, an average nearest neighbor distance of 34 µm, nonetheless, particles of sizes around 40 µm were observed. For the plate material, the section parallel to the rolling direction was found to have equiaxed grains and a finer size of grain than the extruded specimen that averaged 10.7 µm. The intermetallic particles were found to average 3.25 µm, had a nearest neighbor distance of 22.82 µm. However, for the sheet material, the section parallel to the rolling direction was found to have elongated grains that were smaller than found in the extrusion and plate and averaged 5.7 µm. The intermetallic particles were found to average 3.71 µm, had a nearest neighbor distance of 35.45 µm.

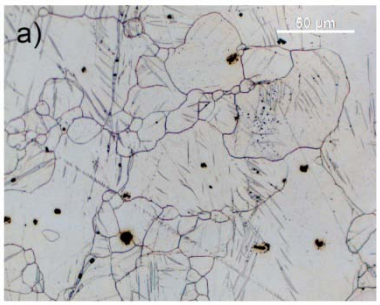

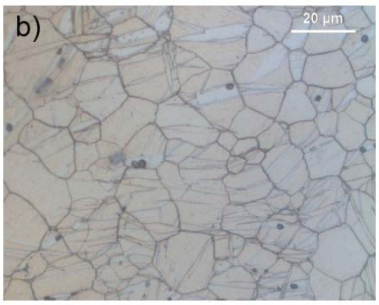

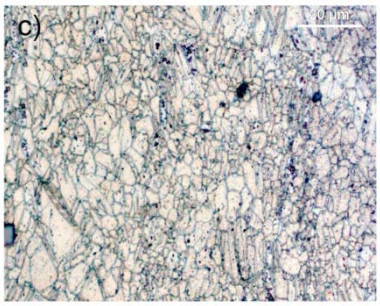

Alloy	Average Grain Size (µm)
Extruded	28.8
Plate	10.7
Sheet	5.7

Figure 20: Microstructure of AZ31 magnesium alloys. The grains are given by a) Extruded, b) plate, and c) Sheet alloys.

For the three alloys all the fracture surfaces showed typical indications of fatigue damage. Figure 21 shows a typical fracture surface for the extruded alloy. The initiation crack sites occurred near surface at inclusion particles. In most cases, fractured particles were identified to be the fatigue crack initiation sites. Also, observed in the SEM images was evidence of twinning on the fatigue fracture surfaces similar to what has been reported elsewhere [12-13]. The mechanisms of twinning and detwinning have the potential to create nucleation sites of a substantial number of micro-cracks that feed ahead of the main propagating crack.

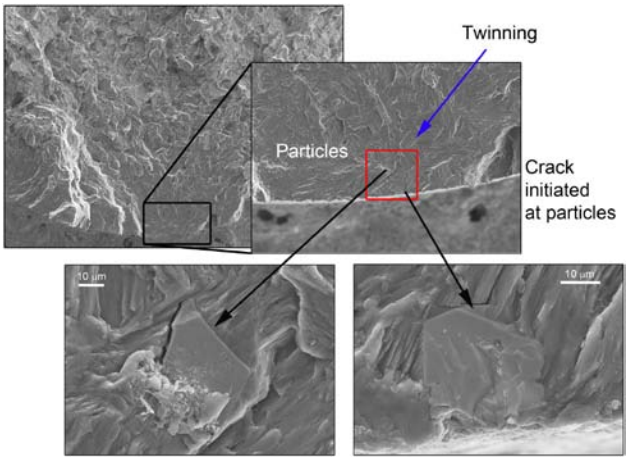

Figure 21: Fractured surface for an AZ31 Magnesium alloy at 0.6% of strain amplitude.

Figure 22 exhibits fractographs for all the three alloys at a strain amplitude of 0.3 percent. Crack initiations sites were located at inclusions near surface for all alloys. In addition, twinning was observed on the extruded material. It is also noted that no twinning was observed on the fracture surfaces that were examined for the sheet materials.

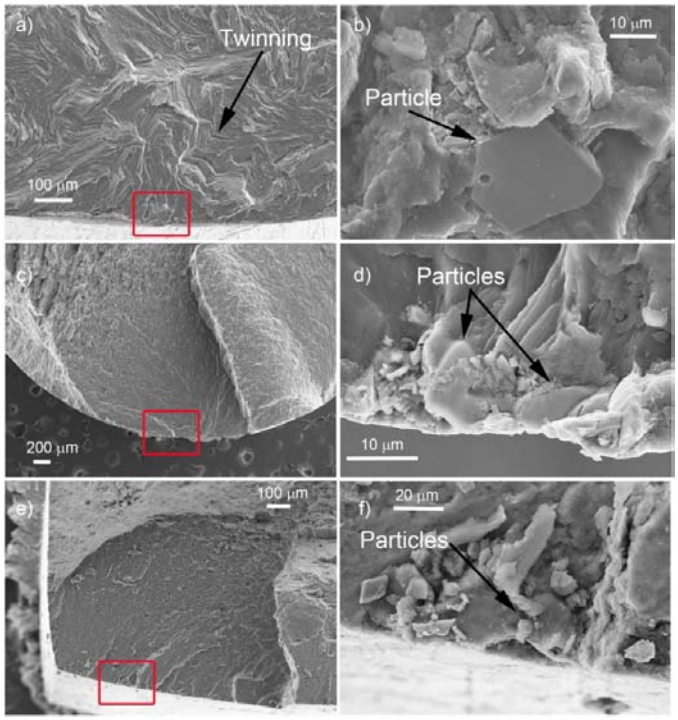

Figure 22: Typical overview of fracture surfaces for AZ31 magnesium alloys at 0.3 % of strain amplitude in the (a) extrusion, (c), plate, and (e) sheet materials. Fatigue cracks were found to initiate from intermetallic particles at the surface in the (b) extrusion, (d), plate, and (f) sheet materials.

Figure 23 shows the correlations of the MSF models to the experimental strain-life data. Larger lives were generally observed for the sheet material and the MSF model reflects this difference also and correlates well for the three materials. The grain size can have an influential impact on fatigue lifetimes [14-15] and as such the small crack formulation can capture this effect. Particle size is the other factor contributing to this difference in fatigue performance as noted in other magnesium alloys [10]. Finally, we note that twinning deformation likely plays an influential role in determining fatigue lifetimes. At this point in the development of fatigue models for magnesium alloys, the effect of twinning is captured through the cyclic stress-strain response. However, future fatigue modeling efforts should include contributions from both slip and twinning deformation in the early stages of damage.

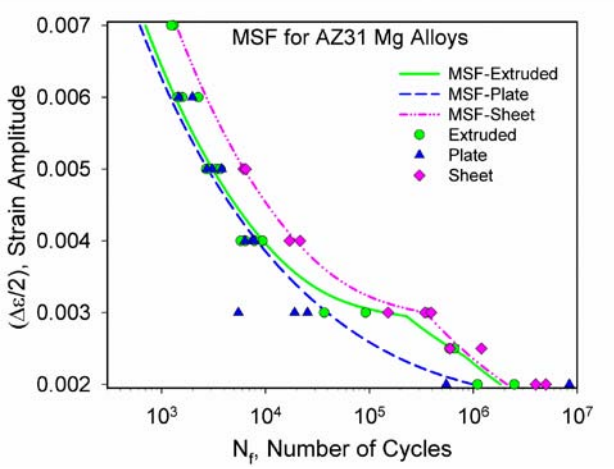

Figure 23: Comparison of the Multistage (MSF) model to the strain-life results of the extrusion, plate and sheet materials.

Fatigue of Friction Stir Spot Welding in Magnesium Alloys

The purpose of this task is to develop a microstructure-sensitive model for predicting fatigue damage in spot welded joints made using friction stir technology. In order to realize this goal, relationships of microstructural and geometrical features to fatigue performance were investigated using AZ31 magnesium alloy sheets joined by friction stir spot welding (FSSW). Two sets of lap-shear coupons were spot welded using different welding conditions. Optical microscopy of the initial state of the microstructure of each set of spot welds revealed differences in the hook formation, sheet thickness in the weld zone, and nugget diameter, and microstructure. Both sets of welds were fatigue tested in load control until failure at various load ratios. Optical microscopy of the failed coupons revealed differences in the fracture mode between the two sets of coupons. Fractography analysis conducted in this study suggested that the effective top sheet thickness largely determined the failure mode, which in turn influenced the final number of cycles to failure. While the height of the interfacial hook was greater in the process with better fatigue performance, it was the larger effective top sheet thickness that promoted crack propagation modes more favorable to greater fatigue resistance. To further aid in determining the cause and effect relationships and to elucidate the mechanisms behind fatigue damage in (FSSW), a linear elastic fracture mechanics model was used to correlate the fatigue life in the two processes. The fatigue model, which is a function of hook size, sheet thickness, and nugget diameter, showed good correlation to the experimental results as shown in fig 24. The use of this model revealed that the fatigue of the (FSSW), was most sensitive to the sheet thickness in the weld zone, followed by hook height, and then nugget diameter. As such, the shoulder plunge depth during the friction stir welding process may likely be the dominant factor in producing durable spot welds using this novel welding technique.

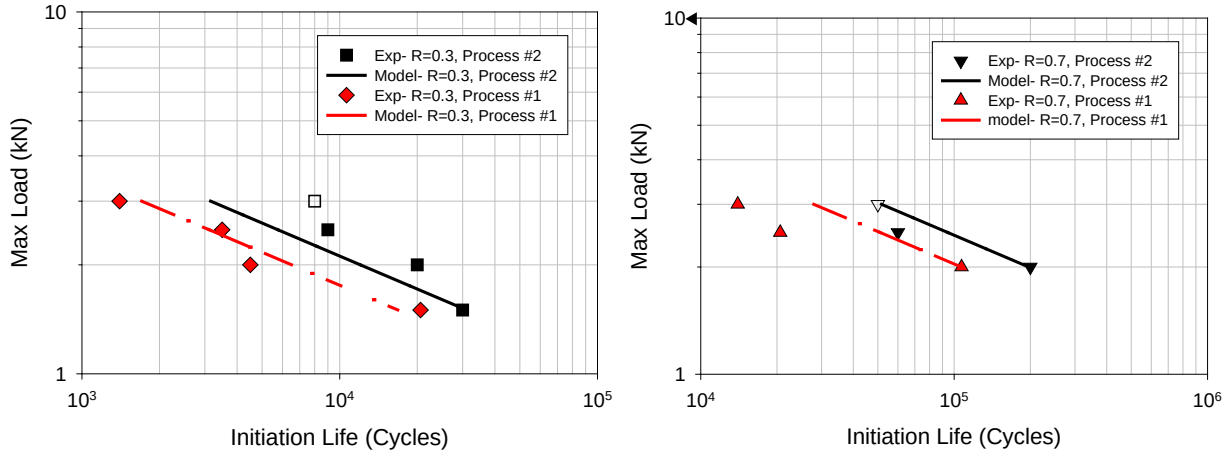

Figure 24: Comparison of the fatigue model to the experimental results of friction stir spot welded lap-joints for two welding conditions (process #1 and #2).

Conclusions

Next the main conclusions of DOE Phase III are listed:

1. Fatigue of base magnesium alloys (AM30, AZ31 and AZ61):
   - Cyclic response showed an asymmetric pattern for all alloys and the observed strain amplitudes. The asymmetry was more emphatic for the first cycles of the cyclic process.
   - Twining in compression and detwining in tension occurred during cyclic loading for all the extruded alloys except for the AZ31 sheet material.

- Mean stress was higher for extruded samples when compared to the transverse direction and AZ31 sheet material.
- The experimental results shown differences in the fatigue response between the transverse and the extruded direction of the applied load.
- Observations of the fracture surfaces under scanning electron microscopy revealed that fractured intermetallic particles initiated fatigue cracks in all three materials. The crack initiation sites were found to occur more frequently at inclusions near the free surface of the specimens for all the materials. However, crack initiation sites were located at regions where profuse twinning was observed.
- Particle size was more important in determining the number cycles than the anisotropy from the texture for magnesium alloys.

2. Multistage fatigue modeling of AM30, AZ31, and AZ61 wrought Mg alloys
   - The MultiStage Fatigue (MSF) model was adapted to capture the influences of the microstructural characteristics and influences of the extruded alloy. As such, the MSF model was able to predict the scatter of the fatigue results with good agreement for all the magnesium alloys.
   - The multistage fatigue model incorporated the differences in microstructure including crystallographic orientation, grain size, particle size, and cyclic hardening parameters in order to capture the differences in fatigue behavior.

3. Molecular Dynamics Simulations of Magnesium:
   - Simulations were performed on magnesium crystals under cyclic loading.
   - Simulations results showed that growth of the crack was affected by the crystal orientation and temperature.

4. Monotonic and cyclic testing for different casting processes
   - Inclusion size and pore shrinkage were the dominate causes of fatigue incubation in the 5 casting processes examined

5. Microstructure and Damage Evolution during Tensile Loading in a AZ61 Magnesium Alloy
   - The microstructural damage evolution for an AZ61 magnesium alloy was evaluated. Three types of particles were identified: Oxide/intermetallic and Mn-Al, and Mg-Al phases.
   - Under uniaxial tension the area fraction of cracked particles composed of (Mn-Al) and (Mg-Al) varies in an exponential pattern as function of strain. .
   - The Horstemeyer and Gokhale damage nucleation model was in good agreement with the observed damage progression of the AZ61 magnesium alloy.

6. Fatigue Modeling of AZ91 and AM60 Magnesium Alloys
   - The Multistage fatigue model was correlated to the experimental strain-life results of the AM60 as-cast, AZ91 as-cast, and the AZ91 T6 magnesium alloys. The mean fits of the model were based microstructure features such as dendrite cell size, pore size, and cyclic hardening parameters in order to capture the differences in fatigue behavior of the three data sets.
   - The Multistage fatigue model showed good correlation of the upper and lower bounds of the strain-life behavior of the AM60 and AZ91 magnesium alloys by employing the maximum and minimum inclusion and dendrite cell sizes. Thus, the inclusion (pore) size had the most influence on the scatter in the fatigue lifetimes. We note that the other material constants were not changed for the estimation of the upper and lower bounds.

7. Fatigue of Friction Stir Spot Welding (FSSW) in Magnesium Alloys
   - Two competing factors were identified to influence the performance of the FSSW joints: (1) the

hook height, and (2) the thickness.

- The linear elastic fracture mechanics model employed was able to account for the competing factors.

Presentations/Publications/Patents

1. J.B. Jordon, J.B. Gibson, M.F. Horstemeyer, H. El Kadiri, J.C. Baird, "Experiments and Modeling of Fatigue Damage in Extruded Mg AZ61 Alloy." TMS 2011 (The Minerals, Metals & Materials Society).
2. J.D. Bernard, J.B. Jordon, M.F. Horstemeyer, "Small Fatigue Crack Growth Observations in a Wrought Magnesium Alloy" TMS 2011 (The Minerals, Metals & Materials Society)
3. M. Lugo, B. Jordon, M. F. Horstemeyer, and M. A. Tschopp, "Microstructural relationship in the damage evolution process of an AZ61 magnesium alloy", TMS 2011 (The Minerals, Metals & Materials Society).
4. T. Tang, D. Wang, J. B. Jordon, and M. F. Horstemeyer, "Stress Intensity Factor Solutions for Friction Stir Spot Welds of Magnesium AZ31 Alloy, TMS 2011 (The Minerals, Metals & Materials Society).
5. H. Badarinarayan, S.B. Behravesh, S.D. Bhole, D.L. Chen, J. Grantham, M.F. Horstemeyer, H. Jahed, J.B. Jordon, S. Lambert, H.A. Patel, X. Su, and Y. Yang, "Monotonic and Fatigue Behavior of Mg AZ31 in Friction Stir Spot Welds: An International Benchmark Test in the "Magnesium Front End Research and Development Project," TMS 2011 (The Minerals, Metals & Materials Society).
6. J.B. Jordon, M.F. Horstemeyer, S.R. Daniewicz, H. Badarinarayan, and J. Grantham, "Fatigue Characterization and Modeling of Friction Stir Spot Welds in Magnesium AZ31 Alloy," Journal of Engineering Materials and Technology, 132, 2010.
7. M. Lugo, M. A. Tschopp, J. B. Jordon, and M. F. Horstemeyer, "Microstructure and Damage Evolution during Tensile Loading of AZ61 Magnesium Alloy", Scripta Materialia, 64, pp. 912-915, 2011.
8. T. Tang, S. Kim, M. F. Horstemeyer, and P. Wang, "Atomistic modeling of crack growth in Magnesium single crystal", Engineering Fracture Mechanics, 78, Issue 1, pp. 191-201, 2011.
9. J.B. Jordon, J.B. Gibson, M.F. Horstemeyer, H. El Kadiri, J.C. Baird, A.A. Luo, "Effect of Twinning, Slip, and Inclusions on the Fatigue Anisotropy of Extrusion-textured AZ61 Magnesium Alloy, Material Science Eng A, 528, p 6860-6871, 2011.

References

[1]. D.L. McDowell, K M.F Horstemeyer, J. Fan, 2003, Microstructure-based fatigue modeling of cast A356-T6 alloy Engineering Fracture Mechanics, v 70, n 1, p 49-80

[2]. Y. Xue, D.L. McDowell, M.F. Horstemeyer, M.H. Dale, J.B. Jordon, 2007, Microstructure-based multistage fatigue modeling of aluminum alloy 7075-T651, Engineering Fracture Mechanics, v 74, n 17, p 2810-2823.

[3]. M.F. Horstemeyer, and A.M. Gokhale, 1999, A Void nucleation model for ductile metals, International Journal of Solids and structures, 36, p 5029-5055.

[4]. B. Cotterell, and J.R. Rice, 1980, Slightly curved or kinked cracks, International Journal of Fracture 16, p 155–169.

[5]. D.W. Brown, A. Jain, S.R. Agnew, and B. Clausen, 2007, Twinning and Detwinning During Cyclic Deformation, Materials Science Forum, Vols. 539-543, p 3407-3414

[6]. Y. Xue, H. El Kadiri, M.F. Horstemeyer, J.B. Jordon, H. Weiland, 2007, Micromechanisms of multistage fatigue crack growth in a high-strength aluminum alloy, Acta Mater. 55, p 1975-1984.

[7]. Y. Xue, A. Pascu, M.F. Horstemeyer, L. Wang, P.T. Wang, 2010, Microporosity effects on cyclic

plasticity and fatigue of LENS™-processed steel, Acta Mater. 58, p 4029-4038.

[8]. J.B. Jordon, M.F. Horstemeyer, N. Yang, J.F. Major, K.A. Gall, J. Fan, 2010, Microstructural Inclusion Influence on Fatigue of a Cast A356 Aluminum Alloy, Metall Mater Trans A. 41A, p 356-363.

[9]. S. Groh, E.B. Marin, M.F. Horstemeyer, D.J. Bammann, 2009, Dislocation motion in magnesium: a study by molecular statics and molecular dynamics, Modell Simul Mater Sci Eng. 17, p 1-15.

[10]. J.B. Jordon, J.B. Gibson, M.F. Horstemeyer, H. El Kadiri, J.C. Baird, A.A. Luo, 2011, Effect of twinning, slip, and inclusions on the fatigue anisotropy of extrusion-textured AZ61 magnesium alloy, Material Science and Engineering A, 528, p 6860-6871.

[11] K. Shiozawa, Y. Tohda, S-M. Sun, 1997, Crack Initiation and small Fatigue Crack Growth Behaviour of Squeeze-cast Al-Si Aluminum Alloys, Fatigue & Fracture of Engineering Materials and Structures. 20, p 237-247.

[12]. F. Yang, S.M. Yin, S.X. Li, and Z.F. Zhang, 2008, Crack Initiation Mechanism of Extruded AZ31 Magnesium Alloy in the Very High Cycle Fatigue Regime, Materials Science and Engineering A, 2008, 491, p 131-136.

[13]. S. Morita, S. Tanaka, N. Ohno, Y. Kawakami, and T. Enjoji., 2010, Cyclic Deformation and Fatigue Crack Behavior of Extruded AZ31B Magnesium Alloy, Materials Science Forum, 2010, Vols 638-642, p 3056-3061.

[14]. Y. Ochi, K. Masaki, T. Hirasawa, X. Wu, T. Matsumara, Y. Takinaga, and K., Higashi, 2006, High Cycle Fatigue Property and Micro Crack Propagation Behavior in Extruded AZ31 Magnesium Alloy. Materials Transactions, 47, No. 4, p 989-994.

[15]. S. Ishihara, Z. Nan, and T. Goshima, 2007, Effect of the Microstructure on Fatigue Behavior of AZ31 Magnesium Alloy. Materials Science and Engineering A, 468, p 214-222.

Key Words

Fatigue, Magnesium Alloys, Structure-Property Relations, Multistage Modeling, Plasticity, Cyclic Damage, Cracks, twinning, Spot Welds, Friction Stir Spot Welds, Finite Element Analysis.

Brief Description of Report

The wrought magnesium alloys, AM30, AZ31, and AZ61, and a cast AZ91 alloy provided by our automotive partners, were investigated. Monotonic and cyclic tests programs were conducted to evaluate the mechanical behavior of the magnesium alloys. In addition, experiments and simulations were conduced to quantify structure-property relations with the intent to develop a microstructure-sensitive fatigue model for magnesium alloys. For extruded magnesium alloys, in-depth experimental studies were performed for purpose of calibrating physics-based MultiStage Fatigue (MSF) models. For additional modeling purposes, monotonic damage in Mg AZ61 alloy was characterized and modeled. Experiments were also conducted on cast AZ91 to quantify sources of fatigue initiation. Regarding fatigue performance of joints, relationships of microstructural and geometrical features were investigated using AZ31 magnesium alloy sheets joined by friction stir spot welding (FSSW).

MISSISSIPPI STATE UNIVERSITY

Southern Regional Center for Lightweight Innovative Design

Phase III

Final Scientific & Technical Report

October 1, 2009-September 30, 2011

For compliance with contract requirements of Award DE-EE0002323

Task 4

CORROSION OF MAGNESIUM ALLOY

Submitted December 27, 2011

TASK 4: CORROSION OF MAGNESIUM ALLOY

Table of Contents

TASK 4: CORROSION OF MAGNESIUM ALLOY

Principal Investigator: Mark F. Horstemeyer
Chair Professor, Computational Manufacturing & Design
Center for Advanced Vehicle Systems
Mississippi State University
PO Box 5405, Mississippi State, MS 39762-5405
(662) 325-5449; fax: (662) 325 5433; *e-mail:* *mfhorst@cavs.msstate.edu*

Participants: H. Martin, C. Walton, S. Groh

William Joost: Technology Area Development Manager
e-mail: *william.joost@ee.doe.gov*

Magda Rivera: Project Manager
e-mail: *magda.rivera@netl.doe.gov*

Contractor: *Mississippi State University (MSST)*
Contract No.: *DE-EE0002323*

Objective

- Understand and model the mechanisms of corrosion and hydrogen embrittlement in Mg alloys.

Approach

- Experimental data to quantify the mechanism of corrosion in Mg alloy.
- Molecular dynamics to quantify the effect of hydrogen on dislocation properties and void growth in Mg.
- Development of a macroscopic model for corrosion.

Accomplishments

- Identified mechanisms at the origin of the plastic flow in a Mg single crystal with a pre-existing pore.
- Developed a Mg potential for dislocation purposes and of the pair Mg-H to model hydrogen effects.
- Characterize the effect of hydrogen on the dislocation core structures.
- Compared the corrosion mechanisms of a 3.5% NaCl aqueous solution on as-cast AM60 Mg using an immersion testing technique and a cyclical salt spray testing technique over 60 hours.
- Compared the corrosion mechanisms of a 3.5% NaCl aqueous solution on as-cast AZ91 Mg using an immersion testing technique and a cyclical salt spray testing technique over 60 hours.
- Compared the corrosion mechanisms of a 3.5% NaCl aqueous solution on extruded AZ31 Mg using an immersion testing technique and a cyclical salt spray testing technique over 60 hours.
- Compared the corrosion mechanisms of a 3.5% NaCl aqueous solution on as-cast AZ61 Mg using an immersion testing technique and a cyclical salt spray testing technique over 60 hours.
- Compared the corrosion mechanisms of a 3.5% NaCl aqueous solution on extruded AM30 Mg using an immersion testing technique and a cyclical salt spray testing technique over 60 hours.

Introduction

Understanding the corrosion mechanisms that ultimately leads to the failure of metals is of utmost importance. Magnesium is currently being investigated for use in the aerospace and automobile industries, but its high corrosion rate relegates it to locations unexposed to the environment (Makar and Kruger (1993); Song and Atrens (2003)). Because of its electrochemical potential as illustrated by the galvanic series, magnesium alloys corrode quickly when exposed to saltwater (Shaw (2003)). Furthermore, the presence of rare earth elements, such as cerium, in the eutectic regions surrounding the grains of AE44 can also lead to galvanic corrosion (Alvarez et al. (2010); Bakkle and Westengen (2005)). Understanding the corrosion mechanisms of pitting, intergranular corrosion, and general corrosion could help control corrosion in the future.

The current research was designed to study the effects of alloying elements on magnesium, including various percentages of aluminum and the addition of zinc, rare earth elements, or manganese. This research also examined the effects of surface finish, specifically comparing an as-cast surface versus an extruded surface. All effects were studied in one of two environments – a cyclical salt spray environment or an immersion environment. Ultimately, the data gathered will be used to calibrate an Internal State Variable Model that will be used to predict the corrosion of magnesium alloys. The development of a magnesium interatomic potential using the Modified Embedded-Atom Method (MEAM) to describe accurately dislocation properties is detailed in Section 2. The experimental set-up and main results for the comparison between immersion and salt spray are detailed in Section 3. Concluding remarks are given in Section 4.

Modeling

In this section, the development of a magnesium interatomic potential using the Modified Embedded Atom Method (MEAM) to describe accurately dislocation properties is presented. The goal is to compare different atomic potentials for Mg based on the relaxed $<10\bar{1}0>$- generalized stacking fault (GSF) energy curve and the Peierls stress of an edge dislocation lying in the basal plane and then develop a new potential that satisfies both more appropriately.

Van Swygenhoven and coworkers (2004) claimed that the nature of slip in nanocrystalline metals cannot be described in terms of an absolute value of the stacking fault energy, but a correct interpretation requires the GSF energy curve to include both the stable and unstable stacking fault energies. In this way, a simple measure for the relative tendency of a material to nucleate full dislocations is given by the ratio of the unstable to stable stacking fault energy. If this ratio is close to unity, it will be easier for full dislocations to be nucleated, and if it is high, it will be more difficult and mostly extended stacking faults from single partial dislocations will be observed in Molecular Dynamics (MD) simulations. Unfortunately, the unstable stacking fault energy is not experimentally accessible, and the stable stacking fault energy values are reported with large scatter in magnesium, ranging from 60 mJ/m^2 up to 150 mJ/m^2 based on the experimental data and between 29 mJ/m^2 and 47 mJ/m^2 using first principles methods. In addition, although experiments do not give access to the complete GSF energy curve, first principle calculations can be used as an input for the development of an interatomic potential.

The Embedded-Atom Method (EAM) and Modified Embedded-Atom Method (MEAM) potentials are based on molecular dynamics principles. The total energy of an atomic system, E, is calculated by summing the individual embedding energy F_i of each atom I in the atomic aggregate, as follows:

$$E = \sum_i E_i = \sum_i F_i\left(\sum_{j\neq i}\rho_i(r_{ij})\right) + \frac{1}{2}\sum_i\sum_{j\neq i}\Phi_{ij}(r_{ij}) \quad (1)$$

where, j is any neighboring atom, r_{ij} and Φ_{ij} are the mean separation and pair potential, respectively, between atoms i and j. The EAM models used for this work were those of Liu et al. (1996) and Sun et al. (2006). These two EAM models are essentially identical, with the exception of the form of the embedding

energy function employed; In Liu et al., the embedding energy was represented by a general function that needed to be determined, while in Sun et al., the embedding energy function was represented by a square root. The MEAM models studied in this effort were those of Baskes and Johnson (1994) and a new set of MEAM parameters developed to model dislocations more accurate during this study. Compared to the EAM potentials, the MEAM models present the advantage of taking into account the angular dependence of bonding. The coefficients of these potentials were chosen to fit material properties such as the lattice parameter, cohesive energy, unrelaxed vacancy formation energy, elastic constants, crystal lattice, liquid and melting properties.

Using the Mg database given in Table 4.1, a new set of parameters to model magnesium using the MEAM formalism was determined. The lattice parameters, elastic constants, energy of both the fcc and bcc phases, and the vacancy formation energy obtained with the MEAM parameters given in Table 4.2 are reported in Table 4.1. Relatively good agreement between the target value and the value calculated using the MEAM parameters was obtained except for the energy of the fcc phase.

Using a lattice of small dimensions, the $<10\bar{1}0>$-GSF energy curves calculated using either the Liu et al., Sun et al. and Baskes and Johnson potentials are plotted in Figure 4.1A and compared with the first principle results reported by Datta et al. (2008). Although the Baskes and Johnson MEAM potential was able to reproduce the physical properties reported in Table 4.1, its application for dislocation purposes was compromised by the discontinuity in slope of the GSF energy curve due to the neglect of second nearest neighbor interactions. On the other hand, calculations performed with the Sun et al. and Liu et al. potentials exhibited behavior similar to the DFT results until the intrinsic stacking fault was formed (label D_2 in Figure 4.1(A)); then fairly large deviations were experienced. For a displacement larger than 2 Å, the EAM models did not reproduce both the shape and the magnitude of the GSF obtained by Datta and coworkers.

Table 4.1. Mg database for the development of a MEAM potential.

Properties	Units	Target value	New MEAM potential
a	Å	3.203	3.202
c/a	-	$0.994x(8/3)^{0.5}$	$0.99x(8/3)^{0.5}$
$E_{coh} = E_{hcp}$	eV	1.51	1.51
E	GPa	35.2	35.2
c_{11}	GPa	59.3	57.7
c_{33}	GPa	61.6	60.0
c_{44}	GPa	16.4	16.3
c_{11}-c_{12}	GPa	16.8	16.8
E_{bcc}	eV	0.031	0.025
E_{fcc}	eV	0.026	0.008
E_{vac}	eV	0.40	0.35

Table 4.2. Mg MEAM coefficients.

A	α	β_0	β_1	β_2	β_3	r_e (Å)	E_c (eV)	t_0	t_1	t_2	t_3	C_{min}	C_{max}
0.7	5.49	4.6	0.2	0.4	0.8	3.19	1.51	1	4.64	19.97	-6.52	0.5	2.8

To remove the discontinuity in slope of the GSF energy curve obtained with the Baskes and Johnson MEAM potential, a decrease of the screening parameter (C_{min}) from 2.0 to 0.5 was required. This change introduced second nearest neighbor bonds. Such a change of the screening functions affected all the physical properties reported in Table 4.1. Therefore, the other parameters of the MEAM potential needed to be adjusted accordingly. The $<10\bar{1}0>$-GSF energy curve calculated using the improved MEAM potential is shown in Figure 4.1(A).

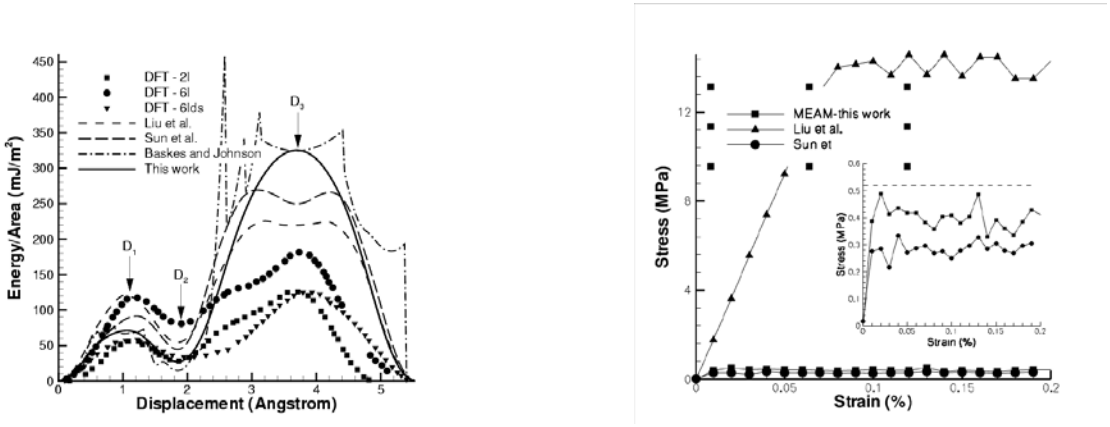

(A) (B)

Figure 4.1: Generalized stacking fault energy curves (A) and Strain-stress curves obtained crystals oriented for basal slip (B) calculated with different interatomic potentials.

Until the intrinsic stacking fault was formed, the MEAM prediction followed the lower bound given by Datta et al. (2008). Although a maximum energy was reproduced for a displacement of 3.7 Å, the magnitude of the energy was out of the range given by Datta et al. The magnitude of the second maximum was strongly affected by the difference of energy between the simple cubic and hexagonal crystal structure. However, such a difference of energy was not taken into account in the material database, and therefore, the second maximum was not adjusted for the fitting. No size effect was observed when a lattice of large dimensions was considered for the calculations of the GSF-energy curves.

As a benchmark of the improved potential, the dislocation core structure of the edge dislocation lying in the basal plane, and its Peierls value were tested. Dislocations were introduced in the crystal following the methodology given by Groh et al. (2009). Except for the Baskes and Johnson MEAM potential that could not be used to minimize the dislocation structure because of the discontinuities in the slope, edge dislocations from the basal plane were dissociated into two Shockley partials bounding an intrinsic stacking fault of length d_{sf}. The separation distance is given as a function of the Poisson coefficient, intrinsic stacking fault energy, and Burgers vector using the isotropic elasticity (IET) (Hirth and Lothe (1992)). Using the anisotropic elasticity theory (AET), the separation distance is given by

$$d_{sf}^{aniso} = \frac{b^2}{32\pi\gamma_I}\left[4K_e - \frac{K_s}{3}\right] \tag{2}$$

with

$$K_s = (c'_{44}c'_{55})^{1/2}; \quad K_e = (\overline{c}'_{11} + c'_{12})\left[\frac{c'_{44}(\overline{c}'_{11} + c'_{12})}{c'_{11}(\overline{c}'_{11} + c'_{12} + 2c'_{44})}\right]^{1/2} \tag{3}$$

where the elastic constants are given by

$$c'_{11} = c_{11}; c'_{12} = c_{13}; c'_{44} = c_{44}; c'_{66} = c_{66}; c'_{22} = c_{33}; \overline{c}'_{11} = (c'_{11}c'_{22})^{1/2} \tag{4}$$

For the elastic constants obtained with both Liu et al. and the improved MEAM potential, the elasticity framework (isotropic versus anisotropic) did not affect significantly the separation distance. On the other hand, as the elastic constants were sacrificed by Sun et al. to accurately reproduce the thermal properties of Mg the elasticity framework (isotropic versus anisotropic) strongly affected the prediction of separation distance (see Table 4.3).

Table 4.3. Evolution of the separation distance between partial dislocations using different interatomic potentials and comparison with isotropic/anisotropic elasticity theory for different cell size (in Burgers vector, b).

	Separation distance (nm)		
	Liu et al.	Sun et al.	This work
IET	1.56	1.28	2.58
AET (Eq. 2)	1.90	2.22	2.87
Cell dimension (b*b)			
30x30	1.24	1.76	2.52
100x100	1.53	2.17	2.66
200x200	1.54	2.16	2.80
300x300	1.53	2.16	2.81

Independent of the potential considered, the atomistic predictions of separation distance were size independent for a cell size bigger than 100bx100b (where b is the magnitude of the Burgers vector) as shown in Table 4.3. Based on the flexible *ab-initio* boundary condition method, Yasi et al. (2009) calculated the dislocation core structure of an edge dislocation lying in the basal plane using a cylinder of radius 22b. Their results confirmed the dissociation in two partials with a separation distance of 1.67 nm. Compared to their results, only the prediction obtained with the Sun et al. potential and a computational box of small dimension agreed with that value, while predictions were underestimated and overestimated using the Liu et al. and the MEAM potentials, respectively. Such a difference can be attributed to the value of the intrinsic stacking fault energy. In our case, the potential was fit based on the data reported by Datta et al. (2008) which represents a lower bound, while the intrinsic stacking fault obtained with the Liu et al. potential represents an upper bound.

Figure 4.1(B) shows the strain-stress behaviors calculated with the three different potentials and using a simulation cell of dimension 200bx200b along the line and displacement directions oriented to model the motion of an edge dislocation lying in the basal slip plane with a strain increment of 10^{-4}. As shown in Groh et al. (2009), no significant effect of the strain increment was found. Using the Liu et al. potential, the stress increased linearly up to 15 MPa before it stabilized. The corresponding shear modulus was 18.7 GPa, which is in good agreement with the value reported by Liu et al. (C_{44} = 18.1 GPa). So, for this potential, the Peierls stress was close to 15 MPa, a value one order of magnitude larger than the experimental value reported by Conrad and Robertson (1957). On the other hand, both the MEAM and Sun et al. potentials gave a Peierls stress in the order of 0.3-0.5 MPa, which is in closer agreement with the experimental data.

Experimentation

Experimental Set-Up

Twelve as-cast AZ91 coupons (25.4 mm x 25.4 mm x varying thickness) were cut from a squeeze cast control arm while twelve as-cast AM60 coupons (25.4 mm x 25.4 mm x varying thickness) were cut from a low pressure permanent mold control arm. Twelve extruded AM30 coupons (25.4 mm x 25.4 mm x varying thickness), twelve extruded AZ31 coupons (25.4 mm x 25.4 mm x varying thickness)), and twelve extruded AZ61 coupons (25.4 mm x 25.4 mm x varying thickness) were cut from crash rails. Each set of specimens was divided into two groups of six coupons. The coupons were then weighed and measured using calipers to determine the initial characteristics of the coupons.

The coupons were placed in either an immersion test, consisting of a 3.5% NaCl aqueous solution in an aquarium with aerator to ensure adequate oxygen within the system, or a Q-Fog machine using equal times of 3.5% NaCl aqueous solution spray, 100% humidity, and drying phases. The samples were removed and analyzed after 1 hr, 4 hrs, 12 hrs, 36 hrs, and 60 hrs. The coupons were then rinsed in distilled water to remove any residual salt, dried, weighed, and measured for comparison to the initial characteristics. Optical micrographs and laser profilometry scans were than taken of the surfaces.

Results

For all figures, the data points representing each magnesium alloy are the same shape and color. The trend lines are sold for the immersion environment and dashed for the salt spray environment. Figure a shows the immersion surfaces, while figure b shows the salt spray surfaces. Figure 4.2 shows the changes in weight of the various magnesium alloys. Figure 4.3 shows the changes in thickness of the various magnesium alloys. When examining Figures 4.2a and 4.3a, all surfaces exposed to the immersion environment lost weight and thickness, except for AM30 which gained thickness. When examining Figure 4.2b, only AE44 lost weight, while the other alloys all gained weight. Figure 4.3b shows that four of the alloys lost thickness, while both AZ91 and AM30 gained thickness.

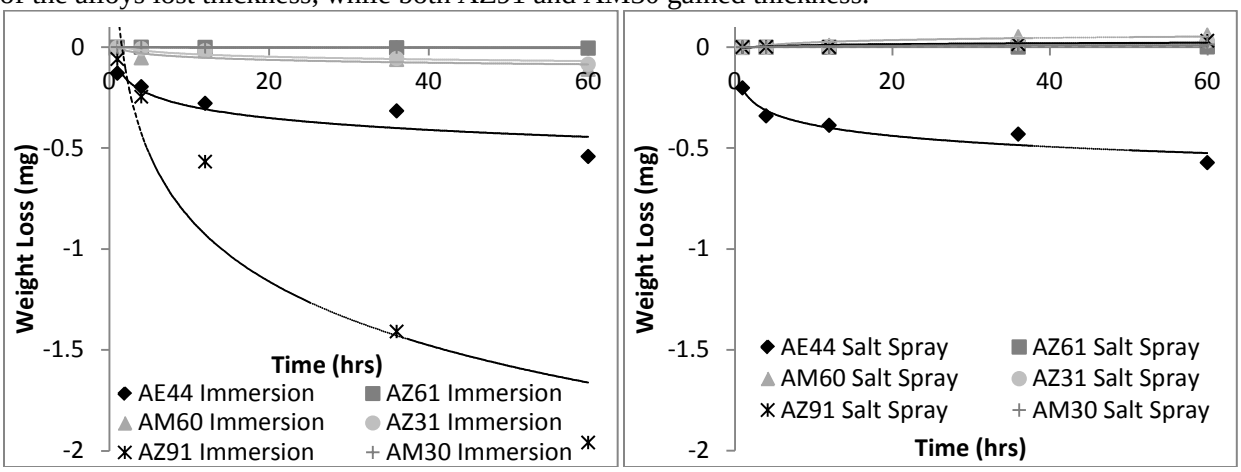

(a) (b)

Figure 4.2: Weight loss of the various magnesium alloys over the experimentation time. Notice that the immersion AZ91 lost the most weight for both environments, while the AE44 surfaces lost almost the same amount of weight in both environments. Also notice that some surfaces gained weight in the salt spray environment.

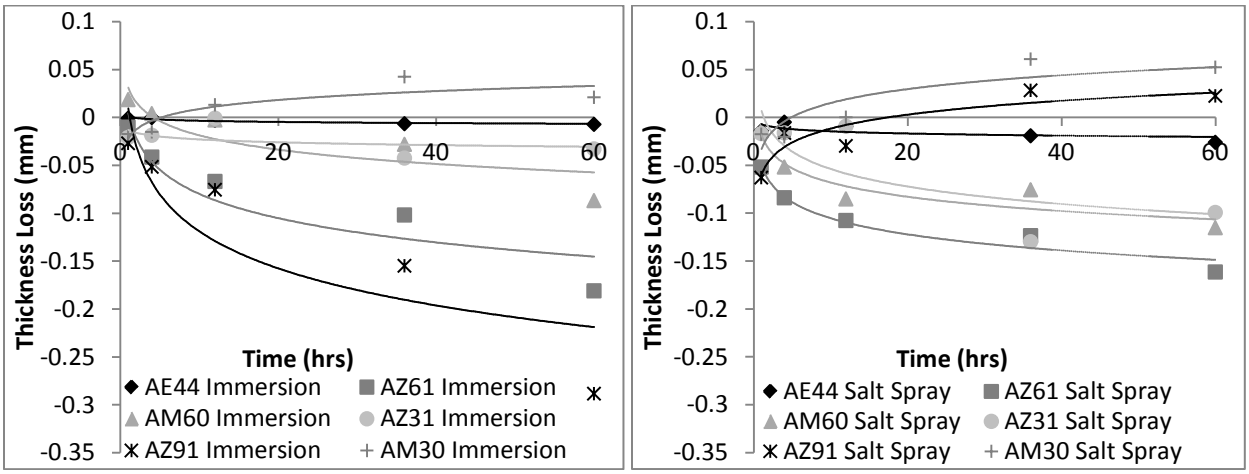

(a) (b)

Figure 4.3: Thickness loss of the various magnesium alloys over the experimentation time. Notice that the immersion AZ91 lost the most thickness for both environments, while the AZ61 surfaces lost almost the same amount of thickness in both environments. Also notice that some surfaces gained thickness in the salt spray environment, while only AM30 gained thickness in the immersion environment.

Figure 4.4 shows the changes in the pit number density of the various magnesium alloys. When examining Figure 4.4a and 4.4b, the AZ61 alloy experienced the highest amount of pit nucleation for both environments, while the AM60 alloy experienced the least amount of pit nucleation for both environments. There were decreasing trends in pit nucleation for the AZ31, AZ91, and AM30 alloys in

both environments, while the AE44 and AZ61 alloys experienced a second order polynomial trend in pit nucleation in both environments. The pit nucleation on the AM60 alloy did not drastically increase or decrease for either environment.

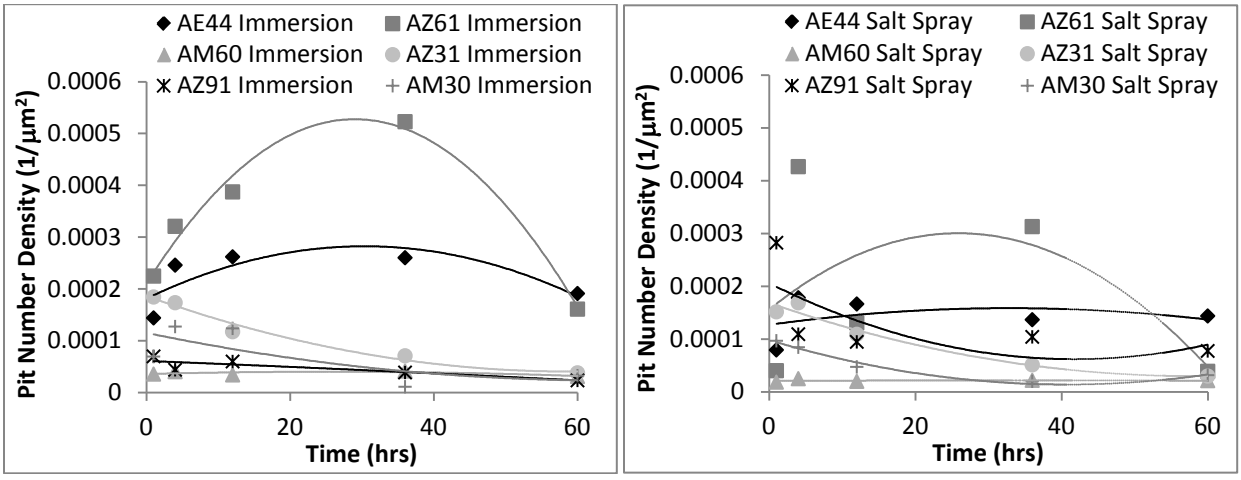

(a) (b)

Figure 4.4: Pit number density of the various magnesium alloys over the experimentation time. Notice that AZ61 experienced the most pit nucleation in both environments, while AM60 experienced the least pit nucleation in both environments. Also notice that salt spray environment experienced less pit nucleation than the immersion environment.

Figure 4.5 shows the changes in the in-plane pit area of the various magnesium alloys. When examining Figure 4.5a, one can see that the AM30 surface experienced the fastest pit growth, while AZ31 experienced the highest pit growth. When examining Figure 4.5b, one can see that both AZ31 and AM30 experienced high amounts of pit growth. The other alloys all experienced some second-order polynomial pit growth, although it is difficult to see the differences in the AE44, AZ61, AM60, and AZ91 alloys.

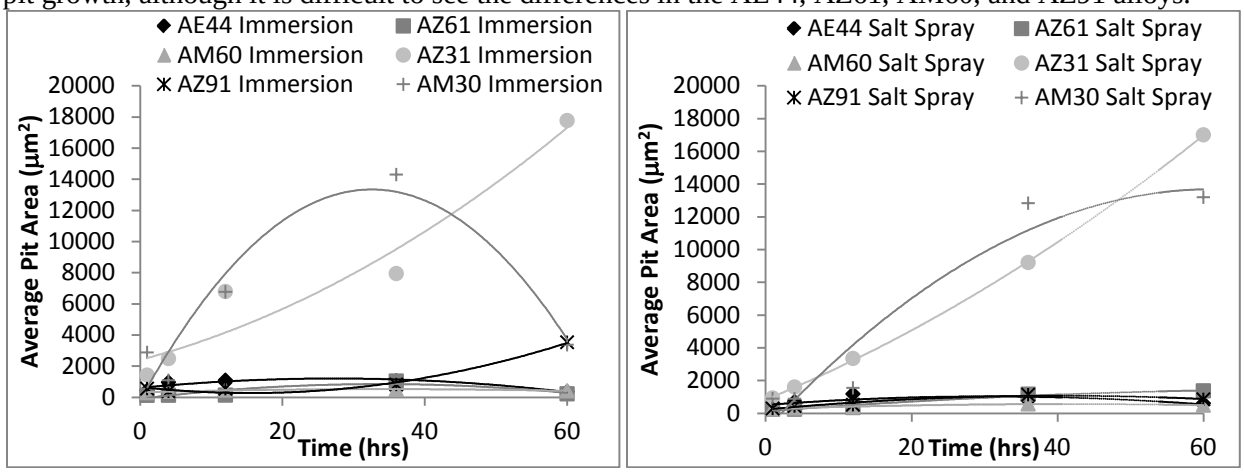

(a) (b)

Figure 4.5: Average in-plane pit area of the various magnesium alloys over the experimentation time. Notice that the highest amounts of growth were on AZ31 and AM30 for both environments. The growth on the AZ31 surface was unaffected by environment, while the growth on the AM30 surface was affected by the environment.

Figure 4.6 shows the changes in the in-plant pit area of the remaining four magnesium alloys when AZ31 and AM30 are removed from both environments. In the immersion environment, AZ91 experienced the largest in-plant pit area, while AE44, AM60, and AZ61 all experienced slight second-

order polynomial trends in pit area. In the salt spray environment, AZ61 experienced a continuous increase in pit area, while the other three alloys experienced second-order polynomial trends in pit area.

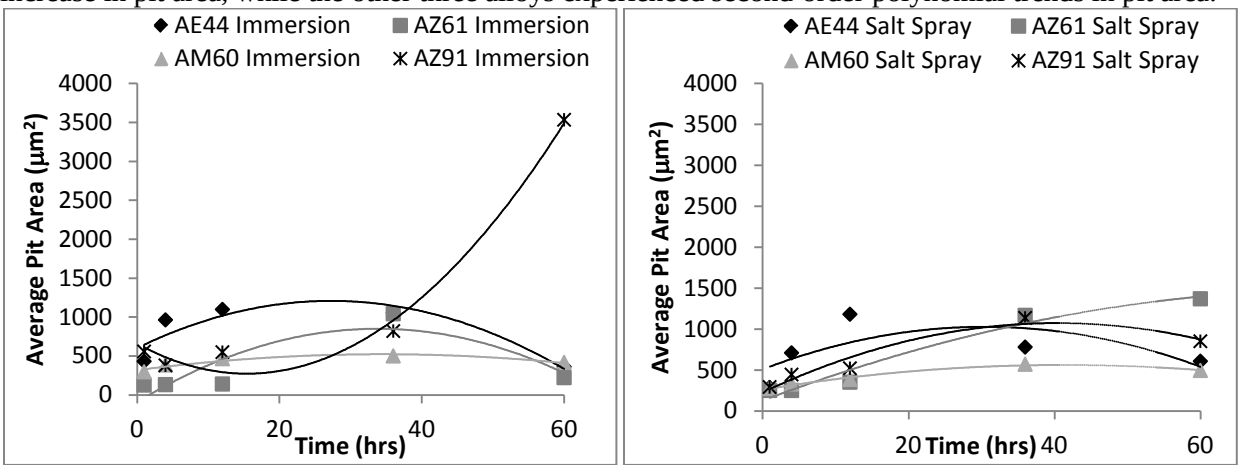

(a) (b)

Figure 4.6: Average in-plane pit area of the various magnesium alloys over the experimentation time, with AZ31 and AM30 removed. Notice that, except for AZ91 and AZ61, the alloys in both environments experienced similar pit area changes. In the immersion environment, AZ91 experienced a large increase in pit area. In the salt spray environment, AZ61 experienced a continuous increase in pit area.

Figure 4.7 shows the changes in the pit depth of the various magnesium alloys. When examining Figure 4.7, notice that the AZ91 data was divided by 10 to fit onto the graph and that the AZ91 pits were the deepest overall. Also notice that the AM60 surface had the second deepest pits for both environments. In Figure 4.7a, the AE44 pits ended with the shallowest pits. In Figure 4.7b, the AE44 pits and the AZ91 pits were the shallowest pits.

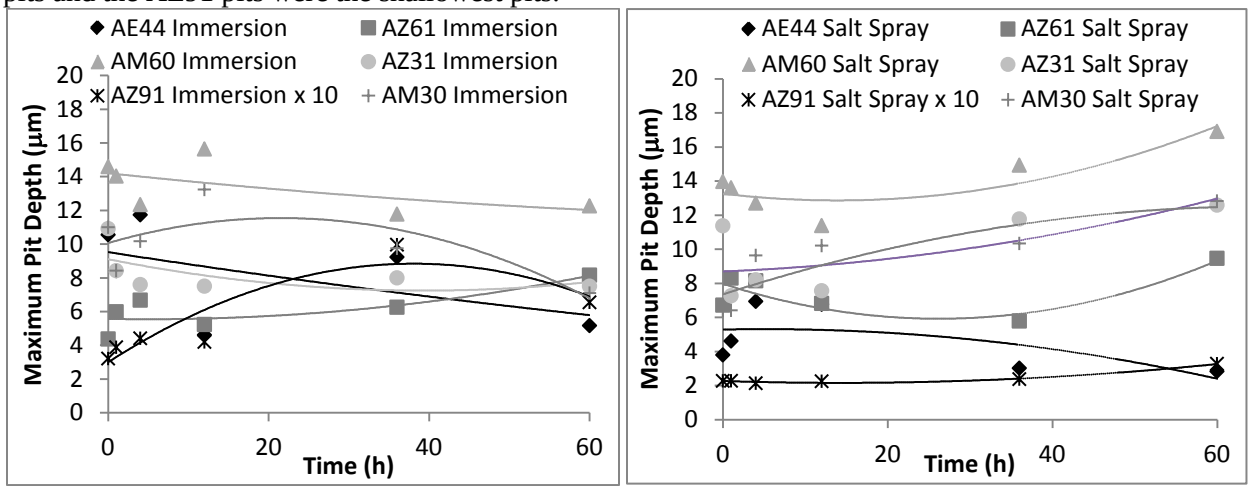

(a) (b)

Figure 4.7: Pit depth of the various magnesium alloys over the experimentation time. Notice that AZ91 had the highest pit depth in both environments, as the AZ91 surface was divided by 10 to fit on the graph. AM60 had the second highest pit depth in both environments, while AE44 had the smallest pit depth in both environments.

Figure 4.8 shows the changes in the nearest neighbor distance of the various magnesium alloys. Examining Figure 4.8a shows that the AM60 surface had the highest nearest neighbor distance, while AE44 had the smallest nearest neighbor distance. When examining Figure 4.8b, the highest nearest neighbor distance was AM30, while the lowest nearest neighbor distance was AE44.

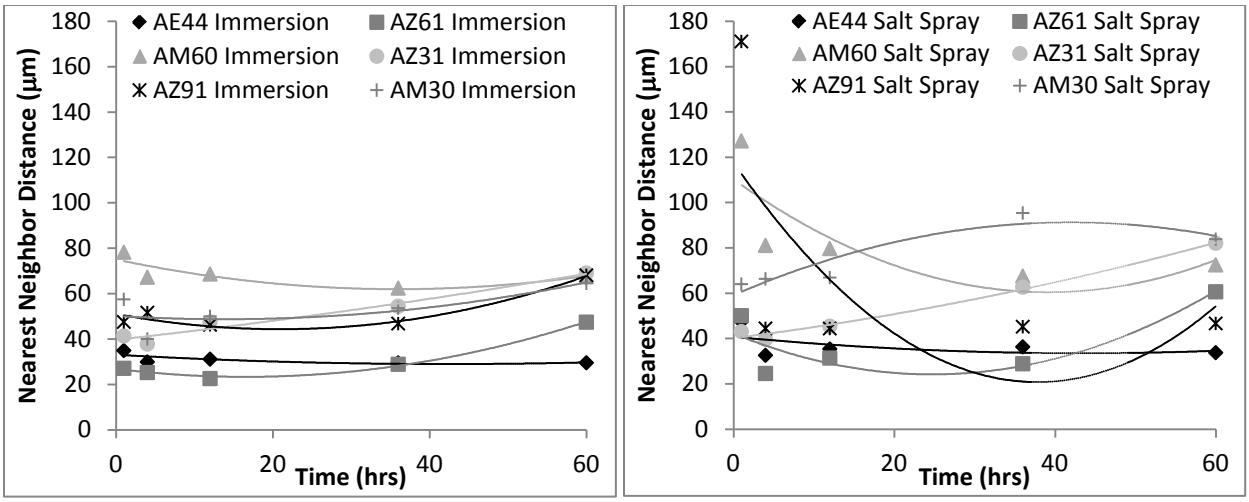

(a) (b)

Figure 4.8: Nearest neighbor distance of the various magnesium alloys over the experimentation time. Notice that the lowest nearest neighbor distance for both environments was AE44, while there were not trends with respect to the highest nearest neighbor distance.

Figure 4.9 shows the changes in the intergranular corrosion area fraction of the various magnesium alloys. Figure 4.9a shows that AE44 experienced the highest amount of intergranular corrosion while AZ91 experienced the least amount of intergranular corrosion. Figure 4.9b shows that AM30 experienced the highest amount of intergranulcar corrosion while AZ91 experiences the least amount of intergranular corrosion.

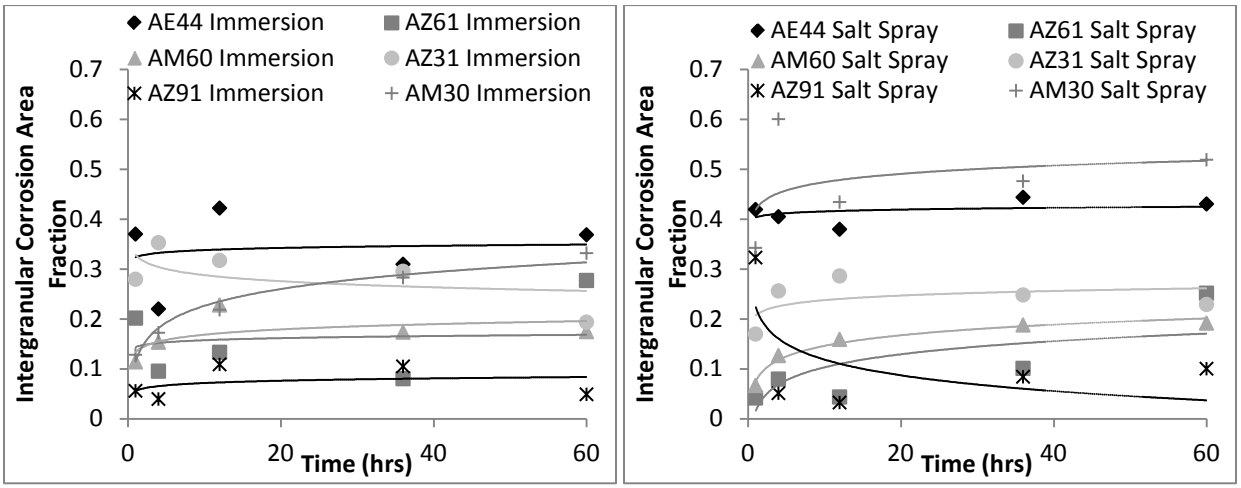

(a) (b)

Figure 4.9: Intergranular corrosion area fraction of the various magnesium alloys over the experimentation time. Notice that the lowest intergranular corrosion area fraction for both environments was AZ91, while the highest intergranular corrosion area fraction differed based on environment.

Discussion

The following conceptual model is presented in order to theoretically place the different mechanisms in a framework for future mathematical modeling following the work of Horstemeyer et al. [26, 27] as follows:

$$\phi = \phi_{GC} + \phi_{PC} + \phi_{IC} \quad (1)$$

where ϕ is the total damage, which can be thought of as the area fraction or volume fraction lost, from all forms of corrosion; ϕ_{GC} is the area or volume fraction lost due to general corrosion; ϕ_{PC} is the area or

volume fraction lost due to pitting corrosion; and ϕ_{IC} is the area or volume fraction lost due to intergranular corrosion. In this context, pitting corrosion is defined as the following:

$$\phi_{PC} = \eta_p \nu_p c \quad (2)$$

where η_p is a nucleation of pits and can be directly measured as the pit number density; ν_p is the pit growth and can be measured by the average pit area; and c is the coalescence and is a function including the nearest neighbor distance. The conceptual model that is introduced here can describe and unite the different corrosion mechanisms (general, pitting, and intergranular) in terms of measurable quantities (pit number density, pit area, pit nearest neighbor distance, and volume/mass loss).

General Corrosion

General corrosion is the removal of the outmost layer of magnesium through a reaction with water. When examining Figures 4.2 and 4.3, the immersion environment experienced the most general corrosion with respect to both weight loss and thickness loss. All six magnesium alloys lost weight and five of the six magnesium alloys lost thickness, excluding AM30. The weight and thickness losses occurred because of the continuous presence of water that allowed for the general corrosion reaction to occur without interruption. On the other hand, only AE44 lost both weight and thickness in the salt spray environment (Figs. 4.2b and 4.3b). The other five alloys all gained weight. Three additional alloys, AZ61, AZ31, and AM60, did lose thickness while two alloys, AZ91 and AM30, gained thickness. The weight and thickness gains are due to the drying phase of the salt spray cycle. This drying phase allowed for pit debris and salt residuals to remain in place, thereby increasing the weight and/or thickness. However, this does not mean general corrosion did not occur, only that the weight and thickness loss caused by general corrosion was replaced by salt residuals and pit debris.

When looking at the overall general corrosion trends, there are no trends based on alloying elements or on forming method. If the percentage of aluminum alone was responsible for the prevention of corrosion, one would expect that the AZ91 alloy would have the least amount of general corrosion and that the AZ31 and AM30 alloys would have the most amount of general corrosion. However, what is seen instead is that there is not definitive trend based on the percentage of aluminum. The same can be said of the forming method. If the as-cast skin alone protected the alloys from corrosion, then the AZ91, AM60, and AE44 alloys would experience less general corrosion than the AZ61, AZ31, and AM30 alloys. Again, there is no definite trend with regards to general corrosion based on forming method. Overall, the environment and the surface reactions have more of an effect on general corrosion than the alloying elements or the forming method.

Pit Nucleation

Pit nucleation is the development of pits on the surface due to the reaction between the magnesium surface and chloride ions present in the saltwater. Pit nucleation is determined from the pit number density, or the number of pits per unit area. Examining Figure 4.4 shows that more pits formed on the immersion surface than on the salt spray surface for all alloys. As with general corrosion, more pits could form on the immersion surfaces due to the continuous presence of water that carried the chloride ions. Pit nucleation could occur at any point during the experimentation time, as the chloride ions were present constantly to initiate nucleation. The salt spray surface, on the other hand, only experienced exposure to the chloride ions during the salt spray phase of the cycle. During the salt spray phase, pits could nucleate. During the humidity and drying phases, though, pits could not nucleate as there were no additional chloride ions to initiate nucleation.

When comparing the alloying elements, if the percentage of aluminum alone is responsible for reducing corrosion, one would expect to see that the AZ31 and AM30 surfaces experienced more pit nucleation, regardless of environment. However, the AZ31 and AM30 surfaces both experienced a decrease in pit nucleation for both environments. In the salt spray environment, the AM30 surface does experience slightly less pit nucleation, indicating that manganese may affect corrosion more than zinc. However, in the immersion environment, both surfaces experience almost the same amount of pit nucleation. This indicates that pit nucleation is affected by more than just the environment or the alloying

elements. In addition, AZ61 and AE44 experienced higher amounts of pit nucleation than the other four alloys. When comparing the pit nucleation of AZ61 with the pit nucleation of AZ31, the percentage of aluminum alone does not alone cause a reduction in pit nucleation. Instead, general corrosion may be acting more strongly on the AZ31 surface, reducing the number of pits, while the AZ61 surface may be able to better withstand general corrosion.

When comparing the forming method, there is a slight difference between the as-cast surfaces and the extruded surfaces. For both environments, AZ61, an extruded surface, experienced the highest pit nucleation. In addition, AM60, an as-cast surface, experienced the lowest pit nucleation for both environments. While this seems to indicate that there was a difference in pit nucleation with respect to forming method, examining the other alloys shows this is not the case. AE44, an as-cast surface, experienced higher pit nucleation values in both environments as compared to AZ31, an extruded surface. If forming method alone was responsible for pit nucleation, then the extruded surfaces, which lack the as-cast skin, should experience more pit nucleation. Overall, pit nucleation appears to be affected by an interaction between the forming method, the alloying elements, and the environment, with none of the corroding factors playing a more significant role than the others.

Pit Growth

Pit growth is the spread of the pits across the surface (in-plane area) and the increase in size of the pits into the magnesium (pit depth). Both the two dimensional growth and the additional third dimension are necessary to understand how the pits are affecting the magnesium alloys.

When examining Figure 4.5, there is minimal difference in the average in-plane pit growth between environments, but a large difference between alloys and forms. The two largest in-plane pit growths are experienced by AZ31 and AM30. In the immersion environment, AM30 does experience some general corrosion resulting in the decrease of pit area, indicating that the pits are shrinking in size. AZ31, on the other hand, increases throughout the experimentation time, indicating that general corrosion never was able to outpace pit growth. In the salt spray environment, both alloys experience high rates of growth. As with the immersion environment, the pit growth on AZ31 never begins to decrease. The pit growth does begin to decrease on AM30, although at a much later point than on the immersion environment. When examining Figure 4.6, there are minimal differences in the average in-plant pit growth between environments and between alloys for everything but the two 3% alloys. While AM60 does have the smallest in-plane pit growth for both environments, the other alloys all strongly resemble each other. By the end of the experimentation time, AZ91 does experience a large increase in pit growth, but, prior to 60 h, the pit growth was equivalent to the other three alloys.

The percentage of aluminum does appear to play a role in pit growth, at least on the two alloys with the lowest percentage of aluminum. However, the percentage of aluminum does not appear to play a role in pit growth for any percentage over 4%. This may be because 4% is the percentage of aluminum needed to increase corrosion resistance or it may be because of the secondary alloying elements. There does not appear to be a definitive trend in regards to corrosion with respect to the alloying elements above 3% aluminum. In addition, the forming method also appears to play a role, again, with respect the alloys containing only 3% aluminum. When examining Figure 4.6, one can see that there appears to be an overlap of the remaining four alloys in both environments, with neither the as-cast nor the extruded surfaces appearing to experience more pit growth. Overall, the percentage of aluminum does play a more significant role with regards to pit growth than the environment or the forming method.

When examining Figure 4.7, the pits formed on the salt spray surfaces are deeper than the pits on the immersion surfaces. For both environments, AM60 had the largest pit depth, followed by all three extruded surfaces. In the immersion environment, the pit depths all experienced a decrease compared with the initial pit depth. This demonstrates that at some point, which was different for each alloy, the rate of general corrosion overtook the rate of pitting corrosion. On the other hand, in the salt spray environment, the pit depths all increased, except for AE44. This indicates that the rate of general corrosion never equaled the rate of pitting corrosion. The differences in the rate of general corrosion versus the rate of pitting corrosion are directly attributed to the presence, or absence, of a continuous

water supply. In the immersion environment, general corrosion was able to remove the magnesium surrounding the pits, thereby reducing the pit depth because the water was continuously reacting with the surface. In the salt spray environment, though, general corrosion was never able to become fully established, as the drying phase prevented a reaction between water and the magnesium surface. However, the drying phase also trapped chloride ions within the pits, thereby allowing the pits to increase in depth. No trends could be determined with regards to the percentage of aluminum or the secondary alloying elements. In addition, there were no definitive trends in regards to the forming method. All of the extruded surfaces experienced higher pit depths in the salt spray environments than the as-cast surfaces, except for AM60. It does appear that the as-cast skin was able to prevent some pit growth into the magnesium, except for AM60. The AM60 as-cast surface did have a higher pit depth than all of the other surfaces, indicating that manganese may play a role in pit growth. Overall, the environment played a greater role in pit depth than the alloying elements or the forming method, although both additional variables did somewhat influence pit depth.

Pit Coalescence

Pit coalescence is the joining of neighboring pits that acts to reduce the number of pits. Pit coalescence is shown by the nearest neighbor distance. When the nearest neighbor distance decreases, this indicates that the pits are growing closer to each other, but have not begun to coalesce. When the nearest neighbor distance increases, this indicates that the pits have coalesced and the distance between the remaining pits is now larger. When examining Figure 4.8, both environments had similar rates of pit coalescence and there were no distinct trends based on alloying elements or forming method. There was a greater spread in the nearest neighbor distances on the salt spray environment for most of the alloys. This indicates that general corrosion did not influence the pit coalescence much in the salt spray environment, while it did greatly influence the pit coalescence in the immersion environment. In the immersion environment, general corrosion would remove the small pits and reduce the pit growth, thereby reducing the ability of the pits to coalesce. In the salt spray environment, because general corrosion was not a significant factor, the pits would increase in size and eventually coalesce. The drastic changes in the nearest neighbor distance show that the pits were growing and were coalescing throughout the experimentation time. Overall, pit coalescence was more influenced by the environment than the alloying elements or the forming method.

Intergranular Corrosion

Intergranular corrosion is the corrosion that occurs specifically along the grain boundaries. When examining Figure 4.9, the salt spray surfaces had slightly higher amount of intergranular corrosion than the immersion surfaces. However, there were no trends with regards to the alloying elements or the forming method. This indicates that general corrosion was affecting the formation of intergranular corrosion more than the other variables, caused by the environment. As with general corrosion, pit nucleation, pit growth, and pit coalescence, the differences between the two environments are because of the continuous presence of water. When the water is constantly present, microgalvanic cells can form between the grain boundaries and the grains, leading to intergranular corrosion. In the salt spray environment, these microgalvanic cells are stopped during the drying phase, meaning less intergranular corrosion can occur. Overall, intergranular corrosion was more influenced by the environment than the alloying elements or the forming method.

Conclusions

To summarize the modeling part, if one is trying to bridge different length scales for analysis of plasticity, damage, fracture, or fatigue, one must be able to run atomistic simulations in which the dislocation behavior is appropriate. We show in this work that the standard procedure of using just the elastic modulus and cohesive energy is really not robust enough to capture the appropriate dislocation behavior. As such, optimizing both the MEAM potential to the generalized stacking fault (GSF) energy curve and the Peierls stress is the key as illustrated in this report. In the absence of experimental data, one

can use *ab initio* modeling results to complete the material database. In this writing, the improved magnesium MEAM model was correlated with both experiments and *ab initio* results. Physical properties such as the lattice parameter, the vacancy formation energy, the GSF energy curves for basal slip, and mechanical properties such as elastic constants and Peierls stress for basal slip were all well captured.

To summarize the experimentation part, the environment and surface reactions have more of an effect on general corrosion and intergranular corrosion than the alloying elements or the forming method. The continuous presence of water in the immersion environment was able to dissolve the magnesium surface and cause microgalvanic cells to form, while the drying phase in the salt spray environment stopped both. For pit nucleation, the three major contributors (environment, alloying elements, forming method) all appear to interact, with no variable being more influential than the others in allowing pit nucleation to occur. For the two-dimension pit growth, the alloying elements, specifically the percentage of aluminum, does appear to have more of an effect on pit growth than the environment or forming method. The 3% aluminum surfaces experienced higher pit growth, likely because there was not enough aluminum to increase the corrosion resistance. The environment has more of an effect on the third dimension of pit growth, although the alloying elements and forming method do appear to slightly contribute to pit depth. General corrosion was able to reduce the pit depth in the immersion environment, while the trapped chloride ions were able to increase the pit depth in the salt spray environment. Pitting coalescence was also more affected by environment than the alloying elements and the forming method. General corrosion was able to reduce the number of pits and the growth of the pits on the immersion surfaces, thereby reducing the pit coalescence. Because general corrosion was not significant on the salt spray surfaces, the number of pits and the pit growth were able to demonstrate pit coalescence.

Publications

1. Groh S, Marin EB, Horstemeyer MF. "Nanoscale void growth in magnesium: A molecular dynamics study." Int J Appl Mech. 2 (2010) 191-205.
2. Martin HJ, Horstemeyer MF, Wang PT. "Effects of salt-spray, humidity, and drying on an as-cast AE44 magnesium alloy." Int J Corro. 2010 (2010) 1-10 doi: 10.1155/2010/602342.
3. Martin HJ, Horstemeyer MF, Wang PT. "Comparison of Corrosion Pitting Under Immersion and Salt-Spray Environments on an As-Cast AE44 Magnesium Alloy." Corros Sci. 52 (2010) 3624-3638.
4. Alvarez RB, Martin HJ, Horstemeyer MF, Chandler MQ, Williams N, Wang PT, and Ruiz A. "Structure-property corrosion relationships of a structural AE44 magnesium alloy." Corros Sci. 52 (2010) 1635-1648.
5. Martin HJ, Horstemeyer MF, Wang PT. "Structure-Property Quantification of Corrosion Pitting Under Immersion and Salt-Spray Environments on an Extruded AZ61 Magnesium Alloy." Corros Sci. 53 (2011) 1348-1361.
6. Walton C, Martin HJ, Horstemeyer MF, Wang PT. "Structure-Property Quantification of Corrosion Pitting Under Immersion and Salt-Spray Environments on an Extruded AZ31 Magnesium Alloy." Corros. Sci., In Press.
7. Martin HJ, Alvarez RB, Danzy J, Horstemeyer MF, Wang PT. "Structure-Property Quantification of Corrosion Pitting Under Immersion and Salt-Spray Environments on an As-Cast AM60 Magnesium Alloy." Invited *NACE-Corrosion* Special Edition, In Review.
8. Song W, Martin HJ, Hicks A, Horstemeyer MF, Wang PT. "Structure-Property Quantification of Corrosion Pitting Under Immersion and Salt-Spray Environments on an Extruded AM30 Magnesium Alloy." In Preparation.

9. Martin HJ, Walton C, Danzy J, Horstemeyer MF, Wang PT. "Structure-Property Quantification of Corrosion Pitting Under Immersion and Salt-Spray Environments on an As-Cast AZ91 Magnesium Alloy." In Preparation.

Presentations

1. Groh S, Marin EB, Horstemeyer MF, and Zbib HM. "Multiscale modeling of the plasticity in an aluminum single crystal" USNCCM09; Columbus, OH; 2009 July.
2. Martin HJ, Horstemeyer MF, Wang PT. "Corrosion mechanisms occurring on AE44 Mg exposed to a 3.5% NaCl Aqueous Solution: Experimental effects." 2009 American Institute of Chemical Engineers Annual Meeting; Nashville, TN; 2009 November.
3. Martin HJ, Horstemeyer MF, Wang PT. "Corrosion mechanisms occurring on AM60 Mg exposed to a 3.5% NaCl Aqueous Solution: Experimental effects." 2009 American Institute of Chemical Engineers Annual Meeting; Nashville, TN; 2009 November.
4. Martin HJ, Horstemeyer MF, Wang PT. "Pit nucleation, growth, and coalescence: Modeling the corrosive effects of Mg exposed to a 3.5% NaCl aqueous solution." 2009 American Institute of Chemical Engineers Annual Meeting; Nashville, TN; 2009 November.
5. Martin HJ, Walton C, Danzy J, Horstemeyer MF, Wang PT, "Comparing Corrosion Mechanisms on Extruded AZ61 and AZ31 exposed to Immersion and Salt Spray Environments," 2010 American Institute of Chemical Engineers Annual Meeting; Salt Lake City, UT; 2010 November.
6. Martin HJ, Walton C, Danzy J, Hicks A, Horstemeyer MF, Wang PT, "Modeling the Corrosive Effects of Various Magnesium Alloys Exposed to Two Saltwater Environments," 2010 American Institute of Chemical Engineers Annual Meeting; Salt Lake City, UT; 2010 November.
7. Martin HJ, Danzy J, Horstemeyer MF, Wang PT, "Comparing the Corrosion Effects of Two Environments on As-Cast AM60 and AZ91," 2010 American Institute of Chemical Engineers Annual Meeting; Salt Lake City, UT; 2010 November.
8. Martin HJ, Walton C, Danzy J, Hicks A, Horstemeyer MF, Wang PT, "Modeling the Corrosive Effects of Various Magnesium Alloys Exposed to Two Saltwater Environments," 2011 The Minerals, Metals, and Materials Society Annual Meeting; San Diego, CA; 2011 February.
9. Martin HJ, Walton C, Danzy J, Hicks A, Horstemeyer MF, Wang PT, "Comparing the Corrosion Effects of Two Environments on As-Cast and Extruded Magnesium Alloys," 2011 The Minerals, Metals, and Materials Society Annual Meeting; San Diego, CA; 2011 February.
10. Walton C, Martin HJ, Danzy J, Hicks A, Horstemeyer MF, Wang PT, "Comparing the Corrosion Effects of Environment and Form on Various Magnesium Alloys," 2011 American Institute of Chemical Engineers Annual Meeting; Minneapolis, MN; 2011 October.
11. Martin HJ, Walton C, Danzy J, Hicks A, Horstemeyer MF, Wang PT, "Modeling Individual and Bulk Pit Characteristics on Various Magnesium Alloys Exposed to Two Saltwater Environments," 2011 American Institute of Chemical Engineers Annual Meeting; Minneapolis, MN; 2011 October.

References

Alvarez RB, Martin HJ, Horstemeyer MF, Chandler MQ, Williams TN, Wang PT, Ruiz A. 2010. Corros Sci. 52: 1635-48.

Bakkle P, Westengen H. 2005. "The role of rare elements in structure and property control of magnesium die casting alloy. In: Neelameggham NR, Kaplan HI, Powell BR (Eds.), TMS – Magnesium Technology, 291-96.

Baskes MI, Johnson RA. 1994. Modelling Simul Mater Sci Eng. 2:147-63.

Conrad H, Robertson WD. 1957. TMS-AIME 209:503-12.
Datta A, Waghmare UV, Ramamurty U. 2008. Acta Mater 56:2531-39.
Fontana MG, Corrosion Principles, in: M.G. Fontana (Eds.), Corrosion Engineering, McGraw-Hill, Boston, 1986, pp. 12-38.
Groh S, Marin EB, Horstemeyer MF, and Bammann DJ. 2009. Modell Simul Mater Sci Eng 17: 075009.
Hirth JP, Lothe J. 1992. Theory of dislocations. Malabar(FL): Krieger Publishing Company.
Liu XY, Adams JB, Ercolessi F, and Moriarty JA. 1996. Modelling Simul Mater Sci Eng. 4:293-303.
Makar GL, Kruger J. 1993. Int Mater Rev 38:138-53.
Martin HJ, Horstemeyer MF, Wang PT. 2010. Inter J Corros. 2010: 1-10 doi: 10.1155/2010/602342.
Shaw BA. 2003. "Corrosion resistance of magnesium alloys. In: Korb LJ, ASM, eds., ASM Handbook, Vol. 13A: Corrosion, Ninth Ed., ASM International Handbook Committee, Metals Park, 692.
Song G, Atrens A. 2003. Adv Eng Mater 5:837-58.
Sun DY, Mendelev MI, Becker CA, et al. 2006. Phys Rev B 73:024116.
Swygenhoven HV, Derlet PM, Frøseth AG. 2004. Nature Mat 3:399-403.
Yasi JA, Nogaret T, Trinkle DR, Qi Y, Hector LG, and Curtin, WA. 2009. Modell Simul Mater Sci Eng 17:055012.

Key Words

Magnesium alloys; pitting; salt spray test; interatomic potential; dislocation.

Brief Description of Report

Understanding the corrosion of magnesium is very important if the use of Mg alloys as a lightweight solution in automobiles is to be accomplished. Corrosion mechanisms, such as pitting, intergranular corrosion, and general corrosion weaken the surface of magnesium alloys, while hydrogen produced during the corrosion processes can weaken the internal structure of the alloys. This report shows that the environment to which the magnesium alloys is exposed is the most influential part of general corrosion, intergranular corrosion, and pit coalescence. Pit nucleation is affected by the environment, the alloying elements, and the forming method equally, while pit growth is more affected by the alloying elements and the environment, with the forming method playing a small role. Examining the corrosion mechanisms experimentally and developing models that explain both the surface corrosion and the internal hydrogen effects on magnesium alloys are essential in determining ways to improve the lifespan of these magnesium alloys when exposed to the atmosphere.

Southern Regional Center for Lightweight Innovative Design

Phase III

Final Scientific & Technical Report

October 1, 2009-September 30, 2011

For compliance with contract requirements of Award DE-EE0002323

Task 5

HIGH RATE DAMAGE AND FRACTURE, EXPERIMENTATION, SIMULATION AND VISUALIZATION

Submitted December 27, 2011

TASK 5: HIGH RATE DAMAGE AND FRACTURE, EXPERIMENTATION, SIMULATION AND VISUALIZATION

Table of Contents

TASK 5: HIGH RATE DAMAGE AND FRACTURE, EXPERIMENTATION, SIMULATION AND VISUALIZATION

Principal Investigator: Philip Gullett
Assistant Professor, Civil and Environmental Engineering
Mississippi State University
Walker Engineering Bldg., Rm. 235 M, Mississippi State, MS 39762
(662) 325-5486; fax: (662) 325-7189; e-mail: pmgullett@engr.msstate.edu

Participants: M.F. Horstemeyer, , D.B. Hardin, T.N. Williams, S. Simunovic (ORNL)

William Joost: Technology Area Development Manager
e-mail: william.joost@ee.doe.gov

Magda Rivera: Project Manager
e-mail: magda.rivera@netl.doe.gov

Contractor: *Mississippi State University (MSST)*
Contract No.: *DE-EE0002323*

Objective

- Evaluate the strain rate failure of magnesium (Mg) for various stress states.
- Develop a damage model for stress-state dependence of dynamic damage evolution.
- Evaluate numerical procedures for the modeling of monotonic fracture of Mg.

Approach

- Characterize material behavior using Split Hopkinson Bar experiments in compression, tension, and torsion.
- Characterize damage nucleation using molecular dynamics.
- Develop damage evolution based fracture criteria.

Accomplishments

- Examined high strain-rate compression, and associated metallurgical evaluation of cast Mg alloys using a variety of casting methods.
- Evaluated the effects of heat treatment.
- Implemented the multi-scale Mississippi State (MSST) material model into a fracture simulation code.
- Compared the MSST material model simulations to experimental test results showing that the modeling approach is capable of predicting actual damage evolution.
- Initial damage distribution is critical for accurate prediction of failure loads.

Introduction

This report summarizes the state of the experimental and numerical simulation study of failure mechanisms in magnesium alloys. The aim is an enhanced, multiscale microstructure-

property model that can be implemented into commercial codes and that can be used in high-fidelity crash simulations for the design and optimization of structural Mg components.

One of the design aspects integral to the development of highly fuel-efficient vehicles is the reduction of overall vehicle weight. Mg has become a central focus in this effort due to its high strength-to-weight ratio, castablility, machinability, and damping. On a component basis, Mg can potentially result in 30 to 75% weight savings over conventional iron-, steel-, aluminum-, and plastic- based designs (Osborn (2005)).

The mechanical performance of structural components under service loads is well understood, as component design is based on well-established principles of linear elastic solid mechanics. Under safety-critical, extreme loading conditions such as crash, the mechanical behavior depends on a complex relationship between component geometry, loading, and material microstructure. In particular, component failure is controlled by microstructural (or smaller scale) phenomena that vary according to deformation history, temperature, strain rate, and stress state.

The DOE and the United States Council for Automotive Research's (USCAR's) United States Automotive Materials Partnership (USAMP) funded the Structural Cast Magnesium Development (SCMD) project, a broad, multi-faceted effort to address concerns related to the use of structural Mg. One outcome of the SCMD project was the effort led by Horstemeyer et al. (Horstemeyer, Oglesby et al. (2007)) to develop a microstructure-property model that included microstructural details that act as the source of damage progression. Horstemeyer's work included detailed multiscale analysis and model development for several Mg alloys targeted for application in structural automotive components.

This current effort attempts to build on the experimental and computational work of Horstemeyer et al. (Horstemeyer, Oglesby et al. (2007)) by extending the investigation of dynamic failure mechanisms and energy-absorption characteristics of Mg through experiment and simulation, as well as provide experimental data for additional Mg alloys.

Strain Rate Response of Cast Magnesium Components

The strain rate sensitivity of cast AZ91 magnesium automotive control arms produced using four different casting processes was examined. The casting processes included squeeze casting, low pressure permanent mold (LPPM), ablation and T-Mag processes. The compressive stress-strain behavior of specimens was evaluated at quasi-static and high strain rates. All of the specimens were tested to fracture. The specimens were obtained from as-received control arms and extracted from the region indicated by Figure 1.

Tests under quasi-static conditions were performed using an Instron 5882 electromechanical machine under constant strain rate controlled at 0.001/s. The high strain rate tests were conducted using a maraging steel Split Hopkinson Pressure Bar (SHPB) apparatus. The analysis of the high strain rate data was conducted using the DAVID software package (Gary (2005)).

Location of test specimens

Figure 1: Cast magnesium automotive control arm. Control arms were cast from AZ91 and AM60B alloys. Specimens taken from the rib section indicated by the dashed line were tested under high rate loading conditions**.**

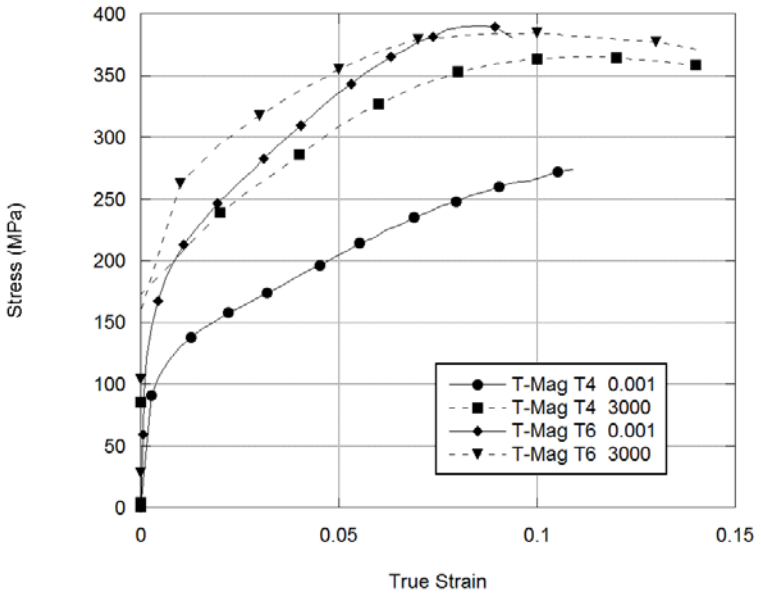

Figure 2: The stress strain response of AZ91 comparing two heat treatments for quasi-static and 3000/sec strain rates. The heat treatment has a pronounced effect at low rates

Figure 2 compares the stress strain response of AZ91 comparing T-Mag castings with two heat treatments. The T6 temper resulted in pronounced increase in quasi-static yield as well as hardening rate. At high rates of loading the T6 temper resulted an increased yield, however the increase was less pronounced than in the quasi-static case. At high rates there was no significant increase in hardening.

Figure 3 shows the results of tests performed at quasi-static (10-3/s) rates while Figure 4 shows the results at strain rates (1000/s – 3000/s). At this rate the observed yield strengths varied from 90 to 110 MPa, with the T-Mag process having the lowest yield strength and squeeze cast the highest. As strain rates increased (Figure 4) all processes exhibited an increase in yield and ultimate strength with an increase in strain rate. The T-Mag in the T-6 condition exhibited the highest yield strength in all cases yet appeared to soften much sooner than the all other cases as compared to their respective strain rates. The Squeeze Cast control arm had the second highest yield strength in all cases and had the highest ultimate strength at 3000/s strain rate. The yield strength of all castings at high strain rates varied between 150MPa to 300MPa while the ultimate strength narrowed the gap to between 365MPa to 410MPa. The dynamic yield and ultimate strengths for set of tests are tabulated in Table 1. The T-6 condition appeared to produce a more robust compressive response for the T-Mag casting process than the T-4 condition.

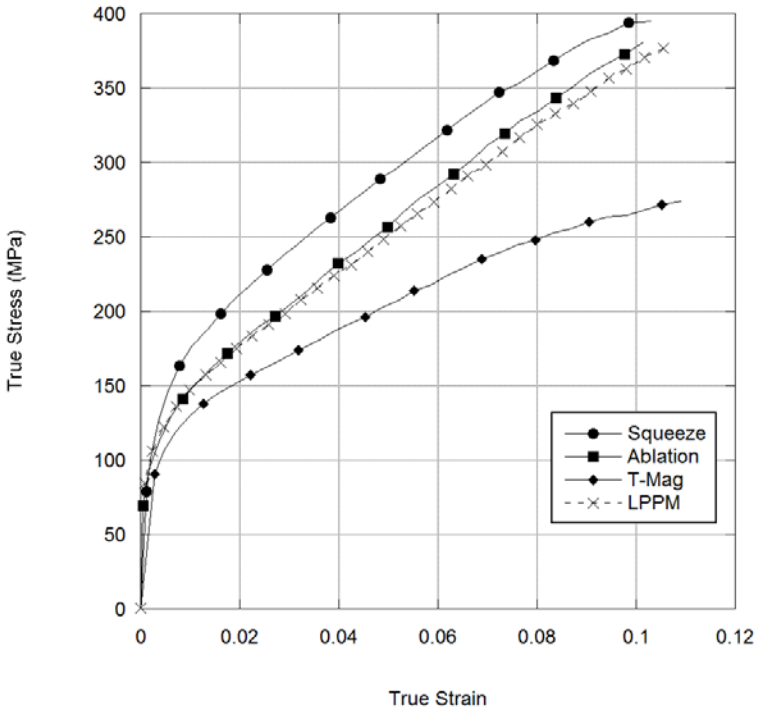

Figure 3: The quasi-static compressive response of AZ91 specimens produced using 4 different casting processes.

Macroscale Fracture & Modeling

For porous materials, the initiation and growth of facture is heavily influenced by the presence of porosity Figure 5. While there are many methods used to predict fracture, very few, however, tie measurable material parameters the physical processes that control ductile crack growth. The approach taken here utilizes a finite-element framework (Rashid (1997); Rashid (1998)) capable of incorporating material-specific ductile fracture mechanisms into the failure model and that is independent of mesh topology. Figure 5 shows an example simulation of fracture of a magnesium alloy AM60 specimen under tensile loading. The initial set-up and of a crack tip patch are shown. The patch moves with the crack tip and allows the predicted path to follow a mesh independant tragectory.

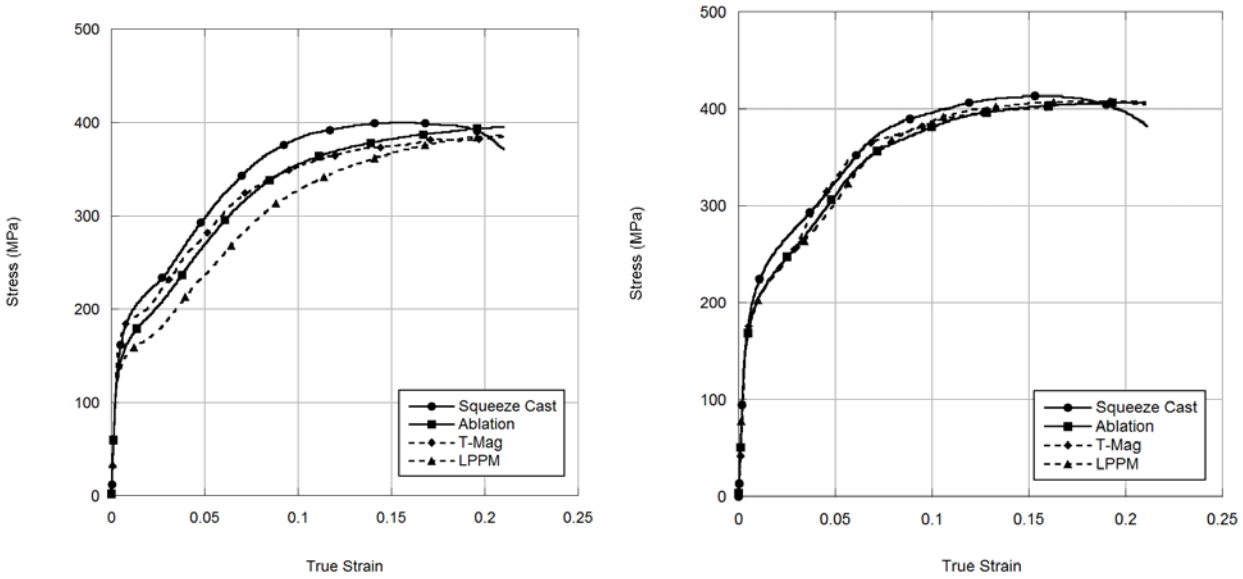

Figure 4: The compressive response of AZ91 specimens produced using 4 different casting processes were tested using the Split Hopkinson Pressure Bar. The compressive response for is shown for strain rates of 1000/sec (left) and 3000/sec (right).

Table 1: Comparison of compressive properties for cast magnesium samples

Process	Yield Strength (MPA@2%)		Ultimate Strength (Mpa)		Fracture Strain (%)	
	1000/s	**3000/s**	**1000/s**	**3000/s**	**1000/s**	**3000/s**
Squeeze Cast	220	265	400	411	21.0	22.5
Ablation	190	235	395	400	23.4	29.5
LPPM	160	235	385	405	23.4	30.0
T-Mag	235	305	365	381	20.0	23.0

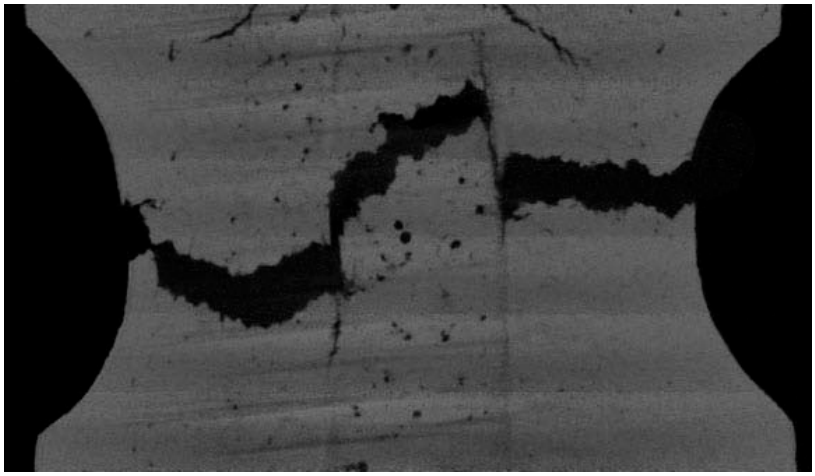

Figure 5: The crack path in this magnesium specimen is heavily influenced by the presence of porosity.

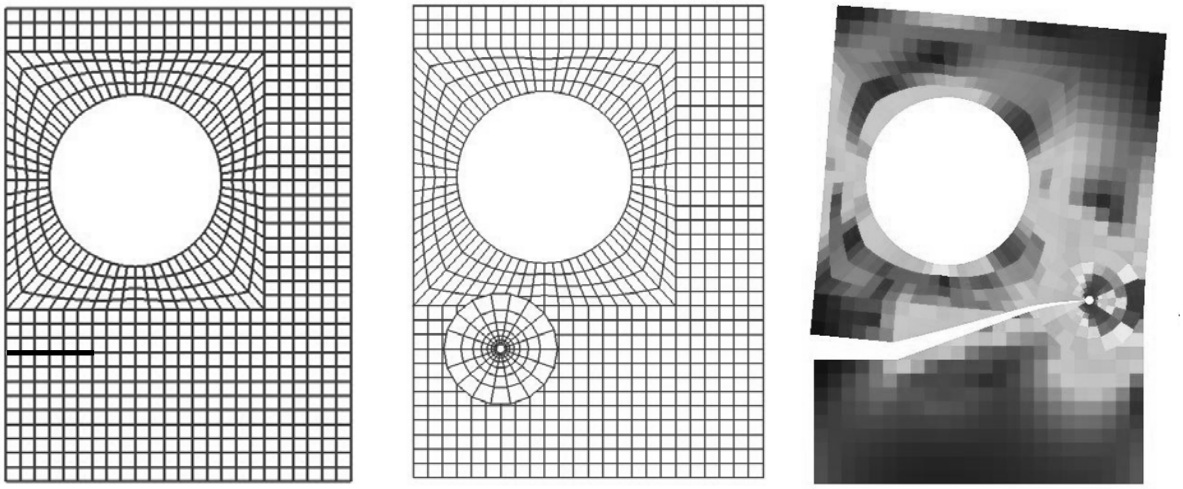

Figure 6: The dark line in the specimen on the left is the initial crack. The middle image shows the patch mesh at the crack tip. The right image shows the predicted, mesh independant path.

Damage nucleation and evolution is predicted using the Mississippi State University Microstructure-Property Model (Bammann, Chiesa et al. (1993); Horstemeyer (1995); Horstemeyer and Gokhale (1999)). The model incorporates nonlinear isotropic and kinematic hardening, temperature, damage, and rate dependence of the material. Because of material model incorporates damage, the crack advance should take into account the damage present. In the current effort, damage was used to define a crack advancement criterion and normal opening force for crack advance direction. The formulation was tested using a Mode-I fracture simulation Figure 6. The results show that the predicted crack path matches the theoretical (straight ahead), while the J2 based damage evolved perpendicular to the crack path prior to crack growth. A mixed-mode loading was also examined Figure 7. The simulation showed that the crack path forumulation predicted the crack kinking. In addition the J2 based damage evolution prior to crack advance is accumulating where the kink will occur, and not in the direction the crack will grow as shown in Figure 7.

Damage Modeling

Finite element simulations are used to study the microstructure-mechanical property model with experimental damage evolution in a monotonically loaded cast magnesium notch tension specimen. Damage progression from growth and coalescence in AM60B magnesium notch specimens was determined from a combination of experiments, finite element simulations, and nondestructive analysis. Experiments were preformed on notch tension specimens to failure, other specimens were loaded to 60, 87, 93, and 95-97% of the predetermined average failure load. Finite element simulations of the notch tests were preformed utilizing the microstructure-property model that incorporated the pertinent initial porosity volume fraction and distribution.

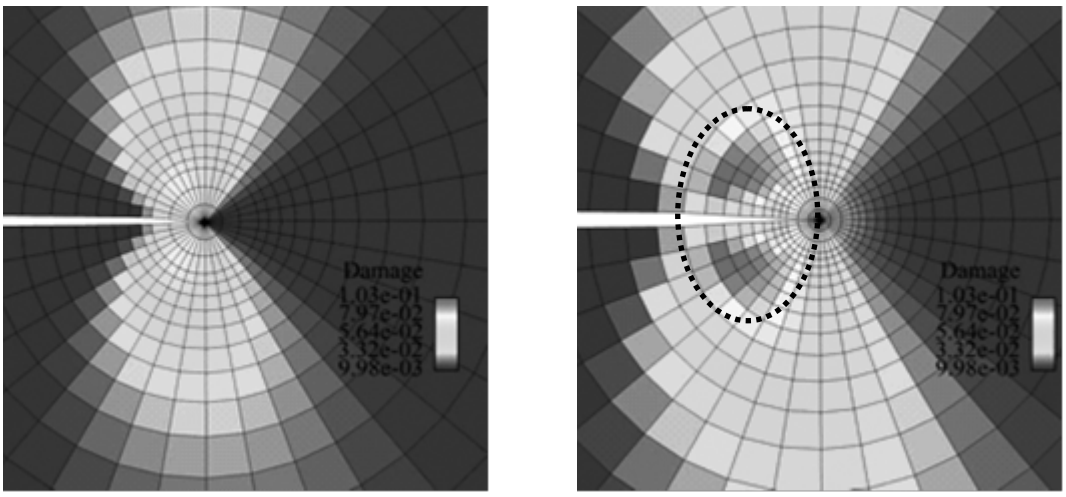

a b

Figure 6: (a) Mode-I damage field prior to crack advance the light area in this image is the region of increasing J2 damage. (b) The dark area in the dashed line is the region of highest J2 damage evolution after Mode-I crack advance.

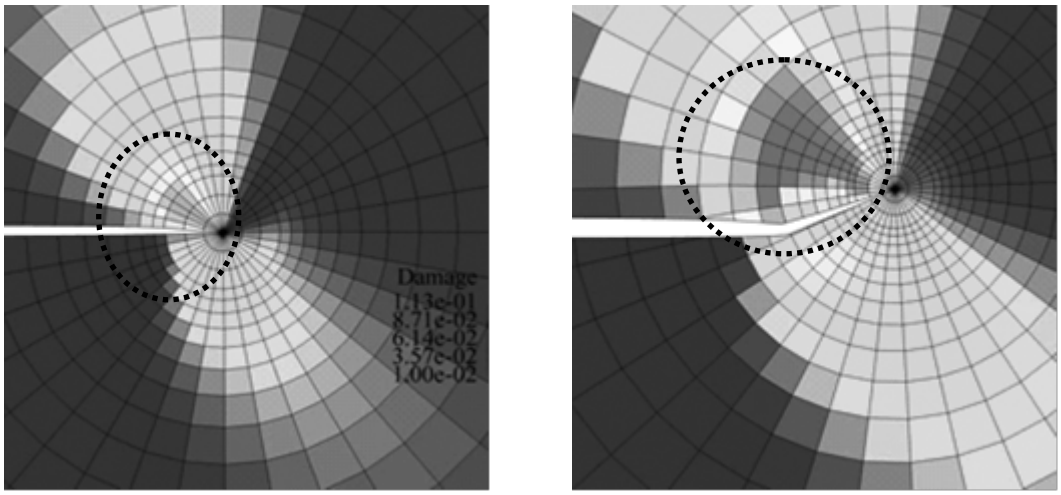

a b

Figure 7: (a) Mixed-mode damage field prior to crack advance. (b) Mixed-mode damage field after crack has advance.

Notch Experiments

Previous work evaluated by Waters 2000, examined the behavior of Nine die cast AM60B magnesium alloy notched Bridgman tensile bars were obtained from the Institute of Magnesium Technology in Quebec, Canada. A picture of tensile bars with three notch geometries is shown in Figure 8. The AM60B magnesium alloy composition of the tensile bars is 5.67% Al, 0.377% Mn, 0.15% Zn, 0.013% Si, 0.0011% Fe, <0.0035% Cu, <0.0001% Ni, <0.0033% with remainder Mg. The specimens used in the study were cold chamber die cast with an injection temperature of 675-670 ºC, metal temperature of 750 ºC, and a die temperature of 300 ºC. The shot weight

was 1.63 kg, the shot sleeve diameter was 3.81 cm, with a shot stroke of 29.21 cm. The average gate velocity was 41.15 m/s, with an average cycle time of 45 seconds.

Figure 8: Three magnesium AM60B notched Bridgman tensile bars, one each from three notch geometries. Top: Series H, notch radius is 0.635 cm. Middle: Series G, notch radius is 0.794 cm. Bottom: Series F, notch radius is 1.27 cm. Total length of tensile bars is 11.4 cm, with an outer diameter (excluding threads) of 1.265 cm.

The average mechanical failure loads and stress strain behavior for each of the three notch geometries using tensile bars from a larger set of 25 specimens. The results are shown in Table 6.3. The average ultimate tensile strengths, UTS, for the notch geometries were determined and are presented along with calculated percentages of average failure loads in Table 6.4. From the average values of ultimate tensile strength, percentages of failure loads were determined and selected for analysis. The percentages selected for analysis were 60, 87, 93, and 95-97% of the predetermined average failure load.

Table 2: Average notch specimen material properties for Series H

Tensile strength	Yield strength	Elongation to failure	Elastic Modulus	Poisson's ratio	Density g / mm^3	UTS
220 MPa	130 MPa	6%	45 GPa	0.35	0.0018	241 MPa

Table 3: Average ultimate tensile strengths and percentages of average failure load for each notch geometry as determined experimentally by Westmoreland Mechanical Testing and Research Laboratory.

Sample	σ_{UTS} (MPa)	60% load (N)	87% load (N)	93% load (N)	95% load (N)
F	241	9879	14327	15314	15642
G	221	9283	13460	14389	14698
H	207	9176	13304	14225	14529

After the tensile bars were initially scanned in their unloaded states using CT, tensile bars were uniaxially loaded at Sandia National Laboratories, Livermore, California using a 50 kip MTS machine. The samples were load controlled, with a strain rate of 5 x 10-4 cm/sec, and loaded up to the percentages of the previously determined average failure load. Selected samples were removed from the MTS after each loading and scanned using CT, then reloaded to the next selected percentage. Finally, the samples were loaded to failure and rescanned. A representative load-displacement curve for the series H tensile bars loaded to 60% of average failure load is presented in Figure 9.

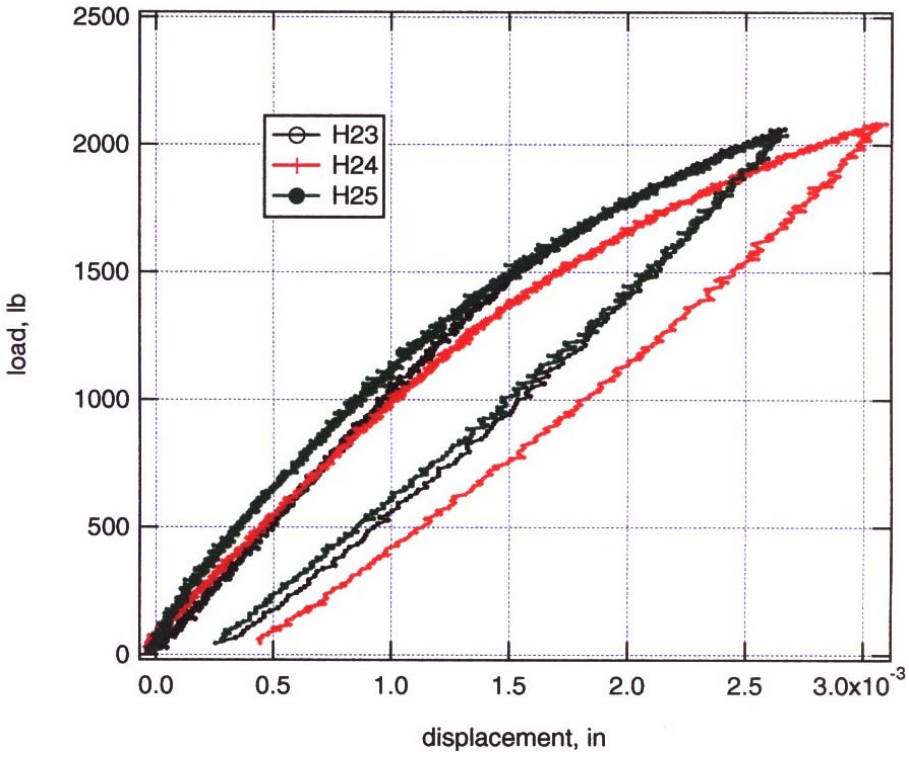

Figure 9: Load displacement curves for Series H tensile bars, loaded to 60% of their average failure load.

Computed Tomography

Computed tomography (CT) is a nondestructive testing (NDT) technique that allows collection of data about internal material damage progression prior to failure. Figure 10 shows an example of initial pre-loading CT scans that were performed on test specimens using third-generation, cone beam geometry KCAT and PCAT CT systems at Lawrence Livermore National Laboratory (described in detail in Waters, 2001). Later CT imaging was performed using the Stanford Synchotron Radiation Laboratory's X-ray tomographic microscope (XTM) in Palo Alto, California, which became available only after specimens had been loaded to 60% of the pre-determined failure load. The data presented in later sections of this report was obtained using the XTM, which is a high spatial resolution, third generation CT system. The radiation source was the 31 pole, X-ray wiggler beamline 10-2 with beamline energy of 25 kV. Tensile bar specimens were mechanically rotated on a stage in front of an X-ray scintillating CdWO4 single crystal of dimensions 25 by 25 by 0.7 mm. This scintillator was optically coupled to a 12-bit CCD camera, with a resulting pixel size of 0.024 mm. For each CT scan, approximately 1000 by 80 pixels in size, 360 projections were acquired over 180 degrees. The XTM uses a parallel

beam geometry X-ray source and has a rectangular field of view of limited height; this limitation made it necessary to obtain multiple CT scans for each test specimen by vertically translating the specimen between scans. This made it possible to obtain CT data over the entire notch region of each specimen. Due to a low signal-to-noise ratio and the lack of beam hardening artifacts in the XTM data, relatively little image pre-processing was required. XTM data from one set of tensile bars, series H with the smallest (6.3 mm) notch radius, was selected for further analysis.

Several data reduction steps were necessary to prepare the raw XTM CT data for inclusion in finite element simulations. The first step was to segment the voids from the dense AM60B material in the CT data volums. The VIEW image processing program was initially used to eliminate any negative values on each CT slice image by applying a threshold of zero to the image, and then user-specified values were utilized in constructing and smoothing tensile bar edges on the image. The slices were stacked to create a 3D volume of binary data representing the tensile bar specimen (excluding voids). Next, the IDL software package was used to build this data into a three-dimensional array, which was then inverted so that dense material appeared to have attenuation values near zero and voids appeared to have attenuation values near the maximum.

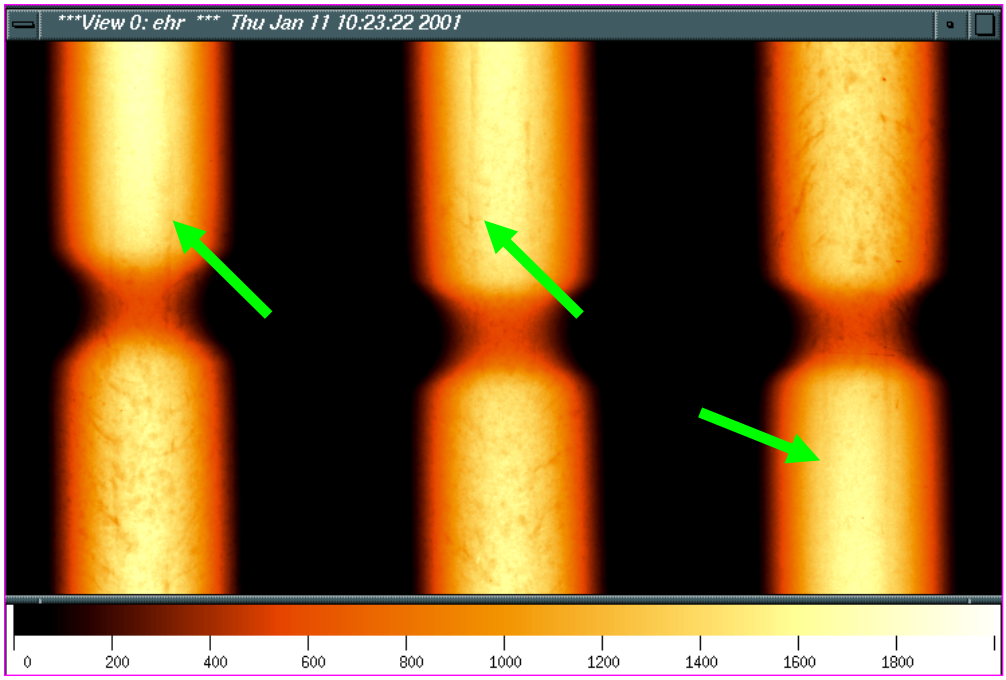

Figure 10: Digitized radiograph of series H tensile bars. Darker areas represent areas of lower density; arrows indicate locations of the flow lines.

Once the data was masked and inverted, a histogram was generated and used to select a minimum threshold value for voids; any value above this threshold was interpreted as a void. After the threshold was applied to the data set, the IDL software was used to apply a cluster analysis routine that identified and labeled unique clusters of void-valued voxels. Any connected void-valued voxels were identified as a single void, and only voids containing more than 100 connected voxels were selected for further analysis. This corresponds to a minimum void

volume of 1.33x 10-3 mm3 and is used to minimize false void detection due to system noise or other errors.

Next, the spatial distribution of void volume fraction (which is average void volume times void density) was calculated. Another IDL routine was used to calculate the total void volume fraction in a series of annuli of increasing diameter at a location on the z-axis. The same routine was applied for different z-axis locations until the entire tensile bar notch region had been analyzed. This data was then used mapped to various finite element discritizations of the notch specimen using a moving least-squares minimization technique.

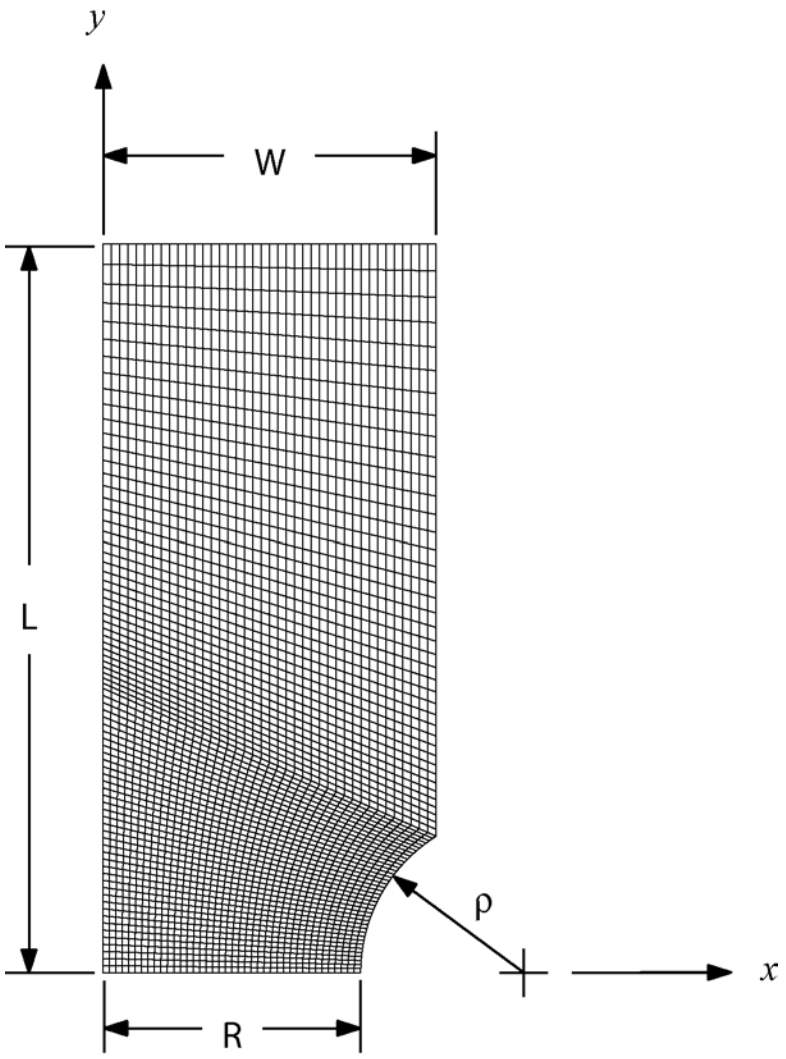

Figure 11: The finite element mesh used to model the test containing 3,200 quadrilateral elements. Element aspect ratios are near the 1:1.

Finite Element Set-up

The cylindrical notch tensile specimen was geometrically represented by a quarter-space, axially symmetric model. The analysis was performed with ABAQUS software and utilized reduced integration, four-node, axisymmetric quadrilateral elements. Meshes of several

resolutions were used in these simulations. The medium resolution mesh is shown in Figure 11. Boundary conditions included uniform quasi-static axial extension of 0.005 mm/sec along the top edge, symmetry along the specimen axis and bottom edge, and a traction free surface on the notch edge. The mesh length was $L = 14mm$, and width, $w = 6.4mm$. The analysis in this report is limited to simulation of H series tensile specimens with $\rho = 3.05\,mm$.

In order to have confidence that the simulation will be correctly predicting the material response on the scale of the entire notched Bridgman tensile specimens, simulations were run to ensure that the model would capture the stress versus strain response of the real material as well as adequately predict the evolution of damage in the material. Figure 12 compares a quasi-static simulation to published experimental data (Horstemeyer et al. 2007) for the constants used in this study. This figure shows a very good correlation between the mechanical response of the simulation and that of the real material. The material constants used in this study were calibrated in Horstemeyer et al. (2007)

The spatial distribution of void volume fraction was determined for specimen H24 which yielded average void volume fractions collocated to a grid of points within the tensile bar region. This data was used to initialize the material property damage parameter on a per element basis for the finite element mesh. The collocated void volume fraction data was mapped to the finite element integration points using a moving least-squares (MLS) surface construction technique. The MLS has a well-developed theoretical basis and has been used in areas ranging from surface generation and contour construction to Galerkin approximations of partial differential equations. With this approach, the value of damage at element integration points is established using a low degree polynomial that best fits the data near the point of interest. The right hand side of Figure 13 shows a scan of the initial element porosities from the data mapping. The chief characteristics of the porosity include a single large pore in the upper left of the specimen, and distinct flow line. The flow line is a cylindrical band of porosity running along the axis, and is presence was characteristic of these samples as shown in Figure 13.

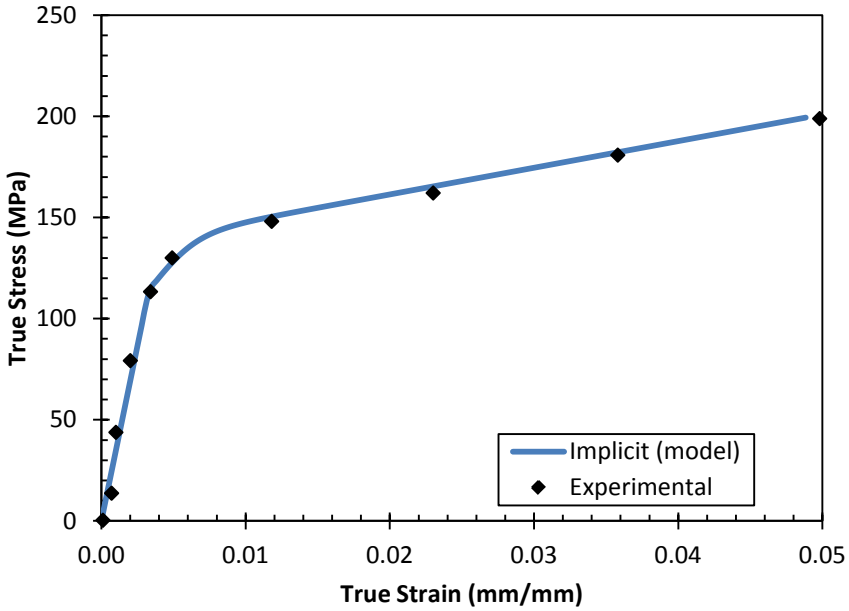

Figure 12: Experimental and simulated load displacement curves.

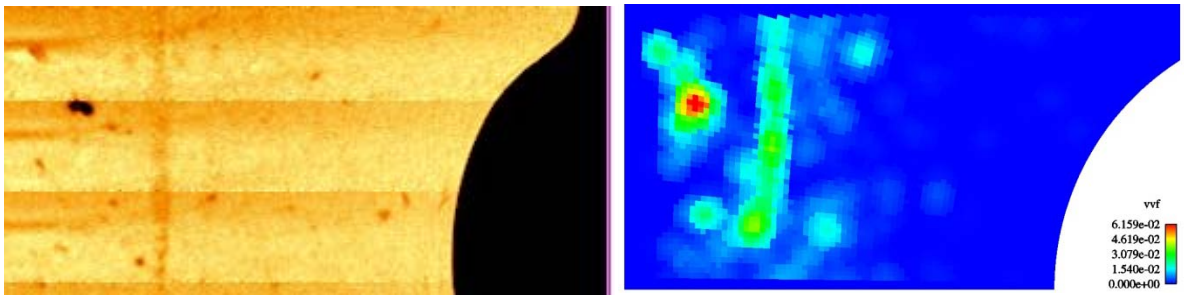

Figure 13: CT porosity data from tensile bar H24 on the left are compared to the initial porosity levels (vvf) in finite element mesh on the right.

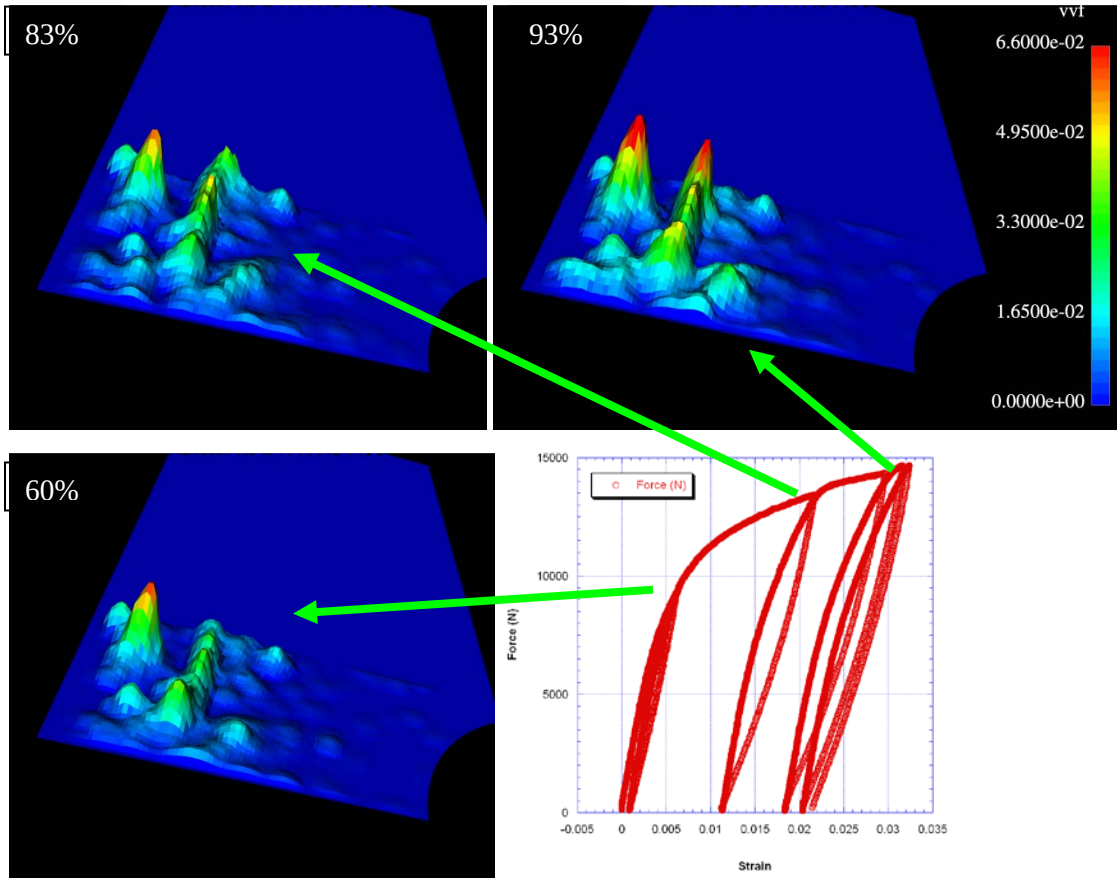

Figure 14: Void volume fraction data derived from CT scans of specimen H24. Contours show void volume fraction at 60, 83, and 93% of average failure.

Comparison of Model Simulations and Experimental Data

Stress triaxiality is the primary driving factor for void growth in porous materials. In a uniform material, the notch geometry induces a smooth stress triaxiality field with a maximum value near the center of the specimen. In a porous or damaged material, stress concentrations induced by the presence of pores, may cause local regions of high stress triaxiality. As a result, void growth occurs where the combined damage and stress triaxiality synergize. The simulations

as well as the damaged samples demonstrate this trend.

The experimentally determined void volume fractions are plotted as surfaces in Figure 14. The corresponding void volume fractions from the finite element simulations are plotted in Figure 15. At 60% of the average failure load, the void volume fraction consists of a large concentration of porosity near the top of the flow line. By 83% of the average failure load the experimental results show growth in both the large void as well as voids along the flow line adjacent; at 93%, pronounced growth has occurred in the large void an a single peak in the flow line directly adjacent to the primary void. A similar growth trend is observed in the simulation. Damage accumulates in the large void as well as along the flow line. Here the level of accumulation is greatest at the in the large void and at the base of the flow line where the stress triaxiality is largest. At 93% of the average failure stress, damage in the large pore has continued to increase while growth along the flow line is pronounced, but of smaller magnitude than that of the large pore. When compared to the experimental results, the simulation shows the same general trend, that is growth along the flow line and of the large pore. The simulation however, over predicts growth in the large void. This is most likely due to the fact that pore was not itself an axially symmetric feature, but a three dimensional off-axis sphere-type structure. And results presented by Jones (2004) demonstrated a sphere-shaped void will grow more slowly than a cylindrical void due to the differences in stress triaxiality and plastic strains engendered by the geometrical configuration.

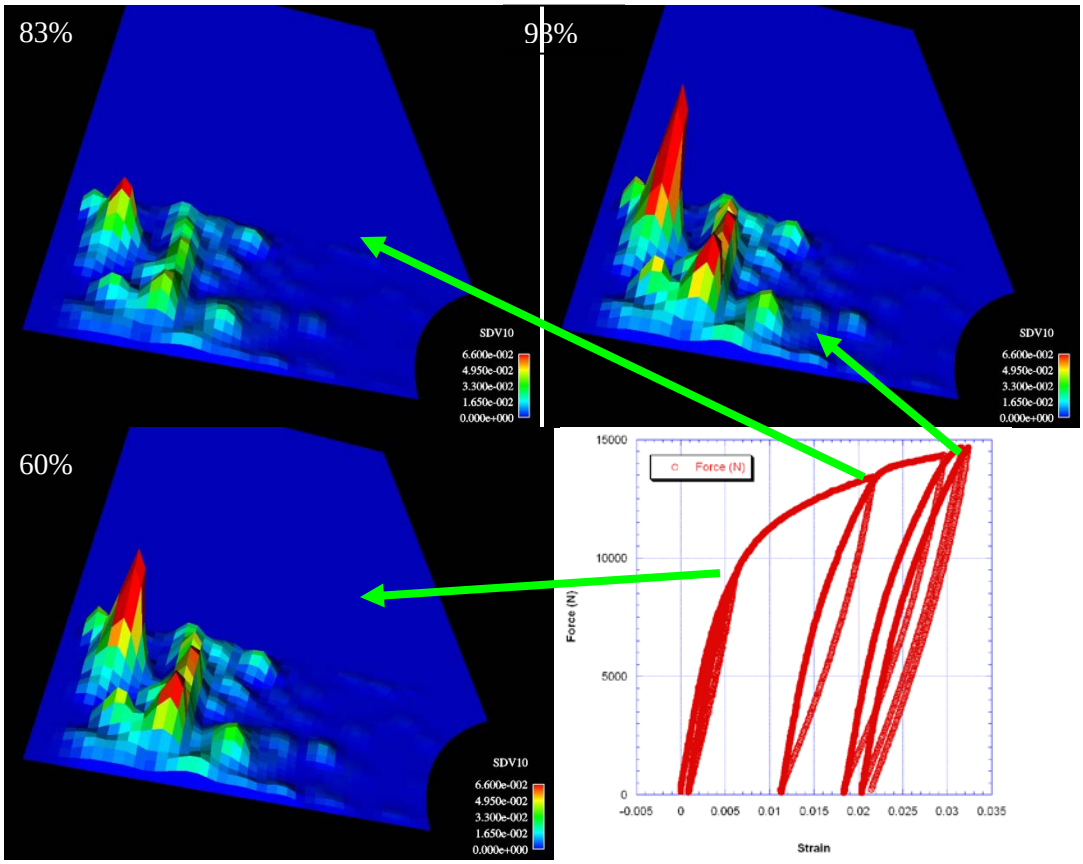

Figure 15: Contour plots of total void volume fraction from the finite element simulation**.**

The first element failure for this simulation occurs at the isolated pore and is shown in the damage contour in Figure 16. The first element failure occurred at 3.3% true strain that corresponds to between 95 and 100% of the average total load.

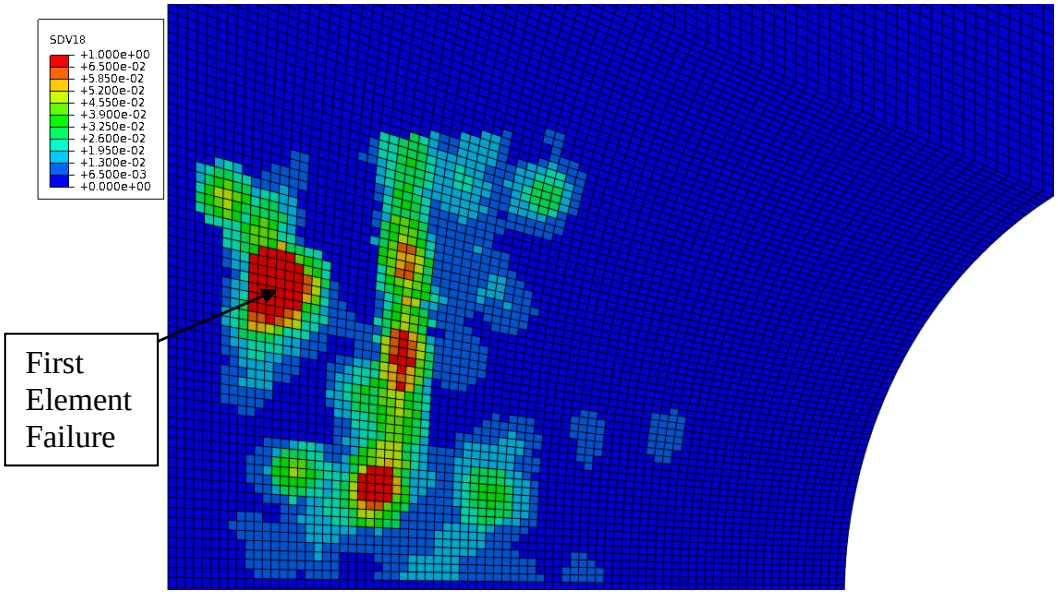

Figure 16: Simulation contour plot of the damage distribution at the time of the first element failure for the implicit finite element simulation of the notch Bridgeman tensile specimen

Figure 17 shows a contour plot of the pressure, von Mises equivalent stress, stress triaxiality, and plastic strain at just prior to the first element failure. The maximum values for each of these different measures of stress and strain occur at various locations around the specimen, however, none of the measures display a maximum at or near the location of first failure. It can be easily seen from Figure 17 that the maximum values for the plastic strain, von Mises stress, and pressure all exist near the notch root. The maximum stress triaxiality exists not at the notch root, but at the point labeled in the figure. In Agarwal et al. (2003), it is shown that pore growth is dependent upon both stress triaxiality and plastic strain; for the real distribution, it seems that the influence of the high porosity being concentrated around the pore and the flow line dominates the influence of plastic strain and stress triaxiality.

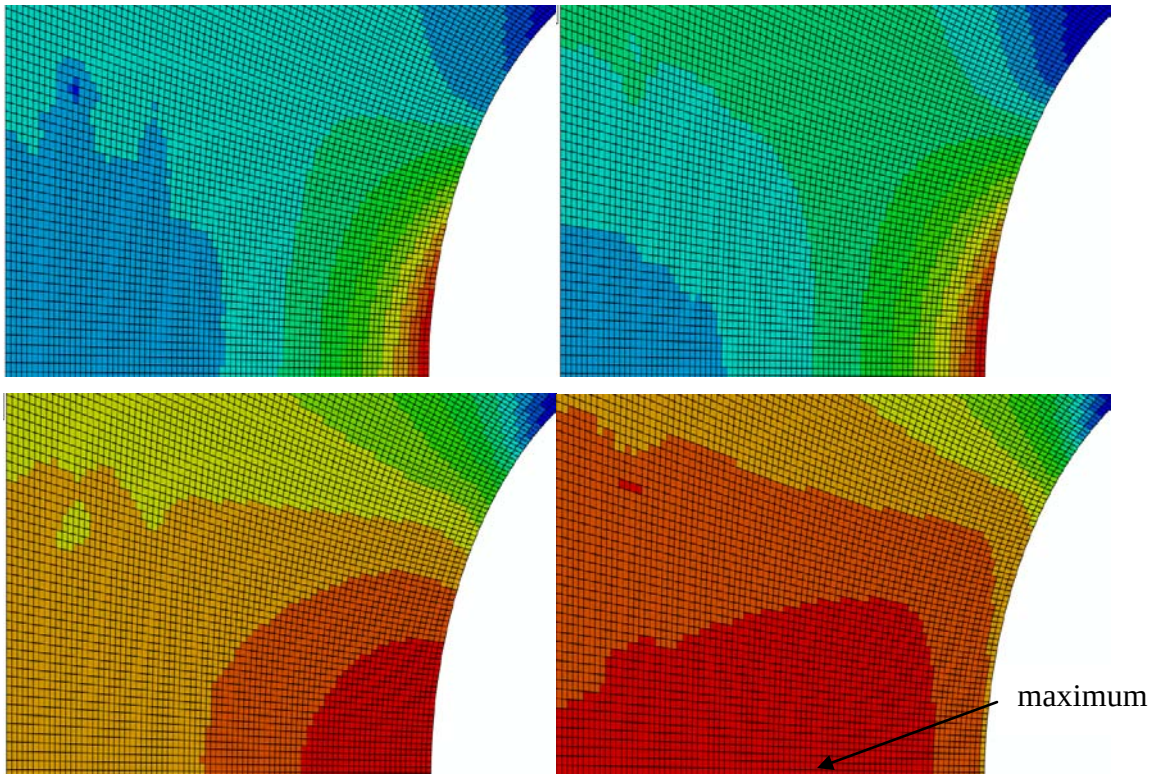

Figure 17: Contour plots of von Mises equivalent stress (top left), effective plastic strain (top right), pressure (bottom left), and stress triaxiality (bottom right) for the simulation of the notch Bridgeman tensile specimen with the actual initial porosity distribution.

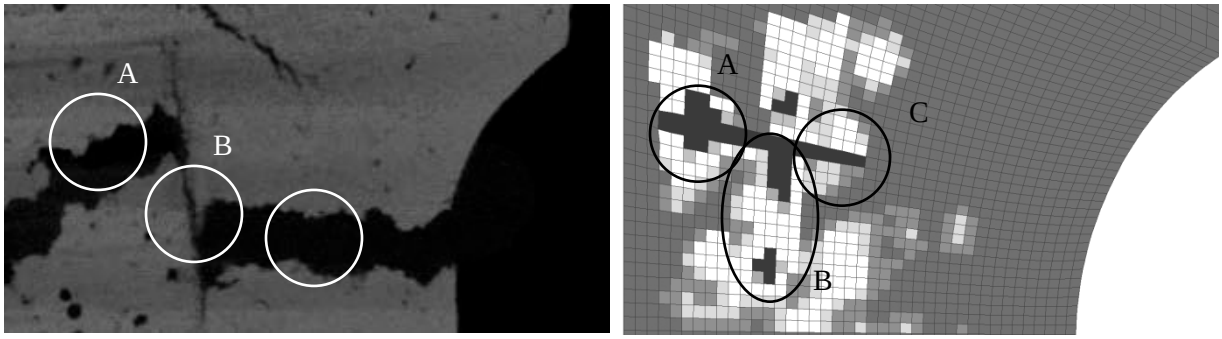

Figure 18: Fractured specimen and predicted damage from the finite element simulation. The black regions in the simulation represent element failures due to damage evolution.

The left-hand side of Figure 18 shows the fractured section of the failed sample, and the right-hand side shows predicted damage state. Three aspects of this failure are captured by the simulation. Area A shows that the fracture passes through the region with high initial porosity levels. The simulation predicted maximum void growth and initial failure in this region. Area B shows an axial fracture along the porous flow line. This fracture connects the region of high initial porosity, A, with the region of highest stress triaxiality, C. Failure along the porous flow line was typical of all tested magnesium bars. Area C shows the radial fracture path across the specimen section in the region of high stress triaxiality. The simulations capture the observed

damage evolution noted for Areas B and C. Significant axial void growth was predicted in Area B as evidenced by the failed and near failed elements along the flow line. Void growth in this area continued after the initial element failure in the large pore. After initial element failure occurs at the large pore, damage progresses radially both toward the specimen center and the notch edge. This predicted failure mode is evidenced by the failed elements aligned radially.

Effect of Initial Porosity Distribution on Evolution of Damage

After observing that, given the initial porosity distribution of a specimen, the MSST model is capable of predicting the general trends in the evolution of that porosity as the specimen undergoes deformation, we examine what effect, the porosity distribution actually has on the predicted component response. Two additional porosity distributions were developed, one with homogeneously distributed porosity in each element in the notched region and the other with randomly distributed damage. For both of these new porosity distributions, the void volume fraction for the entire part is identical to that of the porosity distribution in previous analysis. Figure 20 compares the three different simulations.

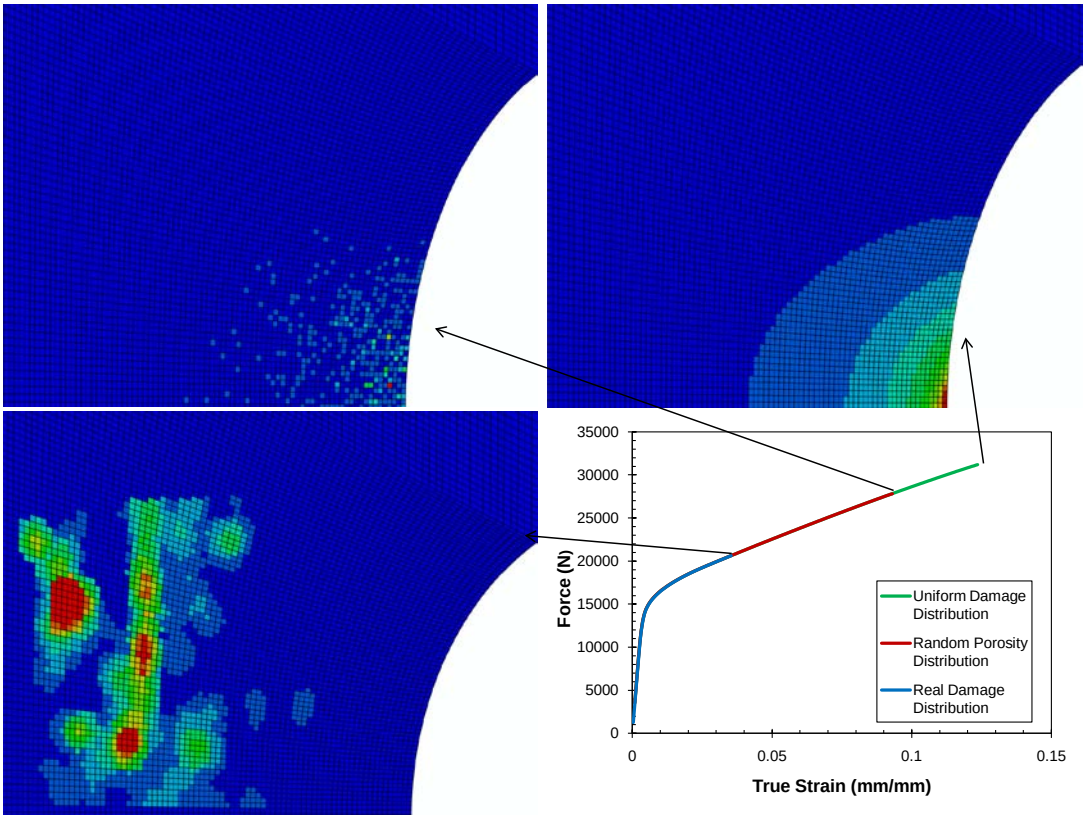

Figure 19: The force versus strain response for each of the three porosity distributions is shown along with damage contours taken as the first element failed in each simulation.

Figure 19 shows that the force versus nominal true strain response for each of the simulations follows the same path regardless of the initial porosity distribution. The difference in the three cases is that the randomly and uniformly distributed cases exhibited first element failure at a much larger strains than the realistic damage distribution. The strain to first failure for the real

distribution is 3.3%. Changing the same volume (area) of porosity into a random distribution yields a first element failure at 8.8% strain, an increase of 167% over the strain to first failure of the real distribution. If the porosity is averaged homogeneously, the strain to failure is 12.3%. That corresponds to an increase of 273% over the real distribution and a 40% increase over the random distribution. Therefore, the initial porosity distribution plays a vital role in simulating the mechanical response of a part near failure.

The damage contours are shown for each simulation at first element failure. The contours show the dramatic differences in predicted damage evolution. For the real distribution, the damage evolution is concentrated around the pore and the flow line. In the random distribution, the damage evolution generally increases as the distance from the notch root decreases, but non-uniform initial damage causes non-uniform damage evolution. Finally, in the uniform distribution, the evolution of damage is focused on the notch root and radiates outward.

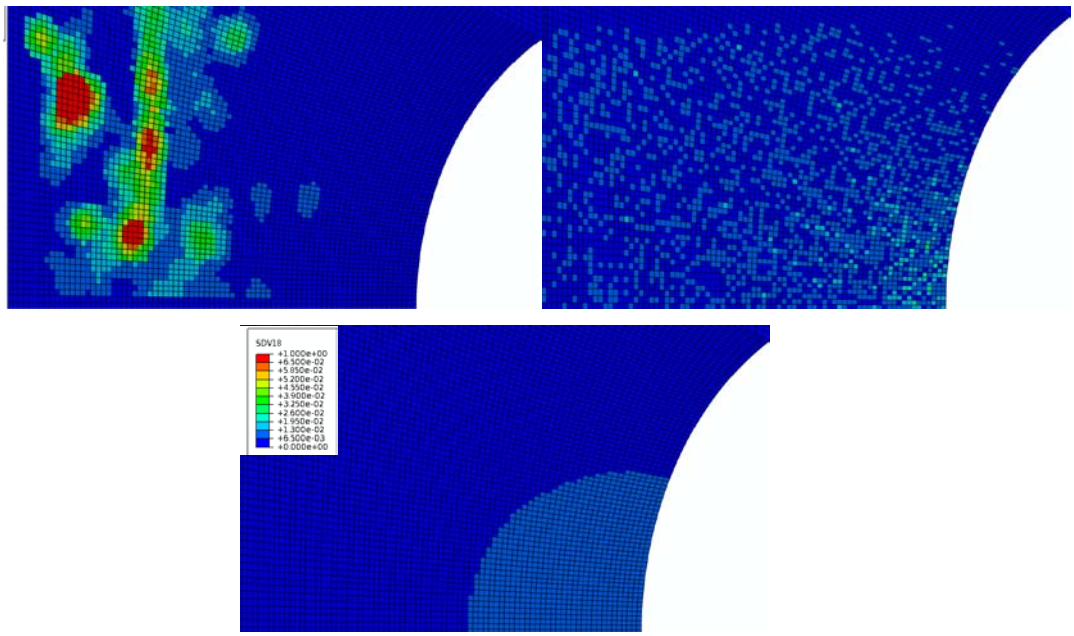

Figure 20: Comparison of the damaged states of the real (top left), random (top right), and uniform (bottom) porosity distribution simulations at 3.3% true strain, which corresponds to first element failure of the real porosity distribution simulation.

Figure 20 shows that at the first element failure of the real initial porosity distribution, the random and uniform distributions are still far from failure initiation. In fact, at this point the maximum damage in the real distribution is 1 (first element failure); however, the maximum damage in the random and uniform distributions are 2.6% and 1.0%, respectively. Within the random and uniform cases, trends about the growth of the voids can also be noted. For the random case, the concentration of elements with elevated damage levels gets much higher as the distance to the notch root decreases. However, there are some elements with damage levels near the maximum at this strain level that are located far from the notch. The damage level does not correspond directly to the position relative to the notch root. The same cannot be said about the uniform distribution. It can be seen that the damage growth seems to be radiating out from the notch root.

The next strain level chosen to compare the response of the two new porosity distributions is 8.8%. This strain corresponds to the first element failure for the randomly distributed porosity case. Figure 21, shows the damage distribution in the randomly and uniformly distributed porosity cases at the point of first element failure in the randomly distributed case.

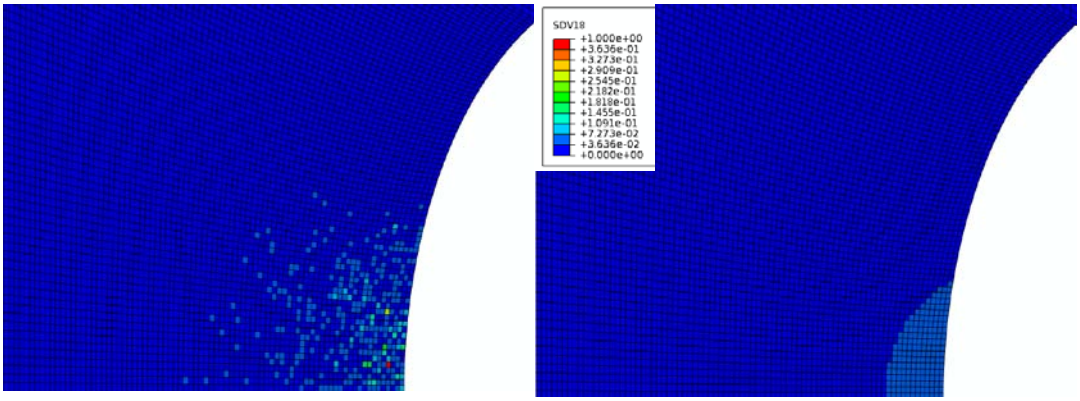

Figure 21: Comparison of the damaged states of the random (left) and uniform (right) porosity distribution simulations at 8.8% true strain, which corresponds to first element failure of the random porosity distribution simulation.

Figure 21 shows that the failure of the randomly distributed case occurs neither directly at the notch root nor at the element with the highest initial porosity. At this level of strain, the uniformly distributed case still continues the trend of highest damage occurring at the notch root and decreasing as the distance from the notch increases. The maximum damage present in the uniformly distributed case is 4.5%.

Figure 22 shows the stress state at first element failure for the random damage distribution. Here, the von Mises equivalent stress, the equivalent plastic strain, and the pressure are all maximum at the notch root, but the stress triaxiality is not. The maximum stress triaxiality occurs near the center of the specimen but not near the element that fails first. The element to fail first had slightly higher initial porosity than the other elements in its proximity, was in an area with high plastic strain levels, and was experiencing high stress triaxiality. Failure occurred where the initial porosity, plastic strain, and stress triaxiality were all elevated and working in tandem.

Figure 23 shows the von Mises equivalent stress, plastic strain, pressure, and stress triaxiality of the uniformly damaged case immediately prior to the first element failure. Like the other two cases, the uniform damage case exhibited a maximum von Mises stress, equivalent plastic strain, and pressure at the notch root, but the maximum stress triaxiality was at the direct center of the specimen. Therefore, if stress triaxiality was the governing factor in determining the damage evolution, then the damage near the center of the specimen would be elevated. So it is observed that in this model, stress triaxiality plays a secondary role in determining the growth of initial porosity. However, unlike the previous two cases, the damage, von Mises stress, equivalent plastic strain, and pressure all directly increase as the distance to the notch decreases. The predicted position of the first element failure for a uniform damage distribution is at the notch root.

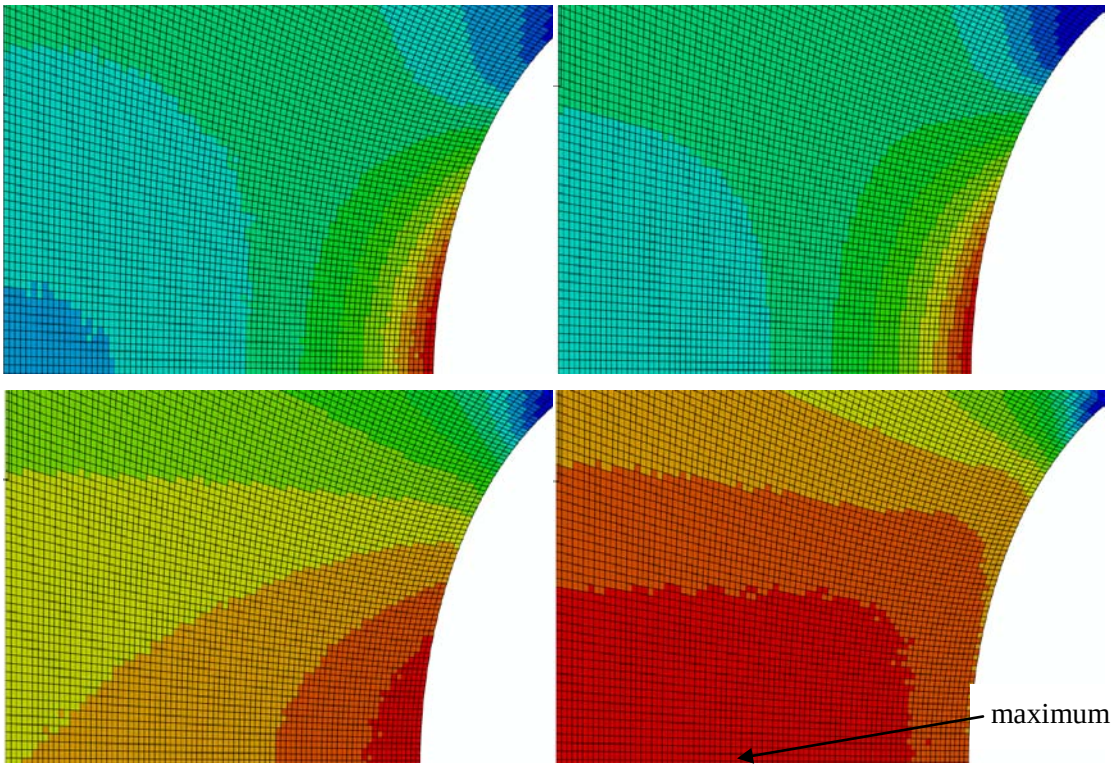

Figure 22: Contour plots of von Mises equivalent stress (top left), effective plastic strain (top right), pressure (bottom left), and stress triaxiality (bottom right) for the simulation of the notch Bridgeman tensile specimen with the random initial porosity distribution.

Several key observations can be drawn from these results. The MSST model is able to predict the damage evolution given the initial porosity distribution yields a result that follows the trends seen in the experimental data. Secondly, it was observed that the initial porosity distribution has no effect on the shape of the force versus strain curve for a notch Bridgeman tensile specimen. The only effect from the initial porosity distribution is on the damage evolution and the eventual first element failure of the specimen. That leads the third and final major observation that the initial porosity distribution plays a major role in predicting the beginning of failure for the specimen.

In summary, this study demonstrates a method of analysis that combines x-ray computed tomography, micromechanical finite element simulations and macro-scale continuum simulation based evaluation of damage evolution. Based on these initial findings, a strong corroboration of simulation with x-ray tomography results for the failure of notch tension specimens under monotonic loading is apparent.

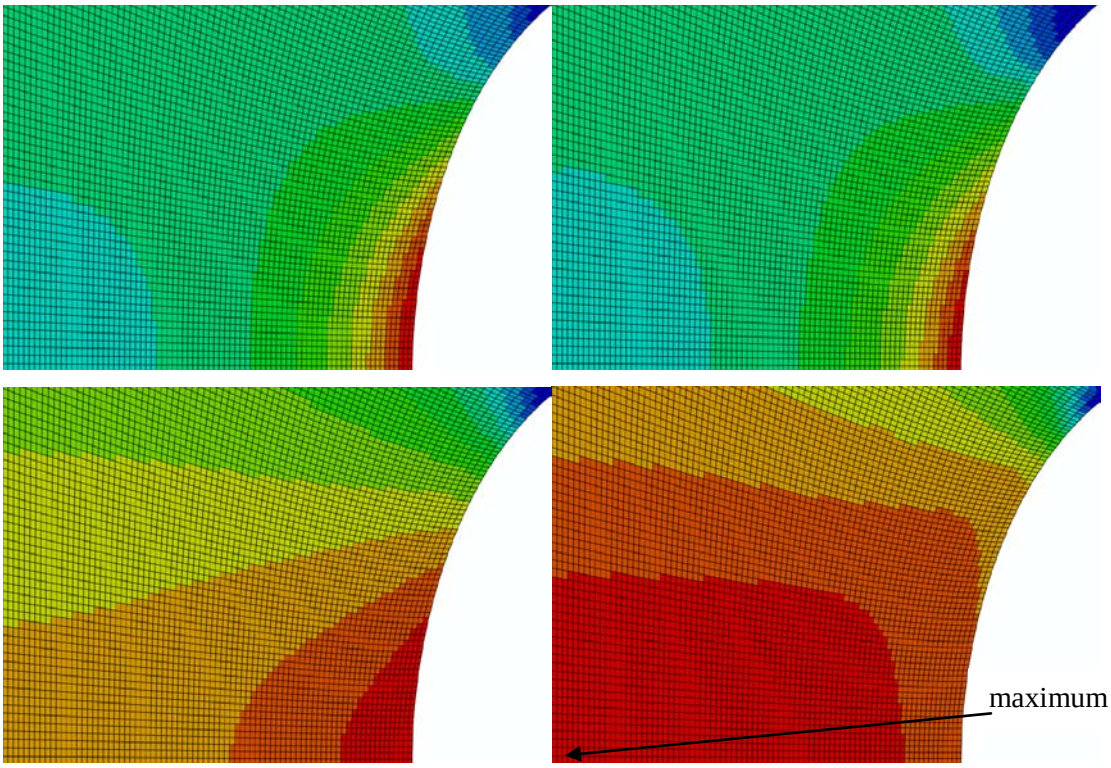

Figure 23: Contour plots of von Mises equivalent stress (top left), effective plastic strain (top right), pressure (bottom left), and stress triaxiality (bottom right) for the simulation of the notch Bridgeman tensile specimen with the uniform initial porosity distribution.

Conclusions

This report summarizes the state of the experimental and numerical simulation study of failure mechanisms in structural magnesium alloys. The aim is an enhanced, multiscale microstructure-property model that can be implemented into commercial codes and that can be used in high-fidelity crash simulations for the design and optimization of structural Mg components.

The key findings for this study are the following:

- The T6 temper increases the quasi-static yield and hardening rate of T-Mag cast AZ91, and a less pronounced effect on the high strain rate response.
- The casting process effects the quasi-static yield of cast AZ91. The effect dimish as the strain rate approaches 3000/sec
- Simulation results show that the model is capable of capturing the trend of elevated pore growth relative to the rest of the specimen in these two regions under the application of a uniaxial tensile load.
- Prediction of failure loading requires material microstructructural details be included in finite element simulations.

References

Agarwal H, Gokhale AM, Graham S, Horstemeyer MF. Material Science and Engineering 2003; A341: 35-42.

Bammann DJ, Chiesa ML, et al. 1993. Failure in ductile metals using finite element methods. Third International Symposium on Structural Crashworthiness. University of Liverpool, Liverpool, UK. London; New York : Elsevier Science Publishers, c1993.

Garrison WMJ, Moody NR. 1987. Ductile fracture. J Phys Chem Solids 48(11):1035-74.

Gary, G. (2005). DAVID manual. From: http://www.lms.polytechnique.fr/dynamique/greef/web4034_david.html.

Gurson AL. 1977. Continuum theory of ductile rupture by void nucleation and growth, part 1: Yield criteria and flow rules for porous ductile media. J Eng Mater Tech 99(1):2-15.

Hirth JP, Nix WD. 1985. Analysis of cavity nucleation in solids subjected to external and internal stresses. Acta Metallurgica 33(3):359-68.

Horstemeyer MF. 1995. Physically-motivated modeling of deformation-induced anisotropy. Mechanical engineering. Atlanta: Georgia Institute of Technology. p. 291.

Horstemeyer MF, Gokhale AM. 1999. A void-crack nucleation model for ductile metals. Int J Solids Struct 36(33):5029-55.

Horstemeyer M, Lathrop J, et al. 2000. Modeling stress state dependent damage evolution in a cast Al-Si-Mg aluminum alloy. Theor Appl Fract Mech 33(1):31-47.

Horstemeyer MF, Oglesby D, et al. 2007. From atoms to autos: Designing a Mg alloy Corvette cradle by employing hierarchical multiscale microstructure-property models for Monotonic and cyclic loads. Mississippi State: Center for Advanced Vehicular Systems.

Osborn RJ. 2005. A joint USCAR-USAMP material project with DaimlerChrysler, Ford, General Motors and Industry. Southfield, Detroit.

Rashid MM. 1997a. A new theory for free-surface formation in solid continua. Int J Solids Struct 34:2303-20.

Rashid MM. 1998. The arbitrary local mesh replacement method: An alternative to remeshing for crack propagation analysis. Compu Meth Appl Mech Eng 154(1):133-150.

Rice JR, Tracey DM. 1969. On the ductile enlargement of void in triaxial stress fields. Journal of the Mechanics and Physics of Solids 17(3): 201-217.

Waters, A.M., Martz, H.E., Dolan, K.W., Horstemeyer, M.F., and Green, R.E., "Three dimensional void analysis of AM60B magnesium alloy tensile bars using computed tomography imagery," *Materials Evaluation*, **58**, 1221-1227 (2000).

Keywords

Magnesium, Lightweight, Damage, Material Modeling, Simulation

Brief Description of Report

This report summarizes the state of the experimental and numerical simulation study of failure mechanisms in magnesium alloys. The aim is an enhanced, multiscale microstructure-property model that can be implemented into commercial codes and that can be used in high-fidelity crash simulations for the design and optimization of structural Mg components. The development effort will focuses on experimental response of Mg alloys that can be utilized for the development of microstructure-property model parameters.

Southern Regional Center for Lightweight Innovative Design

Phase III

Final Scientific & Technical Report

October 1, 2009-September 30, 2011

For compliance with contract requirements of Award DE-EE0002323

Task 6

MATERIALS DESIGN FOR STEEL ALLOYS

Submitted December 27, 2011

TASK 6: MATERIALS DESIGN FOR STEEL ALLOYS

Table of Contents

TASK 6: MATERIALS DESIGN FOR STEEL ALLOYS

Co-Principal Investigator: Seong-Gon Kim
Associate Professor, Physics and Astronomy
Mississippi State University (MSST)
Hilbun Hall, Rm 237, P.O. Box 5405, Mississippi State, MS 39762-5405
(662) 325-8031; e-mail: kimsg@hpc.msstate.edu

Co-Principal Investigator: Mark F. Horstemeyer
Chair in Solid Mechanics & Professor, Mechanical Engineering
Center for Advanced Vehicle Systems (CAVS), MSST
206 Carpenter Bldg., PO Box ME, Mississippi State, MS 39762
(662) 325-7308; fax: (662) 325-7223; e-mail: mfhorst@me.msstate.edu

Co-Principal Investigator: Hongjoo Rhee
Postdoctoral Associate
CAVS, MSST
P.O. Box 5405, Mississippi State, MS 39762-5405
(662) 325-9221; e-mail: hrhee@cavs.msstate.edu

Co-Principal Investigator: Sungho Kim
Postdoctoral Associate
CAVS, MSST
P.O. Box 5405, *Mississippi State, MS 39762-5405*
(662) 325-9241; e-mail: sk5@msstate.edu

William Joost: Technology Area Development Manager
e-mail: william.joost@ee.doe.gov

Magda Rivera: Project Manager
e-mail: magda.rivera@netl.doe.gov

Contractor: *Mississippi State University (MSST)*
Contract No.: *DE-EE0002323*

Overall Goal of the Task

Design a new high-strength steel alloy with improved strength and ductility for automotive applications.

Task Objectives

(1) Identify the fundamental mechanisms at quantum mechanical and micromechanical level that determine overall strength and ductility of steel alloys.

(2) Investigate the interaction among different phases of high-strength steel alloys.

(3) Investigate the effect of micro-alloying elements to the material properties of high-strength steel alloys.

(4) Investigate the effect of various strengthening mechanisms to the material properties of high-strength steel alloys.

Approach

We use a hierarchical multi-scale methodology to investigate the effect of nanoscale precipitates and additives to the overall strength and ductility in steel alloy design for automotive applications. Critical issues being ad-

dressed include: selection of key micro-alloying elements, interaction of precipitate and matrix phases, and ultimately composition-structure-property relationship. At electronic level, quantum mechanical first-principles simulations based on Density Functional Theory (DFT) will be performed. At the atomistic level, accurate atomistic simulations will be performed using Modified Embedded Atom Method (MEAM) and force-matching-embedded-atom-method (FMEAM) potentials. Large scale atomistic simulations will be conducted to study the effect that size, shape, and volume fraction of different inclusion particles have on the material properties of steel alloys. Results will be used to guide quantitative alloy composition designs to improve strength and ductility of steel alloys

Accomplishments

The objectives were met by accomplishing the followings:

- Developed new modified-embedded-atom-method (MEAM) interatomic potentials for Fe-C alloys using the multi-objective optimization (MOO) procedure.
- Performed electronic and atomistic simulations to obtain the electronic, structural and mechanical properties of the main phases of steel alloys.
- Performed DFT calculations on cementite Fe-C alloy phase and optimized the structure.
- Investigated the microalloying effect of vanadium on the strength of BCC ferrite grain boundaries using DFT methods.
- Conducted fundamental materials/mechanical properties characterization and microstructure characterization on advanced high strength steel (AHSS) alloy samples obtained from POSCO, performed thermomechanical treatment and investigated the effect of bake-hardening.
- Performed heat treatment (i.e. intercritical annealing followed by quenching), structure observation, and mechanical tests on TRIP steels to characterize the effect of martensite volume fraction and carbon content in matrix martensite on the mechanical behavior of AHSS.
- Established and maintained close collaborative relationships with industrial partners including POSCO, SmartAluminum, Inc., SAC, Inc., and Wade Service.
- Made many publications and presentations:

Introduction

The fabrication of desired automobile components is often the largest barrier to new materials, since automotive designs call for specific aerodynamic considerations. Despite their desirable material characteristics, high-strength steels have limited fabrication capability because they inherently resist deformation and wear the tooling. Therefore, we have the challenge and opportunities to perform compositional design of high-strength steel alloys in a manner that lowers mass, increases strength and retains workability, but generates required strength after the fabrication step.

Potential components for lightweight and ultra-strength materials are the front end, power train, instrument panels, the chassis system, and car bodies including door panels, for example. We propose to perform compositional design of steel alloys to lower these barriers with a better understanding of the quantum-mechanical and atomistic structure of various constituent composite crystal structures and their interactions, the influence of alloying additions, and the effects of thermo-mechanical treatments on wrought materials during and after processing.

Ductility of materials can be improved by alloying and by the resulting activation of slip systems. We will investigate the origin of these alloying effects by using first-principles methods such as Density Functional Theory (DFT) (Kresse, et al, 1996). We will focus on understanding the extent to which these effects are governed primarily by electronic structure or crystallography.

Computational Approach

We use a hierarchical, multiscale methodology to investigate the effect of nanoscale precipitates and additives to the overall strength and formability in steel-alloy design for automotive applications. In a hierarchical, multiscale framework, numerical methods are run independently at disparate length scales. Then, a bridging methodology such as statistical-analysis methods, homogenization techniques, or optimization methods are used to distinguish the pertinent cause-effect relations at the lower scale to determine the relevant effects for the next higher scale (E and Engquist, 2003). We will adopt the strategy developed by Horstemeyer and his co-workers who used ISVs as a top-down hierarchical approach to bring the pertinent nanoscale, microscale, and mesoscale phenomena into the macroscale (Horstemeyer and Wang, 2003; Olson, 1998).

Critical issues being addressed include: selection of key combination of precipitates and matrices, interaction of precipitate and matrix phases and, ultimately, composition-structure-property relationship. At the electronic level, quantum-mechanical first-principles simulations will be performed to investigate the interfacial interactions between matrix and the primary and the secondary precipitates. All first-principles, total-energy calculations and geometry optimizations are performed within DFT using Blöchl's all-electron projector augmented wave (PAW) method (Blöchl, 1994) as implemented by Kresse et al. (Kresse, et al, 1996). For the treatment of electron exchange and correlation, we generally use the local density approximation (LDA) (Perdew and Zunger, 1981) and sometimes the generalized gradient approximation (GGA) (Perdew et al, 1996) depending on the accuracy required. At the atomistic level, accurate atomistic simulations will be performed using efficient and reliable empirical interatomic potentials such as the modified-embedded-atom method (MEAM) (Baskes, 1992) or force-matching embedded-atom method (FMEAM) (Li et al, 2003) potentials. The interatomic potentials are constructed by optimizing the potential parameters to reproduce various experimental materials properties and atomic-force data from DFT calculations. Large-scale, atomistic simulations will be conducted to study the effect that size, shape, and volume fraction of different precipitates have on the thermo-mechanical properties of steel alloys. Many factors that govern the yield and hardening behavior of solids, such as, crack-tip propagation, dislocation nucleation, dislocation motion, and the interaction of dislocations with grain boundaries, will be investigated through these simulations. Results will be used to guide quantitative alloy composition designs to improve strength and formability of steel alloys. For more detailed description of experimental and computational approach, see Kim, et al (2007).

Experimental Approach

High rate tension tests were performed using a split Hopkinson bar (SHB). The SHB technique is a common mechanism for the determination of the stress-strain response of materials at high loading rates. The SHB generally consists of two long bars, called the incident and transmitted bars, used as transducers to record a stress wave propagating along the incident bar, through the specimen, and along the transmitted bar. The SHB in tension makes use of a loading mechanism to strain the incident bar between the end of the bar and a breaker pin. The load is then released and measured across three strain gages on both the incident (input) and transmitted (output) bars. Strain gages applied to the incident and transmitted bars are used to capture the signals which are amplified being recorded using a computer based data acquisition system. The detailed description of the SHB technique can be found elsewhere (Gama, et al., 2004; Staab, et al., 1991; Metals Handbook, 8, 2000).

Computational Results

MEAM potentials for Fe-C alloys

We developed a new MEAM potential for Fe-C alloys using the multi-objective optimization procedure (Kimi et al, 2009) based on the MEAM potentials for pure Fe and C (Baskes, 2009).

Figure 6.4.1 shows the cohesive energy of Fe-C alloy systems in the B1 and L12 crystal structures as a function of the nearest neighbor distance. Our results show that the MEAM potential for Fe-C alloy

system reproduces DFT calculations reasonably accurately for these two structures over a wide range of nearest neighbor distances.

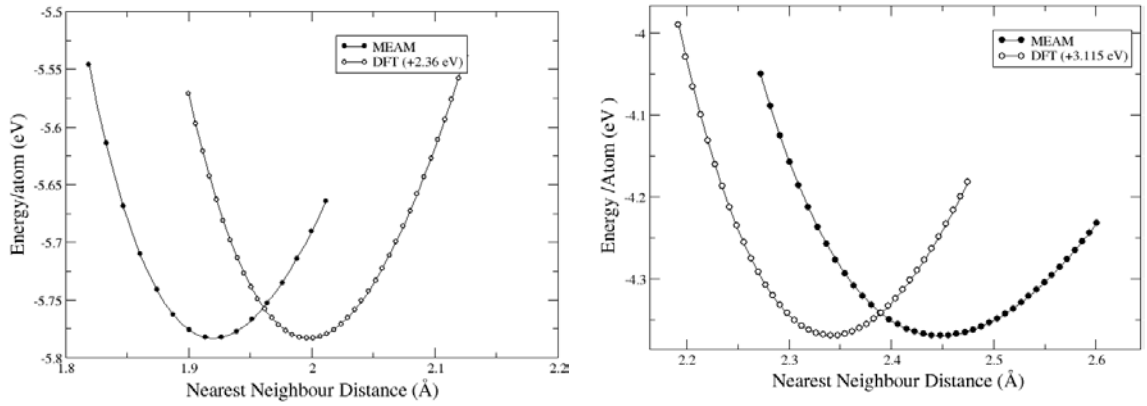

(a) (b)

Figure 6.4.1. The cohesive energy of Fe-C alloy systems as a function of the nearest neighbor distance in Å. (a) FeC in B1 crystal structure and (b) FeC in L12 crystal structure. The result by MEAM potential (filled circles) are compared with those of the DFT calculations (open circles).

We found that the new Fe-C MEAM potential demonstrates excellent agreement with DFT calculations for many important physical quantities as shown in Table 6.4.1. Particularly, our Fe-C potential reproduces the heat of formation results from DFT calculations accurately for three of the main crystal structures of Fe-C alloy system.

Table 6.4.1. Physical properties of B1 and L12 crystal structures computed by the new MEAM potential compared with DFT data.

Physical Property	MEAM	DFT
B1 Heat of formation (eV/atom)	0.262	0.290
L12 Heat of formation (eV/atom)	0.872	0.359
L12 volume ($Å^3$/atom)	9.821	10.270
L12 Bulk Modulus (GPa)	190.403	152.34
L12 Elastic constant C11 (GPa)	284.898	175.7
L12 Elastic constant C12 (GPa)	143.155	140.7
L12 Elastic constant C44 (GPa)	73.9	63.1

To further test the validity of our alloy potential, we computed several physical properties of cementite using our newly developed MEAM potential and compared with DFT and experimental data in Table 6.4.2. Experimental data is included in parentheses in the DFT column.

Table 6.4.2. Physical properties of cementite computed by the new MEAM potential compared with DFT data.

Physical Property	MEAM	DFT (Experimental)
Heat of formation (eV/atom)	0.088	0.01
Volume (Å^3/atom)	9.552	9.710 (9.705)
Bulk Modulus (GPa)	203.5	243(174)
Lattice Constants a,b,c (Å)	5.06,6.70,4.50	4.91,6.63,4.38 (5.09, 6.74, 4.53)
Elastic constants (GPa)		
C11	374.7	413.0
C22	262.0	412.0
C33	318.0	378.0
C12	144.2	154.0
C23	156.4	170.0
C13	138.0	167.0
C44	49.0	82.0
C55	113.7	136.0
C66	109.5	140.0

Furthermore, the order of stability between two interstitial C defects in Fe is correctly reproduced by the new Fe-C potential: 1.304 eV (2.140 eV) for tetrahedral and 1.249 eV (1.250 eV) for octahedral from MEAM (DFT) calculations.

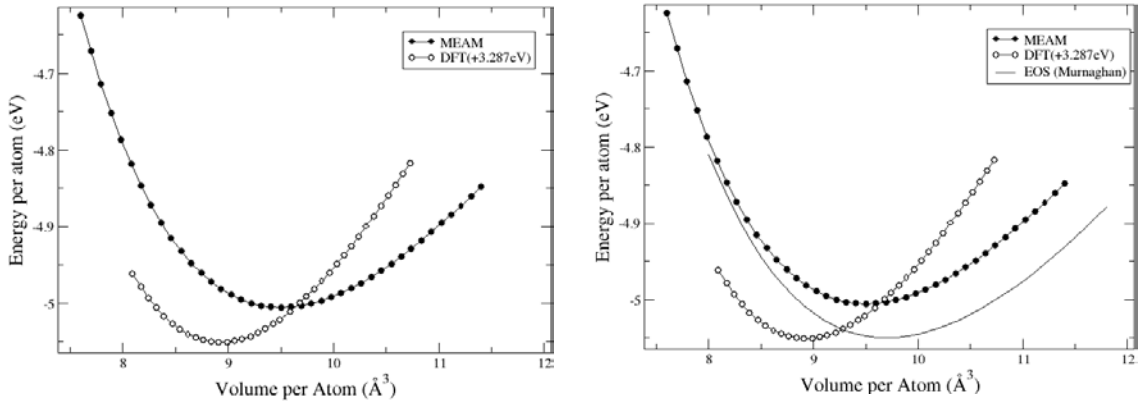

(a) (b)

Figure 6.4.2. The cohesive energy of cementite crystal structure as a function of volume per atom in Å^3/atom.(a) DFT and MEAM curves (b) DFT and MEAM compared to Murnaghan's equation of state curve that is derived from experimental data. The result by MEAM potential (filled circles) are compared with those of the DFT calculations (open circles).

The stability of the potential is demonstrated by the results of two molecular dynamic runs of cementite at high temperature (300K and 800K). These molecular dynamic runs are done at constant NVT simulations. Although the potential energy varies considerably the cementite structure remained reasonably unchanged.

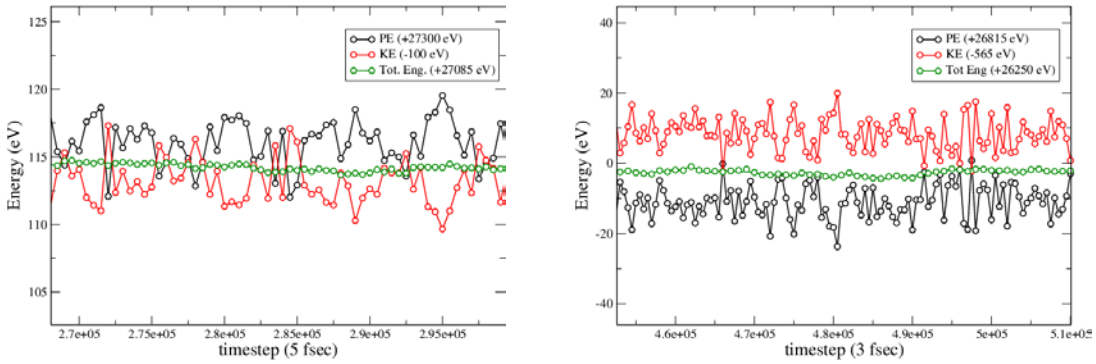

(a) (b)

Figure 6.4.3. Molecular dynamic runs at constant NVT of cementite. (a) At 300 K temperature (b) At 800 K temperature.

The validity of the new potential is further tested by applying it to the melting simulation of cementite crystal. The melting temperature of cementite is not well defined due to its stability. The Fe-C phase diagram indicates a eutectic point at 1420 K (Callister, 2007) where liquid consisting of Fe and C solidifies to form austenite and cementite crystals. For the purpose of this calculation we considered the melting temperature of cementite to be the temperature when cementite loses its crystal structure and becomes a random collection of Fe and C atoms similar to the eutectic point. Conventionally melting temperature calculations are done using a single-phase simulation box. The single phase method, however, generally overestimates the melting temperature. The overestimation is a result of the exclusion of interface effects. In two-phase simulation (TPS) method, a system that has a solid and a liquid phase simultaneously is used to compute the melting temperature more accurately. We performed TPS in the NPT ensemble for a simulation box containing solid and liquid phases of cementite. First, a supercell containing 14x7x7 unit cells of cementite (10,976 atoms), was heated through molecular dynamics (MD) run in the NPT ensemble with T = 1200 K and P = 0. Second, a MD run with half of the atoms in the supercell frozen, was carried out in the NPT ensemble with T = 4000 K and P = 0. The resulting supercell was then subjected to another MD run keeping the same half of atoms frozen, in the NPT ensemble with T = 1500 K and P = 0. The result of this process was a supercell containing solid cementite at 1200 K in one half and liquid cementite in the other half at 1500 K. This supercell was then used in simulations of solidification and melting of cementite. The two-phase supercell was heated through MD runs in the NPT ensemble at where T ranged from 1400 K to 1500 K in 10 K intervals. Each system was equilibrated for at least 5×10^6 time steps, where each time step was 2 fs, totaling to 10 ns. The final state of the system was visually inspected. If the final state appeared have both liquid and solid phases more MD runs were performed until the final state of the supercell contained one phase. Some systems required as much as 32 ns of MD runs to arrive at a single phase. The temperature, total energy, volume, and pressure of the systems were determined through averaging the values of the final 40,000 time steps (80 ps) of each simulation. The variation of properties such as total energy, volume, specific heat and derivative of volume with temperature allows us to clearly determine the melting temperature of cementite. Plots illustrating these variations are presented in Fig. 6.4.4. According to the plots we obtain the melting temperature between 1418 K and 1432 K. This is in good agreement with the experimental eutectic point at 1420 K. The transformation of the two-phase

simulation box to a one-phase simulation box, near the predicted melting temperature is presented in Fig. 6.4.5 and Fig. 6.4.6.

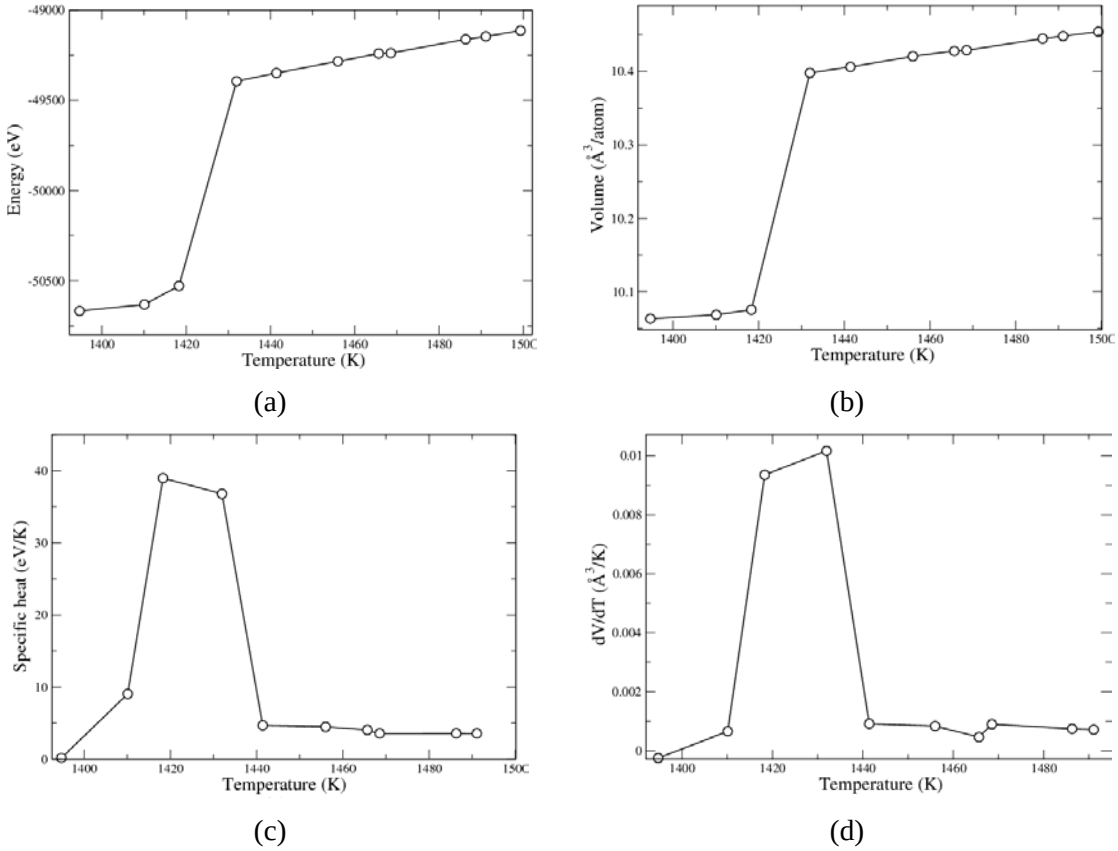

Figure 6.4.4. (a)Energy vs. temperature of the two-phase system. (b)Volume vs. temperature of the two-phase system. (c) Specific heat vs. temperature of the two-phase system. (d) dV/dT vs. temperature of the two-phase system.

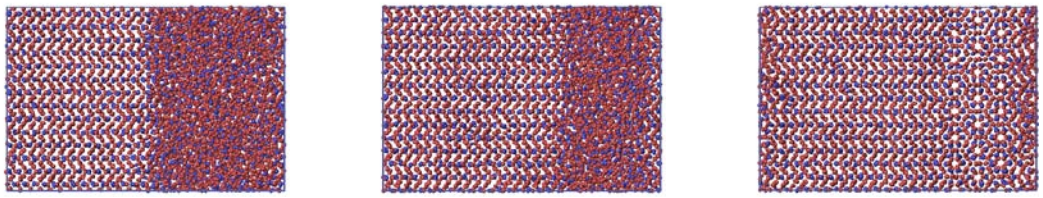

Figure 6.4.5. Snapshots of the two-phase simulation MD run in the NPT ensemble with T = 1420 K and P = 0. (a) Initial state of the simulation box, which include liquid-solid interface of cementite. (b) Intermediate state of the simulation box at 16 ns, as the solid phase starts to propagate. (c) Final state of the simulation box at 32 ns, where the solid state has propagated to the entire region.

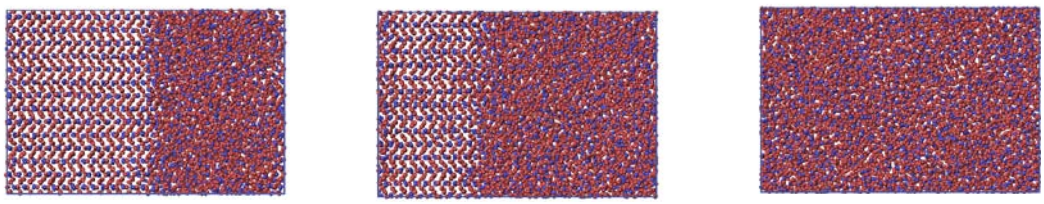

(a) (b) (c)

Figure 6.4.6. Snapshots of the two-phase simulation MD run in the NPT ensemble with T = 1430 K and P = 0. (a) Initial state of the simulation box, which include liquid-solid interface of cementite. (b) Intermediate state of the simulation box at 16 ns, as the liquid phase starts to propagate. (c) Final state of the simulation box at 30 ns, where the liquid phase has propagated to the entire region.

MEAM potentials for Fe-V alloys

We developed a new MEAM potential for Fe-V alloys using the multi-objective optimization procedure (Kimi et al, 2009) based on the MEAM potentials for pure Fe and V (Baskes, 2009). Molecular Dynamics (MD) Simulations: MD simulations are performed in order to observe the materials properties of Fe with increasing amount of V substitution. V atoms are substituted randomly in the bcc Fe matrix. Figure 6.4.7 shows the performance of the developed potential. Energy vs lattice parameter curves are in good agreement with the DFT calculated results. Also the variation of lattice parameter with increasing amount of V substitution has better agreement with experiment compared to the previous potential, as is shown in Figure 6.4.7(c).

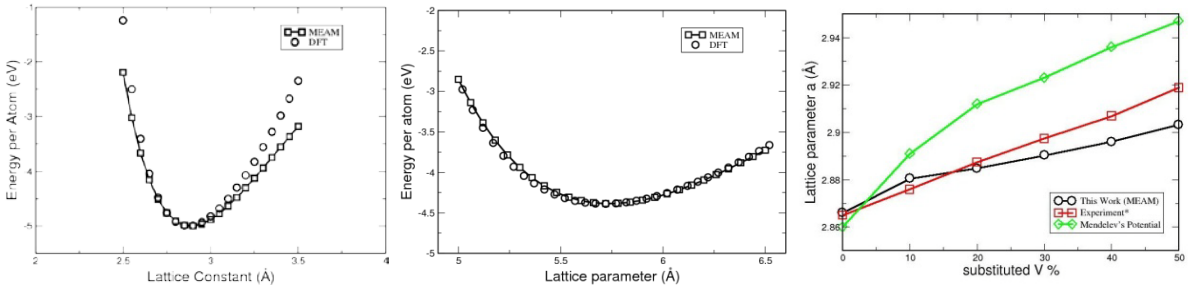

(a) (b) (c)

Figure 6.4.7: Energy vs lattice parameter for (a) FeV and (b) Fe15V. (c) Variation of the lattice parameter with increasing % of V substitution.

Thermal properties such as the coefficient of thermal expansion (CTE) are shown in Figure 6.4.8. CTE decreases with an increasing amount of V substitution. Note that the pure Fe CTE matches closely with the experimentally observed value.

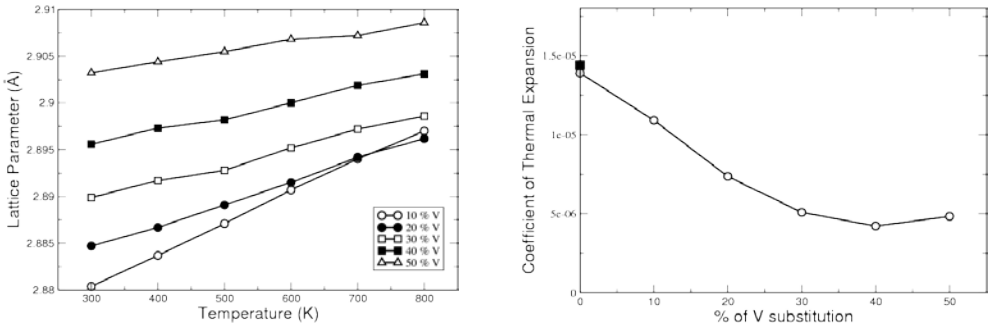

(a) (b)

Figure 6.4.8: (a) Variation of the lattice parameter of Fe with temperature for several % of V substitution. (b) Variation of the coefficient of thermal expansion with % of V substitution.

Variation of specific heat and melting temperature with % of V substitution is shown in Figure 6.4.9. Specific heat decreases with the increase of V substitution, while the melting temperature increases with the V substitution. Note that the pure Fe specific heat and melting temperature matches closely with the experimental results.

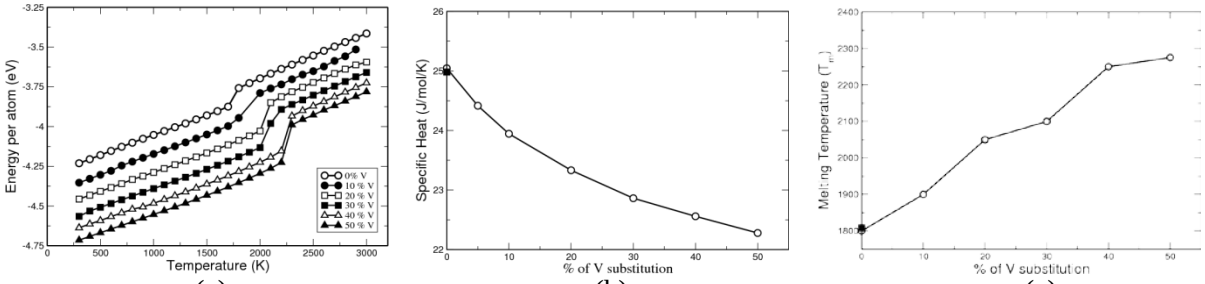

(a) (b) (c)

Figure 6.4.9: (a) Energy variation with temperature for several % of V substitution. (b) Variation of specific heat with several % of V substitution. (c) Variation of melting temperature with % of V substitution.

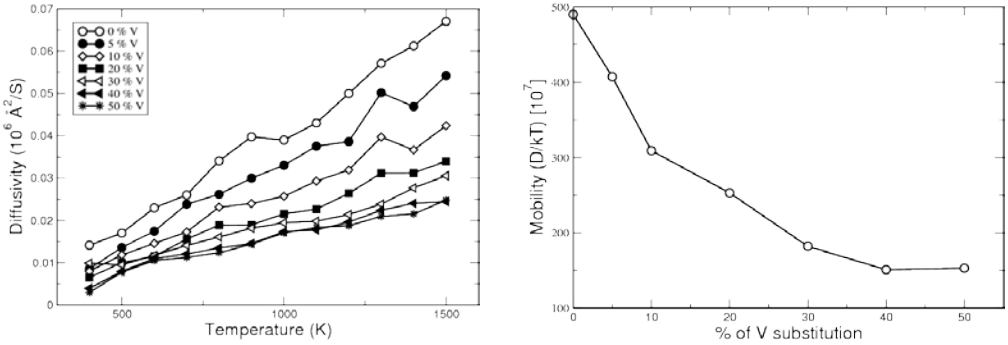

(a) (b)

Figure 6.4.10: (a) Variation of diffusivity with temperature for several % of V substitution. (b) Variation of mobility with several % of V substitution.

We investigated the effect of V substitution on the mobility of the Fe-V system. Figure 6.4.10(a) shows the temperature dependence of self diffusivity of Fe for different V concentration. From the slopes of these curves, the mobility of the Fe-V can be computed and they are shown in Figure 6.4.10(b).

The effect of V on the grain boundaries in ferrite

Vanadium (V) is one of the most important micro-alloying elements for steels. We used DFT to study the effect of V atoms in ferrite. Since grain boundaries are commonly present in the ferrite phase of most AHSS alloys, we investigated the effect of V atoms on the strength of grain boundaries in ferrite. We obtained the optimized grain boundary structure of Fe BCC Σ3(111)[1(-1)0] shown in Figure 6.4.11. The grain boundary formation energy from our calculation is 0.113 eV/Å^2.

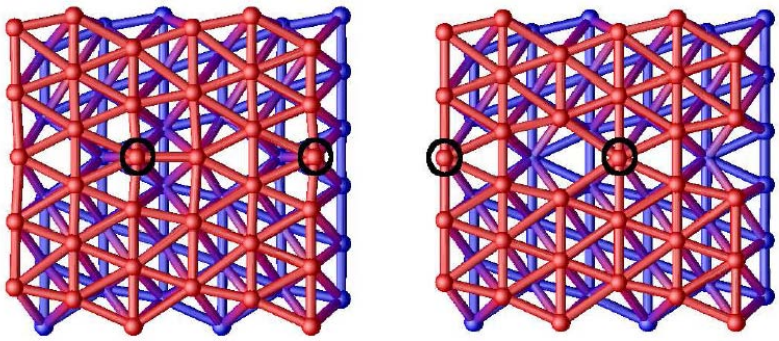

(a) (b)

Figure 6.4.11: The optimized structure of V defect in Fe BCC grain boundaries. (a) Interstitial and (b) substitutional defects. V atoms are circled to distinguish from Fe atoms.

Figure 6.4.11 shows the optimized structure of interstitial and substitutional V defects segregated into the grain boundary. The V interstitial formation energy on the grain boundary is -4.20 eV from an isolated V atom and 1.13 eV from a V atom in bulk. The V atom lowers its energy by forming an interstitial defect in the grain boundary. The micro-alloying element can also be segregated on the grain boundary as a substitutional defect. The V substitutional formation energy on the grain boundary is -6.08 eV from an isolated V atom and -0.75 eV from a V atom in bulk. The negative sign indicates that the V substitution for Fe atom on this grain boundary is an exothermic process. Compared to interstitial formation energy, the substitutional formation energy is lower by 1.8 eV, which means that substitution defects occur far more often than interstitial defects. Therefore we focus on the substitutional segregation on the grain boundary in this project. The V segregation energy into the grain boundary is the difference of the grain boundary formation energy from V defect formation energy in bulk. In order to calculate the V segregation energy into the grain boundary we calculated two V point defect formation energies in bulk. One is interstitial point defect formation energies which are -1.36 eV for tetrahedral interstitial from an isolated V atom and 3.97 from a bulk V atom while octahedral interstitial defect energies are higher by 0.43 eV. The other is substitutional point defect formation energy which is -6.06 eV from an isolated V atom and -0.73 eV from a bulk V atom. The substitutional defect formation energies are again lower than interstitial one by 4.70 eV. From the calculatated energies we can conclude that V atoms exist mostly as substitutional defects in bulk and segregate into substitutional defects in grain boundaries. The V segregation energy from bulk to grain boundary is the substitutional defect formation energy in grain boundary substracted by the substitutional defect formation energy in bulk. We obtained -0.03 eV as the segregation energy of V atoms. The surface formation energy of (111) is calculated to be 0.167 eV/ $Å^2$. The V segregation energy from bulk into surface is calculated as -9.57 eV. The grain boundary cohesion energy (GBCE) without V is calculated as 1.43 eV while the GBCE with segregated V is 1.54 eV. The V segregation increases GBCE by 0.11 eV. Therefore, from our DFT calculation results we can conclude that the segregated V atom in grain boundary significantly strengthen the grain boundary against the brittle grain boundary fracture.

Experimental Results

Thermomechanical treatments were performed to investigate effects of modified structures on the mechanical behavior of DP steels. For a bake-hardening heat treatment, flat dog-bone shaped tensile specimens machined from steel sheets were deformed by an Instron machine at different pre-strainings of 0 (as-received condition), 1, 2, and 5%, and then heat treated at 170^{o}C for 20 min. After finishing such heat treatment, the specimens were cooled down to room temperature in air. By using these specimens, high strain-rate Hopkinson tensile tests were carried out at similar strain rates (~550/s). Figure 6.5.1 shows stress versus strain curves obtained from high strain-rate tensile tests on the as-received and baked speci-

mens underwent different pre-strainings. Yield strength, flow stress level, and maximum tensile strength strongly depend on the pre-strained and heat treated conditions.

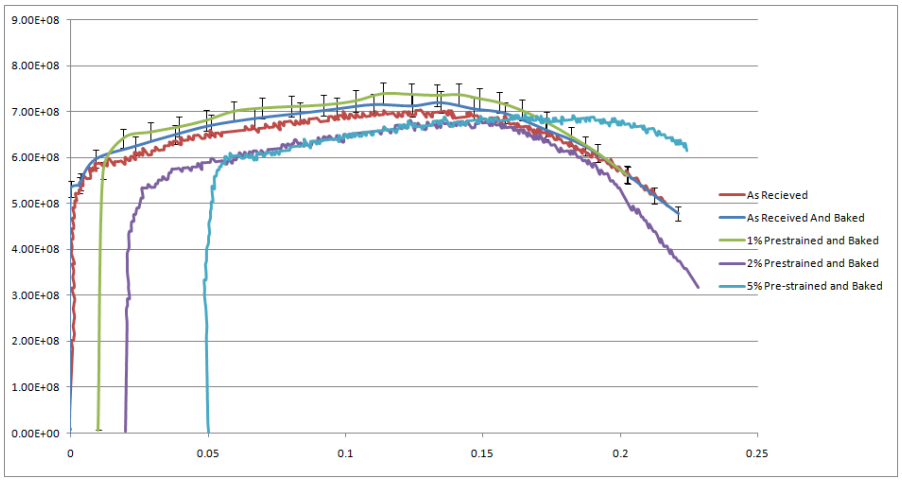

Figure 6.5.1. Stress versus strain curves obtained from high strain-rate Hopkinson bar tests in tension on the as-received and baked specimens underwent different pre-strainings.

Conclusions

The goal of this project is to investigate the effect of nanoscale precipitates and novel additives to the overall strength and formability of advanced high strength steel alloys. We developed new MEAM potentials for Fe-C and Fe-V alloy systems and tested their validity against experimental measurements and quantum mechanical first-principles calculations. Quantum mechanical first-principles simulations based on DFT were performed on the main phases of AHSS to investigate the microalloying effect of V on the grain boundaries in ferrite. We obtained the structure of V defects in one of the most common grain boundaries in ferrite and their formation energies. Our calculation shows that the segregated V atoms significantly strengthen the grain boundary against the brittle grain boundary fracture. We performed thermomechanical treatments on DP steels to investigate effects of modified structures on their mechanical behavior. We also performed thermomechanical treatment and investigated the effect of pre-strain on bake-hardening of DP steels. Our results show that yield strength, flow stress level, and maximum tensile strength strongly depend on the pre-strained and heat treated conditions.

Presentations/Publications/Patents

1. Seong-Gon Kim, M. F. Horstemeyer, M. I. Baskes, Masoud Rais-Rohani, Sungho Kim, B. Jelinek, J. Houze, Amitava Moitra, and Laalitha Liyanage, *"Semi-empirical Potential Methods for Atomistic Simulations of Metals and Their Construction Procedures,"* J. Eng. Mater. Technol., 131 (4), 041210 [9 pages] (2009).
2. Amitava Moitra, Sungho Kim, Seong-Gon Kim, Seong Jin Park, Randall German, and Mark Horstemeyer, *"Atomistic Scale Study on Effect of Crystalline Misalignment on Densification during Sintering Nano Scale Tungsten Powder,"* book chapter in "Advances in Sintering Science and Technology", eds. Rajendra K. Bordia and Eugene A. Olevsky, pp. 149-160, ISBN:9780470408490 (2010).
3. Amitava Moitra, Sungho Kim, Seong-Gon Kim, Seong Jin Park, Randall German, and Mark Horstemeyer, "Investigation on sintering mechanism of nanoscale tungsten powder based on atomistic simulation ", Acta Materialia 58, 3939—3951 (2010).
4. Sungho Kim, Seong-Gon Kim, Mark Horstemeyer, *"Vanadium effects on a BCC iron sigma 3 grain boundary strength"*, Proceedings: Collected Proceedings: Deformation, Damage, and Fracture of Light Metals and Alloys (2011).
5. Seong-Gon Kim, M. F. Horstemeyer, Hongjoo Rhee, Sungho Kim, "Task 6: Materials Design for Steel Alloys in the Southern Regional Center for Lightweight Innovative Designs (SRCLID)," DOE

Southern Regional Center for Lightweight Innovative Designs (SRCLID) Phase II Final Report, Chap 6 (2010).

6. Amitava Moitra, Seong-Gon Kim, and Mark F. Horstemeyer, "Structural and thermal properties of Calcium using a MEAM potential," preprint, submitted to Calphad.
7. L. Liyanage, Amitava Moitra, J. House, Sungho Kim, Seong-Gon Kim, and M. F. Horstemeyer, *"A modified embedded-atom-method potential for Fe-C alloy systems,"* In preparation.
8. J. House, Sungho Kim, Amitava Moitra, L. Liyanage, Seong-Gon Kim, and M. F. Horstemeyer, *"The vacancy-assisted diffusion of V atoms in cementite: An ab-initio study,"* preprint.
9. Bohumir Jelinek, Jeffrey Houze, Sebatian Groh, Seong-Gon Kim, Mark Horstemeyer, G. J. Wagner, M. I. Baskes, "MEAM potentials for Al, Si, Mg, Cu, and Fe alloys," 2010 SEAPS Meeting, Baton Rouge, LA, Oct. 20 – Oct. 23, 2010.
10. Sungho Kim, Seong-Gon Kim, Mark Horstemeyer, *"Vanadium effects on a BCC iron sigma 3 grain boundary strength"*, 2011 TMS Annual Meeting, San Diego, CA, March 2011.
11. L. Liyanage, Amitava Moitra, J. House, Seong-Gon Kim, Mark Tschopp, Sungho Kim, and M. F. Horstemeyer, *"A modified embedded-atom-method potential for Fe-C alloy systems,"* 2011 APS March Meeting, Dallas, TX, March 2011.
12. Seong-Gon Kim, "Structural, elastic and thermal properties of cementite (Fe3C) from Modified Embedded Atom Method (MEAM) potential," Colloquium at Korea Aerospace Research Institute, Daejeon, KOREA, November 23, 2011.
13. Seong-Gon Kim, "Structural, elastic and thermal properties of cementite (Fe3C) from Modified Embedded Atom Method (MEAM) potential," Colloquium at Pohang University of Science and Technology (POSTECH), Pohang, KOREA, November 29, 2011.

References

Baskes, M. I. *"Modified embedded-atom potentials for cubic materials and impurities"*, Phys. Rev. B **46**, 2727 (1992).

Baskes, M. I. "*Modified embedded-atom potentials for Fe*," unpublished.

Blöchl, P. E. *"Projector augmented-wave method,"* Phys. Rev. B **50**, 17953 (1994).

W. Callister, Materials science and engineering: an introduction (John Wiley & Sons, 2007), URL http://books.google.com/books?id=t34JSwAACAAJ.

E, W. and Engquist, B. *"Multiscale Modeling and Computation"*, Notices of the AMS, **50**, 1062-1070 (2003).

Gama, B.A., Lopatnikov, S.L., Gillespie, J.W., Jr., 2004. "Hopkinson bar experimental technique: a critical review," Appl. Mech. Rev. 57, 223-250.

Staab, G.H., Gilat. A., 1991. "A direct-tension split Hopkinson bar for high strain-rate testing," Experimental Mechanics, 31, 232-235.

Metals Handbook, 8, 2000. American Society for Metals, Materials Park, OH.

M. F. Horstemeyer and P. Wang. *"Cradle-to-grave simulation-based design incorporating multiscale microstructure-property modeling: Reinvigorating design with science"*, Journal of Computer-Aided Materials Design, **10**, 13—34 (2003).

Kim, Seong-Gon; Horstemeyer, Mark F.; German, Randall; Rhee, Hongjoo; Kim, Sungho. *"Task 2: Materials Design for Steel Alloys,"* DOE FY 2006-2007 Annual Report, Chap. 4, 52—62 (2007).

Kim, Seong-Gon; Horstemeyer, Mark F.; Baskes, M. I.; Rais-Rohani, Masoud; Kim, Sungho; Jelinek, B.; Houze, J.; Moitra, Amitava; Liyanage, Laalitha. *"Semi-empirical Potential Methods for Atomistic Simulations of Metals and Their Construction Procedures,"* J. Eng. Mater. Technol., 131 (4), 041210 [9 pages] (2009).

Kresse, G.; Furthmüller, J."*Efficient iterative schemes for ab initio total-energy calculations using a plane-wave basis set"*, Phys. Rev. B **54**, 11169 (1996).

Li, Youhong; Siegel, Donald J.; Adams, James B.; Liu, Xiang-Yang. "*Embedded-atom-method tantalum potential developed by the force-matching method*," Phys. Rev. B **67**, 125101 (2003).

Olson, G. *"Systems design of hierarchically structured materials: Advanced steels"*, Journal of Computer-Aided Materials Design, **4**, 143—156 (1998).

Perdew, J. P. and Zunger, A. *"Self-interaction correction to density-functional approximations for many-electron systems"*, Phys. Rev. B **23**, 5048 (1981).

Perdew, J. P.; Burke, K.; Ernzerhof, M. *"Generalized Gradient Approximation Made Simple"*, Phys. Rev. Lett. **77**, 3865 (1996).

Key Words

Advanced high strength steel (AHSS) alloys, strength, ductility, Dual Phase (DP) steels, Density Functional Theory (DFT), Modified Embedded Atom Method (MEAM), atomistic simulation. Grain boundaries.

Southern Regional Center for Lightweight Innovative Design

Phase III

Final Scientific & Technical Report

October 1, 2009-September 30, 2011

For compliance with contract requirements of Award DE-EE0002323

Task 7

SIMULATION-BASED DESIGN OPTIMIZATION

Submitted December 27, 2011

TASK 7: SIMULATION-BASED DESIGN OPTIMIZATION

Table of Contents

TASK 7: SIMULATION-BASED DESIGN OPTIMIZATION

Principal Investigator: Masoud Rais-Rohani
Professor, Aerospace Engineering
Mississippi State University
318C Walker Engineering Bldg., Mississippi State, MS 39762
(662) 325-7294; fax: (662) 325-7730; e-mail: masoud@ae.msstate.edu

Participants: K. Motoyama, A. Najafi, M. Rouhi, C. Tamasco, A. Parrish, and M. Kiani

William Joost: Technology Area Development Manager
e-mail: william.joost@ee.doe.gov

Magda Rivera: Project Manager
e-mail: magda.rivera@netl.doe.gov

Contractor: *Mississippi State University (MSST)*
Contract No.: *DE-EE0002323*

Objective

- Development and application of numerical and analytical methods for modeling, analysis, and optimization of automotive structures made of lightweight (metallic and composite) materials.

Approach

- Computational modeling, finite element simulations, and design optimization of components and structures made of metallic and composite materials. The developed techniques are used to investigate the (1) role of process control parameters on process simulation-based optimization; (2) manufacturing process effects on performance simulation and optimization of sheet-formed components; (3) crash simulations and multi-objective optimization of a full vehicle model with magnesium structural components; (4) influence of nano-reinforcement on energy absorption of components made of hybrid multiscale polymer composite materials.

Accomplishments

- Developed a computational framework for finite element simulation and optimization of single- and multi-stage sheet-stamping process.
- Developed a methodology for sequential coupled process-performance simulation and optimization of sheet-stamped components.
- Performed metamodel-based multi-objective crashworthiness optimization of a full vehicle model with magnesium structural components.
- Developed a computational tool for stiffness and strength modeling of nano-enhanced composite materials with application to finite element simulation of energy absorbing components.

Introduction

This final report provides a summary of activities conducted under the simulation-based design optimization task of the DOE/SRCLID project. The areas of emphasis in this report include simulation-based optimization of the sheet stamping process, examination of manufacturing process effects on

performance of structural components and the optimization of both process and product attributes, multi-crash scenario simulations of a full vehicle model with lightweight magnesium alloy components together with metamodel-based multi-objective crashworthiness optimization, and examination of the effect of nano-enhanced polymer matrix on energy absorption of crush tubes made of hybrid composite materials.

Coupled Finite-Element Simulation and Optimization of Sheet Forming Process

The objective of this study is to develop a computational framework that can be used for rapid exploration of the design space involving alternative sheet-forming process scenarios (e.g., hot, cold, single-stage, multi-stage) and models (i.e., two-or three-dimensional geometries) of varying degrees of complexity [Tamasco 2011]. The integration of numerical design optimization and forming process simulation makes it possible to take advantage of advanced and computationally efficient numerical search techniques to find the optimum set of process control parameters for forming a stamped part.

The computational framework as shown in Fig. 1 consists of three main components: a process simulation program based on nonlinear finite element analysis (FEA), an optimization code, and a response filtering and organization program for data flow management. The process simulation model requires an initial set of process control parameters, determination of the die and workpiece geometries, as well as initial process parameters such as press speed, die holding force, friction coefficient, die temperature, workpiece temperature, and ambient temperature. The initial design parameters are passed into the process simulation FEA code that creates an output containing the process responses. The raw data from the process simulation must be filtered and organized to obtain relevant information for use in design optimization. A MATLAB code was developed for this purpose.

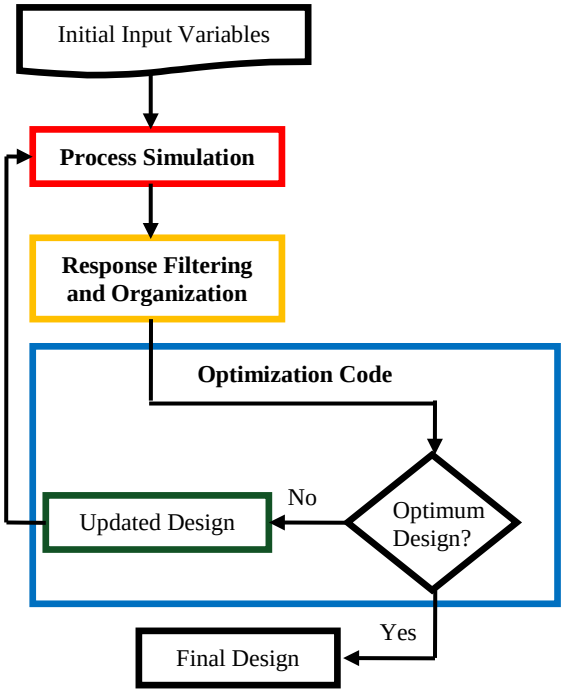

Figure 1. General process simulation-based optimization framework.

Different general-purpose FEA codes (e.g., ABAQUS, MSC Marc, LS-DYNA, PAM-STAMP) have been used to model both thin and thick sheet-forming processes. We chose Simufact.forming [Simufact 2011] as it allows a virtual modeling of the entire sheet-forming process by defining the geometry, boundary conditions, and properties of the individual forming tools and the workpiece for a single- as well as multi-stage forming processes. Built on MSC Marc implicit nonlinear FEA solver,

Simufact.forming can model different failure conditions as well as the material grain size evolution during the different stages of the forming process.

In setting up the forming simulation, part geometries are imported as CAD models and assigned to different components (e.g., blank, dies, punch). Forming induced responses such as Cockroft Latham damage [Marc 2010], effective stress, effective plastic strain, major strain, minor strain, grain size, and damage are output directly for each element integration point whereas springback, thinning, and forming limit diagram (FLD) failure must be calculated as post-processed responses based on Simufact.forming output.

Both the average and maximum values of each response are used in the optimization problem, allowing the designer to control both the overall quality of the workpiece (with the averages) as well as indication of localized problems in the product (with extreme values).

Application Problem

Components with complex shapes often require two or more forming stages, with each stage requiring a different set of dies to create an incremental change in the shape. Here, a design optimization problem involving the multi-stage forming process of an axisymmetric component is considered [Tamasco 2011]. Although the complete forming of the selected component requires seven stages, only the first two stages are considered to reduce the overall computation cost. Figure 2 shows the initial and final geometry of the workpiece (modeled as a strip) in the first three forming stages and how they relate. The workpiece has been rotated 180° to show a cross-sectional view of the full component.

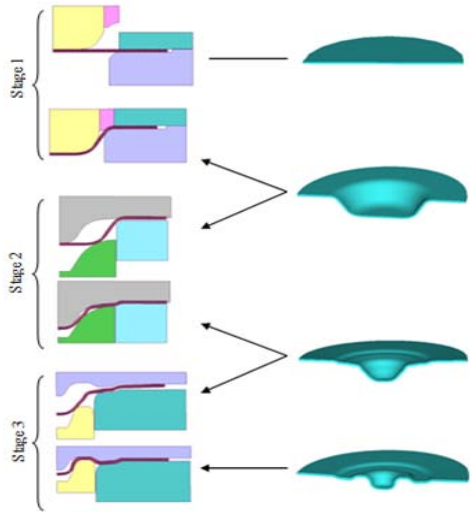

Figure 2. Forming process stages of an axisymmetric component.

Both selected stages have different input variables including press speeds, friction coefficients, initial workpiece temperatures, and die temperatures. The blank used has an initial thickness of 5.1 mm and is modeled using arbitrary quadrilateral axisymmetric ring elements developed specifically for axisymmetric applications. These are four-node, isoparametric elements that represent a constant strain throughout the element. Because of the constant strain, a fine mesh is required to capture material behavior. Stage 1 uses a mesh of 800 elements. Because of its complexity, stage 2 requires a mesh of 3,000 elements for convergence. The re-meshing option utilizes a front advancing quad technique on both stages of this simulation. The linking of the two stages occurs using the first stage's results file. Simufact.forming reads the output files from the first stage to set the beginning parameters for the second stage. These parameters include damage, temperature, displacement, and strains for each element and integration point.

Thinning and damage are two of the main concerns in this example as the displacement in the first stage has the ability to cause excessive thinning of the part. Damage and thinning appear to be correlated as shown in Fig. 3, especially in regions with excessive thinning.

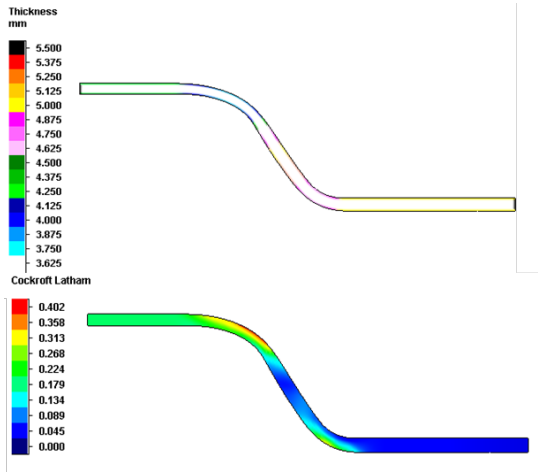

Figure 3. Stage 1 results showing thickness and damage distributions.

A sensitivity analysis was performed using eleven design variables: a persistent ambient temperature (TA), die temperature for stages 1 (TD1) and 2 (TD2), initial workpiece temperature for stages 1 (TWP1) and 2 (TWP2), friction coefficient for stages 1 (μ1) and 2 (μ2), press speed for stages 1 (P1) and 2 (P2), and blank holding force for stages 1 (F1) and 2 (F2). This sensitivity analysis was set up using a partial factorial design of experiments approach. The sensitivity is represented as a normalized main effect of each design variable on a given response. The baseline model is described in Table 1 with the corresponding responses given in Table 2.

Table 1. Initial values of process parameters

	Ambient Temperature (^{0}C)	Workpiece Temperature (^{0}C)	Die Temperature (^{0}C)	Friction Coefficient	Press Speed (mm/s)	Holding Force (kN)
Stage 1	20	20	20	0.5	20	100
Stage 2	-	20	20	0.5	20	1000

The design variables take either a high or low value at each design point taken to be +/- 35% of their baseline value, respectively. The 35% bounds were selected by manually testing the simulation to find the widest range of design variable variance that still allowed for simulation convergence. Only the responses from stage 2 of this simulation are used.

Table 2. Baseline response values for the multi-stage forming simulation

	Damage	Grain Size (mm)	y-springback (m)	x-springback (m)	Thinning
Average	1.36E-01	3.95E-07	2.12E-04	1.25E-05	1.52E-04
Maximum	5.85E-01	1.19E-07	9.74E-02	8.41E-05	1.35E-03

Figure 4 shows the normalized main effects of the design variables on second stage damage. An increase of 35% in press speed in stage 1 causes a 3.5% increase in the average damage, with the other sensitivity values interpreted the same way. For damage, the most influential design variables are the first-stage friction coefficient and first-stage press speed. The negative value for the first-stage friction indicates that a 35% increase in the stage 1 friction causes a 1.47% decrease in the average damage in stage 2. The remaining response sensitivities can be seen in Figs. 5-8. The collection of figures shows that the responses of stage 2 vary with all of the selected design variables from stage 1 and stage 2.

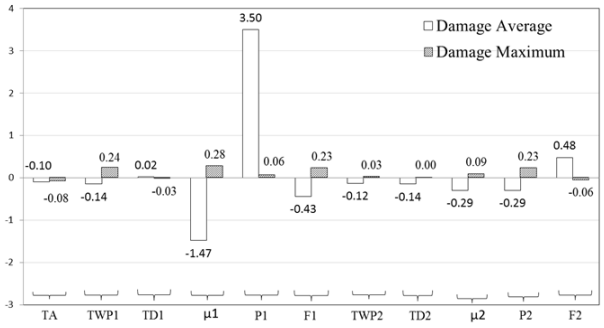

Figure 4. Normalized main effects of design variables on damage.

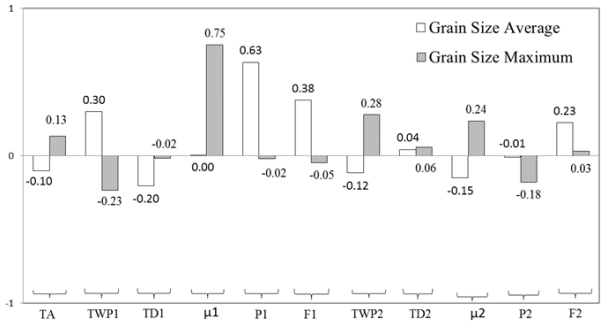

Figure 5. Normalized main effects of design variables on grain size.

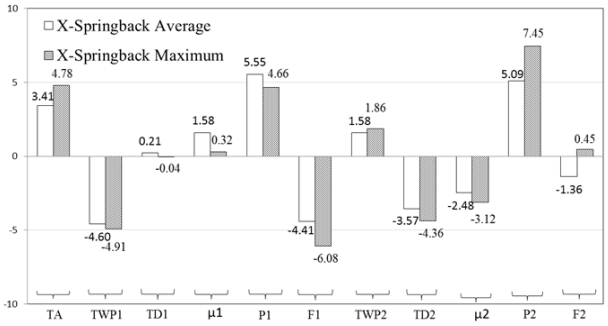

Figure 6. Normalized main effects of design variables on x-springback.

This process design problem was optimized using thinning maximum and thinning average at the end of stage 2 as the two objective functions to be minimized given equal weight factor to both objectives. Constraints were placed on the remaining responses with the exception of grain size with a 5% margin over the baseline values. The responses were formulated as a percentage of the baseline value and only the responses from the second stage are considered. The design variables were given lower and upper bounds equal to 0.35 and 1.35 times the corresponding baseline values, respectively.

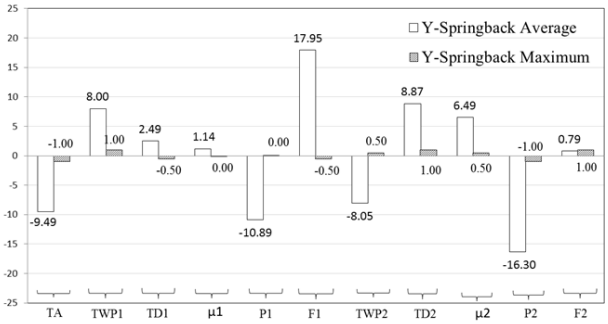

Figure 7. Normalized main effects of design variables on y-springback.

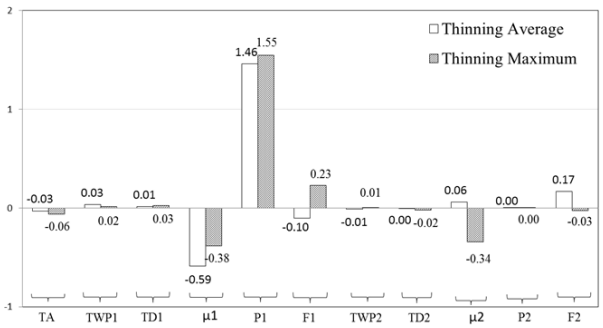

Figure 8. Normalized main effects of design variables on thinning.

The optimum design variables are given in Table 3 with the corresponding response values in Table 4. The optimization of this multi-stage process simulation was successful in decreasing the thinning average and the thinning maximum. Among the eleven design variables, μ_1, μ_2, and TD1 saw the greatest change relative to the corresponding baseline values. Thinning average decreased by 6.2% while thinning maximum decreased by 2.9%. In the optimization process, the y-springback average was decreased by 21% while the increase in the other responses such as grain size was within the specified margin of 5%.

Table 3. Comparison of Baseline and optimum design variable values

		Ambient Temp (^{0}C)	Workpiece Temp (^{0}C)	Die Temp (^{0}C)	Friction Coefficient	Press Speed (mm/s)	Holding Force (kN)
Stage 1	Baseline	20	20	20	0.5	20	100
	Optimum	20.1	21.7	10.7	0.33	19.9	100
Stage 2	Baseline	-	20	20	0.5	20	1000
	Optimum	-	20	21.8	0.33	22.4	1000

Table 4. Optimum response values

		Baseline	Optimum	% of Baseline	% Change
Damage	Avg	1.36E-01	1.35E-01	99.5	-0.5
	Max	5.85E-01	5.55E-01	94.8	-5.0
Grain Size	Avg	3.95E-08	4.03E-08	102.2	2.2
	Max	1.19E-07	1.19E-07	99.6	-0.4
Y-Springback	Avg	2.12E-04	1.67E-04	79.0	-21
	Max	9.74E-02	9.74E-02	100.0	0.0
X-Springback	Avg	1.25E-05	1.28E-05	102.5	2.5
	Max	8.41E-05	8.74E-05	104.0	4.0
Thinning	Avg	1.52E-04	1.43E-04	93.8	-6.2
	Max	1.35E-03	1.31E-03	97.1	-2.9

Sequential Coupled Process-Performance Simulation and Optimization

In sequential coupled process-performance simulations, both material properties and component geometry can evolve from one stage to the next for a more accurate prediction of the structural performance measures. Coupling of the material, process, and performance models is an important step in modeling the actual physical behavior of the material and structure while facilitating the progress toward integrated material-process-product design.

The focus of this investigation is to develop a computational framework for sizing optimization of sheet-formed components, especially those made of magnesium alloys, by considering the manufacturing process effects on performance responses using both classical and microstructure-based plasticity models. In this investigation, sheet-forming simulation (deep drawing and springback) and crush simulation are coupled in a sequential nonlinear FEA framework to investigate the effect of manufacturing process and product design parameters on energy absorption characteristics of thin-walled tubes. The analysis results from each simulation are used to establish the initial state in the subsequent simulation. The coupled process-performance simulation is combined with numerical design optimization where both geometric attributes and manufacturing process parameters are treated as design variables. Surrogate models for manufacturing-induced and performance affiliated responses are developed using radial basis functions and applied in solving the integrated process-performance optimization problem [Najafi 2011]. The specific objectives pursued include (1) examining alternative approaches for introducing the effects of manufacturing and material microstructure in plasticity constitutive models; (2) modeling of the mixed boundary / initial value problem for energy absorption in components made of a magnesium alloy; (3) designing a multilevel decomposition and optimization scheme suitable for coupled process-performance systems; and (4) applying the developed computational framework to design optimization of an energy absorbing component produced using a sheet forming process.

Application Problem

A double-hat tube, modeled by joining two identical single hat sections, is used to illustrate the coupled simulation and optimization approach. For forming simulation, two sets of blank/holder/die geometries are defined in the FE model. The same die set is mirrored with respect to blank plane considering the thickness of the blank that offsets the model to have a clearance of blank sheet thickness between two sheets. ABAQUS/Explicit is used for the deep drawing (loading) simulation, ABAQUS/Standard for the springback (unloading) simulation under isothermal condition, followed by ABAQUS/Explicit simulation for the crush analysis. The sequential coupled simulation process is depicted in Fig. 9.

Two different material models have been investigated, one based on piecewise linear isotropic hardening and the other using an internal state variable plasticity model. Here, the results based on the classical plasticity model are shown with a more in-depth discussion of both models appearing in [Najafi 2011].

Coupling scheme is utilized by transferring residual stresses and the equivalent plastic strains as the material state variables. The yield surface expands due to the isotropic hardening assumption in the model; therefore, the instantaneous yield point varies during the loading process. The yield point at the end of the forming simulation is captured by finding the plastic strain. Material data for AZ31 magnesium alloy sheet is used for all the simulations. To include rate dependency, the stress-strain curves for two extreme rates are considered with those for the other rates found through interpolation. The material behavior in terms of true stress versus true strain is plotted in Fig. 10 for the two extreme strain rates. Adiabatic heating is not considered in any of the simulations. The elastic modulus, Poisson's ratio, and density are chosen to be 45 GPa, 0.33, and 1.738 kg/m^3, respectively.

The geometric attributes are the tube cross-sectional dimensions (i.e., width, height, corner radius, and blank thickness) whereas the manufacturing process parameters are holding force, punch velocity and workpiece-die set friction coefficients. The friction coefficients for holders, dies, and punch are assumed to be equal but can be treated as different design variables. "Width" is translated into the punch width,

"corner radius" is translated into the die and holders' corner radius, "thickness" is assigned directly to the shell elements that define the blank whereas "height" is captured by controlling the punch travel distance in the direction normal to the blank surface. The rate of holding force application is kept constant in all the simulations. Punch velocity is assumed to be constant in the direction perpendicular to the sheet metal; this parameter along with the height determines the deep drawing simulation termination time.

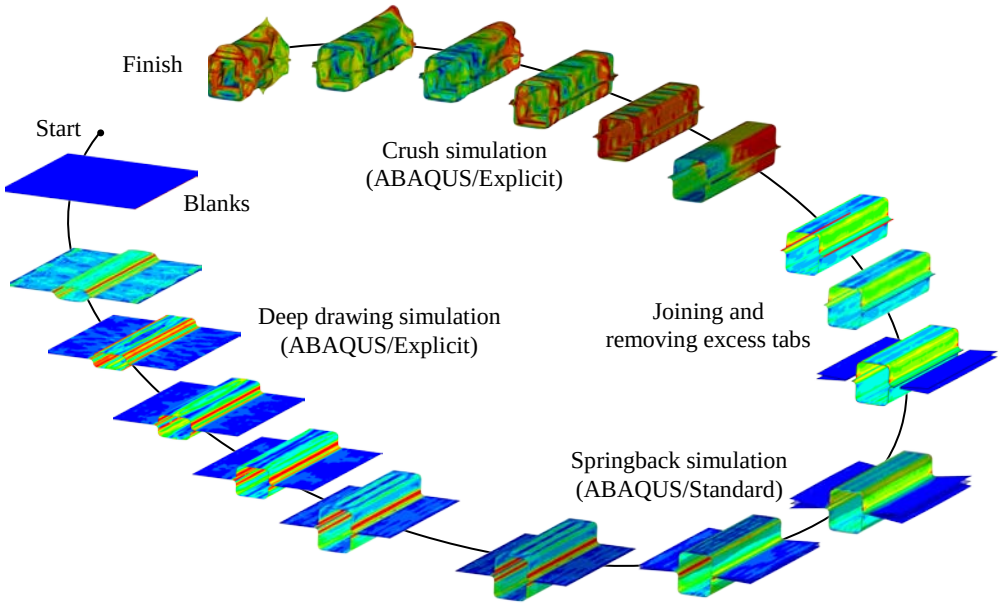

Figure 9. Sequential coupled forming-springback-crush simulations of double-hat tubes.

Six responses are assigned and defined as objective functions in the optimization problem. Rupture and thinning are the responses extracted from the deep drawing simulations, springback is a response calculated from the springback simulation and the maximum crush force and the mean crush force are the responses calculated from the crush simulation as the main two parameters to evaluate the energy absorption behavior of the double hat tubes.

Rupture is found by extracting the principal major and minor plastic strains in each element, which are compared against the forming limit diagram reported in the literature [Lee et al. 2008]. FLD that is used in this study is assumed to behave linearly in both compressive and tensile plastic strains.

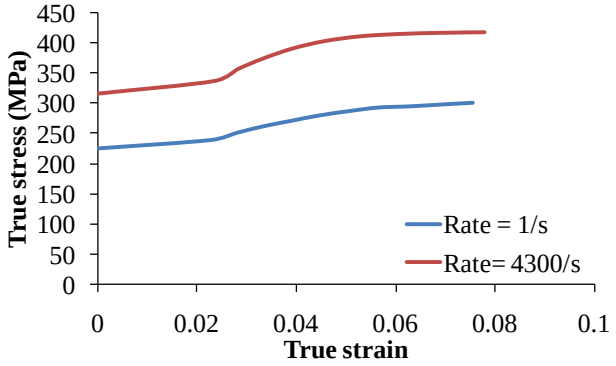

Figure 10. AZ31 sheet stress-strain curves for two different strain rates.

An automated procedure through a developed FORTRAN code is used to extract the rupture and thinning results from the ABAQUS binary file, calculate the principal strains, and incorporate the equations for each response without using ABAQUS CAE in deep drawing and springback simulations.

The maximum crush force is calculated from the contact force history of the rigid wall in the crush simulation and the mean crush force is calculated from the area under the crush force versus crush distance divided by the effective crush distance. These results are extracted and filtered using a Python scripting application available in ABAQUS and the developed FORTRAN code to calculate the mean crush force values.

A sensitivity analysis was performed to investigate the sensitivity of the selected responses to variation in each design variable [Najafi 2011]. The sensitivity results showed that sheet thickness and corner radius have significant effect on rupture response, with friction coefficient, punch velocity, and holding force having minimal effect. The rupture response was found to have a direct relationship with some parameters such as thickness and punch velocity and inverse relationship with others, corner radius being the most notable. The global measure of thinning was affected the most by changes in the corner radius, followed by blank thickness and height. In comparison, the manufacturing process parameters appeared to be less influential. Springback response appeared to be most sensitive to changes in blank thickness. Both the maximum and mean values of the crush force increase as a result of increasing the blank or tube thickness. Generally, sensitivities to the geometric parameters seem to be greater than those of the manufacturing process parameters.

To reduce complexity and computational cost of design optimization involving high fidelity simulations, reduced-order or surrogate models are often used. Different metamodeling techniques have been developed for this purpose. To train or construct a metamodel, a set of design points is selected using a sampling approach, and a design of experiments is performed to evaluate the desired response value at each design point. Radial basis functions (RBF) are used because they are suitable for representing highly nonlinear responses using relatively small number of training points. Depending on the response, a specific type of RBF function, response transformation, and an appropriate value of the tuning parameter, c can be used to enhance the metamodel prediction accuracy. Table 5 shows the list of responses and the associated error measured using cross-validation normalized root-mean-square error (NRMSE) metric [Lin et al. 1999].

Table 5. Metamodel parameters and error estimates

Response	RBF Type	Response Transformation	c	NRMSE
Rupture	Gaussian	-	1.00	2.2%
Thinning	Gaussian	ln(Thinning)	0.001	2.0%
Springback	multiquadric	ln(1e7 × springback)	0.500	1.8%
Max Crush Force	multiquadric	-	0.500	4.5%
Mean Crush Force	multiquadric	-	0.100	3.7%
Tube Mass	Gaussian	-	0.010	4.6%

When faced with competing objectives, the optimization problem becomes one of finding the non-dominated design points that form the Pareto frontier. Traditionally, manufacturing process parameters are optimized considering only manufacturing objectives. However, in this study, to enhance the energy absorption behavior of the crush tube while improving the manufacturing responses, seven design variables are selected. The multi-objective optimization problem for the coupled process-performance problem is defined as finding the optimum values of design variables that would minimize rupture, thinning, springback, mean crush force, maximum crush force, and mass subject to side constraints on design variables. The design variables represent width, height, corner radius, thickness, holding force, punch velocity, and friction coefficient. The optimization problem was solved using the multi-objective genetic algorithm toolbox in MATLAB with tournament selection algorithm, crossover fraction of 80%, and the function tolerance of 1e-4. Table 6 lists the forty-five design points that make up the Pareto frontier. The Pareto optimal points are also shown in separate performance and process criteria domains in Fig. 11. A group of seven Pareto optimum tube designs and the corresponding crush responses are shown in Fig. 12.

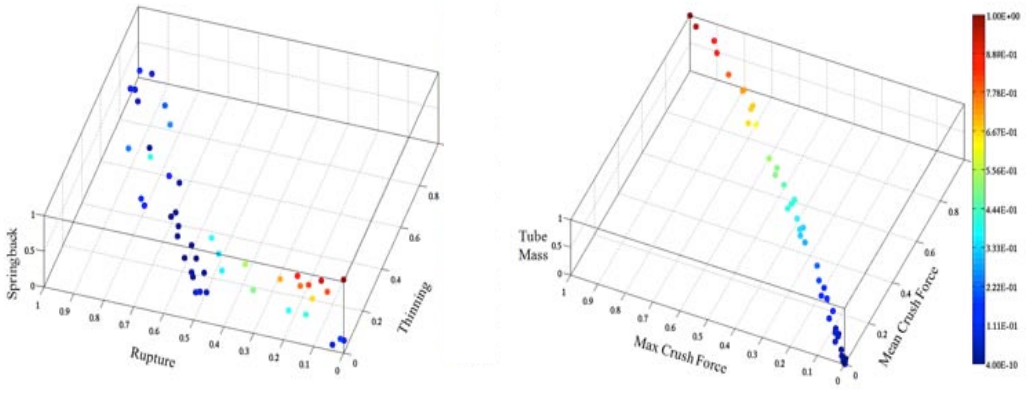

Figure 11. Pareto frontier in the performance (left) and process criteria domains.

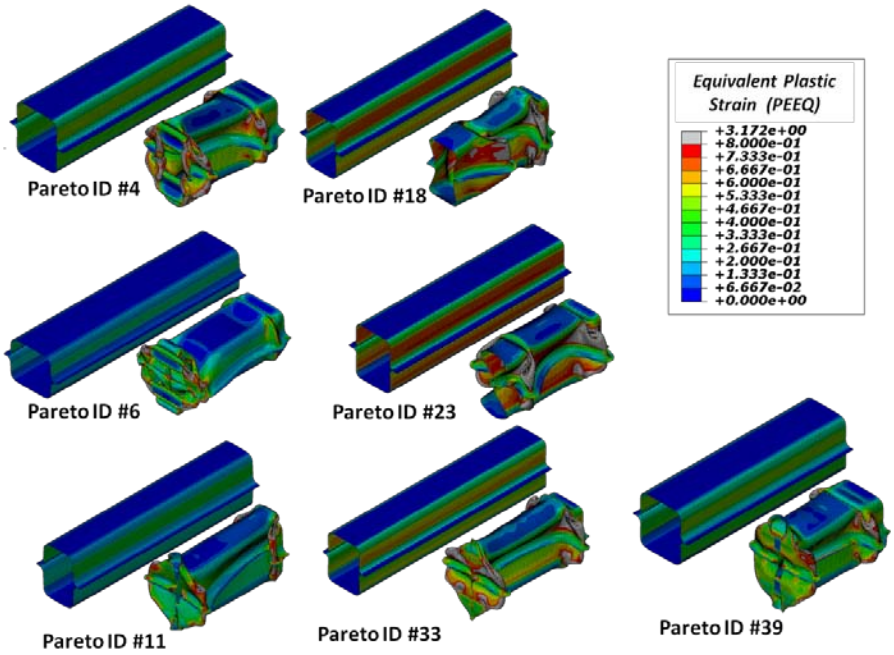

Figure 12. Geometry, equivalent plastic strain, and crush mode of sample points on Pareto frontier.

Examination of the Pareto optimum points in Table 6 shows that no design point is superior to the rest in all selected objectives. Hence, depending on the importance of a particular objective, a Pareto design point may be preferred over the rest.

Based on the results of this study, the following conclusions can be drawn: (1) the manufacturing effects can have considerable influence on the performance characteristics of formed components; (2) the manufacturing process parameters could be chosen to achieve the manufacturing objectives as well as to enhance the energy absorption characteristics of the thin wall components; and (3) Optimal selection of manufacturing process parameters causes an increase of approximately 7% in the mean crush force.

Table 6. Non-dominated design points forming the Pareto frontier

Pareto point ID	Width (mm)	Height (mm)	Corner Radius (mm)	Thickness (mm)	Holding Force (kN)	Punch Velocity (m/s)	Friction Coefficient	Rupture	Thinning	Springback	Max Crush Force (kN)	Mean Crush Force (kN)	Tube Mass (kg)
1	43.4	27.9	4.86	1.28	25.1	6.95	0.20	848.0	17.3	2.25	86.0	36.2	0.11
2	49.0	30.8	6.36	1.55	22.5	6.24	0.23	624.2	17.0	2.32	113	46.2	0.15
3	40.4	31.9	5.55	1.31	26.9	5.12	0.18	455.4	16.7	3.16	95.9	38.8	0.12
4	**58.4**	**33.2**	**5.35**	**2.09**	**32.4**	**6.85**	**0.23**	**2217**	**18.4**	**0.24**	**172**	**64.0**	**0.23**
5	65.4	22.7	6.28	1.28	26.7	6.08	0.22	684.0	15.9	1.52	93.7	32.3	0.13
6	**51.7**	**24.6**	**6.09**	**1.30**	**27.2**	**5.76**	**0.21**	**474.8**	**16.3**	**1.63**	**84.0**	**30.3**	**0.12**
7	54.9	22.9	5.55	1.28	25.3	6.73	0.21	594.6	16.5	1.09	85.1	29.1	0.11
8	65.8	35.1	6.32	2.26	32.4	6.68	0.20	1544	18.2	1.21	195	71.4	0.27
9	63.3	35.6	6.44	2.26	32.4	6.68	0.20	1534	18.2	1.14	194	71.6	0.27
10	59.0	34.8	6.13	2.24	31.9	6.57	0.23	1924	18.3	0.61	187	69.5	0.25
11	**40.1**	**31.9**	**6.33**	**1.65**	**28.2**	**5.00**	**0.18**	**569.7**	**16.8**	**3.39**	**119**	**47.8**	**0.15**
12	44.0	31.9	3.88	2.25	30.0	6.46	0.27	3902	19.0	1.21	162	62.0	0.21
13	41.4	31.8	5.98	1.85	28.2	5.22	0.19	1143	17.4	2.98	134	53.4	0.17
14	44.8	31.9	3.74	2.13	30.0	6.42	0.27	3752	19.1	1.23	154	57.7	0.20
15	39.4	31.9	6.46	1.35	28.2	5.00	0.18	762.9	16.1	3.49	100	41.5	0.12
16	44.2	31.9	3.75	1.88	28.4	6.52	0.23	3130	18.9	1.88	135	51.3	0.18
17	40.5	31.9	4.45	1.99	28.3	5.08	0.28	2701	18.8	1.57	141	54.5	0.18
18	**42.2**	**32.8**	**4.24**	**2.25**	**30.3**	**6.22**	**0.22**	**3606**	**18.8**	**1.76**	**164**	**63.7**	**0.21**
19	55.9	33.3	5.12	2.25	31.2	6.57	0.24	2764	18.6	0.44	182	67.0	0.24
20	57.8	30.9	5.35	2.08	28.9	6.61	0.22	2047	18.2	0.51	167	63.6	0.22
21	40.7	31.9	5.88	1.63	27.4	5.15	0.19	811.9	17.1	3.09	117	46.9	0.15
22	41.4	31.9	6.13	1.68	28.2	5.16	0.18	724.3	17.0	3.20	122	48.4	0.16
23	**48.5**	**31.9**	**3.91**	**2.16**	**30.5**	**6.46**	**0.27**	**3685**	**19.0**	**1.03**	**160**	**58.6**	**0.21**
24	63.5	34.2	5.71	2.26	32.0	6.65	0.20	1984	18.3	0.78	193	70.3	0.26
25	40.1	32.0	6.34	1.51	29.2	5.57	0.22	503.7	16.9	2.88	108	44.2	0.14
26	57.7	33.6	5.22	2.17	32.2	6.61	0.23	2485	18.5	0.34	179	65.7	0.24
27	49.2	32.3	5.00	2.25	30.2	6.60	0.26	3062	18.6	0.80	170	64.7	0.23
28	40.6	32.5	3.78	2.19	28.7	6.34	0.26	3872	19.0	1.52	157	61.3	0.20
29	54.2	33.0	5.00	2.12	31.5	6.66	0.25	2707	18.6	0.42	168	62.1	0.22
30	42.4	31.9	5.24	2.02	29.1	6.09	0.19	2195	18.2	2.24	146	59.3	0.19
31	39.6	31.9	6.15	1.81	28.2	5.01	0.18	951.1	17.2	3.27	131	52.5	0.17
32	42.3	33.2	4.45	2.24	31.6	6.62	0.19	3423	18.8	1.93	164	64.4	0.21
33	**41.7**	**27.5**	**3.92**	**1.81**	**29.0**	**5.97**	**0.28**	**2648**	**18.7**	**1.45**	**119**	**44.8**	**0.16**
34	45.0	31.3	3.75	2.17	30.3	6.12	0.26	3741	19.0	1.33	156	58.2	0.21
35	43.4	32.3	5.04	1.74	29.6	5.88	0.21	1699	18.0	2.18	126	49.7	0.17
36	40.1	31.9	3.97	1.91	29.0	6.02	0.21	2983	18.8	2.33	135	53.6	0.17
37	41.3	31.8	5.54	1.93	28.9	5.41	0.19	1652	17.8	2.65	139	55.7	0.18
38	43.9	32.7	4.56	2.08	31.3	6.27	0.23	3027	18.7	1.47	152	58.8	0.20
39	**60.4**	**34.9**	**6.28**	**2.26**	**32.1**	**6.59**	**0.19**	**1631**	**18.1**	**0.95**	**190**	**71.3**	**0.26**
40	40.7	32.2	4.97	1.43	29.8	4.99	0.23	1029	17.7	2.55	102	38.7	0.13
41	42.7	34.8	5.63	2.10	29.5	5.17	0.21	2003	18.1	2.15	159	60.3	0.21
42	61.5	32.4	5.47	2.22	30.2	6.52	0.23	2230	18.3	0.53	185	67.8	0.25
43	56.8	32.8	5.36	2.25	32.4	6.61	0.21	2405	18.4	0.49	183	69.0	0.24
44	57.8	33.6	5.24	2.25	32.2	6.58	0.23	2610	18.5	0.41	185	68.0	0.25
45	52.6	34.5	4.55	2.26	31.7	6.56	0.27	3338	18.9	0.69	178	64.2	0.24

Simulation and Optimization of Vehicle Structures Made of Magnesium Alloy

Stricter regulations on fuel economy and growing concerns over automobile emissions have led to an increased focus on vehicle weight reduction through the application of lightweight materials, especially in auto body structures. However, a one-to-one material substitution in absence of a thorough consideration of the overall crash characteristics may not result in a safe design.

In this study, we investigated the effects of using lightweight magnesium alloy body-in-white parts on crashworthiness characteristics and optimum design of a full-vehicle model. Full frontal impact (FFI), offset frontal impact (OFI), and side impact (SIDE) simulations were performed on a validated 1996

Dodge Neon model using explicit nonlinear transient dynamic FEA in LS-DYNA. The FFI scenario models an impact into a rigid wall at a speed of 56 km/hr. Velocity for validation and testing for SIDE was 52 km/hr to coincide with test data. The impact occurs at a 27° angle from an impact vehicle with honeycomb material simulating the front of another automobile. The OFI simulations were validated at 60 km/hr based on available test data and used for this study at 56 km/hr to coincide with FFI simulations. The Neon model impacts a honeycomb material barrier in front of a rigid wall at 40% offset. Figure 13 shows the Neon model in each crash simulation.

Crash responses considered include the intrusion distances at the toeboard and dashboard for FFI and OFI and at the door for SIDE (Int Toe, Int Dash, and Int Door), resultant acceleration at a location on the B-pillar in all three scenarios (Accel), and internal energy absorption of the selected parts in all three scenarios (Int Eng). These responses were chosen because of their relevance to occupant safety and the acceleration response location was chosen to be near the approximate head location of an occupant during a crash. The response measurement locations are shown in Fig. 14.

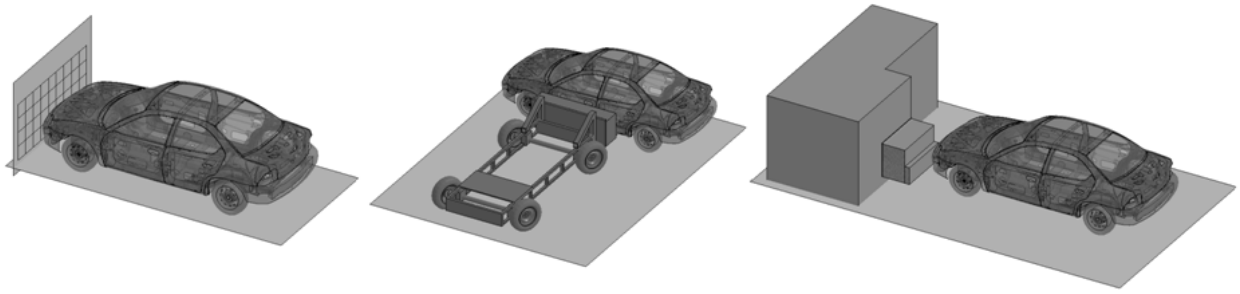

(a) (b) (c)

Figure 13. (a) FFI, (b) SIDE, and (c) OFI scenarios.

A preliminary study identified twenty-two parts of the vehicle body structure, as shown in Fig. 15, with significant contributions to energy absorption and structural stiffness. These contributions included approximately 40% of the energy absorption in all three crash scenarios with contributing mass of 105 kg or 8% of the vehicle mass at 1,333 kg. We converted the parts in Fig. 14 into AZ31 magnesium alloy with adjustable wall thickness while keeping the remaining parts the same as in the baseline model.

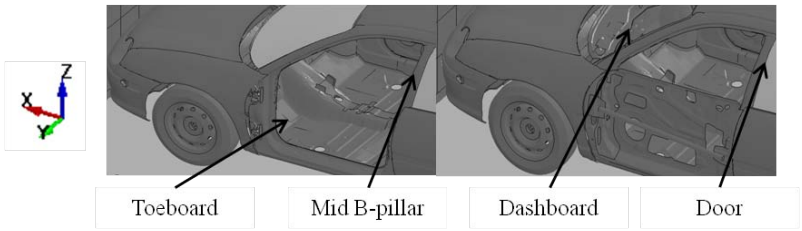

Figure 14. Structural response measurement locations.

The material model used here follows a piecewise linear plasticity law considering separate tension and compression properties and maximum plastic strain failure criterion with plastic deformation treated as the major mechanism for energy absorption. Studies at the component level show that the localized regions in the deformed component experience different load paths [Peixinho and Doellinger 2010]. In this study, Material Type 124 (MAT_124) in LS-DYNA is used to model the material behavior of magnesium parts based on the work by Wagner et al. [2010]. The stress-strain curves for AZ31 under tensile loading were obtained from experimental data. Since similar data was unavailable for AZ31 under compressive loading, the ratio of AM30 magnesium alloy extrusion under compression and tension along with AZ31 tension data were used to approximate the stress-strain curve for AZ31 compression as $AZ31(RD)_{comp} = (AZ31(RD)_{ten}/AM30\ (ED)_{ten})\, AM30(ED)_{comp}$, where RD and ED represent the

rolling and extruded directions, respectively, under tension (*ten*) and compression (*comp*). AZ31 properties in the transverse direction (*TD*) for tension and AZ31 (*RD*) for compression were used to define the MAT_124 material card.

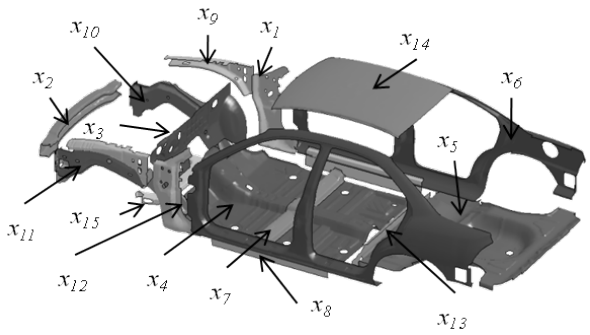

Figure 15. Structural components modified in the optimization process.

To establish a baseline model of Neon with magnesium parts, the thicknesses of selected parts were adjusted so as to maintain the same total internal energy absorption as the original steel parts. This was done using the relationship $t_{Mg} = t_{St}\,(T_{St}/T_{Mg})$, where t_{Mg} and t_{St} are the thicknesses of magnesium and steel parts, respectively, and T_{Mg} and T_{St} are the toughness values of steel and magnesium derived from integrating the stress-strain curves for each material from 0 to 0.3 strain. An average of the thicknesses found using the toughness under compression and the toughness under tension was used.

Figure 16 shows the acceleration curves at the B-pillar response location for the steel and magnesium baseline models in the three crash scenarios.

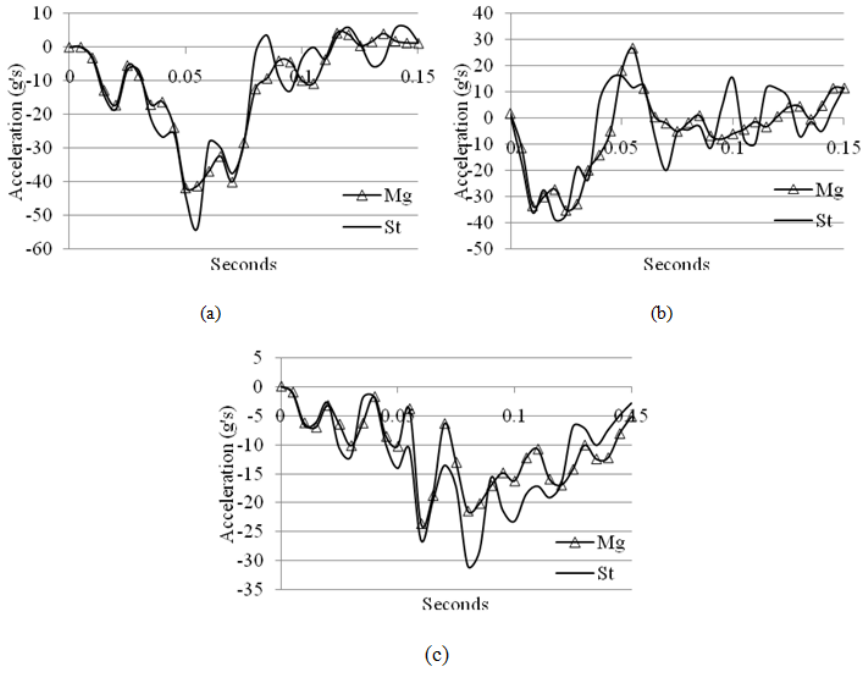

Figure 16. Acceleration at B-pillar response location for (a) x-dir. FFI, (b), y-dir. SIDE, (c) x-dir. OFI.

Response approximation is necessary in crashworthiness optimization as FE crash simulations tend to be very computationally expensive and many responses have non-smooth (noisy) behavior. Response

surrogate models in the form of analytical functions can be developed using a number of metamodeling techniques. A metamodel is built using data sets obtained through FE simulations or physical tests at the training points selected using a design of experiments (DOE) model, such as Latin hypercube sampling (LHS), based on the specified bounds of the design variables.

Due to symmetry of some of the parts in the vehicle model, only fifteen thickness values are needed for the twenty-two parts. With the fifteen thickness variables as input, forty-five design points were found using LHS in the range of ±50% of the baseline thicknesses that together with the baseline design point resulted in a total of forty-six training points. Each training point represents a different combination of thickness values for the selected parts. Three separate (FFI, OFI, SIDE) LS-DYNA simulations were performed at each training point to provide the responses necessary for metamodel construction.

Stand-alone metamodels for each response were developed and some (i.e., radial basis function, Kriging, and support vector regression) were tuned for maximum accuracy before being used to construct an optimized ensemble of metamodels [Acar and Rais-Rohani 2008]. The mathematical description of each metamodel is provided in Parrish [2011]. The models were tuned by selecting the parameter or combination of parameters that produced the least error for each response. Cross-validation generalized mean square error (GMSE) was used as the error metric. Initially, a metamodel was created using all except one training point, and the predicted response was compared to the actual response (from LS-DYNA) at the excluded training point to determine the local error. This process was repeated for all training points and the average was used as the global error of the metamodel. The optimized ensemble metamodel was then used to approximate the responses at the baseline design point and compared to the simulation response value at the initial design for both materials. This served as a baseline error when evaluating the accuracy of each optimum design.

The maximum error for the steel baseline occurred for the intrusion at the toeboard for OFI with 15% error. This was followed by 9% error for intrusion at the dashboard for OFI and 5% error for intrusion at the toeboard for FFI. The remaining responses for steel had less than 2% error at the baseline design when predicted with the ensemble. The maximum error for the magnesium baseline was 4% for the acceleration at mid. B-pillar for FFI. The remaining magnesium responses had less than 2% error.

The metamodel-based multi-objective optimization problem was formulated and solved to determine a magnesium design that would match the crashworthiness properties of the steel baseline while taking advantage of the weight savings offered by the lightweight magnesium alloy.

The multi-objective constrained optimization problem is formulated as

$$\begin{aligned} \min \quad & F(x) = f(R_j(x), j = 1,5) \\ s.t. \quad & R_j(x) \le R_{jSt} \qquad j = 6,8 \\ & R_j(x) \ge R_{jSt} \qquad j = 9,11 \\ & 0.5x_{Mg} \le x \le 1.5x_{Mg} \end{aligned}$$

where $F(x)$ is the vector of objective functions representing the differences between the intrusion distances of the magnesium design and the corresponding values in the baseline steel model, R_{jSt} for $j = 6,8$ are the baseline steel accelerations, R_{jSt} for $j = 9,11$ are the baseline steel internal energies, and x_{Mg} are the baseline magnesium part thickness values.

Several approaches may be used to solve this optimization problem. Due to the conflict that often exists among the different objectives, there are multiple optimal solutions that fall on the Pareto frontier. Depending on the level of preference (weight) given to an individual objective, a different point on the Pareto frontier may be selected as the desired Pareto optimum design. In this problem, the Pareto frontier would be defined in a five-dimensional space. Given the nonlinearity of the constraint functions involved, we chose compromise programming formulation to combine the multiple objectives into a single composite objective function expressed as

$$F(x) = \sqrt{\sum_{j=1}^{5} W_j \left[\frac{f_j(x) - f_j^T}{f_j^W - f_j^T} \right]^2}, \; j = 1..5$$

where W_j is the weight factor for the jth objective, $f_j(x)$ is the jth objective, f_j^T is the target value of the jth objective taken to be equal to the corresponding response value in the steel baseline design, and f_j^W is the worst known value of the jth objective taken to be equal to the corresponding response value in the magnesium baseline design. Given the importance of all intrusion distances to vehicle safety, we chose equal weight factors for all the objectives.

Table 7. Comparison of responses of the optimum magnesium design to the steel baseline model

	FFI		SIDE		OFI		Mass
	Accel	Int Eng	Accel	Int Eng	Accel	Int Eng	
Mg Optimum	52 g's	65 kJ	44 g's	22 kJ	35 g's	39 kJ	50.7 kg
Relative to St Baseline	-12.6%	4.5%	-8.6%	-0.4%	-2.8%	-0.1%	-51.8%

The optimization problem was solved using sequential quadratic programming (SQP) methodology with eight different initial design points. Since SQP is a local optimizer, different initial design points may lead to different local optima from which the best optimum can be selected. Surrogate-based results of the responses of interest are found in Table 7 along with a percentage comparison to the steel baseline response values. A decrease in intrusion distance, acceleration, and mass along with an increase in internal energy would be favorable. A constraint violation tolerance of 1.5% was defined when solving the multi-objective optimization problem. Table 7 shows that the optimum design produces better results for the acceleration constraints and FFI internal energy response with a minimal reduction in the OFI and SIDE internal energy responses.

Table 8. Design variable summary (thicknesses in mm)

Part	Part No.	Design Variable	Steel Baseline	Magnesium Baseline	Magnesium Optimum
A-Pillar	310,311	x_1	1.611	2.597	1.984
Front Bump	330	x_2	1.956	5.975	6.649
Firewall	352	x_3	0.735	1.072	1.515
Front Floor Panel	353	x_4	0.705	1.136	1.592
Rear Cabin Floor	354	x_5	0.706	1.138	1.696
Outer Cabin	355,356	x_6	0.829	1.366	2.049
Cabin Seat Reinforcement	357	x_7	0.682	1.099	1.649
Cabin Mid Rail	358,359	x_8	1.050	1.692	1.636
Shotgun	373,374	x_9	1.524	3.620	1.810
Inner Side Rail	389,391	x_{10}	1.895	3.966	4.141
Outer Side Rail	390,392	x_{11}	1.522	3.186	2.754
Side Rail Extension	398,399	x_{12}	1.895	3.966	5.950
Rear plate	415	x_{13}	0.710	1.144	1.717
Roof	416	x_{14}	0.702	1.157	0.791
Suspension Frame	439	x_{15}	2.606	5.342	4.931

Design variable values representing wall thickness of individual parts in mm at the baseline and optimized designs are shown in Table 8. Figure 17 shows the plot of optimum design variable values normalized with respect to the corresponding baseline values with five reaching the upper bound, one at the lower bound, and the rest scattered between the two bounds. It appears that the parts defined by design variables x_5, x_6, x_7, x_{12}, and x_{13} (see Table 8) play a more critical role than the rest.

Figure 18 shows that the intrusion distance responses at the optimum design are considerably less than those of the magnesium baseline model and most are near to or less than those of the steel baseline design with IntToe of FFI and IntDoor of SIDE being about 16% to 18% higher. The values shown in Fig. 18 are the LS-DYNA simulation results at the point of optimum rather than the metamodel predictions. The optimum magnesium parts have a combined mass that is about half that of the baseline steel design, 50.7 kg compared to 105.2 kg, and is 8 kg heavier than the baseline magnesium design.

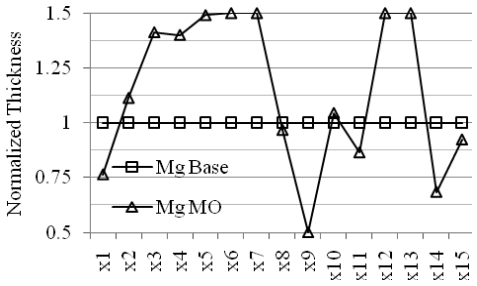

Figure 17. Normalized design variables in magnesium baseline (Mg Base) and optimum (Mg MO) designs.

Results show that the magnesium designs have lower mass than the steel designs and similar or better crashworthiness when considering acceleration and internal energy as design constraints. The optimized model with selected parts replaced with magnesium was 54.5 kg lighter than the steel baseline and 37.3 kg lighter than the optimized steel model [Parrish 2011] with similar crash responses.

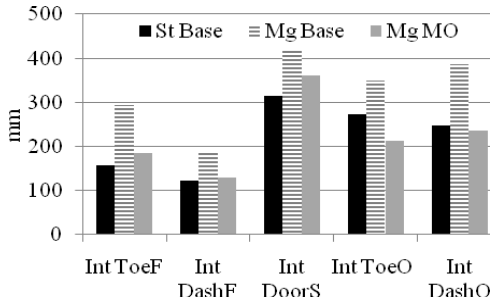

Figure 18. Comparison of intrusion distances in FFI (F), SIDE (S), and OFI (O) scenarios in steel baseline (St Base), magnesium baseline (Mg Base), and magnesium optimum (Mg MO).

Figures 19 through 21 show simulation responses of three designs for FFI, SIDE, and OFI, respectively. Most notable differences are in the door area for the FFI scenario, the door and roof for SIDE, and the roof for OFI. The overall crash response of the magnesium at the point of optimum appears to be fairly close to that of the steel baseline model.

The results of this investigation show that under the combined crash scenarios with the selected material models and design constraints, the vehicle model with magnesium alloy parts can be optimized to maintain or improve the crashworthiness characteristics with up to 50% weight savings in the redesigned parts.

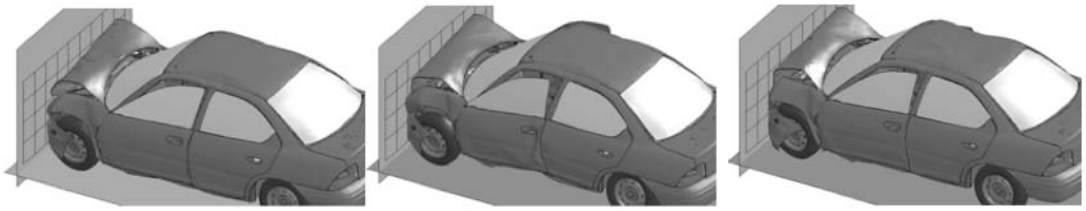

(a) (b) (c)

Figure 19. FFI simulation responses in (a) steel baseline, (b) magnesium baseline, and (c) magnesium optimum.

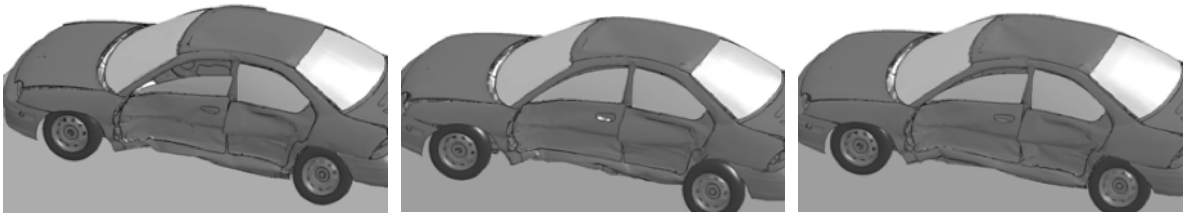

(a) (b) (c)

Figure 20. SIDE simulation responses in (a) steel baseline, (b) magnesium baseline, and (c) magnesium optimum.

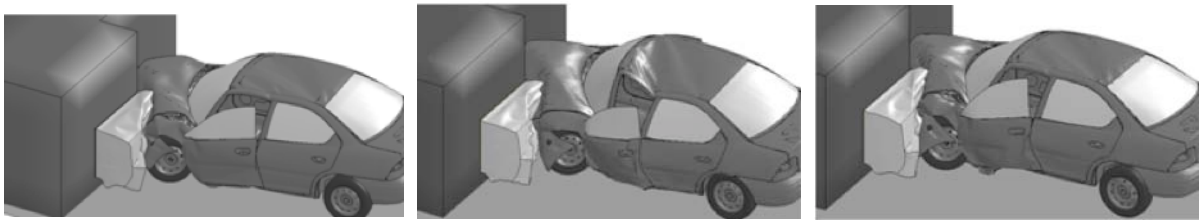

(a) (b) (c)

Figure 21. OFI simulation responses in (a) steel baseline, (b) magnesium baseline, and (c) magnesium optimum.

Modeling and Simulation of Components Made of Nano-Enhanced Hybrid Composite Materials

Microscopic images of fiber-reinforced polymer materials show the presence of a three-dimensional interphase region between the matrix and the fiber with unique properties that are different from those of the fiber and the matrix. There is considerable variability in the shape and size of the interphase. Also, the mechanical properties of the interphase are found to vary from one location to another in a manner that can be characterized as a functionally graded material.

In this study the variation of an interphase property (e.g., Young's modulus, Poisson's ratio), from the surface of the inclusion to the outmost layer of the interphase at some distance *x*, is modeled by using a general form of equation for functionally graded materials as

$$P = P_{in} + (P_{out} - P_{in}) \left(\frac{x}{L}\right)^n$$

where P represents the property of interest in the interphase at distance x away from the surface of the inclusion, with P_{in} and P_{out} representing the interphase property at $x = 0$ and $x = L$, respectively. The

parameter n is the interphase variation parameter, a constant power determining the nonlinearity of the graded property. By changing the value of n, the rate of variation of the interphase property from P_{in} to P_{out} can be adjusted as shown in Fig. 22.

Since in the multi-inclusion model [Nemat-Nasser and Hori 1993] each domain is assumed to have constant properties leading to a modified property equation expressed as

$$P = P_{in} + (P_{out} - P_{in})\left(\frac{\alpha - 1}{N}\right)^n$$

where α represents the interphase subdivision in the range of 1 to N with the assumption of piecewise constant properties in each interphase subdivision.

A MATLAB code was developed using the multi-inclusion technique to calculate the overall stiffness properties of the nano-enhanced matrix. The program input consists of the mechanical properties and volume fractions of the constituent materials (inclusion and matrix), thickness of the interphase L, as well as the interphase variation parameter n and the number of interphase subdivisions, N. Table 9 shows the effective elastic modulus of a carbon nanofiber (CNF) reinforced vinyl ester with different elastic properties of a homogeneous interphase assuming a double-inclusion representation with CNF aspect ratio of 100, CNF volume fraction of 0.01, N =1, and n = 0.

Table 9. Effective Young's modulus of CNF reinforced vinyl ester for different interphase thicknesses and elastic moduli with E_f = 450 GPa, E_0 = 3. 5 GPa, N = 1, and n = 0.

Interphase modulus E_I (GPa)	IPTR*	Effective modulus E_c (GPa)
0 (No Interphase)	0.0	4.21
	0.1	4.26
100	0.5	4.47
	1.0	4.83
	0.1	4.21
2.0	0.5	4.19
	1.0	4.15

*IPTR (Interphase thickness ratio) = Interphase thickness/ fiber radius

As expected, when the homogeneous interphase has greater elastic modulus than the matrix, the overall stiffness of the composite material increases by increasing the thickness of the interphase; otherwise, the overall stiffness decreases.

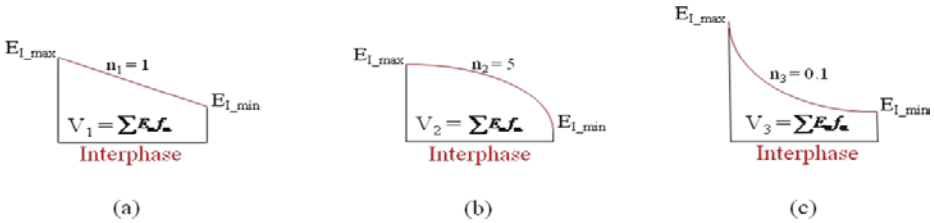

Fig. 22. Three different graded profiles for the interphase region with $V_1 = V_2 = V_3$ = interphase volume fraction weighted by the elastic modulus.

In the case of inhomogeneous interphase, the overall stiffness of the composite material is taken as the weighted average of the stiffness properties of the different phases of the coating (interphase) region based on their corresponding volume fractions. This gives the impression that the parameter that is important to the overall properties is not the profile geometry of the gradient interphase, but rather the weighted volume fraction of the interphase region. To study the effect of the profile, we altered the value

of n such that the volume ratio of the interphase region weighted by the elastic modulus remains constant (i.e., $\sum E_\alpha f_\alpha$= 0.0516). The resulting profiles for n = 0.1, 1, and 5 are shown in Fig. 22.

For a nanoreinforced material, the effect of n is captured in Table 10. To make the weighted volume fraction of the interphase equal in different profiles shown in Fig. 22, the maximum (E_{Imax}) and minimum (E_{Imin}) elastic moduli of the interphase region are adjusted as shown in Table 10. The results show that as long as the weighted volume fraction of the interphase is kept constant, the profile shape of the interphase region does not affect the overall elastic properties of the composite material. It should be noted that the overall elastic modulus of the composite material with no interphase using the Mori-Tanaka scheme is E_c = 6.236 GPa, which is approximately 60% of the value found by including the effect of interphase.

Table 10. Effective Young's modulus for different interphase profiles with E_f = 450 GPa, E_0 = 3. 5 GPa, AR = 100, and V_f = 0.03824

E_{Imax} , E_{Imin} (GPa)	E_c (GPa)		
	n = 1	n = 5	n = 0.1
450, 3.5	10.466		
350, 84	10.538		
250, 164	10.564		
150, 244	10.561		
3.5, 362	10.503		
254, 3.5		10.542	
190, 250		10.567	
138, 450		10.530	
450, 182			10.570
150, 207			10.570
3.5, 219			10.569

Figure 23 shows a circular tube model with length of 90 mm and a nominal diameter of 50.8 mm. The laminate configurations considered in this study follow [θ/0/-θ/0/-θ/0/θ] ply patterns, where the orientation angle θ may vary from 0° to 90°. The ply thickness is assumed to be 0.19 mm. The tube is held fixed against a rigid wall (support) at one end and pressed by another rigid wall (impacting plate) at the other end to crush it. In order to obtain a stable crush pattern, similar to that observed in the experiment, a trigger mechanism, in the form of small axisymmetric conical groove with a length of 5.13 mm and diameter of 52.36 mm is placed at the loaded edge of the tube. The mechanical properties of the matrix and the fiber are shown in Tables 11 and 12, respectively.

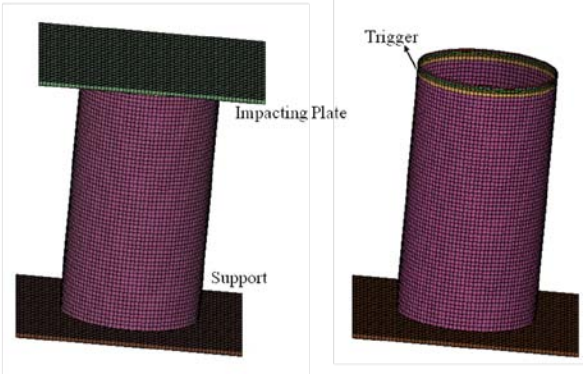

Figure 23. The crush tube model and the trigger mechanism.

Table 11. Mechanical properties of polymer matrix

Density, ρ (ton/mm^3)	1.23E-9
Young's modulus, E_m (MPa)	3447
Poisson's ratio υ_m	0.35
Tensile strength (MPa)	97.91
Compressive strength (MPa)	241.3
Shear strength (MPa)	175.8

The crush simulations are performed using the explicit FEA capabilities of Solution 700 of MD Nastran with micromechanics-based progressive failure analysis (PFA) capabilities of GENOA, implemented as a material library (MATM). The contact friction coefficient between the rigid walls and the tube is set at 0.1 to prevent slippage between surfaces. To prevent element-element inter-penetration due to excessive deformation, a self-contact condition is defined for all the element surfaces of the tube with the same friction property. After performing a mesh sensitivity analysis, the number of elements was set to 7680 with all uniformly distributed throughout the tube. The rigid walls at the bottom and top are each modeled using 1600 rigid elements. Hughes-Liu shell element formulation including an hourglass control option is used in this analysis.

Table 12. Mechanical properties of fiber

Density, ρ (ton/mm^3)	1.77E-9
Normal Modulus, E_{11} (MPa)	288200
Transverse Modulus, E_{22} (MPa)	18750
Shear modulus G_{12} (MPa)	8963
Shear modulus G_{23} (MPa)	4826
Poisson's ratio υ_{12}	0.20
Poisson's ratio υ_{23}	0.25
Tensile strength (MPa)	5226
Compressive strength (MPa)	2675
Shear strength S_{12} (MPa)	2413
Shear strength S_{23} (MPa)	2413

In this work, all the tensile failure modes for fiber and matrix are considered to be catastrophic with the degradation factor of 1%, whereas the matrix shear and compressive failure are considered to be non-catastrophic with the degradation factor of 15%. The fiber compressive failure due to fiber micro-buckling is also considered as a catastrophic failure. Transverse failure and delamination criteria are considered to be catastrophic for the matrix as well. The total material stiffness in ply level is calculated from superposition of the softened properties of each constituent.

Figure 24 shows the crush process obtained from the finite element simulation based on the above assumptions with the composite material having no nano-reinforcements. The simulation results are based on quasi-static/constant loading condition with the crosshead speed of 1 mm/min.

As the crush process progresses, continuous fronds may appear as a result of delamination in the crush zone. This phenomenon is caused mainly by the central bundle wedge that spreads radially inward, outward or both from the wall of the tube that forms a severely strained zone (compressive-tensile zone) as the moving rigid wall presses the tube further. This behavior is captured in the simulation model through two steps at the moment the damaged elements are deformed only outward/inward. The shell elements cannot be split to show possible inward and outward deformation in some cases. Once an element reaches the critical value of strain or other catastrophic failure, it will either lose stiffness or get removed from the model. The deformation pattern resulting from extensive failure and the sliding friction between the rigid wall and tube as well as the self contact between deformed and failed regions of the tube are captured phenomenologically in this simulation. Figure 25 shows the energy absorption behavior of the tube characterized based on the crush force versus crush distance curve ($\theta = 45°$).

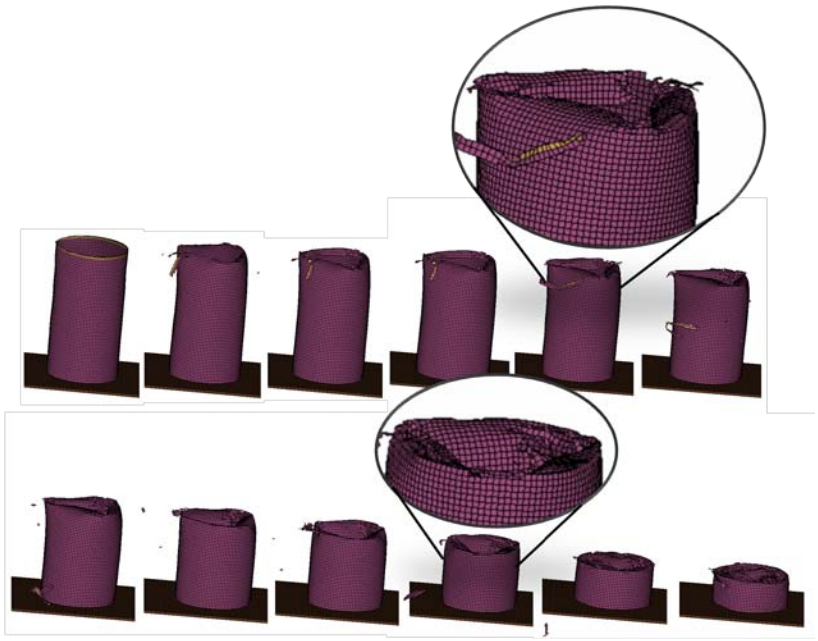

Figure 24. The crush simulation result showing the damage progression.

Normalizing the area under the curve of force-displacement plot by dividing it by the mass of the structure will give a measure called the specific energy absorption (SEA). This value may be used as a measure to compare different designs in terms of their performance in the crush process. In this study, the energy per volume has been used as SEA. The effect of orientation angle on the crush performance and the normalized energy absorption for different ply angle θ in [θ/0/-θ/0/-θ/0/θ] configurations are shown in Fig. 26. They concluded that the normalized energy absorption has a non-monotonic variation with angle θ. The mean crush force increases up to an angle of 15 degree and then drops for the 20-degree angle before reaching the maximum value near 60 degrees.

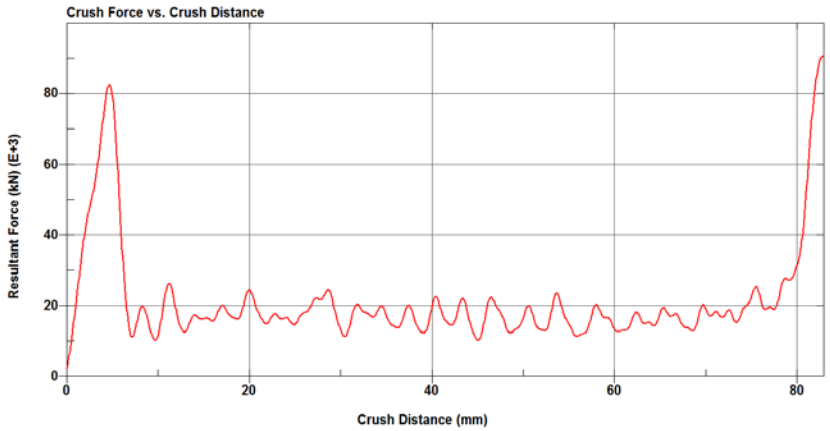

Figure 25. The crush force versus crush distance as a measure for energy absorption behavior.

All of the results shown so far for the crush tube were for the case without nanoreinforcement. The nano-enhanced matrix with uncertain properties in the constituent materials is used in the following analysis.

In considering the effect of nano-enhanced matrix on crush performance of the composite tube in Fig. 23, the random variability in the matrix, CNF, and the fiber are modeled using the statistical properties shown in Table 13.

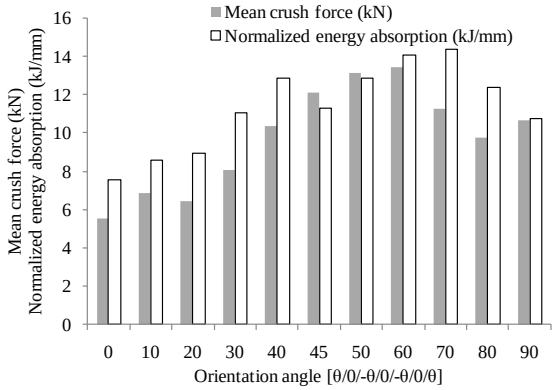

Figure 26. Effect of orientation angle in [θ/0/-θ/0/-θ/0/θ] layup on the energy absorption characteristics.

Table 13. Random variables and their statistical properties

Design Variable	Mean	Standard Deviation
Fiber Volume Fraction (FVF)	9.76E-03	0.003
Neat matrix Young's Modulus, E_m (GPa)	3.45E+00	0
Neat matrix Poisson's Ratio, ν_m	3.50E-01	0
Neat matrix Strength, S_m (MPa)	9.75E+01	5
Neat matrix Shear Strength, SS_m (MPa)	1.76E+02	10
Nanofiber Diameter, D_f (nm)	1.51E+02	30
Nanofiber Aspect Ratio	1.49E+02	30
Nanofiber Failure Stress (MPa)	1.20E+03	205
Interfacial Shear Strength, (MPa)	1.74E+02	36
Nanofiber Waviness, λ/a	2.25E+04	6425

The samples collected from these random variables cannot be used directly as input for material properties of the matrix in the crush simulations. An intermediate step is required to generate the nanoreinforced matrix properties. The properties of the nanoreinforced (enhanced) matrix along with the fiber volume fraction are the actual random variables used in the process of building the DOE, which relates the input variables to the corresponding SEA and mean crush force of the crush tube.

For the tube model with diameter of 54.22 mm, 0° ply thickness of 0.23 mm, +/-θ° ply thickness of 0.22 mm, and θ = 77°, five different random samples of properties in Table 13 are used to generate the random material properties and the corresponding tube response characteristics shown in Table 14.

Table 14. Enhanced matrix and fiber properties

	Random Sample				
Property	1	2	3	4	5
Enhanced matrix modulus, MPa	4.04E+03	4.14E+03	4.28E+03	4.43E+03	4.38E+03
Enhanced matrix Poisson's ratio	0.341	0.339	0.337	0.335	0.336
Enhanced matrix strength, MPa	100.69	110.30	102.41	116.58	111.13
Fiber volume fraction	0.598	0.476	0.463	0.406	0.531
Mean crush force, N	24,975	21,721	21,063	19,923	23,362
SEA, J/mm^3	9.2	8.0	7.8	7.4	8.6

During the loading process after a short distance beyond the trigger mechanism is crushed, crush force drops from a peak value and fluctuates a small amount until the end of the crush process as shown in Fig. 25. In order to save on computational time, subsequent simulations were performed up to a crush distance equal to 10% of the tube length with the crush mode of samples 1 and 2 shown in Fig. 27.

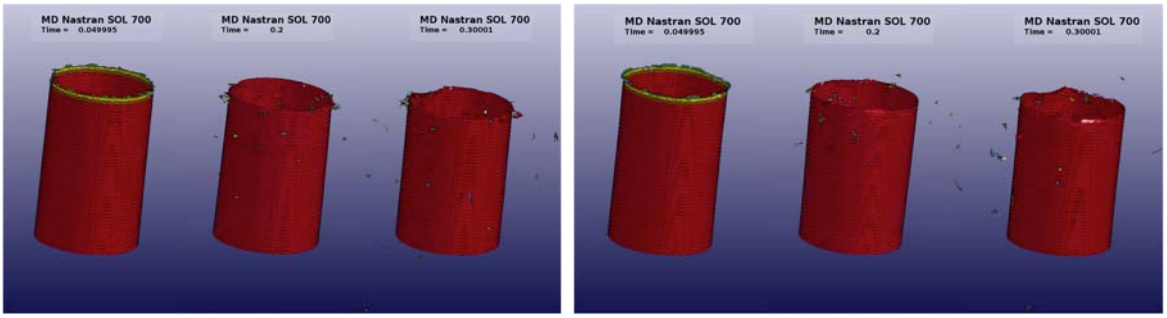

(a) (b)

Figure 27. Crush mode after a stroke length of 10% for random sample 1 (a) and 2 (b).

A more detailed description of this investigation can be found in Rouhi [2011].

Publications/Presentations/Patents

1. Parrish, A., Rais-Rohani, M., and Najafi, A., "Crashworthiness Optimization of Vehicle Structures with Magnesium Alloy Parts," *International Journal of Crashworthiness*, in press, 2011.
2. Rouhi, M., *Modeling and Optimization of Nano-Enhanced Polymer Composite Structures Under Uncertainty*, PhD Dissertation, Computational Engineering, Mississippi State University, 2011.
3. Najafi, A., *Coupled Sequential Process-Performance Simulation and Multi-Attribute Optimization of Structural Components Considering Manufacturing Effects*, PhD Dissertation, Computational Engineering, Mississippi State University, 2011.
4. Tamasco, C., *Sheet-Stamping Process Simulation and Optimization*, MS Thesis, Aerospace Engineering, Mississippi State University, 2011.
5. Parrish, A., *Crashworthiness Optimization of Vehicle Structures Considering the Effects of Lightweight Metals and Dummy Models*, MS Thesis, Aerospace Engineering, Mississippi State University, 2011.
6. Najafi, A. and Rais-Rohani, M., "Mechanics of Axial Collapse in Multi-Cell, Multi-Corner Crush Tubes," *Thin-Walled Structures*, Vol. 49, 2011, pp. 1-12.
7. Najafi, A. and Rais-Rohani, M., "Coupled Sequential Process-Performance Simulation and Multi-Attribute Optimization of Thin-Walled Tubes," Proceedings of the ASME 2011 International Design Engineering Technical Conferences, Washington, D.C., Aug 29-31, 2011.
8. Najafi, A., Rais-Rohani, M., and Hammi, Y., "Multi-Attribute Integrated Forming-Crush Simulation Optimization Using Internal State Variable Model," 1st World Congress on Integrated Computational Materials Engineering (ICME), Seven Springs, PA, Jul 10-14, 2011.
9. Najafi, A., Marin, E., and Rais-Rohani, M., "Influence of Anisotropic Texture on Crushing Behavior of Square Tubes," Proceedings of the 52nd AIAA/ASME/ASCE/AHS/ASC Structures, Structural Dynamics and Materials Conference, Denver, CO, Apr 4-7, 2011.
10. Tamasco, C., Rais-Rohani, M., and Buijk, A., "Sheet-Stamping Process Simulation and Optimization," Proceedings of the 7th AIAA Multidisciplinary Design Optimization Specialist Conference, Denver, CO, Apr 4-7, 2011.
11. Rouhi, M. and Rais-Rohani, M., "Modeling and Uncertainty Quantification of Nanofiber Enhanced Polymer Composite Materials with Functionally Graded Interphase Properties,"

Proceedings of the 52nd AIAA/ASME/ASCE/AHS/ASC Structures, Structural Dynamics and Materials Conference, Denver, CO, Apr 4-7, 2011.

12. Parrish, A., Rais-Rohani, M., and Najafi, A., "Crashworthiness Optimization of Vehicle Structures Made of a Lightweight Magnesium Alloy," Proceedings of the 7th AIAA Multidisciplinary Design Optimization Specialist Conference, Denver, CO, Apr 4-7, 2011.

References

Acar, E. and Rais-Rohani, M. "Ensemble of Metamodels with Optimized Weight Factors," *Structural and Multidisciplinary Optimization*, Vol. 37, No. 3, 2008, pp. 279-294.

Lee, S., Kwon, Y., Kang, S., Kim, S., and Lee, J., "Forming Limit of AZ31 Alloy Sheet and Strain Rate on Warm Sheet Metal Forming," *Journal of Materials Processing Technology*, Vol. 201, No. 1-3, 2008, pp. 431-435.

Lin, Y., Krishnapur, K., Allen, J., and Mistree, F., "Robust Design: Goal Formulations and A Comparison of Metamodeling Method, Proceedings of DETC-99, 1999 ASME Design Engineering Technical Conferences, Las Vegas, NV, Sep 12-15, 1999.

Marc Volume C: Program Input, V. 2010. MSC Software Corporation, Santa Ana, CA, 2010.

Najafi, A., *Coupled Sequential Process-Performance Simulation and Multi-Attribute Optimization of Structural Components Considering Manufacturing Effects*, PhD Dissertation, Computational Engineering, Mississippi State University, 2011.

Nemat-Nasser, S., and Hori, M., Micromechanics: Overall Properties of Heterogeneous Solids, Elsevier, Amsterdam, 1993.

Parrish, A., *Crashworthiness Optimization of Vehicle Structures Considering the Effects of Lightweight Metals and Dummy Models*, MS Thesis, Aerospace Engineering, Mississippi State University, 2011.

Peixinho N., Doellinger C., "Characterization of Dynamic Material Properties of Light Alloys for Crashworthiness Applications," *Materials Research*. Vol. 13, No.4, 2010, pp. 471-474.

Rouhi, M., *Modeling and Optimization of Nano-Enhanced Polymer Composite Structures Under Uncertainty*, PhD Dissertation, Computational Engineering, Mississippi State University, 2011.

Simufact.forming User's Guide, V. 10.0, Simufact Engineering GmbH, Hamburg, Germany, 2011.

Tamasco, C., *Sheet-Stamping Process Simulation and Optimization*, MS Thesis, Aerospace Engineering, Mississippi State University, 2011.

Wagner, D., Logan, S., Wang, K., Skszek, T., "FEA Predictions and Test Results from Magnesium Beams in Bending and Axial Compression," Proceedings of the SAE 2010 World Congress & Exhibition, Detroit, MI, 2010.

Key Words

Process design optimization, Coupled process-performance simulation, Crashworthiness optimization, Lightweight structures, nano-enhanced polymer materials.

Brief Description of Report

This final report describes the research activities related to the simulation-based design optimization task of DOE/SRCLID project. Particular emphasis is placed on the work done in the areas of finite element simulation and optimization of sheet-stamping, sequential coupled process-performance simulation and optimization of sheet-stamped components, multi-objective optimization of full vehicle models with magnesium structural components, and mechanical modeling of nanofiber enhanced polymer matrix materials and their application in energy absorbing components made of hybrid composite materials.

Southern Regional Center for Lightweight Innovative Design

Phase III

Final Scientific & Technical Report

October 1, 2009-September 30, 2011

For compliance with contract requirements of Award DE-EE0002323

Task 8

A MODIFIED LENS PROCESS FOR CONTROLLED NET SHAPING-INDUCED LOCAL MICROSTRUCTURE AND PROPERTIES

Submitted December 27, 2011

TASK 8: A MODIFIED LENS® PROCESS FOR CONTROLLED NET SHAPING-INDUCED LOCAL MICROSTRUCTURE AND PROPERTIES

Table of Contents

TASK 8: A MODIFIED LENS® PROCESS FOR CONTROLLED NET SHAPING-INDUCED LOCAL MICROSTRUCTURE AND PROPERTIES

Principal Investigator: Sergio Felicelli
Coleman and Whiteside Professor, Mechanical Engineering
Mississippi State University
Carpenter Engineering Bldg., Rm. 210, Mississippi State, MS 39762
(662)325-1201; e-mail: felicelli@me.msstate.edu

Co-Principal Investigator: Liang Wang
Assistant Research Professor
Center for Advanced Vehicular Systems
Mississippi State University
P.O. Box 5405, Mississippi State, MS 39762-5405
(662) 325-9235; email: liangw@cavs.msstate.edu

William Joost: Technology Area Development Manager
e-mail: william.joost@ee.doe.gov

Magda Rivera: Project Manager
e-mail: magda.rivera@netl.doe.gov

Contractor: *Mississippi State University (MSST)*
Contract No.: *DE-EE0002323*

Objective

- We aim to produce net shape alloy components with optimized as deposited microstructures by developing new manufacturing methodologies based on the Laser Engineered Net Shape (LENS®) process.
- These methodologies aim to modify the thermal history of the material to control grain sizes and phase transformations. The modification of the thermal history will be guided by simulation tools that calculate optimized heat flux distribution and cooling rates, which can achieve a desired microstructure.
- To demonstrate our objective, we will explore different materials such as low alloy steels, stainless steels, and aluminum alloys, deposited in form of single walled builds and other geometries that can be representative of an actual component.

Approach

Our approach will proceed in the following sub-tasks:

Sub-Task 1:

- We will study the solidification phenomena occurring in the molten pool during the LENS® process in order to predict the microstructure of the deposited material, including the formation of dendrites, grains, and pores.
- We will develop a solidification model that solves the transport equations in the pool using a combination of cellular automaton and lattice Boltzmann techniques.

- With the model, we will investigate the microstructure formation under different process parameters that affect the cooling rate during solidification.
- Given the temporary unavailability of our LENS® machine, we will use an outside provider to obtain samples fabricated under different conditions. Stainless steel 316 will be initially used for this research.
- The microstructure of the samples will be characterized with SEM, XRCT, and optical microscopy in order to compare with model predictions.
- The validated model will then be used to explore new process conditions that result in a finer and more uniform microstructure and that can be confirmed experimentally in a systematic way.

Sub-Task 2:

- We will develop an in-house capability to build parts with the LENS® machine at MSST. Currently, we have a LENS®-750 old model donated to MSST by TARDEC in 2006. This machine has had a number of technical issues that have prevented us from building usable parts.
- We plan to upgrade the current LENS® machine by allocating a new laser unit, changing the laser deposition head, and inert gas control system.
- The possession of this in-house capability is considered essential to executing our fundamental research and design, performing necessary experiments, securing a fast supply of samples, and advancing our knowledge of this technology.
- In addition, the ability to operate our own LENS® machine opens the possibility of using LENS® in other projects at MSST or proposes joint research that involves this technology.

Sub-Task 3:

- We will produce the Cu-H13 bimetallic samples using LENS® process, which can be applied to tooling die industry due to the high strength of H13 and high thermal conductivity of Copper.
- We will develop a thermal-mechanical model to predict the residual stress in the LENS® deposited Cu-H13 tool steel.

Accomplishments

1. Dendrite Growth Modeling: Solidification simulation development for dendritic growth under convection occurring in the molten pool during LENS® process with celluar automaton and lattice Boltzmann methods
2. LENS® System Upgrade: Allocate a new laser system (1kW IPG fiber laser) to CAVS and install to the current LENS® 750 system, upgrade the LENS® system and receive the operation training
3. Thermo-mechanical model: Develop a finite element model to simulate the temperature distribution and residual stress in the LENS® deposited Cu-H13 tool steel bimetallic parts for tooling die application

Dendritic Growth Modeling

In this work, a solidification model is developed to simulate dendritic growth under convection. The cellular automaton (CA) technique for interface tracking is coupled with a transport model - the lattice Boltzmann method (LB) - for calculating heat and solute transfer by both convection and diffusion during solidification.

Our approach will proceed in the following two main subtasks: 1: Model the solidification phenomena occurring in the molten pool during the LENS® process in order to predict the microstructure of the deposited material, including the formation of dendrites, grains, and pores, 2: Develop an in-house capability to build parts with the LENS® machine at MSU.

In the present work, the LB is adopted to numerically calculate the fluid flow, solute transport and heat transfer. The governing equations and boundary conditions for transport phenomena and fluid flow can also be found in literature.

The energy and solute transport simulated by the LB method was validated by comparing the simulation results of temperature and composition distribution to analytical solutions. Also, the LB-CA model was validated by modeling the free growth of a single dendrite and comparing the tip velocity and equilibrium liquid composition to those obtained by the analytical LGK model with various undercoolings. Figure 8.1 shows the tip growth velocity and equilibrium concentration of the steady-state growth of an Al-3wt%Cu dendrite as a function of undercooling. As observed, a good agreement is obtained between LB-CA and the values calculated by the LGK theory as well as those obtained by a Finite Element (FE) – CA model previously developed by the authors.

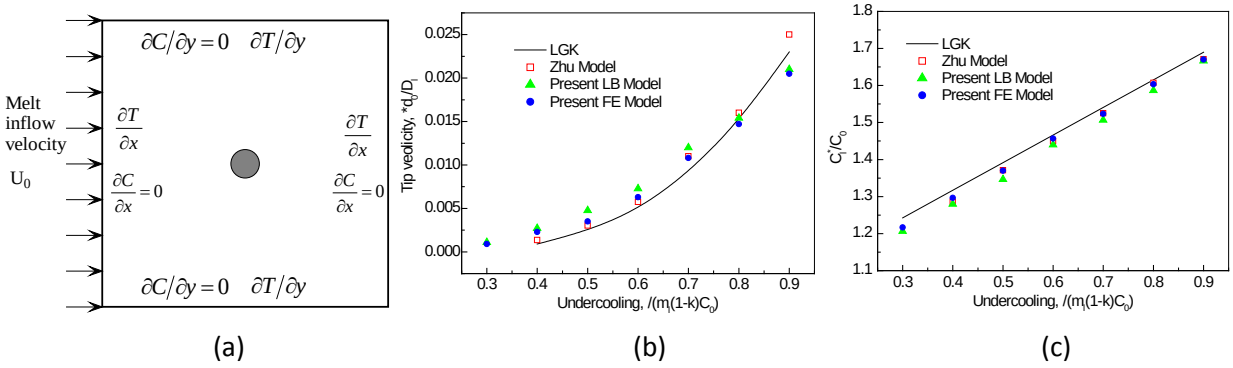

Figure 8.1. (a) Schematic of dendrite growth model and boundary conditions (changed to achieve different undercoolings). Comparison between numerical simulations and LGK model predictions of the steady-state (b) tip velocity and (c) tip equilibrium liquid composition for Al-3.0wt%Cu alloy

All the performed simulations of dendrite growth were done for a binary Al-3wt% Cu alloy. In the example of Figure 8.2, a single nucleus with 0-degree preferential direction was placed at the center of a calculation domain of 90×90μm discretized with a 300×300 grid. Three cases were studied for different boundary condition: Case 1 – constant undercooling and no convection; Case 2 – constant temperature gradient (400 K/m) imposed on the four boundaries and no convection; Case 3 – inflow imposed on the left wall ($\boldsymbol{U_{in} = 0.023 m/s}$). Figures 2(a-c) show the single dendrite morphologies and composition fields for simulation cases 1 – 3 by the LB-CA model. By comparing the dendrite morphologies shown in Figures 2(a) and (b), it is observed that the cooling rate due to the heat extraction from the boundaries enhances the side branching and thus the formation of secondary arms. By comparing the dendrite morphologies shown in Figures 2(a) and (c), it is noticed that the growth of dendrite arms is enhanced in the upstream side. As the dendrite grows, solute rejected to the liquid ahead of the solid/liquid interface is washed away by the upstream fluid flow, which leads to an asymmetrical solute distribution and dendrite morphology.

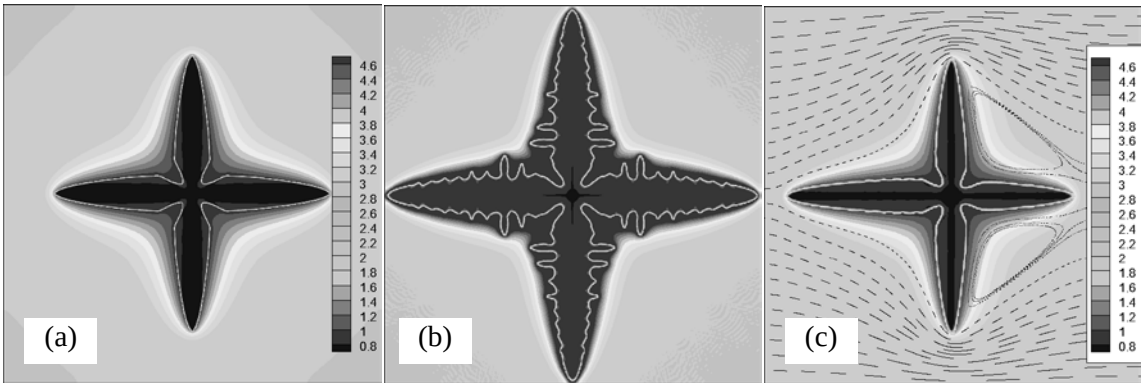

Figure 8.2. Dendrite morphology and solute map with various boundaries conditions. (a) solute diffusion only; (b) solute + heat ; (c) inflow at left side ($U_{in} = 0.023m/s$).

A multiple dendrite case is considered in the next example. Figure 8.3 presents the simulated evolution of equiaxed multi-dendrite growth. The domain is assumed to have uniform initial temperature and composition. Seven nuclei with an initial composition kC_0 and random preferred growth orientations ranging from 0 to 90 degrees with respect to the horizontal direction were randomly distributed in the calculation domain.

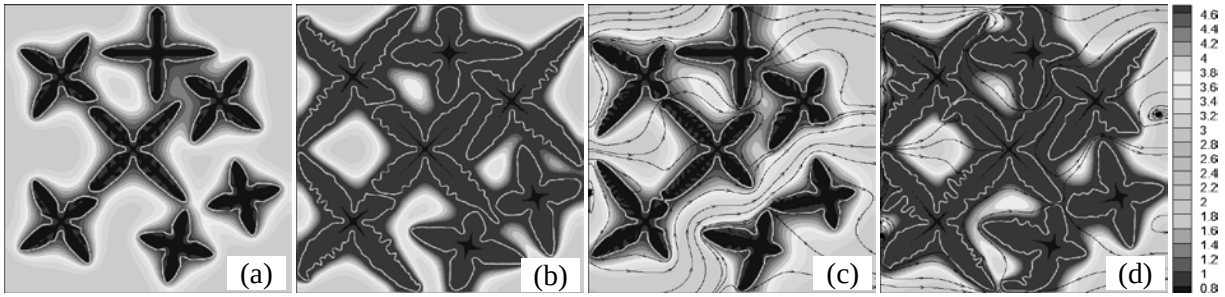

Figure 8.3. Equiaxed growth of multiple dendrites of Al-3.0 wt% Cu alloy solidified with (a) solute transport only, (b) a constant heat flux at boundaries, (c) constant inflow velocity at left side, and (d) inflow velocity and constant heat flux at boundaries.

Figure 8.3(a) shows the simulated dendrite morphologies considering only solute transport. It is observed that the dendrites develop the main primary arms along their crystallographic orientations but without secondary arms. The growth of some primary arms is suppressed by nearby dendrites. A cooling rate due to heat flux imposed at the boundaries enhances the side branching as shown in Figure 8.3(b). Figure 8.3(c) is similar to the simulation of Figure 8.3(a) but with convection added, due to an imposed inflow on the left boundary. Compared to Figure 8.3(a), the primary dendrite arms shown in Figure 8.3(c) are coarser and longer in the upstream direction than those in the downstream direction. Finally, Figure 8.3(d) shows the simulated dendrite morphologies when both solute and heat transfer with convection are included in the model. The melt flow washes away the interdendritic composition and enhances the dendrite growth and the merging between dendrites. It is observed that convection promotes the removal of solute from the solid/liquid interface in the upstream side and thus increases the interface stability, resulting in coarsening of the dendrite morphology.

LENS® System Upgrade

We upgraded the LENS® system after the new laser was installed in Sep 2010. Now the system is back to working conditions with the following capabilities:

1. 1 kW brand new laser system: The brand new laser system was installed in the LENS® machine with proper operation. The output of the laser power is about 110% of the nominal value.
2. Substrate bonding with optimized process parameters: When the process parameters were fine tuned and the substrate was cleaned carefully, the deposited material can be built on the substrate without the bonding problem.
3. Well-controlled atmosphere in the chamber with the oxygen below 2.0 ppm: After fixing the leaking problem and replace the front door of the chamber, now the atmosphere in the chamber is well controlled and the oxygen can be easily controlled below 2.0 ppm.
4. Substrate preheating up to 600F: The substrate preheating function is working properly and can heat the substrate up to 600F within 30 minutes.
5. Multiple choices of scanning strategies: The LENS® slicing software can provide multiple choices of the scanning strategies for studied geometries. For example, the laser and powder delivery nozzle assembly can scan the same layer twice before increasing the working distance in the Z direction.
6. Flexible geometries through CAD design: The geometry files can be obtained from CAD software (Pro-Engineering, CAD Drawing, etc.) and send to the LENS® computer.
7. Flexible adjustments of laser power and powder flowrate during the operation: The laser power and powder flowrate can be adjusted during the laser operation. This is very helpful in particular for the first few layers of the deposition close to the substrate. The large variation of the laser power input is necessary at the first few layers due to the large heat sink of the substrate.

After repairs made to the LENS® machine were complete, samples were made to ensure the machine was functional. Several samples were made using various simple geometries. Although the machine was operating correctly, the laser did not seem to produce a large amount of power. After running extensive tests to find the problem, the issue was not resolved. The decision was made to wait until the training to solve the problem.

Training on the LENS® machine was provided by Richard Grylls, from Optomec, on May 23-26. The training included basic operation of the LENS® machine, programming, substrate preparation, laser and powder alignment, and cleaning of the machine. Also during the training, a 50 percent drop, in the laser power, was found between the laser and the deposition head. After further investigation, it was found that a mirror was damaged. To fix this problem, a new mirror was ordered to replace the damaged one. During the repair, Richard pointed out the need for a straight deposition head to replace the laser wrist. Richard also recommended that the oxygen sensor be recalibrated, to ensure a desirable atmosphere.

After the training, a new deposition head was designed from suggestions by Richard. Also, a new laser power meter was ordered. While the deposition head was being made, the old cooling system was removed, because it was leaking coolant into the glovebox. The coolant is also believed to have affected the atmosphere of the glovebox. A light was also added inside the glovebox to provide a better view of the samples being made.

Currently, the parts for the new deposition head are being machined. After the deposition head is installed, recalibration of the oxygen sensor will occur. The machine is expected to be fully operational and producing samples soon.

Achievements

1. Ordered a new mirror and installed on the top of the LENS® machine
2. The power meter does not work, a power meter was received from Optomec
3. Removed two items from the powder flow lines – the pinch-valve, and the Army-installed box.
4. Alignment of the laser beam and received 50% output laser power
5. Laser and powder flow alignment
6. Laser focus point test, powder flow focus point test, baggie test
7. Run a few tests to build single wall and square samples with AISI 316L stainless steel powder
8. Go through all operation manuals including run log, set-up sheet, toolpath, checklist, documentation procedure, sample preparation procedure, powder requirement, partprep software, netfabb software, DMC command, advanced DMC command
9. Created toolpath DMC files for line build with variation of power and powder flow rate
10. Introduced each part in the LENS® system including powder flow meter, bubbler, argon recirculator, dri-train system, vacuum pump, anti-chamber, laser, chiller, oxygen sensor, axis magnifier, and ICM 2900 control panel.
11. LENS® workstation control V2.7.7 instruction
12. Laser head design

Finite Element Modeling of LENS® Deposited H13 Tool Steel on Copper Substrate

A three-dimensional thermo-mechanical finite element model is developed to simulate the temperature history and residual stress in a Cu-H13 sample (H13 powder on a solid Cu substrate) deposited by the LENS® process. The laser power and scanning speed along with two different scanning strategies are optimized to obtain a pre-defined molten pool size for each layer. The temperature history and cooling rates obtained from the thermal analysis are used for the residual stress analysis in the built part. In order to verify and compare the results, the model is also applied to a H13-H13 sample (H13 powder on a solid H13 substrate). Different distributions of residual stress, depending on different material samples, scanning speeds and scanning strategies, are discussed. The simulated stress distributions are compared with the available experimental results in literature.

Figure 8.4 shows the geometry and finite element mesh used in this study. The thin wall is developed by depositing 10 single layers of material, each with a length of 10 mm, a width of 1.0 mm, and a thickness of 0.5 mm, over the surface of a substrate having the geometry of 14 by 5 by 5 mm. Three different scanning speeds (2, 5 and 10 mm/s) and two different scanning strategies, alternative (Fig. 8.5(*a*)) and unidirectional (Fig. 8.5(*b*)), are investigated for both the Cu-H13 and H13-H13 samples. The idle time is kept 0.02 s for the alternative scanning, and 0.2 s for the unidirectional scanning.

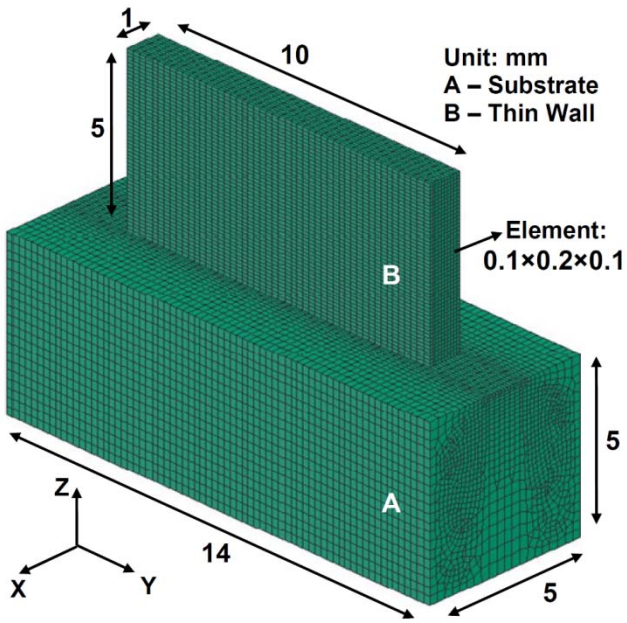

Figure 8.4. Geometry and meshing of the thin wall and substrate used for the thermo-mechanical model.

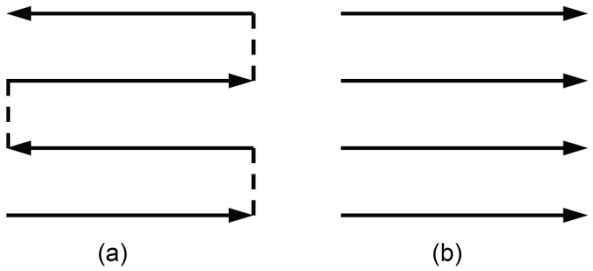

Figure 8.5. Scanning strategies used in this study, (a) alternative, (b) unidirectional.

A schematic clarification for the increase of laser power with scanning speed is shown in Figure 8.6. As we increase the scanning speed from V_1 to V_2 without changing the laser power (Q_1), the laser beam covers more distance along the layer for a certain time gap; that means, any point on a layer gets less heating time and receives less energy. As a result, we obtain a molten pool with higher surface radius but with lower depth. In other words, during the deposition of the layer A on the layer B with a scanning speed of V_2 and a laser power of Q_1, the molten pool will not sufficiently penetrate into the layer B. Consequently, there will be a lack of fusion between the two layers, which increases the possibility of pores and cracks in the final deposited part. One possible way to ensure proper fusion between layers A and B is to increase the laser power to Q_2 at scanning speed V_2.

Figure 8.7 shows the molten pool size and shape as the laser beam approaches the center of layers 2 to 10 in the Cu-H13 sample at different scanning speeds. A steady molten pool size indicates relatively steady temperature distribution for each pass, which results in uniform phase proportion and microstructure for the finished part. For a fixed scanning speed the molten pool size is kept approximately same for each layer. However, with the increase of scanning speed the pool size increases as, at a higher speed, the laser beam travels more distance for a certain time gap. This finding provides some guidance on the in-situ melt pool close-loop control system in the LENS® process. In the current melt pool control system, the approximately constant melt pool size is predefined and maintained for all process parameters during the deposition. However, the predefined melt pool size should be increased for higher scanning speed in order to reduce the risk for the lack of fusion between the adjacent layers, which is one of the main causes to form porosity in the LENS® deposited parts.

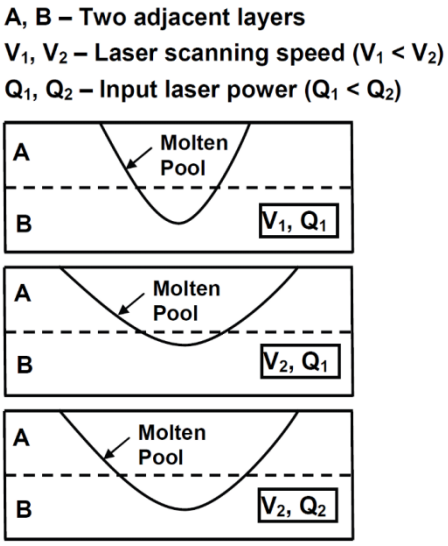

Figure 8.6. Schematic illustration of the increase of input laser power with scanning speed.

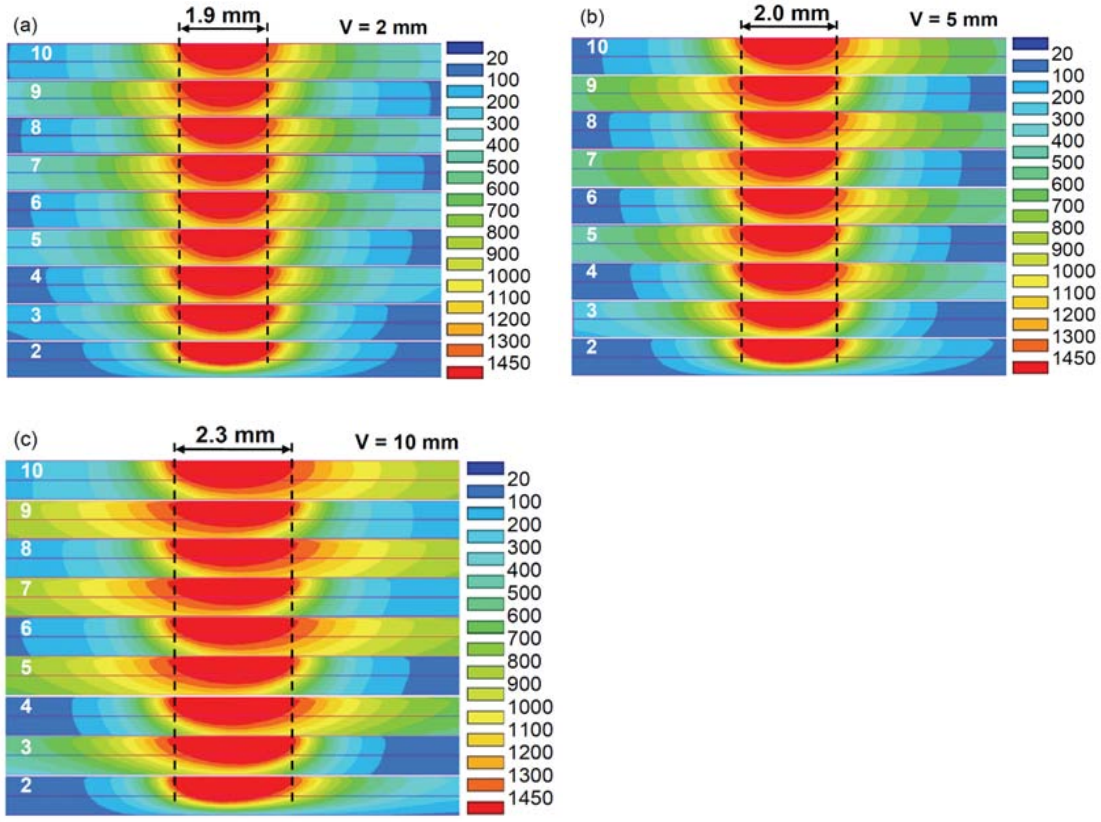

Figure 8.7. Molten pool size and shape as the laser beam approaches the center of layers 2 to 10 of Cu-H13 sample for alternative scanning at speed (a) 2 mm/s, (b) 5 mm/s, and (c) 10 mm/s.

Figure 8.8 shows the distribution of residual stress in the Cu-H13 sample for alternative scanning at the speed of 2 mm/s after the deposited part has cooled to room temperature. It can be observed that the stress concentration is higher at a region near to the free edges of the first layer. The Z-component of the

residual stress is found to be more dominant than the other components, which is consistent with the experimental investigation performed by Pratt et al. [1] on AISI 410 LENS® plates.

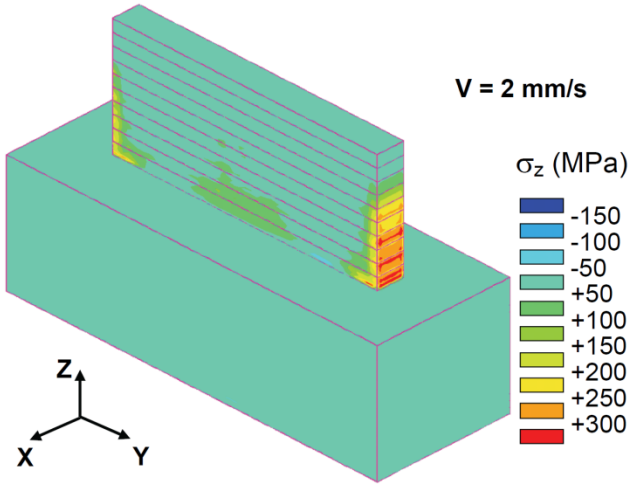

Figure 8.8. Residual Stress (σ_z) contours in the Cu-H13 sample for alternative scanning at speed 2 mm/s.

A qualitative comparison between the simulated residual stress distributions in the H13-H13 sample, for alternative scanning at the speed of 2 mm/s, and the experimental results on AISI 316 LENS® plates [2] is shown in Figure 8.9. It is worth mentioning that the measurements were performed on a wall with different geometry (25.4 by 1.5 by 90 mm) and material (stainless steel AISI 316). Five data points from the experiment are considered to compare the trend of residual stress distributions as well as the stress values at the free edges. Both simulated and experimental results show that the residual stress (σ_z) is tensile near the free edges and compressive near the center. In spite of the material and geometric dissimilarities, the simulated tensile stress values at the free edges closely approximate the experimental values obtained for AISI 316 LENS® plates.

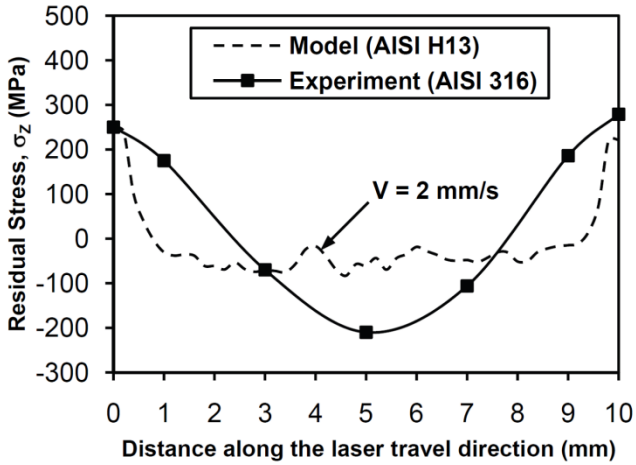

Figure 8.9. Qualitative comparison of the simulated residual stresses in H13-H13 sample for alternative scanning strategy with the published experimental results for AISI 316 LENS® plates [2].

Conclusions

1. This dendritic solidification work presented a new solidification modeling technique to simulate dendrite growth that uses lattice-Boltzmann to solve the transport equations and cellular automaton to track the interface. Simulations of single and multiple-dendrite growth with the

binary Al-3.0wt%Cu alloy were performed showing good stability and accuracy. When compared with a finite element – cellular automaton model, the LB-CA model showed significant improvement in scalability for problems involving solidification under convection.

2. The LENS® 750 unit was upgraded with new laser system. The operation training was conducted at CAVS. Additional upgrades including laser deposition head, well-controlled inert gas environment are necessary before the system is fully functional.
3. A three dimensional thermo-mechanical finite element model is developed to simulate a 10-pass LENS® deposition of H13 powder on a solid Cu substrate (Cu-H13 sample), using the SYSWELD software package. In parallel to the Cu-H13 sample, the same model is also applied to a H13-H13 sample (H13 powder deposited on a solid H13 substrate) to compare and verify the results.
4. The input laser power is optimized for each layer, considering three different scanning speeds and two different scanning strategies, to maintain a steady molten pool size and a fixed pool depth of one and half layers thickness. The z-component (growth direction) of the residual stresses is found to be more dominant than the other components, and is compressive near the center of the wall and tensile at the free edges. The simulated results are consistent with the published experimental results of previous researchers.

Presentations/Publications/Patents

1. Talukdar, T., Wang, L., Felicelli, S.D., "Thermo-mechanical Modeling and Simulation of LENS® Desposited Bimetallic Parts: H13 Tool Steel on Copper Substrate", *Journal of ASTM International*, Special Issue on Thermal Process Modeling, Simulation and Optimization, Submitted, 2011.
2. Zaeem, M.A., Yin, H., Felicelli, S.D., and Wang, L., "Simulation of Dendrite Growth in Solidification of Al-3.0 wt.% Cu Alloy using Cellular Automaton and Phase-field Methods," in Review, *Metallurgical and Materials Transaction B*, 2011.
3. Yin, H., Felicelli, S.D., Wang, L., "Solidification Model Combining Lattice Boltzmann and Cellular Automaton Methods," *Acta Materialia*, Vol. 59, 2011, pp. 3124-3136.
4. Wang, L., Felicelli, S.D., Coleman, J., Johnson, R., Taminger, K., Lett, R., "Microstructure and Mechanical Properties of Electron Beam Deposits of AISI 316L Stainless Steel", in ASME International Mechanical Engineering Congress, November 11-17, 2011, Denver, CO.
5. Talukdar, T., Wang, L., Felicelli, S.D., "Effect of Process Parameters on the Residual Stress in LENS®-Deposited H13 Tool Steel on Copper Substrate", in ASME International Mechanical Engineering Congress, November 11-17, 2011, Denver, CO.
6. Zaeem, M. A., Yin, H., Felicelli, S., "Comparison of Cellular Automaton and Phase Field Models to Simulate Dendritic Solidification", in 4th Int. Multi-Conference on Eng. and Tech. Innovation, Orlando, FL, 183-186, 2011.
7. Yin, H., Wang, L., Felicelli, S.D., "Solidification Model Coupling Lattice Boltzmann Method with Cellular Automaton Technique," in Shape Casting: 4th International Symposium, eds. M. Tiryakioglu, J. Campbell, P.N. Crepeau, TMS, Warrendale, PA, 2011, pp. 29-36.

References

1. Pratt P., Felicelli S.D., Wang L., and Hubbard C.R., "Residual Stress Measurement of Laser-Engineered Net Shaping AISI 410 Thin Plates Using Neutron Diffraction," *Metallurgical and Materials Transactions A*, Vol. 39, 2008, pp. 3155–3163
2. Rangaswamy P., Holden T.M., Rogge R.B., and Griffith M.L., "Residual Stresses in Components Formed by the Laser-engineered Net Shaping (LENS®) Process," *Journal of Strain Analysis for Engineering Design*, Vol. 38, 2003, pp. 519–527

Key Words

Laser Engineered Net Shaping, LENS®, cellular automaton, lattice Boltzmann, finite element method, dendrite growth, cooling rate, solidification, residual stress

Brief Description of Report

A coupled cellular automaton and lattice Boltzmann model was developed to simulate the dendritic solidification microstructure in the molten pool during the LENS® process. The model was used to simulate single and multiple dendrite growth with the binary Al-3.0wt%Cu alloy. The simulation results were compared with a finite element – cellular automaton model, showing that the LB-CA model has significant improvement in scalability for problems involving solidification under convection. With regard to the LENS® system upgrade, a new laser unit was allocated and the operation training was conducted at CAVS. Additional upgrades including laser deposition head, well-controlled inert gas environment are necessary before the system is fully functional. To demonstrate the LENS® application in the tooling die industries, a three dimensional thermo-mechanical finite element model was developed to simulate the LENS® deposition of Cu-H13 tool steel bimetallic materials. The commercial software SYSWELD was used to model a 10-pass LENS® deposition of H13 powder on a solid Cu substrate. The input laser power is optimized for each layer, considering three different scanning speeds and two different scanning strategies, to maintain a steady molten pool size and a fixed pool depth of one and half layers thickness. The z-component (growth direction) of the residual stresses is found to be more dominant than the other components, and is compressive near the center of the wall and tensile at the free edges. The simulated results are consistent with the published experimental results of previous researchers.

List of Acronyms

LENS® – Laser Engineered Net Shaping
PDAS – Primary Dendrite Arm Spacing
SDAS – Secondary Dendrite Arm Spacing
CA – Cellular Automaton
LB – lattice Boltzmann
MSST – Mississippi State University
SEM – Scanning Electron Microscope
OM – Optical Microscope
XRCT – X-Ray Computed Tomography
HAZ – Heat Affected Zone

MISSISSIPPI STATE UNIVERSITY

Southern Regional Center for Lightweight Innovative Design

Phase III

Final Scientific & Technical Report

October 1, 2009-September 30, 2011

For compliance with contract requirements of Award DE-EE0002323

Task 9

STRUCTURAL NANOCOMPOSITE DESIGN

Submitted December 27, 2011

TASK 9: STRUCTURAL NANOCOMPOSITE DESIGN

Table of Contents

TASK 9: STRUCTURAL NANOCOMPOSITE DESIGN

Principal Investigator: Thomas E. Lacy
Associate Professor, Aerospace Engineering
Mississippi State University
P.O. Box A, Mississippi State, MS 39762
(662) 325-2754; fax: (662) 325-7730; e-mail: lacy@ae.msstate.edu

Participants: H. Toghiani, C.U. Pittman, Jr., S. Nouranian, J. Yu

William Joost: Technology Area Development Manager
e-mail: william.joost@ee.doe.gov

Magda Rivera: Project Manager
e-mail: magda.rivera@netl.doe.gov

Contractor: *Mississippi State University (MSST)*
Contract No.: *DE-EE0002323*

Objective

- Design of low-cost nanoreinforced composite systems for automotive structural applications.

Approach

- A multiscale design methodology is being employed to investigate the effects of nanoreinforcements on the mechanical properties of fiber-reinforced composites for automotive structural applications. This work addresses the following critical issues: fabricating coupon scale samples for static and dynamic testing and development of a multiscale materials modeling strategy for assessing high-performance nanocomposites subjected to static and dynamic loadings.

Milestones, Metrics and Accomplishments

- A full factorial experimental design/response surface methodology was employed to examine nanocomposite formulation and processing variables that lead to optimal dynamic mechanical and impact properties, as well as to tailor nanocomposite architectures.
- A synergistic multiscale modeling approach has been developed using molecular dynamics, micromechanics, and progressive failure simulations to predict the effective properties and nonlinear material response of structural nanocomposites.

Introduction

Establishment of structure-property relationships for polymers (Shonaike, 2003), polymer composites (Chasiotis et al., 2005), and polymer nanocomposites (Thostenson, 2006), which account for relevant irreversible processes manifested at fundamentally different spatial and temporal scales, is increasingly becoming a focal point in materials modeling and simulation efforts. Development of a coherent integrated multiscale analysis framework is crucial for determining the effect of microstructural features in polymers (Fermeglia and Pricl, 2007; Valavala et al., 2007; Bouvard et al., 2009) and nanoscale reinforcements in polymer nanocomposites on micro-, meso-, and macroscale material behavior (Tadmor et al., 2000; Gates et al., 2005; Odegard et al., 2005; Buryachenko et al., 2005; Zeng et al. 2008; Maiti,

2008). This is particularly true when describing lower length scale phenomena not amenable to direct observation or physical measurements. The efficient transfer of scale-specific model data in computations performed at successively higher or lower length scales is one key challenge in multiscale composites modeling (Zeng et al., 2008). Specification and validation of an appropriate "handshake" protocol linking calculations performed at disparate spatial or temporal scales has posed a serious obstacle in multiscale material model development for polymer nanocomposites (Zeng et al., 2008). These difficulties are mainly due to the complex nature of these materials and poor knowledge about the key mechanisms influencing the material behavior at different time and length scales. Establishment of a robust Integrated Computational Materials Engineering (ICME) framework for polymer composite design and analysis requires seamless integration between high fidelity scale-specific models.

In this work, key issues in the multiscale modeling of thermoset vinyl ester (VE) matrices reinforced with pristine and oxidized vapor-grown carbon nanofibers (VGCNFs) are addressed. The issues raised here will apply generally to thermoset nanocomposites of all types. VGCNF/VE nanocomposites are relatively low-cost material systems with promising mechanical properties for use in nano-enhanced continuous fiber structural composites (Plaseied et al., 2008; Plaseied and Fatemi, 2009; Hutchins et al., 2009; Nouranian et al., 2011a). A combination of molecular dynamics (MD) simulations, micromechanics, and hybrid finite element calculations is being used to determine nanocomposite material behavior spanning the molecular, nano-, micro-, meso-, and macroscales (Figure 1). Because of the relatively high surface-area-to-volume ratio associated with nanoreinforcements, MD simulations are being performed to investigate the formation of a distinct interphase region at the VGCNF/VE interface. Nanoreinforcements are mixed with a liquid resin and then the resin is cured to form the nanocomposite. Prior to curing, the redistribution of liquid monomers (characterized in terms of the local monomer mole ratio) can occur near the nanoreinforcement's surface, which can generate an "interphase" region (Jancar, 2009) in the cured nanocomposite. MD simulations have also been used to generate the crosslinked resin network employing knowledge of monomer reactivity ratios, chemical regio-selectivity, and growing radical concentrations. Then, the VGCNF/VE interphase properties and interfacial strengths will be estimated based upon VGCNF pull-out simulations. Also, the resin mechanical and dynamic mechanical properties will be calculated (Ray, 1988; Brown and Clarke, 1998; Qi et al., 2005).

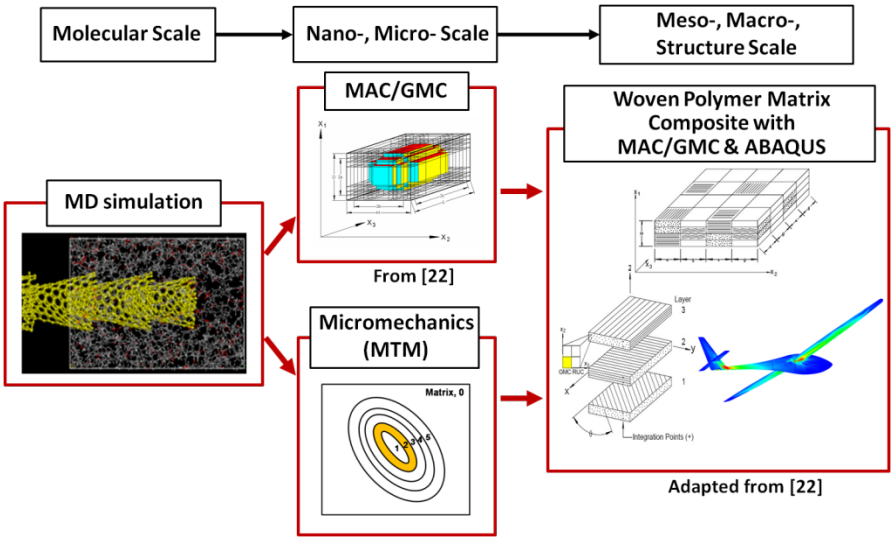

Figure 1: Multiscale modeling in composites (Adapted in part from (Arnold et al., 1999)).

Appropriately averaged VGCNF/VE interphase properties and interfacial strengths developed using MD simulations will be employed in analytic and/or computational micromechanics models aimed at determining effective material properties of VGCNF/VE nanocomposites. A parametric study investigating the effect of interphase properties on bulk nano-phased matrix properties was previously performed by Yu et al. (2011a) and is briefly summarized in this work. That study accommodated both hollow and wavy nanofibers. The NASA special-purpose composite failure analysis code, MAC/GMC (Micromechanics Analysis Code with the Generalized Method of Cells) (Arnold et al., 1999) is being used in conjunction with the ABAQUS (2009) finite element solver to simulate progressive failure of composites at the micro-, meso-, and macroscale in a temporally concurrent, spatially sequential fashion.

Experimental Structure-Property Relations for Nanoreinforced Materials

A crucial aspect of this work is to establish structure property relationships for hybrid composites comprised of a nano-enhanced resin (i.e., VGCNF/VE) and traditional continuous fiber reinforcements. Several previous reports have examined the effect of fabrication and processing variables on the tensile, compressive, flexural, dynamic mechanical, and high strain rate behavior of VGCNF/VE nanocomposites at room temperature. In this report, additional experimental efforts investigating the effect of temperature on nanocomposite dynamic mechanical properties are presented in brief, as are room temperature Izod impact test results. Additional experimental efforts aimed at use of vacuum assisted resin transfer molding (VARTM) and other low-cost hybrid composite fabrication techniques are currently ongoing.

Dynamic mechanical properties

The Dynamic Mechanical Analysis (DMA) of VGCNF/VE nanocomposites using a design of experiments (Montgomery, 2009) approach was previously reported (Nouranian et al., 2011a) incorporating four formulation and processing factors, i.e., VGCNF type (pristine, oxidized), use of dispersing agent (no, yes), mixing method (ultrasonication, high-shear mixing, and high-shear mixing/ultrasonication combination), and VGCNF weight fraction (0, 0.25, 0.50, 0.75, and 1.00 parts per hundred parts resin (phr)). The study aimed at developing a robust statistically rigorous framework for design, fabrication, and predictive response surface modeling of VGCNF/VE nanocomposites. The developed response surface models and optimized factor level combinations were valid for room temperature. However, since polymer properties are highly temperature dependent, knowledge of material behavior over a range of temperatures provides more flexibility in the material design, which is crucial for many applications. Therefore, the previous experimental design was extended to add temperature (in four levels, i.e., 30, 60, 90, and 120 ˚C) as a separate design factor in the study (Nouranian et al., 2011c). This led to new response surface models incorporating two quantitative factors, i.e., VGCNF weight fraction and temperature, which allowed for a temperature-dependent optimization of the nanocomposites' storage and loss moduli. The response surface models were developed for the storage and loss modulus for statistically determined significant sets of qualitative factor level combinations. The predicted storage modulus was a function of three mixing combinations, i.e., high-shear mixing (or high-shear mixing/ultrasonication), ultrasonication with oxidized VGCNFs in the presence of a dispersing agent, and ultrasonication with other VGCNF type/dispersing agent combinations over the entire temperature range (30-120 °C). The three-dimensional (3D) response surfaces for these factor level combinations are shown in Figure 2. In this figure, the storage modulus increases with increasing VGCNF weight fraction and decreases with increasing temperature. A similar but simpler dependence was observed for the loss modulus, where the ultrasonication combinations all had the same effect on the predicted loss modulus. The response surface models were used to identify combinations of formulation and processing factors that would lead to optimal predicted nanocomposite viscoelastic properties over the entire temperature range. The use of high-shear mixing, oxidized VGCNFs without a dispersing agent or pristine VGCNFs with a dispersing agent, and a VGCNF weight fraction of ~0.50 phr are recommended for maximizing the storage modulus at low, moderate, and high temperatures. For a low loss modulus over the same temperature range, the combination of oxidized VGCNFs with no dispersing agent is recommended. However, the combination of pristine VGCNFs with a dispersing agent would yield moderate energy

dissipation (loss modulus). To maximize the loss modulus over the entire temperature range, the use of ultrasonication with ~0.25 phr VGCNF is recommended. Nevertheless, this will result in lower predicted storage moduli compared to the high-shear mixing.

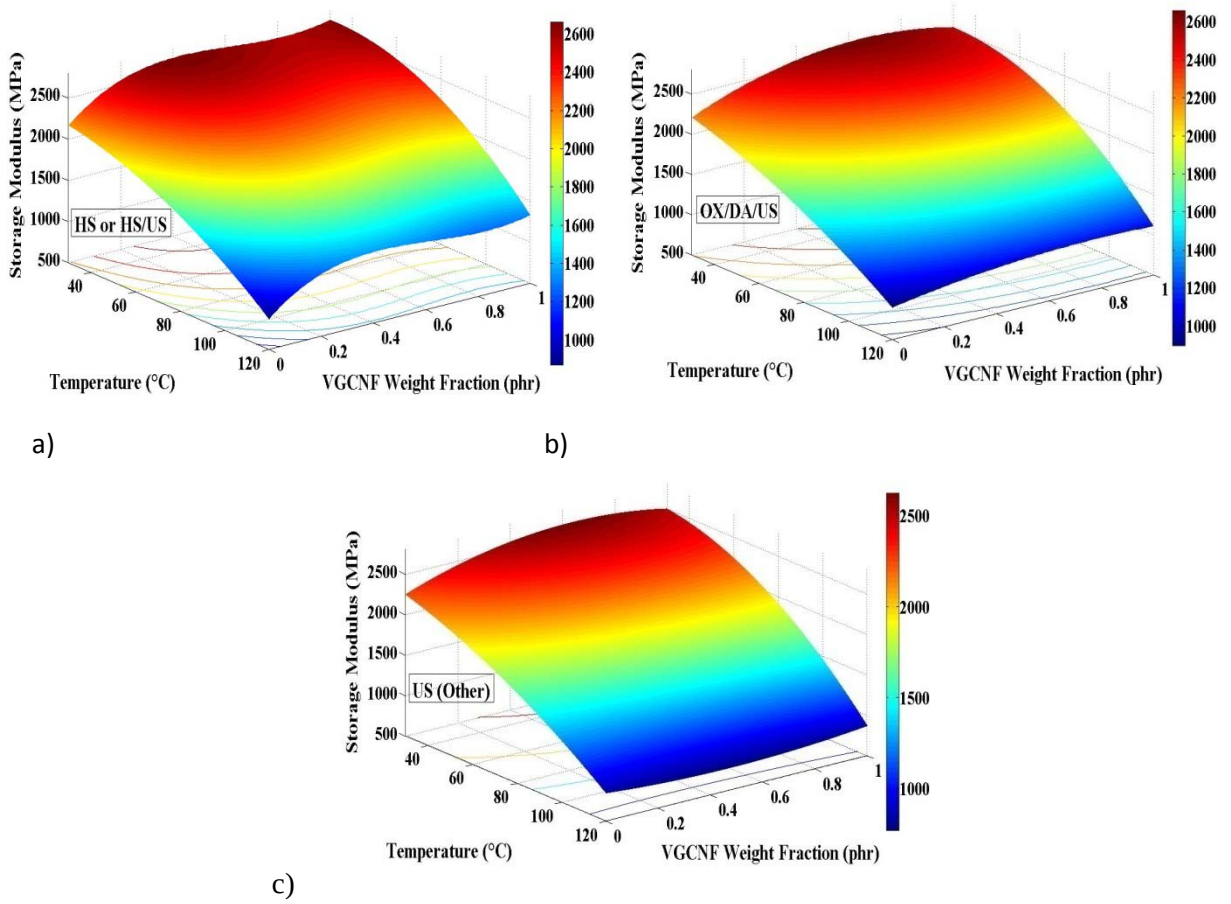

Figure 2: The predicted response surface and contour plots for the storage modulus as a function of VGCNF weight fraction and temperature for a) the case where either high-shear mixing (HS) or coupled high-shear mixing/ultrasonication (HS/US) is used, b) the case where oxidized VGCNF (OX), dispersing agent (DA), and ultrasonication (US) are used, and c) the case where oxidized VGCNF (OX), dispersing agent (DA), and ultrasonication (US) are used.

Impact properties

Notched-Izod impact strength testing was conducted on a series of VGCNF/VE nanocomposites, where a central composite design (CCD) of experiments technique (Myers et al., 2009) was employed (Torres et al., 2011). The CCD allows for a statistical separation of factor effects (i.e., high shear mixing time, ultrasonication mixing time, and VGCNF weight fraction) and their influence on composite strengths using a minimum number of tests. The nanocomposite strength measurements were normalized by the impact strength of neat VE. A statistically significant response surface model was developed based upon the impact strength test results. For example, Figure 3 contains a plot of the normalized impact strength as a function of VGCNF weight fraction for different high shear mixing times, where the ultrasonication time was held constant at its design center point (30 min). As the VGCNF weight fraction increased, the predicted impact strength decreased below that for the neat VE. With extended high shear mixing (greater than 50 min), however, the impact strength for nanocomposites containing lower weight fractions of VGCNFs can exceed that for neat VE. In contrast, increased ultrasonication time can result

in a relative decrease in impact strengths. The optimum formulation corresponded to low VGCNF weight fraction, extended high shear mixing time, with no ultrasonication, resulting in a relative 15% increase in impact strength.

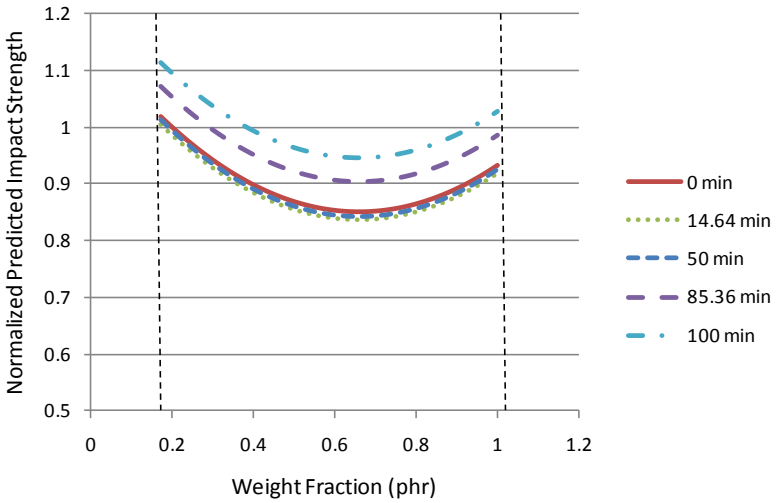

Figure 3: Normalized impact strength as a function of VGCNF weight fraction for different high shear mixing times (Torres et al., 2011).

Nanocomposite Multiscale Modeling

Molecular dynamics simulations of VGCNF/VE nanocomposites

MD simulations may be used to generate a wealth of information for use in higher length scale models. For example, polymer nanocomposite glass transition temperature (Qi et al., 2005), stress-strain responses (Frankland et al., 2003), interfacial properties (Gou et al., 2004), Poisson's ratios, densities and local morphologies, all as a function of temperature or pressure (Ray, 1988; Brown and Clarke, 1998; Qi et al., 2005), can be calculated in a representative simulation cell (computational volume) using MD simulations. One or several of these properties can be used as a direct input from the lower scale, depending on the fidelity of higher length scale models. In this study, the interphase and interfacial properties of VGCNF/VE nanocomposites will be used as input parameters for use in higher length scale computational models.

Interphase formation in polymer nanocomposites is driven by molecular interactions at the nanofiber-polymer interface. The interphase may be regarded as a distinct region with properties different from those of the bulk polymer (Jancar, 2008). This has been studied for thermoplastic matrices with various nanoreinforcements (Ciprari et al., 2006) and extensively so for continuous fiber reinforcements. Thermoplastic interphases can extend hundreds of nanometers from the reinforcement surfaces based on crystalline lamellae directional formation, but such thick interphases have not been observed for thermosets. During thermoset nanocomposite fabrication, the molecular interactions between liquid resin monomers and carbon nanofibers in the pre-curing (liquid resin) stage of nanocomposite fabrication could lead to different interfacial region monomer mole ratios versus those of the bulk resin. Rapid monomer equilibration will occur generating different mole ratios near and at the surfaces. This could lead to a different three-dimensional (3D) crosslinked network, as well as different crosslink densities and matrix microstructure in the interphase during resin curing. Therefore, gradients would be produced in the local matrix properties (Schadler et al., 2007) leading to distinct interfacial properties. Given the high surface-area-to-volume ratios associated with VGCNFs, a relatively small interphase volume fraction could significantly affect bulk composite properties. Hence, knowledge of the interphase structure and

properties should be considered in multiscale modeling of nanocomposites (Montazeri and Naghdabadi, 2010).

MD simulations of VGCNF/VE nanocomposites in the pre-curing stage were performed because of the inherent difficulty in experimental measurement of the interphase formation in thermoset polymer nanocomposites (Nouranian et al., 2011b). The liquid resin was modeled based on a commercial grade of VE resin: Derakane 441-400 (Ashland Co.). This resin is a mixture of VE dimethacrylates with an average molecular weight of 690 g/mol (Li, 1998). It has an average of 1.62 bisphenol-A groups (n = 1.62, where n is the number of bisphenol-A groups) in the dimethacrylate backbone (Li, 1998). A mixture of dimethacrylates with n = 1 (designated as VE1) and n = 2 (designated as VE2) yielding an average value of n = 1.62 was used in the simulation corresponding to a VE1/VE2 mole ratio of 37/61. VGCNFs exhibit stacked-cone (Dixie cup) or bamboo-like structures (Maruyama and Alam, 2002). The pristine VGCNF surface was idealized using two fixed, overlapping flat graphene sheets closely resembling the region of stacked nanocones along the outer surface of the VGCNF (Figure 4). All MD simulations were performed using Materials Studio® v5.0 software (Accelrys, 2011) using a simulation cell size of 60×50×60 $Å^3$ with 3D periodic boundary conditions. VE resin monomers (VE1, VE2, and styrene) were randomly packed around the graphene sheets at 300 K to yield a final simulation cell density of 1.18 g/cm^3. The total number of monomer molecules and their weight fractions are given in Table 1.

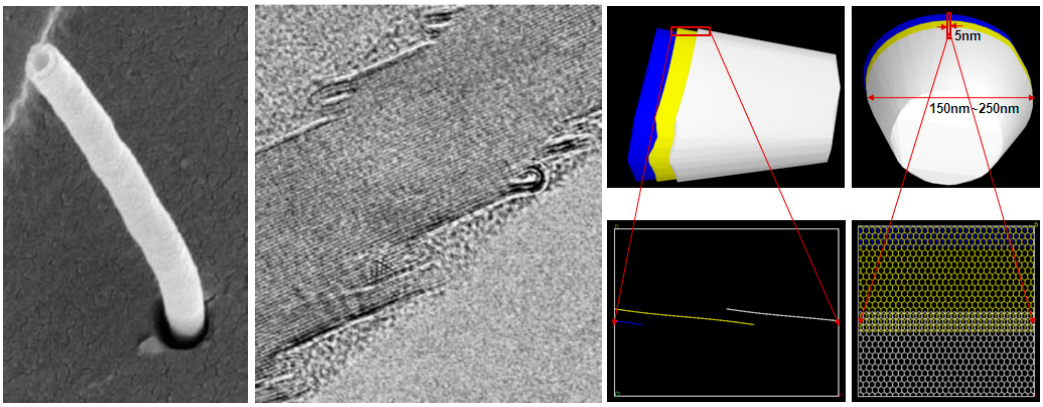

a) b) c)

Figure 4: a) View of a single carbon nanofiber, b) cross section of the stacked nanocone structure of a VGCNF with shingled graphene sheets (adapted from Uchida et al., 2006), and c) a schematic of overlapping graphene sheets along the outer edge of VGCNF stacked nanocones (Nouranian et al., 2011b).

Table 1. Total number and weight fractions of vinyl ester resin monomers (Nouranian et al., 2011).

Resin monomer	Number of molecules	Mass (u)	Weight %
VE1[1]	37	512.599	18.8
VE2[2]	61	796.954	48.2
Styrene	320	104.152	33.0

[1]The dimethacrylate with n = 1, where n is the number of bisphenol-A groups in the dimethacrylate's backbone.
[2]The dimethacrylate, where n = 2.

The Condensed-Phase Optimized Molecular Potentials for Atomistic Simulation Studies (COMPASS) force field, widely used for polymeric systems involving organic and inorganic molecules, was used in this study (Sun, 1998). Geometry optimization (10,000 iterations) was carried out using the

conjugate gradient method to partially relax the molecular structures (Nouranian et al., 2011b). The simulations of monomer equilibration consisted of several steps including the gradual increase of the simulation cell temperature to 600 K and then 1000 K, dynamics simulations at each temperature, gradual cooling of the simulation cell to 300 K and running dynamics simulations for a total cumulative time of ~13 ns. An NVT ensemble (constant number of atoms, N; constant volume, V; and constant temperature, T) and a time step of 0.5 fs were used throughout. The MD simulations were conducted using the following protocol. (1) The temperature was increased from 10 K to 50 K and then to 600 K in increments of 50 K with 1 ps of dynamics simulation at each intermediate temperature except for 300 K, where the simulation time was 100 ps. (2) The simulation was run for a total time of 4 ns at 600 K and then the temperature was increased to 1000 K in 50 K increments (intermediate simulation times were 1 ps). (3) The MD simulation was run for a total time of 4 ns at 1000 K followed by system cooling to 300 K by two cooling procedures: 10 K (designated as C1) and 50 K (C2) decrements (intermediate simulation times were 1 ps). (4) Two separate dynamics simulations following cooling procedures C1 and C2 ran for a total time of 5 ns at 300 K. The elevated temperatures were used to speed up the equilibration process. Figure 5 shows two snapshots of the simulation: one after the geometry optimization step and the other at the end of the simulation run following the first cooling procedure C1 (total run time, ~13 ns). Complete wetting of the graphene surface by monomers at the end of the simulations can be seen in contrast to the initial randomly packed structure.

Concentration profiles were generated for different monomers as a function of the y-coordinate, as defined in Figure 5 (roughly orthogonal to the graphene sheets), to analyze the distribution of liquid resin monomers at the nanofiber resin interface. The simulation volume was divided into a set of 1 Å thick sub-volumes using a series of cutting planes perpendicular to the y-axis. A set of relative monomer concentrations (for styrene, VE1, and VE2) within each subvolume was then defined using the atoms belonging to each specific monomer. The dimensionless relative concentration of a set of atoms contained in a given subvolume (belonging specifically to each of the individual monomers) is defined by the ratio of the number of atoms per unit subvolume to the number density of atoms in the system volume (Materials Studio User's Manual). The sum of all attractive and repulsive interactions of the different liquid resin monomers with the nanofiber surface and all of the monomer-monomer interactions will evolve towards a minimum system energy leading to an equilibrium arrangement of the molecules. This equilibrium determines the gradients in the final monomer distributions in the vicinity of the carbon nanofiber surface. Time-averaged concentration profiles for styrene and other monomers were used as the basis for checking the system's equilibrium status (Nouranian et al., 2011b). The relative concentrations were determined every 50 ps and then time-averaged over each successive 1 and 2 ns interval for the total simulation time of 4 ns performed at 1000 K.

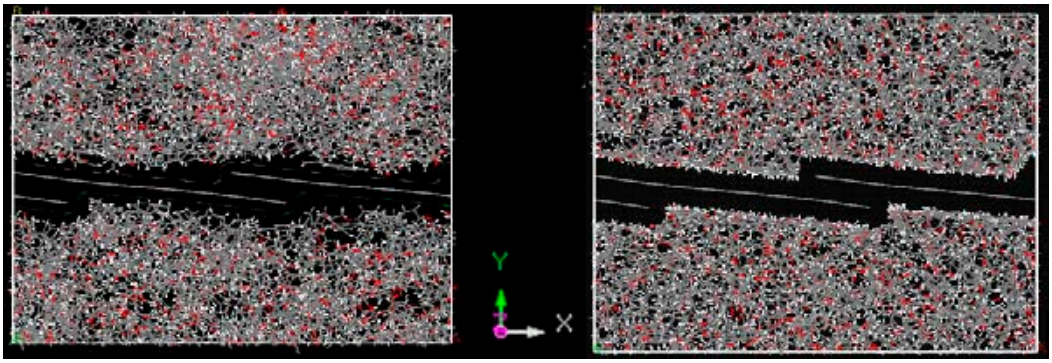

Figure 5: Snapshots of the initial frame after geometry optimization (left) and final frame after dynamics simulation for a total time of ~13 ns (cooling procedure C1).

The spatial and temporal evolutions of the concentration profiles were monitored, and the profiles were compared with each other to ensure that equilibrium was reached before cooling the system to

300 K. Upon cooling, the system must re-equilibrate. The time-averaged concentration profiles for all resin monomers were determined over 5 ns at 300 K following each cooling procedure. Since the effect of cooling protocol on the equilibrium distribution of monomers at 300 K was minimal, the monomer concentration profiles obtained following cooling protocols C1 and C2 were averaged together.

The final monomer distribution represents the amount of each monomer available for free radical polymerization during the crosslinking reaction as a function of perpendicular distance from the graphene sheets. The relative concentrations were averaged over both sides of the overlapping graphene sheets to obtain a more realistic estimate of the monomer distributions roughly perpendicular to an actual carbon nanofiber surface (Figure 6a). Furthermore, the average relative concentration ratios of the monomers (i.e., styrene/VE1, styrene/VE2, styrene/(VE1+VE2), and VE1/VE2) were also calculated (Figure 6b). The average relative monomer concentration ratios versus distance from the surface show how these concentrations (ratios) deviate locally from the relative concentration in the bulk resin. For reference purposes, a relative concentration ratio of unity means that the local monomer distribution is the same as that for the bulk resin.

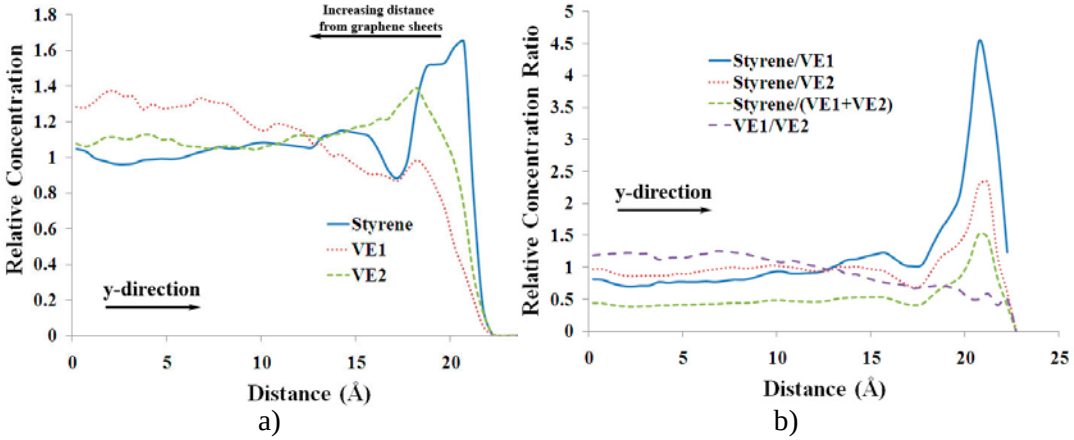

a) b)

Figure 6: (a) Concentration profiles for styrene, VE1, and VE2 and (b) monomer relative concentration ratio. Simulation results were time averaged over 5 ns at 300 K and then spatially averaged over both sides of the graphene sheets (Nouranian et al., 2011b).

The styrene/VE1 relative concentration ratio starts to increase about 10 Å away from the graphene surface and reaches a peak relative concentration ratio that is 4.5 times that of the bulk value near the fiber surface. The styrene/VE2 relative concentration ratio reaches a peak of 2.5 near the fiber surface. Thus, the relative concentration ratio of styrene to the sum of both VE monomers is higher at the interface, while the VE1/VE2 ratio is a relative minimum. These simulations suggest that increased styrene accumulation will occur in an approximately 5 Å thick region adjacent to the fiber surface. If the matrix composition produced by free radical-initiated curing incorporates the monomers in their concentration ratios found in the 5-10 Å liquid region adjacent to the graphene surfaces, the cured matrix composition resulting in that region will differ substantially from that of the bulk matrix structure. A styrene-rich interphase leads to a more compliant matrix layer, since styrene acts as a chain extender in the crosslinking reaction leading to fewer crosslink points and hence, a more flexible interphase. One substantial effect of such a thin soft interphase layer might be modified interfacial shear strength. Since styrene is strongly attracted to the graphene surface, higher interfacial shear strength may be anticipated compared to a more highly crosslinked resin region with a smaller styrene content. The simulations have also been performed on an oxidized VGCNF (Jang et al., 2011).

The details of MD simulations incorporating an idealized oxidized VGCNF surface and the surface oxidation procedure are discussed in (Jang et al., 2011). After equilibration of monomer distributions near the oxidized VGCNF surface, it was found that the relative near-surface monomer distributions (concentration profiles were profoundly different than those for a pristine (unoxidized) VGCNF). To

illustrate these differences, the relative concentration ratios of styrene/VE1, styrene/VE2, and VE1/VE2 were compared for both oxidized and pristine VGCNF surfaces (Figures 7-9). For example, the styrene/VE1 ratio near the oxidized graphene surface was substantially lower than that for a pristine surface (Figure 7). This indicates that less styrene (hydrophobic constituent) and more VE1 (polar constituent) accumulate near the oxidized nanofiber surface. In contrast, the styrene/VE2 ratio near the nanofiber surface was slightly higher for the oxidized case (Figure 8). This shows that less VE2 accumulation occurs near the oxidized surface than for a pristine graphene surface since more of the highly polar VE1 molecules are present near the oxidized graphene and compete for polar surface sites. The VE1/VE2 ratio is larger near the oxidized graphene surface than for a pristine surface (Figure 9), suggesting again that VE1 is enriched and VE2 is depleted in this region.

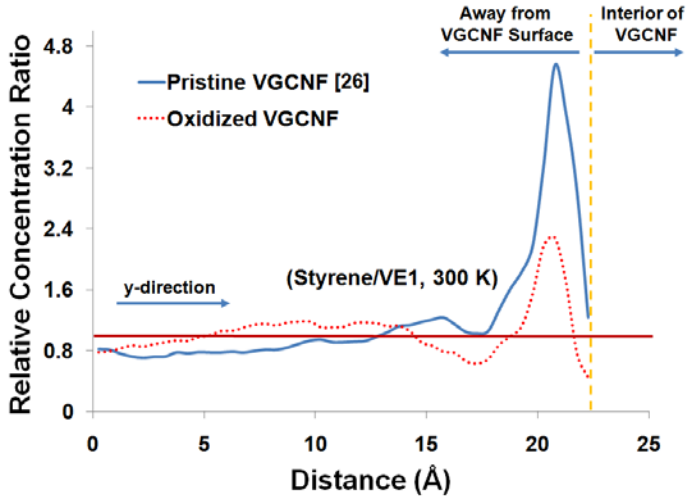

Figure 7: Relative styrene/VE1 concentration ratios at 300 K along the y-coordinate of the simulation cell for pristine versus oxidized graphene sheets (Jang et al., 2011).

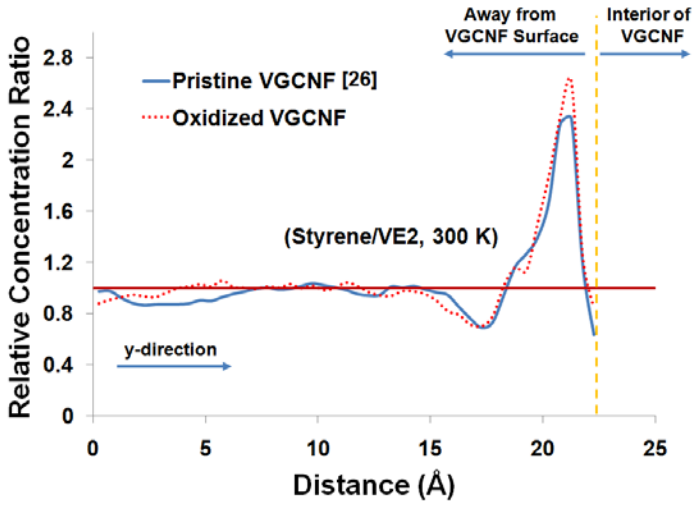

Figure 8: Relative styrene/VE2 concentration ratios at 300 K along the y-coordinate of the simulation cell for pristine versus oxidized graphene sheets (Jang et al., 2011).

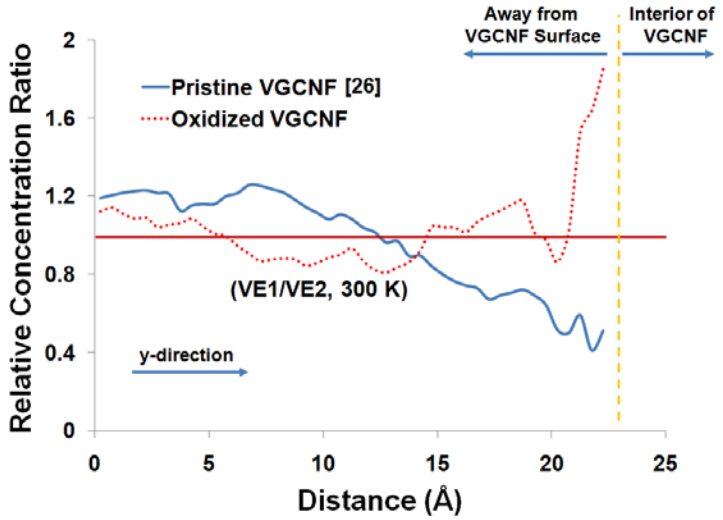

Figure 9: Relative VE1/VE2 concentration ratios at 300 K along the y-coordinate of the simulation cell for pristine versus oxidized graphene sheets (Jang et al., 2011).

Overall, both styrene and VE1 accumulate, in higher concentrations than their bulk value, near the oxidized graphene surface. This relative styrene concentration is less than that near the pristine graphene surface. The styrene accumulation at the oxidized graphene occurs in the unoxidized regions of its basal planes. The VE1 relative concentration is also higher near the oxidized surface than the bulk value, in contrast to its depletion near the pristine surface. Clearly, using oxidation to change the graphene surface chemistry plays a key role in nanofiber-liquid monomer interfacial interactions, leading to different monomer molar ratios and concentrations in the region 5-10 Å from these surfaces. This should have consequences for the cured composites. More VE1 (Figure 9) in the cured network structure in the interphase at the oxidized nanofiber surface would enhance the crosslink density, which implies a stiffer matrix near the VGCNF surface than that of the bulk. Hence, the interphase adjacent to an oxidized graphene surface would be stiffer than that predicted at a pristine surface. Strong polar interactions and hydrogen bonding between the surface oxygen-containing functions and the oxygen functions in VE1 and VE2 promote carbon nanofiber-matrix interfacial adhesion and better interfacial shear strength. Note that only a portion of the oxidized graphene surface displays oxygenated groups. Substantial portions of the surface are non-polar graphene, which interact with styrene and to a smaller degree with the aromatic rings in VE1 and VE2. In the future, graphene (idealized VGCNF) surfaces with various functional groups present at different surface concentrations will be studied in a crosslinked VE matrix using graphene sheet pull-out simulations. These will give estimates of the interfacial shear strength.

Once the equilibrium concentrations of the liquid resin monomers near pristine and oxidized VGCNF surfaces are determined, the resin must be crosslinked to evaluate cured nanocomposite properties. Optimal characterization of the VE curing reaction using MD simulations requires thorough understanding of the key aspects of the free radical polymerization such as regio- (head-to-tail) selectivity, determination of the appropriate reaction distances, monomer relative reactivity ratios, and growing radical site concentrations. These criteria are being integrated into an algorithm that crosslinks the system in a manner similar to the real VE resin curing process. Though several crosslinking algorithms have been proposed for epoxies (Komarov, 2007; Varshney, 2008; Lin and Khare, 2009), no such algorithm exists yet for VE resin that would include the real chemistry of the crosslinking reaction. A robust VE crosslinking algorithm has now been developed as part of this work. Once the VE resin is crosslinked, the effective interphase, interface, and other properties of interest will be determined using MD simulations. The nanofiber/matrix interfacial shear strength will be determined at this stage using nanofiber pull-out simulations similar to those performed using carbon nanotubes (Chowdhury and Okabe, 2007). MD-based estimates for nanocomposite interphase properties and interfacial strengths may be

validated using novel experimental results from the literature (Manoharan et al., 2009; Ozkan et al., 2010). Such data may be used in higher length scale calculations involving multitudes of nanofibers and other structures.

VE resin crosslinking was simulated using elements of polymerization chemistry such as regio-selectivity (head-to-tail chain propagation) and monomer reactivity ratios, which have never been employed in crosslinking simulations. Crosslinked vinyl ester networks with conversions up to 98% were successfully achieved. Volume shrinkage, glass transition temperature, and tensile elastic constants of the equilibrated structures were calculated. The glass transition temperature (Figure 10) and the isotropic Young's moduli (Figure 11) were compared with available experimental data. This newly developed method holds great promise for generating other realistic thermoset and thermoplastic polymer systems containing two or more different monomers. After verification, this method will be used to crosslink equilibrated VE resin systems containing both pristine and oxidized VGCNFs. This novel crosslinking algorithm may easily be adjusted to simulate the actual polymerization for a variety of thermosetting resin systems.

As an aside, several major factors affect the requisite simulation cell size and computational times associated with MD modeling of solid thermoplastics, thermosets, and their nanocomposites. High molecular weight thermoplastics with large entanglement densities and thermosets with extended chemical structures both require relatively large MD simulation cell sizes to properly represent the bulk polymer behavior. Macromolecular systems with slow diffusion rates may require extended equilibration times in MD calculations. In addition, real nanoinclusions are large in comparison to easily tractable simulation cell sizes. Thus, a nanofiber may be represented as passing through the periodic MD simulation cell, which approximates an infinitely long nanofiber. Such an idealization can drastically increase computational times in comparison with simulations involving finite nanofiber lengths (Qi et al., 2005). Moreover, huge differences in calculated elastic properties can result. Finally, optimal characterization of real polymeric and polymer composite systems, which are frequently not at full equilibrium as prepared, is a serious challenge. Such factors drive up the computational costs associated with MD modeling of polymers and polymer nanocomposites.

Despite all of these issues, with carefully designed large scale MD simulations, it is possible to predict polymer glass transition temperature, temperature dependent stress-strain curves and densities, Poisson's ratios, as well as storage and loss moduli. The effect of a variety of nanoreinforcement surface chemistries (including the number of surface-to-matrix covalent or ionic bonding sites per unit area) on interfacial shear strength can readily be probed using MD simulations.

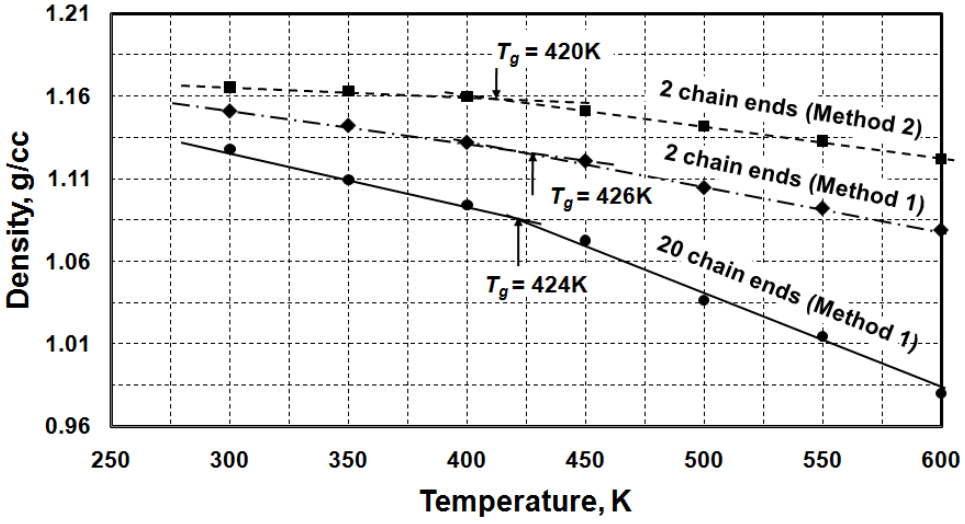

Figure 10: Glass transition temperature (T_g) for cured vinyl ester resins simulated by multiple chain growth (method 1) and single chain growth (method 2) at 98% conversion. T_g values from method 1 with different crosslinking

densities are very close to each other and also close to that predicted by method 2. The experimental T_g for Derakane 441-400 VE resin is 410K.

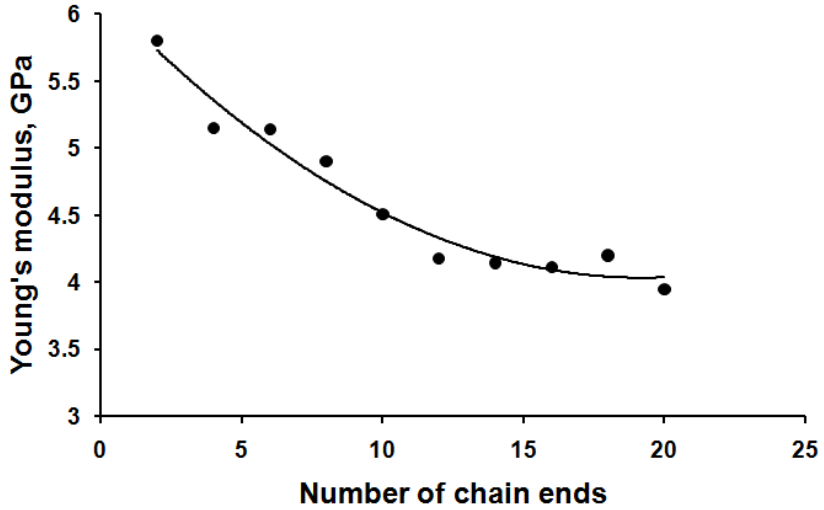

Figure 11: Young's modulus (E) as a function of remaining chain ends from network formation by multiple chain growth method.

Micro- to macroscale simulations of VGCNF/VE nanocomposites

One key challenge in predicting the effective properties of polymer nanocomposites is to account for the role of the nanofiber-matrix interphase properties and interfacial strength on bulk composite properties. While several researchers have performed novel nanofiber pull-out experiments (Manoharan et al., 2009; Ozkan et al., 2010), interphase and interfacial properties are very difficult to experimentally measure because of the inherently small nanoreinforcement sizes. In addition, such properties may play a key role in nanocomposite failure given the relatively high surface-area-to-volume ratio associated with typical nanofibers. Hence, MD simulations may provide one means for generating nanoscale material properties and strengths for use in micromechanical material models. Of course, the nanoreinforcements should be sufficiently large so that they are amenable to a local continuum description.

A number of mean field micromechanics approaches have been developed for predicting effective heterogeneous material properties, particularly for composites containing low volume fractions of reinforcements in an elastic matrix. These include the Mori-Tanaka method (MTM) (Mori and Tanaka, 1973; Benveniste, 1987), the self-consistent method (SCM) (Hill, 1965), and various coated inclusion techniques (Mura, 1987; Nemat-Nasser and Hori, 1993). These approaches are based upon the classic Eshelby solution (Eshelby, 1957) for the stress and strain field due to the presence of an ellipsoidal inclusion in an infinite domain subjected to uniform far-field loading. Mean field approaches have been used to investigate the effect of solid nanofibers or nanoplatelets on bulk nanoreinforced matrix properties (Fisher et al., 2003; Liu and Brinson, 2008), and have been modified to account for the effect of varying degrees of nanofiber waviness (Fisher et al., 2003). As part of the current study, Yu et al. (2011a) developed MTM and SCM models for predicting effective elastic properties for nanocomposites containing *hollow* wavy nanofibers surrounded by an arbitrary number of interphase layers. A parametric study was performed investigating the effect of hollow nanofiber wall thickness, nanofiber-matrix interphase thickness and elastic properties, and degree of nanofiber waviness on effective nanocomposite properties. The interphase modulus was expressed as a fraction of the matrix modulus (i.e., E_i/E_m) since no experimental data (or MD-based estimates of interphase properties) were available. Also, a normalized nanofiber modulus (E_F/E_m) consistent with VGCNF/VE nanocomposites was used. Figure 12a shows a plot of the effective longitudinal modulus, E_L, from (Yu et al., 2011a) as a function of normalized interphase thickness (t/R) for straight hollow fibers (aspect ratio, L/D = 100; volume fraction, 0.63 v%) based upon the MTM. The interphase properties were varied over the range $0.5 \leq E_i/E_m \leq 20$ in order to

encompass both relatively compliant and stiff interphases. A normalized nanofiber wall thickness, R_i/R_o = 0.3, was assumed where $R = R_o$ and R_i are the nanofiber outer and inner radii, respectively. As the average thickness (and volume fraction) of the interphase was increased, there was a significant increase in the predicted effective composite modulus. This underscores the importance of the contribution of the interphase to overall composite properties. Similar results were obtained when calculating the effective transverse modulus (Yu et al., 2011a).

The results shown in Figure 12a suggest that the use of very small amounts of VGCNFs (0.63 v%) results in a substantial improvement in the predicted effective longitudinal modulus of the nanoreinforced matrix. Improvements in experimentally measured moduli, however, typically are less profound (Fisher et al., 2002). The discrepancy between measured and predicted results may be attributed to nanofiber waviness, poor nanofiber dispersion, poor fiber-matrix adhesion, and/or the presence of nanofiber agglomerates in the actual composite specimens. Using the approach developed by Brinson and colleagues (Fisher et al., 2002), Yu et al. (2011a) performed effective modulus calculations for composites containing solid ($R_i / R_o = 0$) and hollow ($R_i / R_o = 0.3$) nanofibers with varying degrees of fiber waviness and 0.63 v% of solid carbon. Two different fiber aspect ratios were considered (L/D = 10, 50). Figure 12b contains a plot of the effective nanocomposite longitudinal modulus, E_L, as a function of the nanofiber waviness ratio (h/λ) as defined in (Fisher et al., 2002), where a nanofiber-matrix interphase is present ($t / R = t / R_o = 0.3$, $E_i / E_m = 10$). Note that for a given nanofiber aspect ratio, the use of *straight* hollow fibers ($h/\lambda = 0$) led to substantially higher modulus values than for straight solid fibers ($h / \lambda = 0$, $R_i / R_o = 0$) with the same volume fraction of solid carbon (0.63 v%). This issue is discussed at length in (Yu et al., 2011a). As the fiber waviness ratio increased to a modest level ($h / \lambda = 0.1$), the predicted modulus for all four cases decreased substantially. For higher degrees of fiber waviness ($h / \lambda > 0.3$), the nanofibers ceased to make a significant contribution to the effective longitudinal modulus. Figure 12b includes the experimentally determined mean fiber waviness ratio, $(h / \lambda)_{EXP} = 0.05$, obtained from transmission electron microscopy (TEM) imaging of VGCNF/VE specimens (Yu et al., 2011b). Given the two dimensional nature of the TEM images and the fact that the sections contained portions of actual nanofibers, the reported value likely represents a *lower bound* on expected h / λ values. The actual mean fiber waviness ratio may be somewhat greater than $h / \lambda = 0.05$, resulting in a significant decrease in the effective modulus in comparison with the straight nanofiber case.

Classical mean field approaches, such as the MTM and SCM, may be used to assess the effect of dilute concentrations of uniformly distributed nanoreinforcements on macroscale elastic properties. However, they are ill-suited for predicting local failure and strength of the composite, since they do not explicitly account for direct interactions between nanoreinforcements. In addition, crucial information regarding fluctuations in the local stress and strain field is lost in the homogenization procedure. As a consequence, traditional mean field theories cannot be efficiently used to predict local evolution of microstructure that leads to changes in macroscale material behavior.

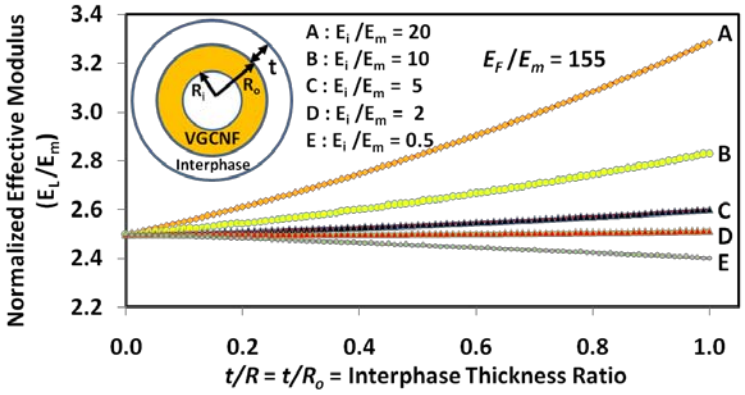

a)

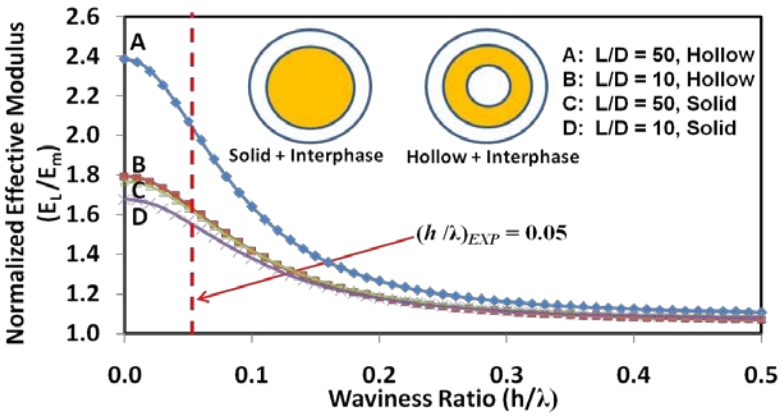

b)

Figure 12: Effect of interphase thickness on effective longitudinal modulus for nanocomposites containing a) hollow straight nanofibers (R_i / R_o = 0.3, L/D = 100, $0.5 \leq E_i/E_m \leq 20$) and b) solid and hollow wavy nanofibers (L/D = 10 & 50, $t/R = t/R_o$ = 0.3, E_i/E_m =10) at 0.63v% VGCNF (Yu et al., 2011a).

Computational micromechanics techniques, however, may be used to simulate progressive failure and evolution of structure within a representative volume element (RVE) or repeating unit cell (RUC). For example, the method of cells (Aboudi, 1989; Aboudi, 1996) is an approximate analytical theory for predicting composite properties and failure based on the assumption that composites are comprised of periodic micro- or mesostructures. Subsequently, the generalized method of cells (GMC) (Paley and Aboudi, 1992; Bednarcyk and Pindera, 2000; Aboudi et al., 2001) extended the method of cells to account for inelastic thermo-mechanical responses, variable fiber configurations, and the presence of an interphase. In the GMC, a RVE or RUC containing an arbitrary distribution of heterogeneities is discretized into a number of finite subvolumes (or cells). Continuity of displacements and tractions are imposed along subvolume boundaries as well as along the RVE (or RUC) boundary. Local evolution of structure in each cell is determined iteratively in a computationally efficient fashion, based upon the uniform prescribed RVE (or RUC) boundary conditions. Effective composite properties, which account for progressive failure within the RVE (or RUC), are obtained using standard homogenization techniques. The GMC may be used to accurately predict macroscale nonlinear composite material behavior and failure as a function of the properties, shapes, orientations, and distributions of constituents manifested at multiple lower length scales (i.e., micro- and mesoscales). In addition, the lower length scale progressive failure predicted using the GMC as a function of macroscale applied load history can be used to provide crucial information on the local internal stress and strain distributions leading to scale-specific damage mechanisms.

The GMC may be coupled with traditional macroscale continuum-based computational solid mechanics techniques to predict progressive failure of both component and global scale structures subjected to variable thermo-mechanical loadings. For example, NASA Glenn Research Center developed the special-purpose multiscale composite failure analysis software, the Micromechanics Analysis Code with the Generalized Method of Cells (MAC/GMC) (Arnold et al., 1999), based upon the GMC theory. MAC/GMC may be used to perform coupled rate-dependent multiscale analyses, design/optimization, computational micromechanics analyses, and life predictions for structures made of multiphase composite materials. MAC/GMC uses a robust local-to-global iteration scheme where a hierarchy of RUCs may be used to explicitly model the composite material structure and morphology over a wide range of length scales. The code may be readily coupled with the ABAQUS (2009) finite element (FE) solver. MAC/GMC can be used to predict local field quantities within each RUC; homogenized material properties at the highest length scale are then calculated at each FE integration point (Arnold et al., 1999). The effect of local damage or failure at the constituent level is automatically propagated at each load or

time step to the global FE scale through the change in homogenized stiffness properties. MAC/GMC is well suited to simulate polymer matrix composites containing woven fiber tows (Bednarcyk, 2000), unidirectional fiber tows, traditional short fibers and particulate reinforcements.

One goal of the current work is to extend MAC/GMC's temporally concurrent, spatially sequential multiscale analysis capabilities to include nanoreinforcements using the code's multi-step homogenization procedure. It is envisioned that key materials data generated using MD simulations will feed directly into nano- or microscale RUC calculations within MAC/GMC's multiscale framework. An essential requirement is to employ an appropriate spatial and temporal averaging strategy for materials data when transitioning between scales, i.e., establish a "handshake" protocol between MD and local continuum level simulations.

Conclusions

In this work, key issues in the development of a multiscale modeling strategy for thermoset composites and nanocomposites are addressed within an Integrated Computational Materials Engineering framework, with a focus on thermoset vinyl ester matrices reinforced with vapor-grown carbon nanofibers. Experimental efforts are coupled with the computational approaches such as integrated molecular dynamics (MD), multiscale computational micromechanics, and global finite element simulations to determine composite material behavior from the molecular to global structural scales. Novel MD calculations were performed to assess the potential for the formation of a distinct interphase region at the nanofiber/matrix interface, which account for the complex physio-chemistry between the liquid resin and carbon nanofiber surface. In the MD simulations, the nanofiber surface was idealized using a pair of overlapping graphene sheets. Based upon the calculated equilibrium redistribution of liquid resin monomers, a thin styrene-rich layer forms at the pristine nanofiber surface that may dictate nanofiber/matrix interfacial properties once crosslinking occurs. In contrast, a surplus of VE1 (vinyl ester with one bisphenol A group in its backbone) and a smaller accumulation of styrene was observed on the surface of the oxidized VGCNFs. This may indicate the build-up of stiffer interphase regions for nanocomposites containing oxidized VGCNFs as opposed to pristine VGCNFs. An innovative crosslinking algorithm is being developed for vinyl ester that accounts for regio-selectivity, monomer relative reactivity ratios, and other key aspects of free radical polymerization. After crosslinking, MD nanofiber pullout simulations will be performed to determine nanocomposite interphase properties and interfacial strengths for use in higher length scale models.

Appropriately averaged materials property data generated using MD simulations will feed directly into local continuum-based nano- or microscale calculations within the NASA MAC/GMC temporally concurrent, spatially sequential multiscale analysis framework. Progressive failure analyses will be performed that aim to establish structure-property relationships over a wide range of length scales, which account for the morphologies and geometries of real heterogeneous materials. This investigation aims to facilitate the development of engineered multiscale materials design by providing insight into relationships between nanomaterial fabrication/processing, chemical and physical characteristics, and interaction and evolution of structure across disparate spatial scales that lead to improved macroscale performance.

Publications

Journals

Jang C, Nouranian S, Lacy TE, Gwaltney SR, Toghiani H, Pittman Jr CU. 2011. Molecular dynamics simulations of oxidized vapor-grown carbon nanofiber surface interactions with vinyl ester resin monomers. Carbon, DOI: 10.1016/j.carbon.2011.09.013 (in press).

- Nouranian S, Jang C, Lacy TE, Gwaltney SR, Toghiani H, Pittman Jr CU. 2011. Molecular dynamics simulations of vinyl ester resin monomer interactions with a pristine vapor-grown carbon nanofiber and their implications for composite interphase formation. Carbon 49(10):3219-3232.
- Nouranian S, Toghiani H, Lacy TE, Pittman Jr CU, Dubien J. 2011. Dynamic mechanical analysis and optimization of vapor-grown carbon nanofiber/vinyl ester nanocomposites using design of experiments. J Compos Mater 45, 1647-1657.
- Yu J, Lacy TE, Toghiani H, Pittman Jr CU, Schneider J. 2011. Determination of carbon nanofiber morphology in vinyl ester nanocomposites. J Compos Mater, DOI: 10.1177/0021998311428361 (in press).
- Yu J, Lacy TE, Toghiani H, Pittman Jr CU. 2011. Effective property estimates for composites containing multiple nanoheterogeneities: Part I. Nanospheres, nanoplatelets, & voids. J Compos Mater (accepted pending minor revisions).
- Yu J, Lacy TE, Toghiani H, Pittman Jr CU. 2011. Effective property estimates for composites containing multiple nanoheterogeneities: Part II. Nanofibers & voids. J Compos Mater (under review).
- Yu J, Lacy TE, Toghiani H, Pittman Jr CU. 2011. Effective property estimates for composites containing multiple nanoheterogeneities. In the Proceedings of the American Society for Composites 26th Annual Technical Conference, September 26-28, 2011, Montreal, Quebec, Canada.

Book Chapters

- Lacy TE, Gwaltney SR, Pittman Jr CU, Toghiani H, Jang C, Nouranian S, Yu J. 2011. Some key issues in multi-scale modeling of thermoset nanocomposites/composites. In: Arnold SM, Wong T, editors. Tools, models, databases, and simulation tools developed and needed to realize the vision of integrated computational materials engineering. Materials Park, OH: ASM International.

Manuscripts and Conference Papers in Preparation

- Nouranian S, Toghiani H, Lacy TE, Pittman Jr CU, DuBien J. Effects of formulation, processing, and temperature conditions on the viscoelastic properties of vapor-grown carbon nanofiber/vinyl ester nanocomposites. To be submitted to Polym Eng Sci, tentative submission date December 2011.
- Lee J, Nouranian S, Torres GW, Lacy TE, Toghiani H, Pittman Jr CU, DuBien J. Flexural properties of vapor-grown carbon nanofiber/vinyl ester nanocomposites. To be submitted to Polym Eng Sci, tentative submission date December 2011.
- Lee J, Nouranian S, Lacy TE, Toghiani H, Pittman Jr CU. Effects of molding and curing conditions on the flexural properties of vinyl ester. To be submitted to Mater Lett, tentative submission date December 2011.
- Torres GW, Nouranian S, Lacy TE, Toghiani H, DuBien J, Pittman Jr CU. Statistical characterization of the impact strengths of vapor-grown carbon nanofiber/vinyl ester nanocomposites using a central composite design. To be submitted to Polym Eng Sci, tentative submission date December 2011.
- Hutchins JW, Sisti J, Ricks T, Nouranian S, Lacy TE, Pittman Jr CU, Toghiani H. Strain rate sensitivity of the compressive response of carbon nanofiber reinforced vinyl ester. To be submitted to Mech Time-Depend Mat, tentative submission date January 2012.
- Yu J, Lacy TE, Toghiani H, Pittman Jr CU. Effective thermal conductivity estimates for nanocomposites containing multiple nanoheterogeneities. To be submitted to Composites: Part B, tentative submission date December 2011.
- Yu J, Lacy TE, Toghiani H, Pittman Jr CU. Effective electrical conductivity estimates for nanocomposites containing multiple nanoheterogeneities. To be submitted to Composites: Part B, tentative submission date December 2011.
- Yu J, Lacy TE, Toghiani H, and Pittman Jr CU. Micromechanically based effective thermal conductivity estimates for polymer nanocomposites," in the Proceedings of the 53rd AIAA/ASME/ASCE/AHS/ASC Structures, Structural Dynamics, and Materials Conference, Honolulu, Hawaii, April 23-26, 2012.

Conference Abstracts

- Nouranian S, Toghiani H, Lacy TE, DuBien JL, Pittman Jr, CU. Designed experimental study of vapor-grown carbon nanofiber/vinyl ester nanocomposites with focus on the effects of formulation and processing factors on the nanocomposite dynamic mechanical properties over a wide temperature range. Conference abstract, the 2011 Annual Meeting. Minneapolis (Minnesota. USA): the American Institute of Chemical Engineers (AIChE), October, 16-21, 2011.
- Jang C, Nouranian S, Lacy TE, Gwaltney SR, Toghiani H, Pittman Jr CU. Molecular dynamics simulations of an oxidized vapor-grown carbon nanofiber and vinyl ester resin interactions leading to a possible interphase formation in the cured nanocomposite. Conference abstract, the 2011 Annual Meeting. Minneapolis (Minnesota. USA): the American Institute of Chemical Engineers (AIChE), October, 16-21, 2011.
- Nouranian S, Jang C, Toghiani H, Pittman Jr CU, Lacy TE, Gwaltney SR. Investigation of vinyl ester resin/vapor-grown carbon nanofiber surface interactions using molecular dynamics simulations. Conference abstract, the 2010 Annual Meeting. Salt Lake City (Utah. USA): the American Institute of Chemical Engineers (AIChE), November 7-12, 2010.

References

ABAQUS 6.7. 2009.Simulia, Inc.

Accelrys, Inc. http://accelrys.com/products/materials-studio/ (date accessed: December 9, 2011).

Aboudi J.1989. Micromechanical analysis of composites by the method of cells. Appl Mech Rev42(7):193-221.

Aboudi J. 1996. Micromechanical analysis of composites by the method of cells – update. Appl Mech Rev 49:s83-s91.

Aboudi J, Pindera MJ, Arnold SM. 2001.Linear thermoelastic higher order theory for periodic multiphase materials. J ApplMech68:697-707.

Arnold S, Bednarcyk B, Wilt T, Trowbridge D.1999. Micromechanical analysis code with generalized method of cells (MAC/GMC) user's guide, v3.0.NASA/TM-1999-209070,Cleveland, OH, USA.

Bednarcyk BA. 2000. Modeling woven polymer matrix composites with MAC/GMC. NASA CR-2000-210370.

Bednarcyk B, Pindera M. 2000. Inelastic response of a woven carbon/copper composite, Part 2: Micromechanics model. J Compos Mater 34(4):299-331.

Benveniste Y. 1987. A new approach to the application of Mori-tanaka's theory in composite materials. Mech Mater 6:147-157.

Bouvard J-L, Ward DK, Hossain D, Nouranian S, Marin E, Horstemeyer M. 2009. Review of hierarchical multiscale modeling to describe the mechanical behavior of amorphous polymers. J Eng Mater Technol131(4):041206-1.

Brown D, Clarke JHR. 1998. Molecular dynamics simulation of an amorphous polymer under tension. I. Phenomenology. Macromolecules 24:2075-2082.

Buryachenko VA, Roy A, Lafdi K, Anderson KL, Chellapilla S. 2005.Multi-scale mechanics of nanocomposites including interface: experimental and numerical investigation. Compos Sci Technol 65:2435-2465.

Chasiotis I, Chen Q, Odegard GM, Gates TS. 2005. Structure-property relationships in polymer composites with micrometer and submicrometer graphite platelets. Exp Mech 45(6):507-516.

Chowdhury SC, Okabe T. 2007. Computer simulation of carbon nanotube pull-out from polymer by the molecular dynamics method. Compos Part A 38(3):747-754.

Ciprari D, Jacob K, Tannenbaum R. 2006. Characterization of polymer nanocomposite interphase and its impact on mechanical properties. Macromolecules 39:6565-6573.

Eshelby JD. 1957. The determination of the elastic field of an ellipsoidal inclusion and related problems.Proceedings of the Royal Society A241:376–396.

Fermeglia M, Pricl S. 2007. Multiscale modeling for polymer systems of industrial interest. Prog Org Coat 58:187-199.
Fisher FT. 2002. Nanomechanics and the viscoelastic behavior of carbon nanotube-reinforced polymers. Evanston IL USA, Northwestern University, Ph.D. Dissertation.
Fisher F, Bradshaw R, Brinson L. 2003. Fiber waviness in nanotube-reinforced polymer composites - I: modulus predictions using effective nanotube properties. Compos Sci Technol 63:1689-1703.
Frankland SJV, Harik VM, Odegard GM, Brenner DW, Gates TS. 2003. The stress-strain behavior of polymer-nanotube composites from molecular dynamics simulations. Compos Sci Technol 63(11):1655-1661.
Gates TS, Odegard GM, Frankland SJV, Clancy TC. 2005. Computational materials: multi-scale modeling and simulation of nanostructured materials. . Compos Sci Technol 65(15-16):2416-2434.
Gou J, Minaie B, Wang B, Liang ZY, Zhang C. 2004. Computational and experimental study of interfacial bonding of single-walled nanotube reinforced composites. Comput Mater Sci 31(3-4):225-236.
Hill R. 1965. A self-consistent mechanics of composite materials. J Mech Phys Solids13:213-222.
Hutchins JW, Sisti J, Lacy TE, Nouranian S, Toghiani H, Pittman Jr CU. 2009. High strain rate behavior of carbon nanofiber reinforced vinyl ester. Proceedings of the 50th AIAA/ASME/ASCE/AHS/ASC Structures, Structural Dynamics, and Materials Conference, Palm Springs, CA.
Jancar J. 2008. Review of the role of the interphase in the control of composite performance on micro- and nano-length scales. J Mater Sci43:6747-6757.
Jancar J. 2009. Interphase phenomena in polymer micro- and nanocomposites. In: Karger-Kocsis, J., Fakirov, S., editors. Nano- and micro-mechanics of polymer blends and composites, Hanser Publications, 241-266.
Jang C, Nouranian S, Lacy TE, Gwaltney SR, Toghiani H, Pittman Jr CU. 2011. Molecular dynamics simulations of oxidized vapor-grown carbon nanofiber surface interactions with vinyl ester resin monomers. Carbon, DOI: 10.1016/j.carbon.2011.09.013 (in press).
Komarov PV, Yu-Tsung C, Shih-Ming C, Khalatur PG, Reineker P. 2007.Highly cross-linked epoxy resins: an atomistic molecular dynamics simulation combined with a mapping/reverse mapping procedure. Macromolecules 40:8104-8113.
Li H. 1998. Synthesis, characterization, and properties of vinyl ester matrix resins. Blacksburg VA USA, Virginia Polytechnic Institute and State University, Ph.D. dissertation.
Lin P–H, Khare R. 2009. Molecular simulation of cross-linked epoxy and epoxy-poss nanocomposite. macromolecules 42:4319-4327.
Liu H, Brinson LC. 2008. Reinforcing efficiency of nanoparticles: a simple comparison for polymer nanocomposites. Compos Sci Technol 68:1502-1512.
Materials Studio® User's Manual. 2010. Accelrys, Inc.
Maiti A. 2008. Multiscale modeling with carbon nanotubes. Microelectronics Journal 39:208-221.
Manoharan MP, Sharma AV, Haque MA, Bakis CE, Wang KW. 2009. The interfacial strength of carbon nanofiber epoxy composite using single fiber pullout experiments. Nanotechnology 20:1-5.
Maruyama B, Alam K. 2002. Carbon nanotubes and nanofibers in composite materials. SAMPE Journal 38(3):59–70.
Montazeri A, Naghdabadi R. 2010. Investigation of the interphase effects on the mechanical behavior of carbon nanotube polymer composites by multiscale modeling. J Appl Polym Sci 117(1):361-367.
Montgomery DC. 2009. Design and analysis of experiments. 7th ed. Hoboken, NJ: John Wiley & Sons.
Mori T, Tanaka K. 1973. Average stress in matrix and average elastic energy of materials with misfitting inclusions. Acta Mater 21:571-574.
Myers RH, Montgomery DC, Anderson-Cook CM. 2009. Response surface methodology: Process and product optimization using designed experiments. 3rd ed. Hoboken, NJ: John Wiley & Sons.
Mura T. 1987. Micromechanics of defects in solids, 2nd Ed, MartinusNijhoff 1–73.

Nemat-Nasser S, Hori M. 1993. Micromechanics: Overall properties of heterogeneous materials, North-Holland 368-386.
Nouranian S, Toghiani H, Lacy TE, Pittman Jr CU, Dubien J. 2011a. Dynamic mechanical analysis and optimization of vapor-grown carbon nanofiber/vinyl ester nanocomposites using design of experiments. J Compos Mater 45:1647-1657.
Nouranian S, Jang C, Lacy TE, Gwaltney SR, Toghiani H, Pittman Jr CU. 2011b. Molecular dynamics simulations of vinyl ester resin monomer interactions with a pristine vapor-grown carbon nanofiber and their implications for composite interphase formation. Carbon 49(10):3219-3232.
Nouranian S, Toghiani H, Lacy TE, Pittman Jr CU, DuBien J. 2011c. Effects of formulation, processing, and temperature conditions on the viscoelastic properties of vapor-grown carbon nanofiber/vinyl ester nanocomposites. To be submitted to Polym Eng Sci.
Odegard GM, Clancy TC, Gates TS. 2005. Modeling of the mechanical properties of nanoparticle/polymer composites. Polymer 46(2):553-562.
Ozkan T, Naraghi M, Chasiotis I. 2010. Mechanical properties of vapor grown carbon nanofibers. Carbon 48:239-244.
Paley M, Aboudi J. 1992. Micromechanical analysis of composites by the generalized cells model. Mech Mater 14:127-39.
Plaseied A, Fatemi A, Coleman MR. 2008. The influence of carbon nanofiber content and surface treatment on mechanical properties of vinyl ester. Polym Compos 16(7):405–413.
Plaseied A, Fatemi A. 2009. Tensile creep and deformation modeling of vinyl ester polymer and its nanocomposite. J Reinf Plast Comp 28(14):1775-1788.
Qi D, Hinkley J, He G. 2005. Molecular dynamics simulation of thermal and mechanical properties of polyimide-carbon nanotube composites. Model Simul Mater Sci Eng 13:493-507.
Ray JR. 1988. Elastic constants and statistical ensembles in molecular dynamics. Comput Phys Rep 8:109-152.
Schadler LS, Brinson LC, Sawyer WG. 2007. Polymer nanocomposites: A small part of the story. *JOM*:53-60.
Shonaike GO, Advani SG. 2003. Advanced Polymeric Materials, Structure Property Relationships, CRC Press.
Sun H. 1998. COMPASS: An ab initio force-field optimized for condensed-phase applications: overview with details on alkane and benzene compounds. J Phys Chem B 102(38):7338-7364.
Tadmor EB, Phillips R, Ortiz M. 2000. Hierarchical modeling in the mechanics of materials. Int J Solid Struct 37:379-389.
Thostenson ET, Chou T–W. 2006. Processing-structure-multi-functional property relationship in carbon nanotube/epoxy composites. Carbon 44(14):3022-3029.
Torres GW, Nouranian S, Lacy TE, Toghiani H, DuBien J, Pittman Jr CU. 2011. Statistical characterization of the impact strengths of vapor-grown carbon nanofiber/vinyl ester nanocomposites using a central composite design. To be submitted to Polym Eng Sci.
Uchida T, Anderson DP, Minus ML, Kumar S. 2006. Morphology and modulus of vapor grown carbon nano fibers. J Mater Sci 41:5851-5856.
Valavala PK, Clancy TC, Odegard GM, Gates TS. 2007. Nonlinear multiscale modeling of polymer materials. Int J Solid Struct 44(3-4):1161-1179.
Varshney V, Patnaik SS, Roy AK, Farmer BL. 2008. A molecular dynamics study of epoxy-based networks: cross-linking procedure and prediction of molecular and material properties. Macromolecules 41:6837-6842.
Yu J, Lacy TE, Toghiani H, Pittman Jr CU. 2011a. Classical micromechanics modeling of nanoreinforced composites with carbon nanofibers and interphase. J Compos Mater Pre-published online DOI: 10.1177/0021998311401092.
Yu J, Lacy TE, Toghiani , Pittman Jr CU, Schneider J. 2011b. Determination of carbon nanofiber morphology in vinyl ester nanocomposites. J Compos Mater Pre-published online DOI: 10.1177/0021998311428361.

Zeng QH, Yu AB, Lu GQ. 2008. Multiscale modeling and simulation of polymer nanocomposites. Prog Polym Sci 33(2):191-269.

Key Words

Automotive Composites, Nanocomposites, Fabrication, Multiscale Modeling, Micromechanics, Finite Element Modeling, Experiments, SEM

Brief Description of Report

A multiscale design methodology is being employed to investigate the effects of nanoreinforcements on the mechanical properties of fiber-reinforced composites for automotive structural applications.

Southern Regional Center for Lightweight Innovative Design

Phase III

Final Scientific & Technical Report

October 1, 2009-September 30, 2011

For compliance with contract requirements of Award DE-EE0002323

Task 10

NATURAL FIBER COMPOSITES FOR STRUCTURAL COMPONENT DESIGN

Submitted December 27, 2011

TASK 10: NATURAL FIBER COMPOSITES FOR STRUCTURAL COMPONENT DESIGN

Table of Contents

TASK 10: NATURAL FIBER COMPOSITES FOR STRUCTURAL COMPONENT DESIGN

Principal Investigator: Sheldon Q. Shi
Associate Professor, Renewable Biocomposites
Mechanical & Energy Engineering
University of North Texas
1155 Union Circle #311098, Denton, Texas 76203-2017
(940) 369-5930; e-mail: sheldon.shi@unt.edu

Participants: Kaiwen Liang, Jinwu Wang, Mohammad Qatu, Mark Tschopp, Tian Tang, Darrel Nicolas, Linda Sites, Jinshu Shi, Ian Fulton, Emily Zhang, Yan Shen, and Wen Che

William Joost: Technology Area Development Manager
e-mail: william.joost@ee.doe.gov

Magda Rivera: Project Manager
e-mail: magda.rivera@netl.doe.gov

Contractor: *Mississippi State University (MSST)*
Contract No.: *DE-EE0002323*

Accomplishments

- An all chemical process was developed to obtain cellulose nanowhiskers (CNW) from kenaf bast fibers.
- Inorganic nanoparticle impregnation (INI) natural fibers were successfully generated from the developed chemical retting and INI processes for natural fiber SMC fabrication.
- A concept was proven on novel techniques on nanophase treatment of natural fibers for processing functional natural fiber nanocomposite products and the conversion of celluloses into carbon materials.
- An attempt has been made to investigate using soybean oil additive into the resin formulation as a sizing agent of natural fiber SMC products. A composite with a 24-hour WA of less than 1.5% could be obtained by the incorporation of carbon nanotube.
- An accelerated weathering test was conducted to determine the strength properties of natural fiber sheet molding compound before and after exposure to cyclic wet/dry cycles in a weathering cabinet. Impregnated kenaf fiber SMC did not show degradation after a exposure for a total of 720 hours at cycles of 4 hours UV exposure at 600 C followed by 4 hours condensation 400 C (ASTM D4329).
- An experimental technique was developed to stress the micro cellulosic fibers. A property comparison was conducted on several representative individual fibers.
- A study was conducted on the effect of pressure in hot pressing and layups on the properties of hybrid polyester composites from randomly woven kenaf fibers with fiberglass.
- Vinyl tris(2-ethoxymethoxy) silane treatment of kenaf fiber was successfully conducted. The water absorption and flexural properties of the resulting fiber composites were improved.
- Amorphous cellulose models were successfully created with the use of ReaxFF. Preliminary molecular dynamic simulations have been presented for amorphous cellulose.

- Principles and practices of life-cycle assessment (LCA) were used to evaluate environmental performance of natural fiber reinforced bio-resin matrix composites. Preliminary results indicated their superiority in environmental performance to a traditional glass fiber polymer composite.

Future Directions

- Investigate chemical modification of natural fiber by several silane with different chemical functional groups.
- Explore the nanoscale mechanisms behind different regimes (elasticity/yield/strain hardening) and address the interface mechanical properties between the cellulose and the polymer.
- Construct a multiscale framework to model the coupled hygro-thermo-mechanical and damage behavior of natural fiber composite materials and structures subjected to external loading and environmental attacks such as heat and moisture diffusion.
- Scrutinize life-cycle inventory data collected from literature and lab, simulate the production processes to generate average technology LCA data and make the data accurate and complete.

Executive Summary

The overall goal of the project is to substitute the glass fiber with natural fiber as reinforcements in polymer matrices to achieve cost and weight savings without compromising the mechanical property requirements. The alkaline retting treatment efficiently removed the hemicellulose and lignin from kenaf bast fiber. Bleaching treatment could remove the remnant lignin from the retted fibers. Pure cellulose fibers in micrometer scale and nanometer scale were obtained by acidic hydrolysis of the bleached fibers. Our kenaf natural fiber SMC has comparative properties compared with the commercial glass fiber SMC. The impregnated kenaf fiber SMC was not degraded during accelerated weathering test. The newly designed SF-I microtester is well suited for measuring mechanical properties of individual micro fibers. Among the 4 fibers used in the testing, bamboo, kenaf, Chinese fir, and ramie, kenaf bast fiber showed the lowest elongation at break and other properties of kenaf were balanced. A detailed procedure was developed to fabricate the laminated natural fiber kenaf-based composites. Various samples are manufactured with modulus of elasticity (MOE) up to 10 GPa and modulus of rupture (MOR) up to 270 MPa. Vinyl tris(2-ethoxymethoxy) silane treatment of kenaf fibers improved the physical and mechanical properties of the resulting kenaf fiber composites. The water absorption of silane treated kenaf fiber composites decreased by 22% compared to the untreated fiber composites. The flexural strength and modulus of silane treated kenaf fiber composites increased by 25% and 8%, respectively. The simulated stress-strain behavior using molecular dynamics (MD) modeling showed the similar trends both qualitatively and quantitatively as those observed in the experimental testing for the amorphous cellulose. The multi-scale model of the moisture absorption process of natural fiber composites was developed on the basis of the theoretical framework of VAMUCH. The preliminary result of life cycle assessment (LCA) demonstrated that the use of modified soybean oil and natural fiber to make sheet molding compound (SMC) had a great potential from an ecological point of view.

Introduction

Kenaf bast fiber is attractive due to its fast growing characteristic, high fiber yield and cellulose content, good mechanical properties, etc. It was reported by Zadorecki and Michell (1989) that the modulus of the fibers increased significantly by breaking down the cellulosic fiber into smaller sizes from solid wood (10 GPa), to single pulp fiber (40 GPa), to microfibrils (70 GPa), and to crystallites (250 GPa). Therefore, research work on high crystalline cellulose fibers, e.g. microfibrils, nanowhiskers, or nanofibers, has drawn great attention in recent years (Henriksson, et al. 2007; Iwamoto, et al. 2005; Kulpinski, 2005; Sui, et al., 2008). Quantitatively characterizing the micro-mechanical properties of

individual natural fibers will help select the most appropriate fiber types and pulping processes to manufacture the targeted grade of fiber reinforced composites. In an effort to present more 'green' material for massive manufacturing that are both competitive in their properties and more environmental friendly, natural fibers are being considered for possible applications in the automotive industry. An exploratory study of the effects of pressure and layup on a hybrid composite of randomly oriented woven kenaf fibers and fiberglass/polyester sheet molding compound (SMC) was conducted.

Natural fiber is easy to absorb moisture due to its hydrophilic nature. Silane treatment of the fibers has shown to be effective in reducing moisture uptake of cellulosic fibers in humid environments (Bisanda and Ansell 1991). Attempts have been made to use the silane treatment of the kenaf bast fibers for the purpose of improving the moisture resistant properties for the natural fiber SMC. Molecular modeling complements the experimental work. MD simulation work has been focusing on the understanding the variables associated with the deformation of thermoplastic polymers. Natural fiber reinforced composites have been generally perceived as renewable, biodegradable and environmentally friendly products. However, it was difficult to quantitatively measure their environmental friendliness and make a sound comparison with other competing materials. A life-cycle assessment is a technique to assess environmental impacts associated with all the stages of a product's life from raw material extraction and processing to product manufacture, distribution, use, repair and maintenance, and disposal or recycling after the end-of-life.

Physical/Mechanical Properties and Durability of Natural Fiber Sheet Molding Compound

***Objective*:** The purpose of this study was to determine the physical and mechanical properties of natural fiber SMC. Durability is an important aspect for the overall performance of the products used in both interior and exterior applications where sunlight and moisture could have an effect. Another objective of this study was to evaluate the performance of natural fiber SMC when exposed to cyclic wet/dry cycles in a weathering cabinet.

***Methods*:** The weathering apparatus used for this study was a Q-U-V Cyclic Ultraviolet Weathering Tester (120V, 60 Hz Model manufactured by The Q-Panel Company, Cleveland Ohio 44145. The Q-Panel uses eight fluorescent UVA 340 lamps (UV range 365nm to 295 nm). The unit is equipped with a 24 hour timer divided into 15-minute tabs to provide a wide range of cycles. The test samples were cut from panels that had been exposed for a total of 720 hours at cycles of 4 hours UV exposure at 60^0 C followed by 4 hours condensation 40^0 C. This exposure procedure is recommended in ASTM D4329 (Stand Practice for Operating Light and Water Exposure Apparatus for Exposure of Plastics). Test samples measured as 2.6 mm x 19.25 mm x 76 mm (t x r x l) were cut from both exposed and unexposed samples. A bending test was performed using a 1.75 mm deflection and a loading speed of 0.5 mm per minute to determine the modulus of elasticity (MOE). Each sample was tested two times to obtain an average value. The MOE results of unexposed controls and exposed samples were compared in order for determining the strength loss due to the weathering effect.

***Results and Discussion*:** Two natural fiber SMC samples were sent to Processing RIC Department at Ford Motor Company, MI for evaluation. Table 10.1 shows the tensile properties of the two ntural fiber SMC panels (about 60 - 65 wt% fiber + $CaCO_3$) with a comparison of Class A glass fiber SMC (EpicBlendSMC ^{TM}). It is shown in Table 10.1 that the natural fiber SMC we developed showed higher tensile modulus than that of glass fiber SMC.

Table 10.1: Tensile properties of retted kenaf fiber SMC and glass fiber SMC

Panel	Tensile Modulus, GPa	Tensile Strength, MPa
Retted Kenaf SMC (Average of 2 panels)	13.7	69.6

Glass Fiber SMC (Class A)	10.1	85

For the product durability testing, the samples were measured and weighted before putting into the QV chamber for testing. The testing samples were removed and weighted two times per week at both the UV and condensation cycles. The samples were also re-positioned weekly in order to provide a uniform UV exposure. After the exposure, the panels were allowed to equilibrate back to the ambient conditions and the weights of the samples were measured. All of the exposed kenaf SMC (about 60 - 65 wt% fiber + $CaCO_3$) samples came back to their original ambient weights after testing. In contrast, both of the fiber glass SMC samples had an approximate 1 g decrease in weight after the exposure (Table 10.2). Visually, glass fiber SMC had significant yellow-brown color change on the exposed face of the panel due to the UV exposure, while the kenaf fiber SMC did not show color changes (Figure 10.1).

Table 10.2: Initial, UV Cycle, Condensation Cycle weights and weight change for samples exposed in a QUV weathering test for 30-days.

Panel	Initial Wt., g	Final Wt., g	Wt. Change, g
Impregnated Kenaf SMC (Average of 2 panels)	111.66	111.70	+ 0.04
Glass Fiber SMC (Class A)	241.35	240.20	- 1.15

Figure 10.1: Natural fiber SMC and glass fiber SMC before and after accelerated weathering test

The individual and average MOE and percent differences are listed in Table 10.3. The carbon nanotube treated kenaf bast fiber SMC show no degradation after the accelerated weathering treatments.

Table 10.3: Flexural properties, 24 hr water absorption and average percent MOE loss of samples exposed in a weathering test.

Panel	Flexural Strength, MPa	Flexural Modulus, GPa	24 hr Water Absorption, %	Strength Loss, %
Impregnated Kenaf SMC (Average of 2 panels)	81.68	9.07	2.32	-5.33

Chemical Components and Morphologies of the Kenaf Bast Fibers obtained from the Chemical Processes

***Objective*:** The objective was to study the morphologies and chemical components of the retted fibers, bleached fibers, microfiber and cellulose nanowhiskers (CNWs).

***Methods*:** Kenaf bast fibers were treated with the chemical processes. Alkaline retting treatment followed by bleaching treatment was applied to remove the hemicellulose and lignin from the raw kenaf bast fibers so that the retted fibers and bleached fibers were obtained. Acidic hydrolysis was conducted on the bleached fibers, and the microfibers and CNWs were obtained. The CNWs had been applied to fabricate polyvinyl alcohol (PVA)/CNW composites and exhibited excellent reinforcement efficiency for tensile properties. The functional groups and crystallinities of the fibers were measured. This study emphasized on the chemical components and morphologies of these fiber types.

***Results and Discussion*:** Chemical components including holocellulose content, α-cellulose content, Klason lignin content and ash content of the raw kenaf bast fibers, retted fibers, bleached fibers, microfibers and CNWs were determined. The ash contents were determined following TAPPI standard T 211-om. 93. Klason lignin contents were estimated in accordance with the method of the Institute of Paper Chemistry (1951). Holocellulose is the total carbohydrate fraction (cellulose and hemicellulose) of the fibers, and its content was estimated by the method of Wise et al. (1946). The term α-cellulose describes that part of cellulose which does not dissolve in 17.5% sodium hydroxide solution. The method employed to investigate the α-cellulose contents was according to the method of German Association of Cellulose Chemists and Engineers (1951). The holocellulose contents, α-cellulose contents, Klason lignin contents and ash contents of the fibers were shown in Table 10.4. Alkaline retting treatment of the kenaf bast fibers at 160°C with the alkaline liquid's autogenous vapor pressure for 1h effectively degraded and dissolved lignin and hemicellulose. The two percentage point difference between the holocellulose content and α-cellulose content of retted fiber indicated a small fraction of hemicellulose remaining in retted fibers. If the lignin in retted fibers, although as few as 0.24%, had not been removed by bleaching treatment, it would result in acid-insoluble residuals in microfibers and CNWs after acid hydrolysis, and thus debase their purity. Bleaching treatment removed not only the lignin, but also the hemicellulose, producing relatively pure cellulosic fibers for the next acid hydrolysis treatment. Microfibers and CNWs obtained from acid hydrolysis were pure cellulose fibers.

Scanning electron microscopy (SEM, Zeiss Supra TM 40) was applied to analyze fibers morphology. Seventy fibers were randomly chosen for their dimension measurement using the "Smart SEM User Interface". The CNW samples for morphology analysis were obtained by placing a drop of the CNW suspension onto a grid without any staining, and drying it in the air at the ambient temperature. The dried samples were examined in a transmission electron microscopy (TEM, JEOL JEM-2000 EX-II). The dimensions of seventy randomly chosen CNWs were measured from the TEM images. The morphology of the raw kenaf bast fiber, retted fiber, bleached fiber, microfiber and CNW was studies from their SEM or TEM images (Figures 10.2 and 10.3). The statistics of the fiber lengths and diameters were shown in Table 10.5.

Table 10.4: Chemical components of the fibers.

	α-cellulose	Holocellulose	Klason Lignin	Ash
Non-treated fiber	45.95%	75.83%	19.10%	5.07%
Retted fiber	92.27%	94.22%	0.24%	2.72%
Bleached fiber	95.19%	95.41%	0%	2.27%
Microfiber	100%	100%	0%	0%
CNW	100%	100%	0%	0%

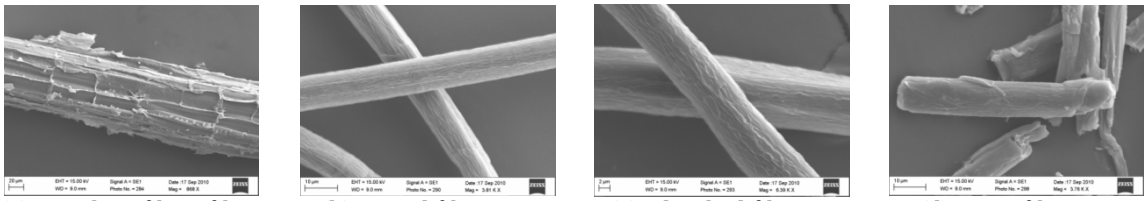

(a) Raw kenaf bast fibers (b) Retted fibers (c) Bleached fibers (d) Microfibers

Figure 10.2: SEM images of the raw kenaf bast fibers, retted fibers, bleached fibers and microfibers.

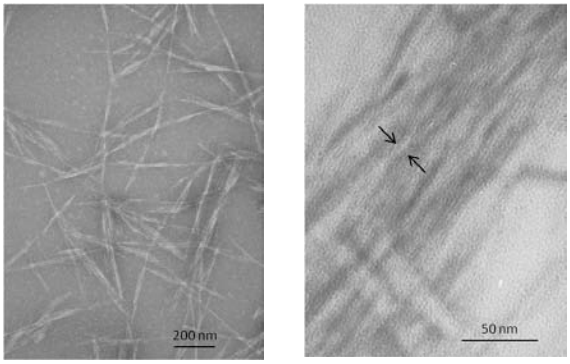

(a) (b)

Figure 10.3: TEM images of cellulose nanowhiskers (CNWs). (a) magnification = 50,000X, accelerating voltage = 100 kV; (b) magnification= 370,000X, accelerating voltage = 100 kV.

Table 10.5: Fiber length and diameter statistics.

		Retted fibers (µm)	Bleached fibers (µm)	Microfibers (µm)	CNWs (nm)
Length	Mean	471.0	215.32	46.39	628.38
	Stdev	606.98	141.62	16.38	360.05
Diameter	Mean	10.70	10.63	9.58	34.75
	Stdev	2.68	2.05	2.25	21.43

The alkaline retting treatment liberated the single fibers from the fiber bundles of the raw kenaf bast fibers. After most of outer layer substances were removed by chemical treatment, retted and bleached fibers had a clean surface. Diameters of retted (10.70 µm) and bleached (10.63 µm) fiber were similar. The length of bleached fiber was reduced from 471 µm (average length of retted fiber) to 215 µm. Acidic hydrolysis treatment broke the bleached fibers through their cross sections, thus the lengths of the fibers reduced significantly. However, the average diameter of microfibers was 9.58 µm and was not significant reduced. The average aspect ratio of the microfiber was 4.97.

A Micro-tension Test Method for Measuring Four Representative Individual Cellulosic Fibers

***Objectives*:** The overall objective of this research was to develop an experimental technique to stress the micro cellulosic fibers and to evaluate mechanical properties of several representative individual fibers.

This work was collaborated with the International Center for Bamboo and Rattan (ICBR), Beijing, China.

***Micro Tensile Test System Development*:** A micro tension testing system was devised to measure the mechanical properties of individual cellulosic fibers. The tensile test system (SF-1 microtester) consists of two ball-and-socket type grips inside an environmental chamber, a load cell (UL-10GR; Minebea Co. Ltd., Tokyo, Japan), a three-dimension adjustable stage with an attached high precision linear ball bearing slide (SKF, Sweden), two horizontal and vertical CCD cameras with macro lenses (Daheng, DH-HV1303UM, 1280 × 1024), and a stepper motor (Oriental Motor, USA) (Figure 10.4). The system can measure tensile modulus, strength, creep, relaxation, and cyclic loading characteristics as well as effect of moisture on mechanical properties of a micro fiber.

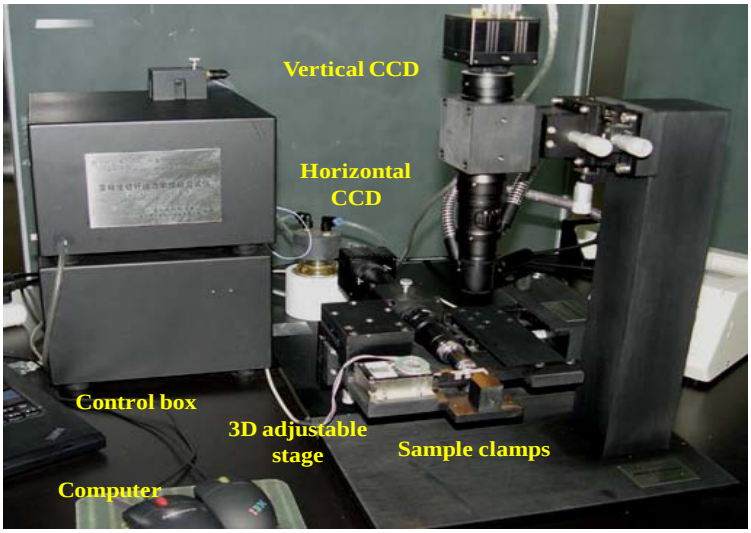

Figure 10.4: Image of the micro tensile test system (SF-1 Microtester I)

***Morphology of Natural Fibers*:** The typical cross-sectional images of an individual fiber by a confocal laser scanning microscope (CLSM) and environmental scanning electron microscope (ESEM) are shown in Figures 10.5 & 6. Both kenaf and bamboo have a thick secondary cell wall with a very small lumen in polygonal shape, which indicates that both fibers undergo extensive cell-wall thickening during maturation. Ramie individual fiber is flattened and typical hexagonal or oval in shape, while those of Chinese fir are rectangular in cross section.

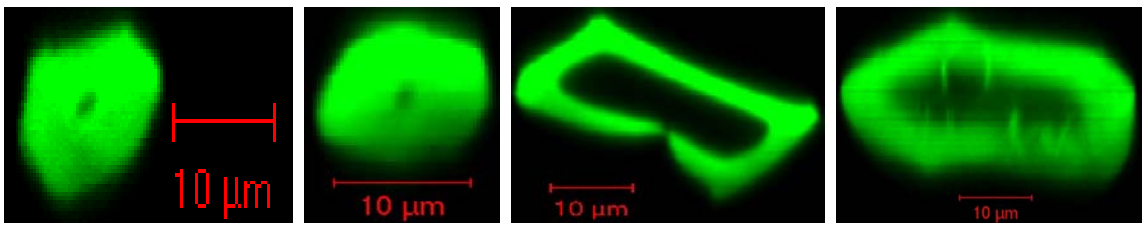

Figure 10.5: The typical CLSM images of cross section of an individual fiber (The left to right: Bamboo, Kenaf, Chinese fir, and Ramie)

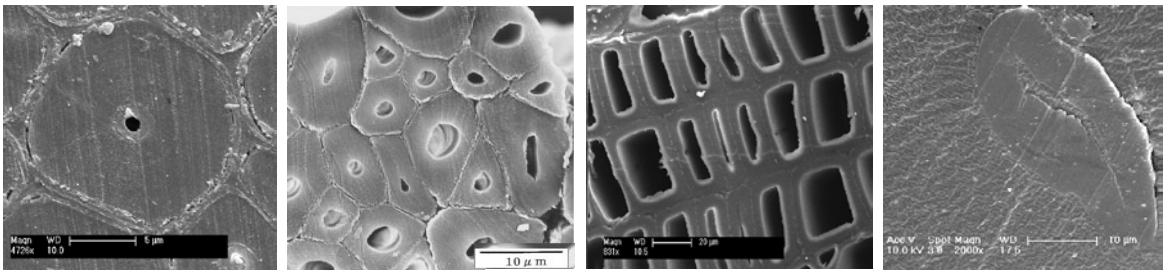

Figure 10.6: The typical ESEM images of cross sections of individual fibers (The left to right: Bamboo, Kenaf, Chinese fir, Ramie)

***Mechanical Properties of Natural Fibers*:** Typical load-displacement curves (Figure 10.7a) and converted stress-strain curves using the cell wall cross-sectional area (Figure 10.7b) show that the fibers are linear and brittle in tensile properties except that the Chinese fir juvenile latewood fiber demonstrated curvilinearity. The averages and standard deviations of tensile modulus, tensile strength, elongation at break, and cross-sectional area of four fibers are summarized in Table 10.6.

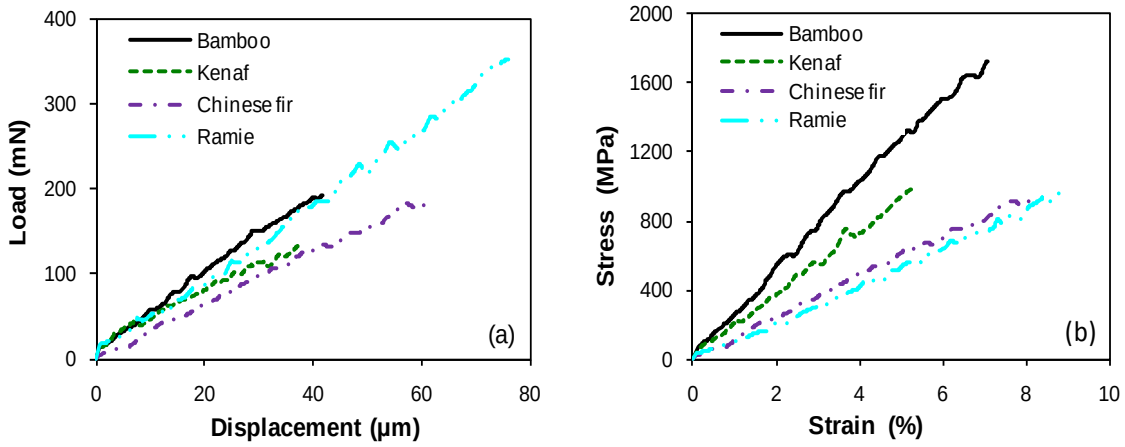

Figure 10.7: The typical load-displacement (a) and stress-strain (b) curves of the individual fibers

Table 10.6: Mean and standard deviation of properties for ramie, fir, kenaf and bamboo

	Tensile Modulus (GPa)			Tensile Strength (MPa)			Cell Wall Area (μm^2)			Elongation at Break (%)		
Ramie	11.4	1.9	C*	1001	153	B	337	78	A	8.9	1.59	A
Chinese Fir	14.2	6.7	C	908	418	B	217	52	B	8.2	2.46	A
Kenaf	19.5	7.6	B	983	194	B	140	44	D	5.4	1.72	C
Bamboo	25.7	4.8	A	1685	293	A	117	35	C	7.0	1.13	B
*Means with the same letter are not significantly different at $\alpha = 0.05$												

Kenaf/Glass Fiber Hybrid Composites

***Objective*:** The objective was to better understand the effect of pressure of hot pressing and layups on the hybrid polyester composites processed from randomly woven kenaf fibers and fiberglass.

***Natural Fiber Composite Fabrication*:** Randomly woven kenaf fibers were used in the study. These materials were provided by Kengro Corporation, Charleston, MS. EB 9496 polyester resin with randomly oriented fiberglass provided by Magna Composites was used to fabricate the SMC.

Flexural Test: The flexural testing was performed using an Instron 5566 tabletop model. The testing procedure was based on the ASTM standard D 790–07. Average moduli of elasticity and rupture for samples used are given in Table 10.7.

Table 10.7: Average moduli of elasticity (MOE) and moduli of rupture (MOR) for hybrid SMC samples

Sample	Curing Pressure % of 6.9, MPa	Lay-up of Kenaf Fiber	MOE, GPa	MOR, MPa
A	20	Single layer	9.95	250
C	40	Single layer	9.82	231
D	60	Single layer	9.82	234
E	80	Single layer	9.34	271
F	80	Double layer	9.92	227
G	60	Double layer	9.39	198
H	40	Double layer	9.04	209
I	20	Double layer	8.26	193
No Kenaf	100	0	9.01	266

Molecular Dynamic (MD) Modeling of Polymers and Polymer Composite Materials

***Objective*:** The objective of this work was to understand the variables associated with the deformation of thermoplastic polymers using atomistic modeling, i.e., chain length, number of chains, strain rates, temperature, etc.

***Methods*:** Molecular dynamics simulations were used to study the deformation mechanisms during uniaxial tensile deformation of amorphous polyethylene. The stress-strain behavior comprised elastic, yield, strain softening and strain hardening regions that were qualitatively in agreement with previous simulations and experimental results (Figure 10.8) (Hossain et al. 2010). The chain lengths, number of chains, strain rate and temperature dependence of the stress-strain behavior were investigated. The energy contributions from the united atom potential were calculated as a function of strain to help elucidate the inherent deformation mechanisms within the elastic, yield, and strain hardening regions.

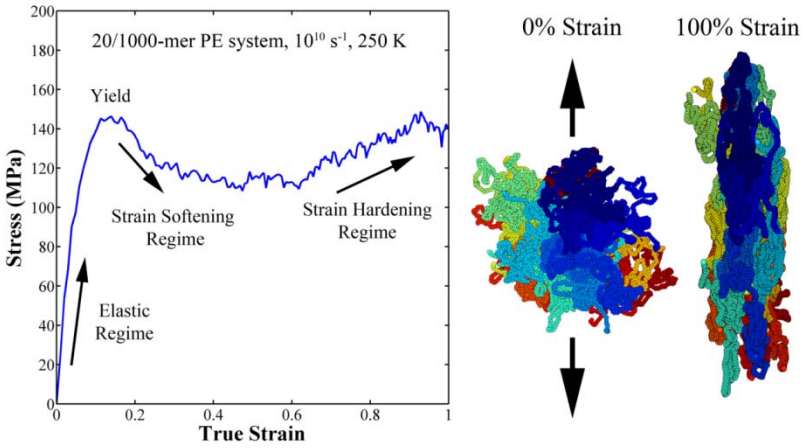

Figure 10.8: Stress-strain response for amorphous polyethylene deformed by uniaxial tensile loading.

***Results and Discussion*:** The results of examining the partitioning of energy showed that the elastic and yield regions were mainly dominated by interchain non-bonded interactions whereas the strain hardening regions were mainly dominated by intrachain dihedral motion of polyethylene. Additional results showed how the internal mechanisms associated with the bond length, bond angle, dihedral distributions, change of free volume and chain entanglements evolve with increasing deformation. Current work is focusing on the deformation behavior of polypropylene and glucose interfaces as a model for the composite materials used in this work. Molecular dynamics and molecular statics simulations will be used to examine elastic and plastic properties of amorphous cells of both glucose and polypropylene as well as the interface mechanical properties between the two materials.

Silane Treatment of Kenaf Fiber

***Objective*:** The objective of this work was to chemically modify kenaf fiber to improve the moisture resistance of the resulting fiber composites. The silane agent used in this work was vinyl tris(2-ethoxymethoxy) silane. An exploratory study of the silane treatment effect on water absorption and mechanical properties was conducted.

***Methods*:**Silane treatment kenaf fiber: Vinyl tris(2-ethoxymethoxy) silane was mixed with an ethanol/water mixture in the ratio of 6:4. 0.6% solution of silane was used. Acetic acid was used to control the pH of the solution at 4 to make sure the complete hydrolysis of the silane. After adjusting the pH, the silane solution was allowed to stand for an hour. The solution was then drained out and the fibers were air dried for half an hour followed by drying in an oven at 103ºC until a constant weight was obtained.

Kenaf fiber composites fabrication: Unstaturated polyester and 1, 1-Di (tertbutylperoxy) Cyclohexane as catalyst in the ratio of 0.985: 0.015 was mixed thoroughly, and evenly poured onto the surface of two fiber sheets. These two sheets were closed together with resin mixture in the core. The sample was put into a stainless steel mold and pressed at 100 ºC and 2.5MPa for 2 hours.

***Results and Discussion*:** The water absorption of silane treated kenaf fiber composites decreased by 22% compared to untreated fiber composites. After 4 weeks of water immersion, the water absorption curve for the silane treated kenaf fiber composites was leveled off, while that of untreated kenaf fiber composites continued to increase (Figure 10.9a). The hydrophilic nature of the kenaf fiber was reduced and hence the water resistance of the resulting fiber composites was improved after the silane treatment of kenaf fibers. Compared to untreated fiber composites, the flexural strength and modulus of the silane treated kenaf fiber composites increased by 25% and 8%, respectively (Figure 10.9b). The silane treatment of kenaf fiber also improved the mechanical properties of the resulting fiber composites.

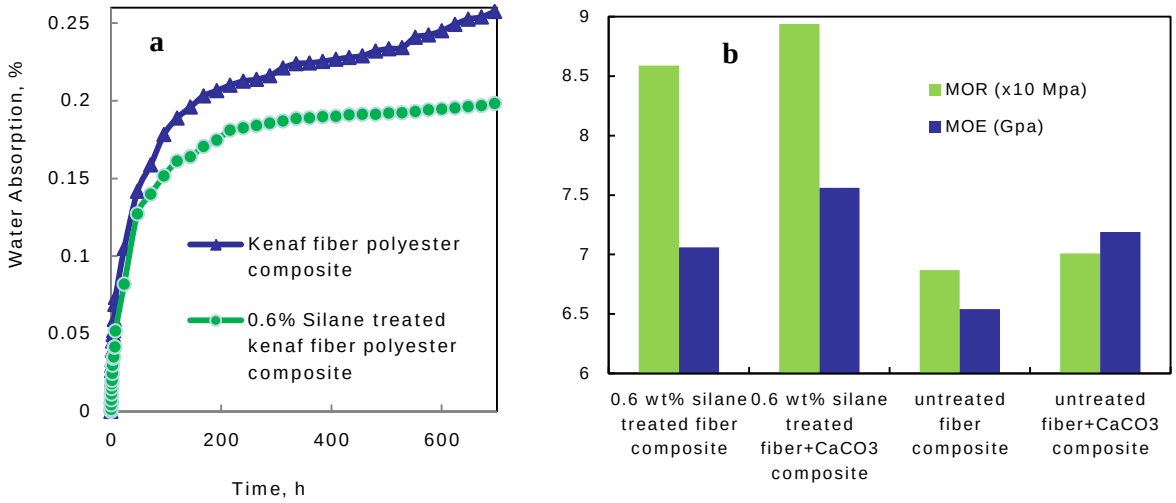

Figure 10.9. a) Water absorption of treated and untreated kenaf fiber composites and b) Flexural properties of treated and untreated kenaf fiber composites.

Molecular Dynamics Simulation of Deformation in Amorphous Cellulose

***Objective*:** The ability to form various ultrastructural composites depended on both the conformational characteristics and the mechanical behavior. The objective of this work was to understand the structure of amorphous cellulose which was a key step to characterize the properties of cellulose fibers.

***Methods*:** Molecular dynamics deformation analysis, followed by minimization, was used to generate the structures for amorphous glucose. Properties related to the deformation were calculated for these models and compared with predicted geometric, energetic and elastic properties of the material to published modeling results and experimental measurements.

Force Field: In this work, the ReaxFF reactive force field (van Duin 2001; Chenoweth 2008) was used to simulate the bonding between the various elements of glucose. ReaxFF was a general bond-order-dependent force field that provided accurate descriptions of bond breaking and bond formation during dynamic simulations. The main difference between the traditional unreactive force fields and ReaxFF was that the connectivity in ReaxFF was determined by bond orders calculated from interatomic distances that were updated every MD step. This allowed for bonds to break and form during the simulation. Equation 10.1 shows that ReaxFF partitions the overall system energy E_{system} into contributions from various partial energy terms, i.e.

$$E_{system}=E_{bond}+E_{under}+E_{over}+E_{val}+E_{pen}+E_{tors}+E_{conj}+E_{vdwaals}+E_{coulomb} \quad (10.1)$$

These partial energies included bond energy E_{bond}, atom under-/overcoordination E_{under}, E_{over}, valence angle E_{val}, penalty energy E_{pen}, torsion angle E_{tors} and conjugation energy E_{conj} terms to properly handle the nature of preferred configurations of atomic and resulting molecular orbital and terms to handle van der Waals $E_{vdwaals}$ and Coulomb $E_{coulomb}$ interactions. These latter non-bonded interactions were calculated between every atom pair, irrespective of connectivity, and were shielded to avoid excessive repulsion at short distances. This treatment of nonbonded interactions allowed ReaxFF to describe covalent, ionic, and intermediate materials, thus, greatly enhancing its transferability.

Simulation Methods: The cellulose repeat unit consisted of two glucose rings bridged by the 1-4 glycosidic bonds. Three chain lengths were tested: 20, 50, and 100 repeat units per chain. Initial densities of 0.8 g/cm^3 were considered. Because the cell parameters were allowed to vary during molecular dynamics simulations, the density could therefore vary in range of 1.28 g/cm^3 to 1.44 g/cm^3. Periodic boundary conditions were applied in all three directions. The initial configuration of the system was generated using commercial Materials Studio software and all subsequent molecular dynamics simulations were performed using the LAMMPS simulation tool with a time step of 0.5 fs. The unit cell models were replicated by 3x3x3 to simulate more atoms. The simulation procedure began with minimization of each system. Next, the system was equilibrated at chosen temperature using NVE-MD simulation with a time step of 0.5 fs. The equilibrated systems were then used to perform the deformation simulations under a uniaxial tensile strain applied at a constant strain rate. The reactive force field used here was to describe the atomic interactions for dynamic bond scission and bond formation. Three different strain rates (10^8, 10^9, and 10^{10} s^{-1}) were applied to the loading boundary with ReaxFF for different numbers of chains and chain lengths. The amorphous cellulose configurations were deformed at 100 K, below the glass transition temperature.

Results and Discussion

Simulation Conditions: With ReaxFF, a suitable time step was required because the charges and bond orders were allowed to change at every time step. The ultimate aim was to simulate the longest possible time with the smallest amount of computational effort. The choice of time step was therefore a compromise between a large value which would require less molecular dynamics MD steps for a given simulated time, and a small value which allowed each time step to be calculated faster. The time step must be sufficiently small that dynamics correctly conserve the total energy of the system. A greater temperature fluctuation was noticed from the initial value in the 1 fs time step case while the temperature is computed more stable using 0.5 fs time step as the simulation cell was equilibrated. The energy (total, kinetic, potential) as a function of simulation time showed the same result. Another sign of instability with the 1 fs was the ejection of atoms from the simulation cell, which could occur if atoms get too close. Therefore, future simulations were needed to use a time step of lower than 0.5 fs.

Glass Transition Temperature: The glass transition temperatures T_g were related to the physical stability of an amorphous formulation. The thermal expansivity of an amorphous cellulose system was expected to decrease at its T_g when it passed from a rubbery to a glassy state. Thus, plotting volume as a function of temperature for amorphous cellulose (Figure 10.10) showed a change in slope at the glass transition temperature. The T_g could thus be identified at the point of intersection between the high- and low-temperature branches in this plot. The NPT ensemble (constant number of particles, pressure and temperature) was used for the MD glass transition temperature simulations, with the pressure fixed at zero bar.

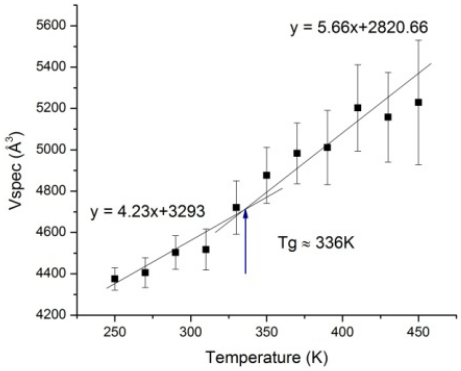

Figure 10.10. Evolution of volume as a function of temperature

Physical and mechanical properties of amorphous cellulose models are shown in Table 10.8.

Table 10.8. Mechanical properties of amorphous cellulose models

Properties	Density (g/cm^3)	T_g (K)	Young's modulus (GPa)	Shear modulus (GPa)	Poisson's ratio
ReaxFF	1.347	336	9.37	3.94	0.189
Literature Value	1.385	296-325	10.42±1.08	5.955±0.673	0.232±0.0313

Thermodynamic and mechanical properties such as density, glass transition temperature, Young's modulus, Shear modulus and Poisson's ratio were calculated and found to be comparable with literature values (Chen et al 2004). We concluded that the amorphous cellulose models with ReaxFF were representative of the amorphous structure in cellulose as far as the mechanic properties were concerned.

Strain-stress: Figure 10.11 shows how the tensile loading leads to a net change in shape of the cell, where the colors represent the different atom types (C, H, O). To investigate the deformation behavior of cellulose, the stress-strain behavior, temperature dependence, and internal energy evolution were monitored as a function of deformation. Figure 10.12 shows the stress-strain behavior for amorphous cellulose at a strain rate of 10^{10} s^{-1}. The red dots were stress values taken at various strain levels and the black line was the averaged response; this scatter was typically of polymer deformation in molecular dynamics. After an initial elastic regime, yield occurs and then strain hardening was observed. The green and blue dots (mainly hidden behind green dots) represented stresses in the directions lateral to the loading direction – these are centered about 0 GPa, a boundary condition indicative of the uniaxial tensile load applied. This stress-strain curve was similar to previous simulations in the literature as well as experimental results (Chen et al 2004).

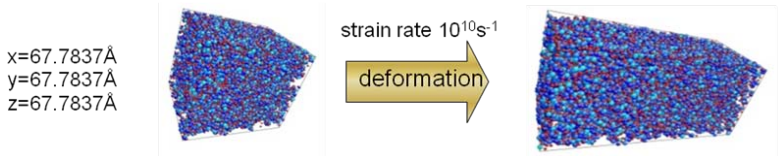

Figure 10.11. The model system in equilibrium at 100K and after being uniaxially deformed. Colors represent different atom types being simulated (C, H, and O).

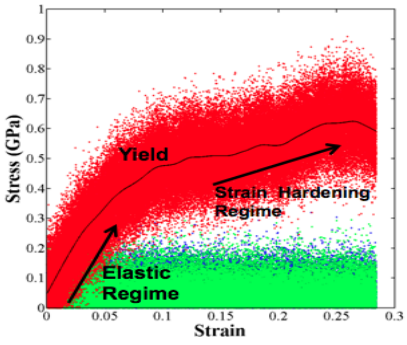

Figure 10.12. A characteristic stress-strain curve for amorphous cellulose (28404 atoms, 100 K temperature, 10^{10} s^{-1} strain rate). Black line is the average stress response in the tensile direction. Red, green, and blue dots show the scatter of the instantaneous stresses the loading direction and two lateral directions, respectively.

Multiscale Modeling of Moisture Absorption Process in Natural Fiber Composites

Objective*:** The objective of this effort was to develop an advanced multiscale modeling framework to investigate the moisture absorption process in natural fiber composites on the basis of a recently developed micromechanics modeling framework, namely, ***Variational ***A***symptotic ***M***ethod for ***U***nit ***C***ell ***H***omogenization (VAMUCH), which takes the ***V***ariational ***A***symptotic ***M***ethod (VAM) as the mathematical foundation.

Methods*:** The ***Variational ***A***symptotic ***M***ethod for ***U***nit ***C***ell ***H***omogenization (VAMUCH) takes the ***V***ariational ***A***symptotic ***M***ethod (VAM) as the mathematical foundation. VAM combines the merits of both variational methods and asymptotic methods. It expands the variational statement asymptotically in terms of small parameters inherent in the problem. The result obtained using variational asymptotic method converges asymptotically to exact solutions if such solutions exist. Variational asymptotic method is applicable to any problem having a variational statement with small parameters and it seamlessly bridges the gap between engineering and mathematical approaches. The commercial finite element software ABAQUS was used to analyze the global transient water absorption process in natural fiber composites according to the effective properties calculated by VAMUCH. If they are of interest, the distributions of local fields can be accurately recovered by VAMUCH according to the global response.

***Results and Discussion*:**

The developed multiscale model has the following functionalities:

(1) It can accurately and efficiently provide the effective water diffusion coefficients. Then, the commercial finite element software, such as ANSYS and ABAQUS, can be employed to analyze the global transient water diffusion process in composite materials and structures as well as the influences of resistance of boundary surface using the water diffusion coefficients provided by VAMUCH.

(2) It can accurately and efficiently recover the distributions of local fields according to the global response of composite materials and structures.

In this study, we investigated the moisture diffusion process in wood fiber polymer matrix composites. The volume fraction of the fiber (V_f) is 30%. Both constituents are isotropic with moisture diffusion coefficient D_f = 30 mm^2/s for wood fiber, and D_m = 0.218 mm^2/s for polymer matrix. Since the finite element method (FEM) is considered as one of the most accurate way to obtain effective properties we also used the results calculated by ABAQUS as a benchmark to verify the VAMUCH outcomes. Table 10.9 shows the effective moisture diffusion coefficients calculated by VAMUCH and ABAQUS. It can be seen that both approaches provide identical results.

After obtaining the effective properties, the global transient moisture diffusion process was performed using commercial software ABAQUS. Here we investigated the transverse moisture diffusion behavior. A two dimensional square finite element (FE) model as shown in Figure 10.13 was used in this study. Eight-node elements were employed. The dimension of FE model is 100 × 100 mm. The top and bottom boundaries were sealed. Moisture can only transfer into the model from both side boundaries. The distribution of the moisture concentration along the horizontal center line at different time were plotted in Figure 10.14 as the water concentration C_a at the side boundary was kept constant as 10 g/mm^3 all the time.

Table 10.9. Effective moisture diffusion coefficients (mm2/s) obtained from VAMUCH and ABAQUS. Subscript 1 represents longitudinal direction while 2 and 3 stand for transverse properties.

Effective D	D_1^*	D_2^*	D_3^*
VAMUCH	9.152	0.4016	0.4016
ABAQUS	9.152	0.4016	0.4016

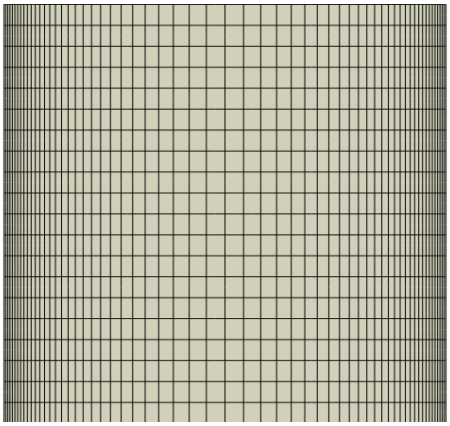

Figure 10.13. Finite element model for the analysis of the global transient moisture diffusion process.

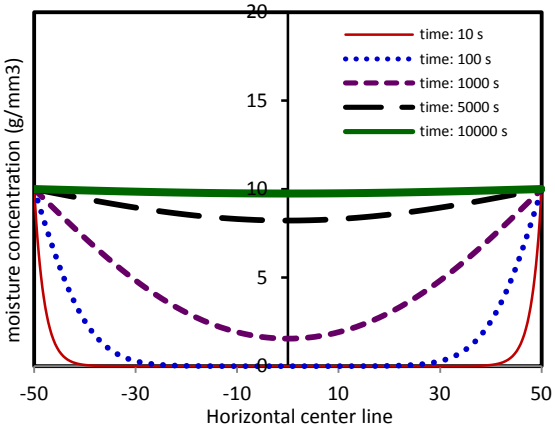

Figure 10.14. Distribution of moisture concentration along the horizontal center line at different time.

Figure 10.15 shows the contour plots of moisture concentration flow flux in y_2 direction at 100 s, respectively, when the water concentration C_a is kept constant as 10 g/mm^3. To quantitatively describe the moisture concentration flow flux, we plotted the distribution of moisture concentration flow flux (g/s.mm2) in y_2 direction along the vertical center line of unit cell at different time in Figure 10.16. It can be seen that the moisture concentration flow flux decreased with time since the gradient of moisture concentration, which is the driving force for moisture diffusion, decreased with time.

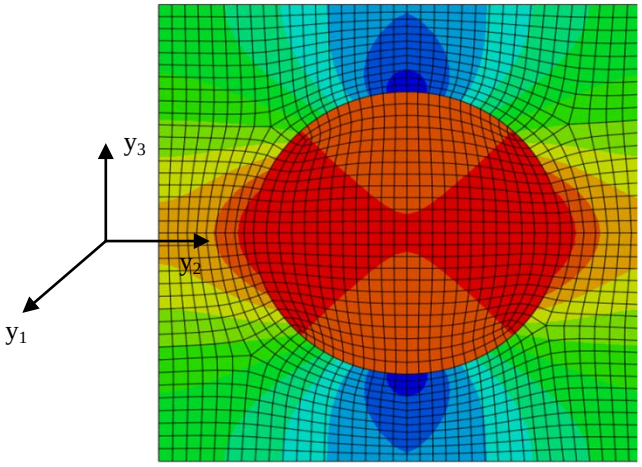

Figure. 10.15. Finite element model for the analysis of the global transient moisture diffusion process.

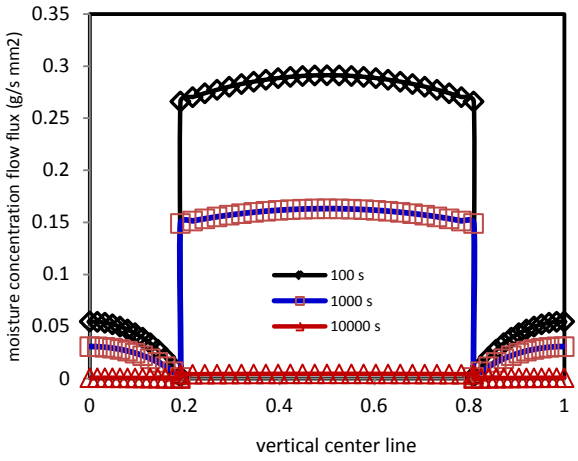

Figure. 10.16. Distribution of moisture concentration along the horizontal center line at different time.

Life-Cycle Assessment of Natural Fiber Polymer Composites

***Objective*:** The objective of this work was to use principles and practices of life-cycle assessment (LCA) to evaluate environmental performance of natural fiber reinforced bio-resin matrix composites and collected the data needed to make LCA calculations.

***Methods*:** A series of kenaf fiber reinforced sheet molding composites (SMC) have been fabricated in the laboratory for scoping and optimization. The life-cycle assessment was conducted on three product scenarios: Formulation 1(kenaf fiber SMC), Formulation 4 (kenaf 20 % soy resin SMC, containing 20% modified soybean oil in solid resin), and glass fiber SMC (Springer, 1983). The data for soybean oil resin

and kenaf fiber reinforced composites were collected from MSU Forest Products lab. The data for unsaturated polyester resin and glass fiber SMC were collected from the literature (Springer, 1983) and SimaPro software. These data include energy and materials balances for manufacturing 1 kg raw materials, intermediates, and products, as well as the emissions to air, discharges to water, and solid wastes to land. These data were then entered into LCA software SimaPro V7.3. Environmental performances were measured by a set of environmental impact indexes come up with by NIST Building for Environmental and Economic Sustainability (BEES), cumulative energy demand and a weighted environmental burden.

Environmental performances of materials are usually compared based on a functional unit: an entity capable of accomplishing a specified purpose. SMCs are supposed to be used for automotive manufacture. Interior parts in cars are still designed for stiffness. To achieve the equal stiffness (Eq.10.2) to a reference material (r subscript), the mass (m) and thickness (t) are calculated by Eqs. 10.3 & 4.

$$\frac{F}{\delta} = \frac{E m^3}{c b^2 l^6 \rho^3} \quad (10.2)$$

$$m = \left(\frac{E_r}{E}\right)^{\frac{1}{3}} \frac{\rho}{\rho_r} m_r \quad (10.3)$$

$$t = \left(\frac{E_r}{E}\right)^{\frac{1}{3}} t_r \quad (10.4)$$

Setting glass fiber SMC as the reference material, the masses required to achieve compatible stiffness were calculated as shown in Table 10.10. The running capacity during the use phase was assumed as: 175, 000 km (12 years). Fuel reduction coefficient on gasoline powered vehicles due to weight reduction of using light materials is selected as 0.34 l/(100 kg *100 km) for a lighter car (lower limit, New European Driving Cycle). The amounts of saved gasoline at use phase were thus calculated as shown in Table 10.10.

Table 10.10 Functional unit with equal stiffness

	Glass Fiber SMC	Kenaf SMC	Kenaf 20% Soy Resin SMC
Density (g/cm^3)	1.87	0.95	1.04
Flexural Strength (GPa)	14	7.38	7.29
Mass (kg) with Equal Stiffness	1	0.63	0.69
Save gasoline at Use Phase (l)	Ref.	2.2	1.8

At the end-of-life disposal, the used products were assumed to be incinerated. Consumption of energy of incineration[3] was selected as: Heat: 0.24 MJ/kg, Electricity: 0.36 MJ/kg; bonus of incineration of plastics energy recovery[3] (LHV = 30.5 MJ/kg), Heat: 26%, Electricity: 10%; bonus of incineration of kenaf energy recovery: (LHV =14 MJ/kg), Heat: 26%, Electricity: 10%. Incineration of discarded glass fiber reinforced plastics generates a lot of black smoke and bad smells and often gives damage to incinerator by fusion of glass fibers, thus without any bonus of energy recovery.

***Results and Discussion*:**

Figure 10.17 indicates that kenaf fiber has less negative environmental impact than glass fiber during a period from raw materials extraction to fiber manufacturing. Figure 10.18 shows that bast fibers consume less energy than other fibers in manufacturing 1-kg fibers. Wood pulp and bast fibers consume less non-renewable energy. Method to calculate Cumulative Energy Demand was based on the method published by Ecoinvent version 2.0 and expanded by PRé Consultants for raw materials available in the SimaPro 7 database. Figure 10.19 demonstrates that natural fibers achieved overall lower environmental burdens. Land uses contributed substantial portions for agri-fibers (jute and kenaf). The scale is chosen in such a way that the value of 1 point is representative for one thousandth of the yearly environmental load of one average European inhabitant. The key environmental measures for three product scenarios were computed with Simapro software and are shown as in Figure 10.20. Negative means carbon credit,

i.e. saving non-renewable resources otherwise being used. Both kenaf-fiber reinforced SMCs perform better than glass fiber SMC in every environmental category. The global warming potential of the kenaf fiber SMC could be only about 45% of that for the glass fiber SMC.

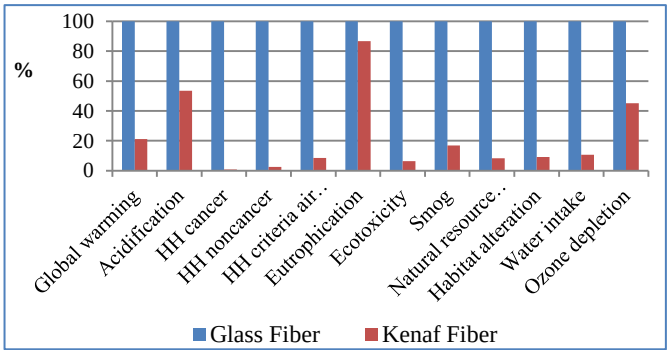

Figure 10.17. Comparison of environmental impacts of fiber productions. BEES impact indexes are selected as characteristics.

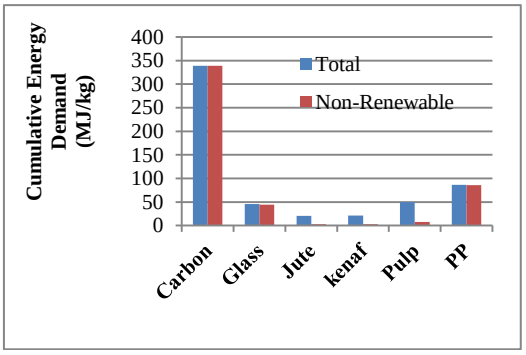

Figure 10.18. Cumulative energy demands of typical fiber productions (per 1 kg fiber)

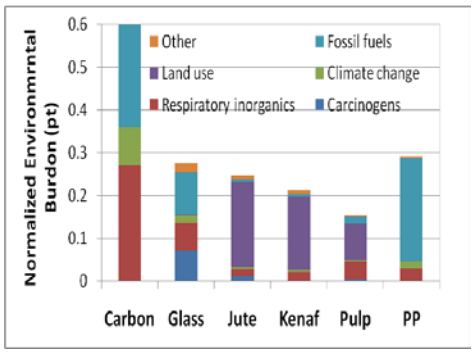

Figure 10.19. Weighted environmental points for typical fiber productions (per 1 kg fiber)

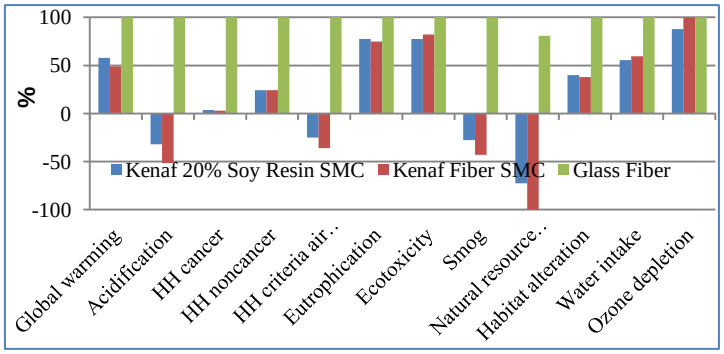

Figure 10.20. BEES environmental impacts of manufacturing three fiber reinforced polymer composites (per functional unit).

Conclusions

The alkaline retting treatment efficiently removed hemicellulose and lignin from kenaf bast fiber. Bleaching treatment could remove the remanent lignin from the retted fibers. Pure cellulose fibers in micrometer scale and nanometer scale were obtained by acidic hydrolysis of the bleached fibers. Our kenaf natural fiber SMC has comparative properties comparing with the commercial glass fiber SMC. The inorganic nanoparticle impregnated kenaf fiber SMC was not degraded after the accelerated weathering test.

The SF-I microtester is well suited for measuring the mechanical properties of individual micro fibers. Among the tested species, the bamboo fiber had the highest tensile strength and modulus and the smallest cell wall cross-sectional area. The ramie had the largest cell wall cross-sectional area and elongation at break, but lowest tensile modulus. Kenaf showed the lowest elongation at break and other properties of kenaf were balanced.

A process to fabricate laminated natural fiber kenaf-based composite was developed. Various samples are manufactured with modulus of elasticity up to 10 GPa and modulus of rupture up to 270 MPa.

Simulation results showed that temperature increase of polymer in high rate tests can be reproduced by augmenting the deformation boundary conditions. This might shed light on the fundamental mechanisms associated with the generation of heat in thermoplastic polymers under high rate deformation.

Vinyl tris(2-ethoxymethoxy) silane treatment of kenaf fiber improved the physical and mechanical properties of the resulting kenaf fiber composites. The water absorption of silane treated kenaf fiber composites decreased by 22% compared to untreated fiber composites. The flexural strength and modulus of silane treated kenaf fiber composites increased by 25% and 8%, respectively.

A suitable timestep as less 0.5 fs is found to use in future simulations with ReaxFF. Thermodynamic and mechanical properties such as density, glass transition temperature, Young's modulus, Shear modulus and Poisson's ratio were calculated and found to be comparable with literature values. The simulated stress-strain behavior using molecular dynamics showed similar trends both qualitatively and quantitatively as those observed in the experimental testing for amorphous cellulose.

A multiscale model of moisture absorption process of natural fiber composites was developed on the basis of the theoretical framework of VAMUCH. Compared with other existing micromechanics approaches, VAMUCH has the following unique features:

- VAMUCH can obtain the complete set of material properties within one analysis *without applying any load and any boundary conditions*, which is far more efficient and less labor intensive than those approaches requiring multiple runs under different boundary and load conditions. It is also noted that VAMUCH can even obtain the complete set of 3D material properties using a one-dimensional analysis of the 1D UC for binary composites. It is impossible for FEA-based approaches.
- VAMUCH calculates effective properties and local fields directly with the same accuracy as the fluctuating functions. No postprocessing calculations which introduce more approximations, such as averaging stress or strain fields, are needed, which are indispensable for FEM-based approaches.
- VAMUCH can recover the local fields using a set of algebraic relations obtained in the process of calculating the effective properties. Another analysis of the microstructures which is needed for FEA-based approaches is not necessary for VAMUCH.

The present methodology can be straightforwardly extended to the effective dielectric, magnetic, and heat conduction properties of heterogeneous materials due to the mathematical analogy of these problems.

The LCA preliminary result demonstrated that the use of modified soybean oil and natural fiber to make sheet molding compound had a great potential from an ecological point of view. LCA is an effective tool and adds a dimension to evaluate new products and associated processes.

Publications/Presentations/Patents

Publications

1. Q. Gao, S. Q. Shi, S. Zhang, J. Li, X. Wang, W. Ding, K. Liang, and J. Wang. 2011. Development of soybean meal based wood adhesives. Journal of Applied Polymer Science. (In Press)
2. K. Liang and S. Q. Shi. 2011. Nanoclay Filled Soy-based Polyurethane Foam. Journal of Applied Polymer Science. 119, 1857-1863.
3. G. Wang, S.Q. Shi, and J. Wang. 2011. Tensile Properties of Four Types of Individual Cellulosic Fibers. Wood and Fiber Science. 43(4), 353-364.
4. G. Wang, S.Q. Shi, and J. Wang. 2011. Microtension Test Method for Measuring Tensile Properties of Individual Cellulosic Fibers. Wood and Fiber Science. 43(3), 251-261.
5. K. Liang and H. Toghiani, C.U. Pittman. 2011. Synthesis, Morphology and Viscoelastic Properties of Epoxy/Polydedral Oligomeric Silsesquioxane (POSS) and Epoxy/Cyanate

Ester/POSS Nanocomposite. Journal of Inorganic and Organometallic Polymers and Materials. 21, 128-142.

6. J. Shi, S. Q. Shi, H. M. Barnes, and C. U. Pittman, Jr. 2011. A chemical process for preparing cellulosic fibers hierarchically from kenaf bast fibers. Bioresources 6(1): 879-890.
7. J. Shi, S.Q. Shi, H.M. Barnes, M.F. Horstemeyer, J. Wang, and E.-B. M. Hassan. 2011. Kenaf Bast Fibers -- Part I: Hermetical Alkaline Digestion, International Journal of Polymer Science, Volume 2011 (2011), 8 pages, 2011. doi:10.1155/2011/212047.
8. J. Shi, S. Q. Shi, H. M. Barnes, M. Horstemeyer, and Ge Wang. 2011. Kenaf Bast Fibers -- Part II: Inorganic Nanoparticle Impregnation for Polymer Composites. Special Issue on "Natural Fibers, Bio- and Nanocomposites", International Journal of Polymer Science. Vol. 2011, ID 736474.
9. K. Liang and S. Q. Shi. 2010. Soy-based polyurethane foam reinforced with carbon nanotubes. Key Engineering Materials Vols. 419 – 420: 477-480. http://www.scientific.net.
10. K. Liang and S. Q. Shi. 2010. Modified soybean oil/polyhedral oligomeric silsesquioxane (POSS) bio-nanocomposites: Synthesis and characterization. Proceedings of 11th International Conference on Biocomposites: Transition to Green Materials, Toronto, Canada. May 2 – 4, 2010.
11. H. Castillo, S. Lee, S. Q. Shi, R. Srinivasan, and J. Shi. 2010. Semi-crystalline polymer-based composites with corn fiber (separated from DDGS) as an interfacial reagent. Proceeding of 11th International Conference on Biocomposites: Transition to Green Materials, Toronto, Canada. May 2 – 4, 2010.
12. K. Liang and S. Q. Shi. 2010. Resins from soybean oil-based additives for natural fiber sheet molding compound (SMC) composites: Synthesis and characterization. Proceedings of Wood Adhesives 2009. September 28 – 30, Lake Tahoe, Nevada, USA.
13. Y. Peng and S. Q. Shi. 2010. Effect of cloisite clay on the dynamic mechanical properties of resin film. Proceedings of Wood Adhesives 2009. September 28 – 30, Lake Tahoe, Nevada, USA.
14. K. Liang and S. Q. Shi. 2010. Nanoclay filled soy-based polyurethane foam. Journal of Applied Polymer Science. 119 (3): 1857 – 1863.
15. J. Shi, S. Q. Shi, H. M. Barnes, C. Pittman. 2010. A chemical process for preparing cellulose nanowhiskers (CNW) from kenaf bast fibers for polymer composites. 2010. Society of Wood Science and Technology (SWST) Convention. Geneva, Switzerland.
16. J. Hua, D. Chen, and S. Q. Shi. 2010. Effect of Incorporating Chinese Poplar in Wood Chips on Fiber Refining. Forest Products Journal. 60 (4): 362 – 365.

Presentations

1. Presented by J. Wang. *Nanophase Treatment of Natural Fiber for Fiber Reinforced Polymer Composites.* 19th Annual International Conference on Composites or NanoEngineering, ICCC-19, Shanghai, China, July 24-30, 2011. (Participants: S. Shi, J. Shi, K. Liang and J. Wang)
2. Presented by S. Shi. *Characterization of Surface Properties for the Inorganic Nanoparticle Impregnation Treated Kenaf Bast Fibers for Polymer Composites.* Presentation at the Forest Products Society 65th International Convention, Double Tree Hotel, Portland, OR, USA, June 19-21, 2011. (Participants: S. Shi, J. Shi, K. Liang and J. Wang)
3. Presented by J. Wang. *Forced Capillary Rise for Thermodynamic Characterization of Surface Tension and Dynamic Contact Angle of Biofibers.* Presentation at the Forest Products Society 65th International Convention, Double Tree Hotel, Portland, OR, USA, June 19-21, 2011. (Participants: J. Wang and S. Shi)

4. Presented by K. Liang. *Kenaf Fiber and Soy Protein Based Biocomposites.* Presentation at the Forest Products Society 65th International Convention, Double Tree Hotel, Portland, OR, USA, June 19-21, 2011. (Participants: K. Liang and S. Shi)
5. Presented by G. Wang. *Develop a Micro-Tension Tester for Measuring Tensile Properties of Cellulosic Fibers.* Poster at the Forest Products Society 65th International Convention, DoubleTree Hotel, Portland, OR, USA, June 19-21, 2011. (Participants: G. Wang, S. Shi, J. Wang, Y. Yu, H. Cheng and S. Cao)
6. Presented by J. Wang. Life cycle assessment of environmental performances of kenaf fiber soy resin sheet molding composites and glass fiber sheet molding composites. Poster at the Forest Products Society 65th International Convention, Double Tree Hotel, Portland, OR, USA, June 19-21, 2011. (Participants: J. Wang, S. Shi, K. Liang and M.F. Horstemeyer)
7. Presented by K. Liang. *Surface Hydrophobizition of Natural Fiber*. Presentation at the 11th International Conference on Wood & Biofiber Plastic Composites, Madison, WI, USA, May 16-18, 2011. (Participants: K. Liang, Y. Shen and S. Shi)
8. Presented by K. Liang. *Kenaf Fiber and Soy Protein Based Biocomposites.* Poster at the 11th International Conference on Wood & Biofiber Plastic Composites, Madison, WI, USA, May 16-18, 2011. (Participants: K. Liang and S. Shi)
9. Presented by S. Shi. *Development of natural fiber sheet molding compound (SMC).* Ontario BioAuto Council Conference, Windsor, Ontario, September 23, 2010 (Over 100 people in the audience) (Participants: S. Shi, K. Liang, M. Qatu, J. Wang, M. Tschopp, D. Nicolas, D. Zhang, L. Sites, J. Shi, I. Fulton, W. Che, and S. Lee)
10. Presented by S. Shi. *Kenaf bast fiber sheet molding compound (SMC) composites with acrylated expoxidized soybean oil*. 64th Forest Products Society (FPS) International Convention, Madison, WI, June 20 - 22, 2010. (Participants: Liang, K. and Shi, S. Q.)
11. Presented by S. Shi. *Graphitization of natural fiber cellulose into carbon fiber*. 64th Forest Products Society (FPS) International Convention, Madison, WI, June 20 - 22, 2010. (Participants: Shi, S. Q., Zhang, S., Jiang, D., Che, W., and Shi, J.)
12. Presented by S. Shi. *Semi-crystalline polymer-based composites with corn fiber (separated from DDGS) as an interfacial reagent*. 11th International Conference on Biocomposites, Toronto, Canada, May 2 – 4, 2010. (Participants: Castillo, H., Lee, S., Shi, S. Q., Srinivasan, R., and Shi J.)
13. Presented by S. Shi. Modified soybean oil/polyhedral oligomeric silsesquioxane (POSS) bio-nanocomposites: Synthesis and characterization. Proceeding of 11th International Conference on Biocomposites: Transition to Green Materials, Toronto, Canada. May 2 – 4, 2010. (Participants: Liang, K. and Shi, S. Q.)
14. Presented by K. Liang. *Modified soybean oil/polyhedral oligomeric silsesquioxane (POSS) bio-nanocomposites: Synthesis and characterization*. 11th International Conference on Biocomposites, Toronto, Canada, May 2 – 4, 2010. (Participants: K. Liang and S. Shi)
15. Presented by S. Shi. *Nanotechnology for Natural Fiber Based Composites*. Harbin Engineering University, Harbin, China, March 10, 2010 (about 25 people in the audience)
16. Presented by K. Liang. Resins from soybean oil-based additives for natural fiber sheet molding compound (SMC) composites: Synthesis and characterization. Proceedings of Wood Adhesives 2009. September 28 – 30, Lake Tahoe, Nevada, USA. (Participants: K. Liang and S. Q. Shi.)
17. Presented by K. Liang. Effect of cloisite clay on the dynamic mechanical properties of resin film. Proceedings of Wood Adhesives 2009. September 28 – 30, Lake Tahoe, Nevada, USA. (Participants: Peng, Y. and Shi, S. Q.)

Patent

1. S. Q. Shi, D. Zhang, J. Shi, and D. Jiang. 4/30/2010. Functional natural fiber nanocomposites and their fabrication techniques. Docket Number: 2009.0734 PROV.

Patent Disclosures

1. D. Zhang and S. Q. Shi. 2/23/2010. Magnetic charcoal and its fabrication. MSU Tech ID: 2010.0767
2. D. Zhang and S. Q. Shi. 8/27/2009. Carbon fiber and functional charcoal from natural cellulosic material. MSU Tech ID: 2009.0744
3. S. Q. Shi, D. Zhang, J. Shi, and D. Jiang. 7/9/2009. Functional natural fiber nanocomposites and their fabrication techniques. MSU Tech ID: 2009.0734

References

1. Bisanda, E.T.N. and Ansell, M.P. 1991. Composites Science and Technology 41: 165-178.
2. Chen, W., Lickfield, G.C. and Yang, C.Q. 2004. Polymer 45(3): 1063-1071.
3. Corbiere-Nicollier, T., Gfeller Laban, B., Lundquist, L., Leterrier, Y., Msnson, J.A.E., and Jolliet, O. Resources, Conservation and recycling, 33 (2001) 267-287.
4. Henriksson, M., Henriksson, G., Berglund, L.A., Lindstrom, T. 2007. Eur Polym J 43:3434-41.
5. Hossain, D., Tschopp, M.A., Ward, D.K., Bouvard, J.L., Wang, P., Horstemeyer, M.F. 2010. Polymer.
6. Iwamoto, S., Nakagaito, A.N., Yano, H. and Nogi, M. 2005. Applied Physic A 81:1109–1112.
7. Kulpinski, P. 2005. Journal of applied polymer science 98:1855–1859.
8. Springer, G.S. 1983. Journal of Reinforced Plastics and Composites 2: 70.
9. Sui ,X., Yuan, J., Yuan, W., Zhou, M. 2008. Chem Lett 37(1):114-115.
10. The Institute of Paper Chemistry. Appleton, W.I. Institute Method, No. 428. 1951.
11. The United Soybean Board and Omni Tech International, Life Cycle Impact of Soybean Production and Soy Industrial Products. 2010.
12. Wise LE, Maxine M and Alfred AD. 1946. Paper Trade Journal 122 (2):35-43.
13. Zadorecki P, Michell AJ. 1989. Polym Compos 10(2):69-77.

MISSISSIPPI STATE UNIVERSITY

Southern Regional Center for Lightweight Innovative Design

Phase III

Final Scientific & Technical Report

October 1, 2009-September 30, 2011

For compliance with contract requirements of Award DE-EE0002323

Task 11

BIO-INSPIRED DESIGN

Submitted December 27, 2011

TASK 11: BIO-INSPIRED DESIGN

Table of Contents

TASK 11: BIO-INSPIRED DESIGN

Principal Investigator: Lakiesha N. Williams
Assistant Professor, Agricultural and Biological Engineering
Mississippi State University
220 Ag and Bio Engineering Bldg., PO Box 9632, Mississippi State, MS 39762
(662)325-3282; fax (662) 325-3853; email: lwilliams@abe.msstate.edu

Participants: J. Liao, H. Rhee, M.F. Horstemeyer

William Joost: Technology Area Development Manager
e-mail: william.joost@ee.doe.gov

Magda Rivera: Project Manager
e-mail: magda.rivera@netl.doe.gov

Contractor: *Mississippi State University (MSST)*
Contract No.: *DE-EE0002323*

Objective

- Determine the structure-property relationships of both soft biological tissues and animal outer armor.
- Use the relationships to develop material models for implementation into finite element codes.

Approach

- Address the structural property relationships of animal soft tissues (liver, skin, tendon) and animal armor (turtle shell, armadillo shells and ram horns), by using similar experimental approaches for all materials.
- Characterization of the change in structure and properties of the materials by capturing its mechanical response along with any structural deformation/damage by using multiple microscopy techniques and tools.

Specific Aims

- Quantify the impact capability of the biological structural materials and soft tissues based on the materials and geometric characteristics, multiscale structures, and mechanical responses.
- Characterize, model, and simulate mechanical behaviors.
- Implement the results from all mechanical experiments into a finite element environment and simulate impact scenarios.
- Contrast/compare the structure-property relations of various biological structural materials to understand mechanisms that lead to the development of novel, bio-inspired safety systems design methodologies.

Milestones, Metrics, and Accomplishments

The objectives were met by accomplishing the following:

- Thorough evaluation of soft tissues (skin, liver and tendon) mechanics via high rate tests and quasi-static mechanical testing;

- Developed a basic framework for the constitutive model of soft tissue (liver), which could potentially be adapted to other tissues and organs.
- Robust and realistic finite element meshes of human head was constructed;
- A basic framework for finite element simulation of human head under blast loads was developed, which could potentially be adapted to other tissues and organs;
- Materials/mechanical properties tests were performed and structure-property relations were investigated of the turtle shell, armadillo shell, rams horn;
- Prepared/submitted many journal articles and presented conference talks.

Introduction

Structure-Property Relationships of Porcine Skin

Head injuries are one of the main causes of death in the United States. According to the National Center for Disease Control and Prevention, "head injuries account for 44% of all injury related deaths in the United States" (sixwise.com, 2009). There has long been a need for predictive human head injury indicators, which today are being used in car crash evaluations, forensic science investigations, and in research, as an alternative to expensive, unpractical, and sometimes unethical animal or human experimentation. The purpose of the present work is to build and validate a numerical model of the human scalp that will realistically model the; skin, connective tissue, aponeurosis, and underlying areolar tissue in a finite element head model. The model will be validated by evaluating pressure and stress distributions in the scalp due to impact. Using finite element modeling software allows us to create a highly detailed graph (or mesh), which we can use to assign mechanical properties to individual layers. We will create an anatomically correct human head (including neck and shoulders). To date, no computational human head scalp model has been developed to include these features.

Structure-Property Relationships of Porcine Tendon

Tendons are the biological tissue that exhibit non-linear viscous property and strain rate sensitivity. The materialistic behaviors of these tissues have been studied extensively over the years (Butler, Grood et al. 1978; Wang 2006). In our study, we focus mainly on the stress state dependency of the tendon tissue. The obtained results will not only help us understand the material properties of the tendon but also help in defining various material parameters while running computational simulations.

Constitutive Model of Porcine Liver

The liver is the most frequently injured intra-abdominal organ (Feliciano, 1989) . In 2007, 1.7 million car accidents resulted in injury in the United States (National Highway Traffic Safety Administration), and one of the most commonly injured abdominal organs in motor vehicle accidents is the liver (Elhagediab, 1998; Rouhana, 1985). Regarding the assessment of automobile-related accidents, current approaches utilize crash dummies to determine optimal safety measures (Feliciano, 1989). The injury metrics for dummies in car crash scenarios are typically force and acceleration; however, real injuries in humans are characterized by damage and fracture (rupture) processes of internal tissues and organs (King, 2000).It is thus important to develop computational models that better represent the human body and are able to predict the risk of human tissue/organ injuries. Recent work in developing a geometrically correct "virtual human" has been performed with the goal of measuring bodily trauma in automobile accidents (Deng, 1999; Haug, 1997; Iwamoto, 2002; Kimpara, 2003). However, soft tissue material properties, which are crucial to a precise human model, are a deficiency.

The development of an accurate computational model requires knowledge of the mechanical properties of different human tissues and organs under different loading conditions, especially in high-impact situations. The response of tissues that may be subjected to high-impact situations such as in automobile accidents, sport injuries, and blunt trauma, these quasi-static tests are limited and cannot be

extrapolated to high rate applications. Mechanical testing thus must be performed at higher strain rates to properly describe the tissue's response during blunt force impacts.

Finite Element Simulations of Blast-Related Traumatic Brain Injury

Blast-related Traumatic Brain Injury (TBI) has become the signature injury of service members in current United States of America (US) military conflicts. Although the use of body armor has substantially reduced soldier fatalities from explosive attacks, these lower mortality rates have been accompanied by a rise in primary and secondary injuries, most notably TBI. Military operations in Iraq and Afghanistan have witnessed an increase in the number of war fighters suffering from TBI due to blast-induced shock waves (Stahura, 2008). More recently, Warden et al. (2009) reported about a female war fighter who suffered from TBI due to Improvised Explosive Devises (IEDs). The female war fighter was diagnosed with multiple long term TBI-associated pathologies. Although many studies have published US war fighters suffering from TBI during their service in Iraq and Afghanistan, limited progress has been made in understanding the physics and pathophysiology of blast-induced TBI. Finite Element Analysis (FEA) of human head could shed light into the nature and damage of the brain tissue due to shock waves.

Recent studies conducted by Belingardi et al. (2005), Elsayed et al. (2008) and Chafi et al. (2010) have present a FE model of the human heads with a higher mesh resolution (2.00×104 - 4.00×104 elements). While Belingardi et al. (2005) and Chafi et al. (2010) presented their work as tool to study TBI and bTBI, Elsayed et al.'s work primarily focused on validating the cavitation induced damage material model for the brain. The material model had viscoelastic and viscoplastic components in its kinematics. Further, Chafi et al.'s work was one the first to model the human head under blast loads. The Boundary Conditions (BCs) for the blast loads were obtained by using varying loads of TNT in the FE code. All of the above mentioned work drew parallels between their simulation results and published brain trauma experimental data and found good correlations for the simulation CPs, principal strains and other Head Injury Criteria (HIC). But none of the above mentioned works were targeted in simulating a published real world scenario of blast injury to study the pathophysiology of bTBI.

To the authors' best knowledge, the current work is the first of its kind in simulated a real world blast scenario incurred by war fighter in Iraq. The case study on the pathophysiology of the war fighter was reported by Warden et al. (2009). In the current study, a detailed mesh of the human head (obtained from Visible Human Project) was used to perform numerical studies on blast-related loads, with a specific viscoelastic-viscoplastic material model for the brain.

Mechanics and Modeling of Animal Outer Armor

Several studies on the structures and mechanical responses of various biological materials have been reported in literature, e.g., (Mayer 2005; Meyers et al. 2008; Meyers et al. 2006; Munch et al. 2008). However, structures and mechanical responses of some biological materials surprisingly have not been studied although they possess superior armor behavior against environmental threats. In this study, we focus exclusively on the material structures, mechanical properties, and compressive deformation behavior of three biological materials whose function is to resist penetration and absorb energy: turtle shell, ram horn, and armadillo shell. Interestingly, all three of these materials are comprised of the same protein - keratin. Keratin is also found in many other tough materials, e.g., skin, hair, fur, claws and hooves. Keratin is classified as either α- or β-keratin, depending on its molecular structure. The protein molecules in α-keratin are arranged in a helical pattern, where, the protein molecules in β-keratin are arranged in a sheet-like pattern. Alpha-keratin is found in mammals, while β-keratin is found in birds and reptiles (Fraser et al. 1972).

McKittrick, et al. (2010) recently reviewed the structure-property relationships in several energy absorbent, mammalian, structural materials, i.e., bones, antlers, teeth, tusks, and hooves, and found that several commonalities permeate through these seemingly very different materials. We extend this study, by investigating the structure-property relationships of a few natural (biological) armor systems, namely turtle shells, armadillo shells, and ram horns. Furthermore, we identify the energy absorbing strategies utilized in these materials and suggest a potential bio-inspired material design based on our findings.

Experimental Approach

Evaluating Structure Property Relationships of Porcine Skin

Porcine skin samples obtained from a local slaughterhouse were used in this study. Porcine scalp histology was used to determined makeup of the porcine scalp tissue structure. The sample shown below in Figure 1 was placed under tension and pulled to 10% strain, fixed with paraformaldehyde, and stained using Hematoxylin and Eosin (H&E).

By performing H&E staining, using a method of parafinization on fixed samples the separate skin layers were clearly distinguishable.

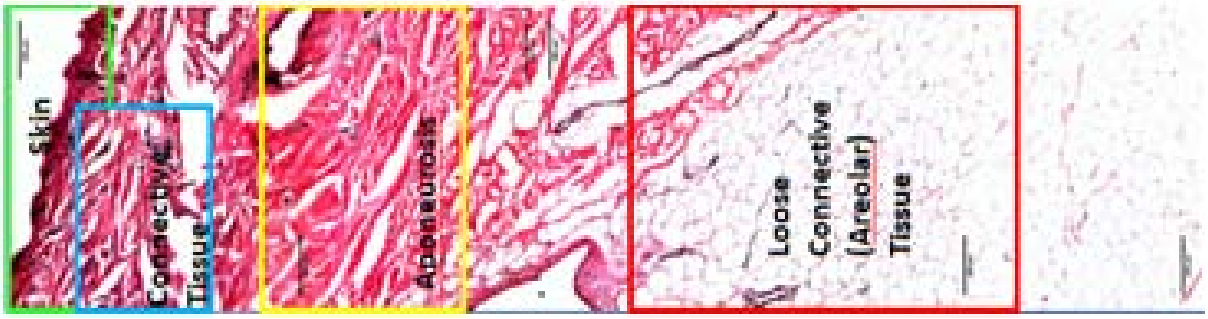

Figure 1. Structural representation of different layers of the skin shown via H&E staining

Due to the noticeably structural differences from staining, multiple stress-strain tests were performed on scalp skin, connective tissue, aponeurosis, and areolar tissues using the Mach1 macro mechanical tester. Tensile scalp composite and areolar average data were used to correlate with the finite element dog bone hyperelastic models. DMA Testing and data analysis were completed on both composite scalp and individual layers to determine the viscoelastic properties. For DMA testing on layers of the scalp, the samples were cut into sections using a vibratome or rotary cutter, while frozen to ensure accuracy.

Evaluating Structure Property Relationships of Porcine Tendon

The objective of this study is to quantify the stress-state nature of the tissue with varying the strain rate and also the role of fiber orientation. The stress state dependency is taken into account by measure the void volume fraction of the samples. All tests were performed in a BSL2 certified laboratory at MSU Ag and Bio Eng Facility. Samples were obtained fresh from the local abattoir (Sansing Meat Service, MS). Excess fat and other tissues were removed from the tendon using scalpel blades. Tissue were tested fresh within 24 hours or kept frozen in - 20°C until tests were done. Sample dimensions were measured using calipers. Tests were done using Mach 1 Micromechanical Testing System® (Biomomentum, Quebec, Canada). Application of load in all mechanical tests was along the fibers (Figure 2).

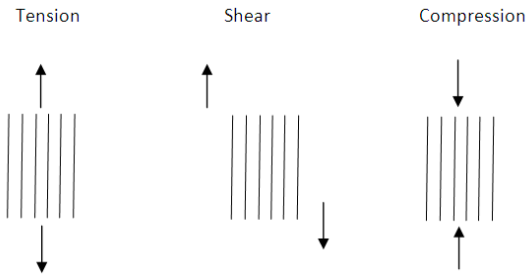

Figure 2. Mechanical test as per fiber orientation of porcine patellar tendon.

A flat disc shaped metal clamp was used for the compression test. Sample thickness was kept at ~5mm to avoid buckling of the tissue. The sample was glued at the bottom and top to avoid any tension created during unloading of the sample. Thickness of the samples was again measured using the "find contact" mechanism in the Mach1 Micromechanical Testing System® (Biomomentum, Quebec, Canada) and the loading velocity was calculated accordingly.

Loading velocity = Strain rate X Thickness (For compression only)

Samples were submerged in Phosphate buffered saline (PBS) solution to simulate physiological conditions and prevent samples from drying during the test. Samples were pre-loaded at 5gm, pre-conditioned (10 times) and then compressed to maximum load using a 10kg load cell. The tests were conducted at three rates - 0.1 /sec 0.01/sec and 1/sec.

Table 1. Test matrix for the strain rate dependency analysis.

Strain rate/ Test type	1/s	0.1/s	0.01/s
Compression	4	6	5

Split- Hopkinson Pressure Bar (SHPB) Finite Element Simulations of Liver tissue

Porcine livers from healthy adult pigs were donated by a local abattoir. The specimens were stored in phosphate buffered saline (PBS) at 4°C soon after extraction and transported to the laboratory. All testing was performed within 12 hours of extraction. A cylindrical die of 30 mm inner diameter was used to cut disc-shaped samples along three orthogonal directions to approximately 27 mm in diameter and 9 mm thick for an aspect ratio of 3:1 (Fig. 1). Cylindrical samples were extracted from three orthogonal directions based on porcine liver anatomy.

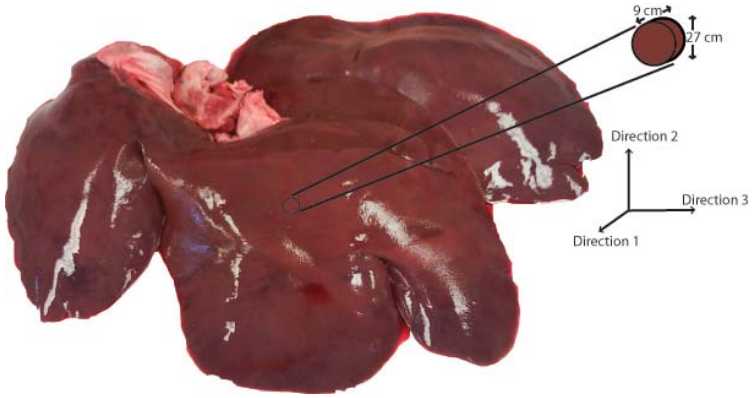

Figure 3. Three orthogonal directions (1, 2, and 3) based on porcine liver anatomy. Representative sample geometry and size.

A customized Polymeric Split Hopkinson Bar (PSHPB) apparatus was used for evaluating strain rate sensitivity, samples were extracted along Direction 1 (Figure 3), and strain rates of 350 s-1 (n=4), 550 s-1 (n=4), 1000 s-1 (n=4), and 1550 s-1 (n=5) were applied. To evaluate directional dependency of tissue behavior, samples were dissected along three orthogonal directions (Directions 1, 2, and 3; n=4 for each direction) and tested at a strain rate of 350 s-1. Liver tissue was kept moist with PBS throughout the testing procedure. Data was processed via David Viscoelastic Software (Zhao et.al,1997).

Finite Element (FE) simulations were aligned to the PSHPB test results of liver tissue in ABAQUS solutions (Simulia Inc., 2009). The striker, incident and transmitted bars were considered as elastic materials. To initiate the FE simulation, the striker bar was set into motion and the speed was in accordance with SHPB experiment, for selected strain rate.

Three-Dimensional Human Head Mesh

In this study, a human head Finite Element (FE) model was developed and simulated in ABAQUS/Explicit (Simulia Inc., 2009) under blast range Boundary Conditions (BCs). The finite element mesh of male head was developed from axial Computed Tomography (CT) and high resolution cryosection images obtained from the National Library of Medicine's Visible Human Project (Ackerman, 1998). The skull was segmented from the CT images. Brain, CSF and outer contour of the head were segmented from the cryosection images. To enable the simulation of blast loading condition, an air mask was also added to the model. The mesh contained hybrid volume elements including hexahedral elements within each part and tetrahedral elements on the surface to provide smooth and conforming interface between parts and coincident nodes and elements across boundaries. Figure 4 shows the human head mesh and a sagittal cut off view of the head mesh. The number of nodes and elements for each part is listed in Table 2.

Table 2. List of the number of nodes and elements of the parts in the human head model used for Finite Element (FE) blast simulations

Parts	Nodes	Hexahedral Element	Tetrahedral Elements	Total Elements
Head	87339	35797	208846	244643
Skull	32933	3940	112153	116093
CSF	16609	950	59497	60447
Brain	18554	7876	44739	52615
Air	154900	90032	254150	344182
Whole Model	297947	138595	679385	817980

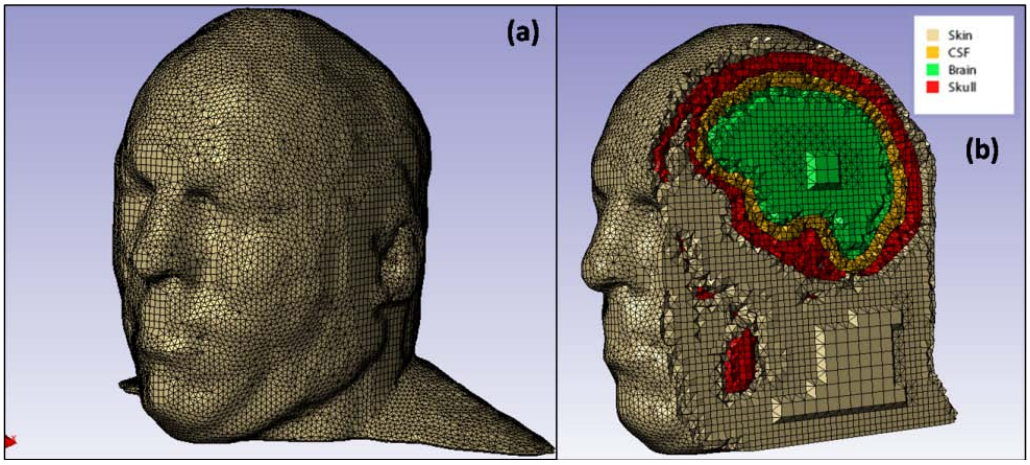

Figure 4. An (a) human head mesh consisting of 800,000 elements (b) scalp/skin, skull, cerebro-spinal fluid and brain. The elements were mostly tetrahedral in shape.

Human Head Finite Element Model

The human head FE model was then built in ABAQUS/Explicit to simulate the injury undergone and a blast pressure-history profile was used at a distance of 3.00×10^{-2} m from the head. Due to the lack of experimental data available on blast loads, experimental pressure-history profile of a low and high intensity blast by Mouritz (2001) was used as the Boundary Condition (BC) for the Finite Element Analysis (FEA). Chafi et al. (2010) showed that the change in surface-to-surface interactions, from tied to frictionless finite sliding, had no effect on the results of blast simulations. Hence, the surface-to-surface interaction properties were chosen from literature (Belingardi et al., 2005). The surface-to-surface interaction properties for the various components of the human are reported in Table 3.

Table 3. List of the surface-to-surface interaction properties of the various parts of the human head FE model.

Surface Interaction	Interaction Property	Coefficient of friction
Air-Scalp/Head	Tie	-
Scalp/Head-Skull	Finite Sliding	0.3
Skull-CSF	Finite Sliding	0.1
CSF-Brain	Finite Sliding	0.1

The scalp, skull and CSF were treated as elastic materials. Elastic properties for the human scalp skull, skull and CSF were obtained from published literature and were treated as elastic materials (Willinger et al. 1999; Belingardi et al., 2005; Chafi et al., 2010). An Internal State Variable (ISV) based constitutive model, MSU TP Ver. 1.1 (Bouvard *et al.*, 2010), was used for the brain parenchyma. MSU TP Ver. 1.1 was calibrated and verified to the brain tissue high strain rate experimental data (Prabhu et al., 2011). An overview of MSU TP Ver. 1.1 is given in Table 4. Table 5 defines the materials constant of MSU TP Ver. 1.1 for the brain tissue. The constitutive model (MSU TP Ver. 1.1) presented in this research effort captures both the instantaneous and long-term steady-state processes during deformation and could admit microstructural features within the internal state variables.

Initially, the low intensity blast pressure profile was used to verify the IntraCranial Pressures (ICPs) observed during the simulation. The peak positive pressure observed at the coup of the brain was 2.00×10-1 MPa at the coup site and a peak negative pressure of 1.00×10-1 MPa at the countercoup site. Chafi et al. (2010) reported similar values of peak positive pressure (2.20×10-1 MPa) and peak negative pressure (1.5×10-1 MPa) at the coup and countercoup sites respectively for a 8.84×10-2 lb TNT blast load. Once meaningful values of ICPs were obtained for low intensity blast load, Mouritz's high intensity blast load was applied as the BC in the FE model to simulate the blast scenario reported by Warden et al. (2009).

Table 4. Summary of the Model Equations for MSU TP 1.1 (see Bouvard et al., 2010)

Term/Function	Description
$\overline{\psi} = \overline{\psi}\left(\overline{\mathbf{C}}^{\mathbf{e}}, \overline{\xi}_1, \overline{\xi}_2, \overline{\mathbf{E}}^{\beta}\right)$	Free energy
$\boldsymbol{\sigma} = J^{e-1}\boldsymbol{\tau} = J^{e-1}\mathbf{F}^{\mathbf{e}}\overline{\mathbf{S}}\mathbf{F}^{\mathbf{eT}}$ $\overline{\mathbf{S}} = \mathbf{2}\frac{\partial\hat{\overline{\psi}}}{\partial\overline{\mathbf{C}}^{\mathbf{e}}}$	Cauchy Stress second Piola-Kirchhoff stress
$\boldsymbol{\tau}_1 = \mathbf{R}^{\mathbf{e}}\overline{\mathbf{M}}_1\mathbf{R}^{\mathbf{eT}}$ $\overline{\mathbf{M}} = 2\mu\overline{\mathbf{E}}^{\mathbf{e}} + \left(K - \frac{2}{3}\mu\right)\mathrm{Tr}\left(\overline{\mathbf{E}}^{\mathbf{e}}\right)\overline{\mathbf{I}}$ $\mathbf{F} = \mathbf{F}^{\mathbf{e}}\mathbf{F}^{\mathbf{p}},\ \mathbf{F}^{\mathbf{e}} = \mathbf{R}^{\mathbf{e}}\mathbf{U}^{\mathbf{e}},\ \overline{\mathbf{E}}^{\mathbf{e}} = \ln(\mathbf{U}^{\mathbf{e}})$	Kirchhoff Stress (elasto-viscoplastic part) Elastic Law (Mandel Stress) Deformation Gradient
$\overline{\kappa}_1 = \frac{\partial\hat{\overline{\psi}}}{\partial\overline{\xi}_1}\ \overline{\kappa}_2 = \frac{\partial\hat{\overline{\psi}}}{\partial\overline{\xi}_2}$ $\overline{\boldsymbol{\alpha}} = \frac{\partial\hat{\overline{\psi}}}{\partial\overline{\mathbf{E}}^{\beta}}$	Stress-like internal state variables
$\dot{\mathbf{F}}^{\mathbf{p}} = \overline{\mathbf{D}}^{\mathbf{p}}\mathbf{F}^{\mathbf{p}}$ $\overline{\mathbf{D}}^{\mathbf{p}} = \frac{1}{\sqrt{2}}\dot{\gamma}^{p}\overline{\mathbf{N}}^{\mathbf{p}}$ with $\overline{\mathbf{N}}^{\mathbf{p}} = \frac{\mathbf{dev}\overline{\mathbf{M}}_1}{\left\|\mathbf{dev}\overline{\mathbf{M}}_1\right\|}$	Flow rule Equivalent plastic shear strain-rate

$\dot{\bar{\gamma}}^{p} = \dot{\bar{\gamma}}_0^{p}\left[\sinh\left(\frac{\left\langle \bar{\tau} - \left(\bar{\kappa}_1 + \bar{\kappa}_2 + \alpha_p \bar{\pi}\right)\right\rangle}{Y}\right)\right]^{m}$ with $\bar{\tau} = \frac{1}{\sqrt{2}}\left\|\overline{\mathbf{DEV}}\left(\overline{\mathbf{M}} - \bar{\boldsymbol{\alpha}}\right)\right\|$ and $\bar{\pi} = -\frac{1}{3}\overline{\mathrm{Tr}}\left(\overline{\mathbf{M}}\right)$ $\dot{\bar{\xi}}_1 = h_0\left(1 - \frac{\bar{\xi}_1}{\bar{\xi}^*}\right)\dot{\bar{\epsilon}}^{p}$ $\dot{\bar{\xi}}^* = g_0\left(1 - \frac{\bar{\xi}^*}{\bar{\xi}^*_{sat}}\right)\dot{\bar{\epsilon}}^{p}$ $\dot{\bar{\xi}}_2 = h_1\left(\dot{\bar{\epsilon}}^{p} - 1\right)\left(1 - \frac{\bar{\xi}_2}{\bar{\xi}_{2sat}}\right)\dot{\bar{\epsilon}}^{p}$ with $\bar{\lambda}^{p} = \frac{1}{\sqrt{3}}\sqrt{\overline{\mathrm{Tr}}\left(\overline{\mathbf{B}}^{\mathbf{p}}\right)}$ and $\overline{\mathbf{B}}^{\mathbf{p}} = \mathbf{F}^{\mathbf{p}}\mathbf{F}^{\mathbf{p}T}$ $\dot{\bar{\boldsymbol{\beta}}} = R_{s_1}\left(\overline{\mathbf{D}}^{\mathbf{p}}\bar{\boldsymbol{\beta}} + \overline{\boldsymbol{\beta}\mathbf{D}}^{\mathbf{p}}\right)$ and $\bar{\boldsymbol{\beta}}(\mathbf{X},0) = \mathrm{I}$	Polymer chain resistance to plastic flow Polymer chain crystallization at large strain Evolution equation of $\bar{\boldsymbol{\beta}}$
$\{\mu, K, \dot{\gamma}_0^{p}, m, Y\}$ $\{\bar{\xi}_0^*, \bar{\xi}_{sat}^*, h_0, g_0, C_{\kappa_1}\}$ $\{h_1, \bar{\xi}_{2sat}, C_{\kappa_2}\}$ $\{R_{S1}, \lambda_L, \mu_R\}$ $\{\alpha_p, \bar{\xi}_{10}, \bar{\xi}_{20}\}$	Material constants

Table 5. Values of material constants for brain material using MSU TP 1.1Viscoplasticitymodel.

Model Constants	Values
μ(MPa)	25
K (MPa)	12492
$\gamma_{vo}(s^{-1})$	100000
m	1
Y_o (MPa)	8.2
α_p	0
λ_L	5
μ_R	0.0493197
R_{s1}	1.4
h_o	47.2095
ξ^o_1	0.75
ξ^*_{sat}	0.01

ξ^*_o	1.2
g_o	0.3
$C\kappa_1$ (MPa)	0.4
h_1	0
e^o_{s2}	0
e^{sat}_{s2}	0.4
$C\kappa_2$ (MPa)	0

Mechanics and Modeling of Animal Outer Armor

The structures and fracture surfaces of turtle shells, armadillo shells, and ram horns were investigated using optical microscopy (OM) and scanning electron microscopy (SEM). Sectioned specimens were cleaned by an ultrasonic cleaner and then cold mounted in epoxy. The mounted specimens were then sputter-coated with gold and examined under a SUPRA-40 field emission gun (FEG)-SEM (CarlZeiss SMT Ltd.).

Compression tests were performed at strain rates of 0.001, 0.01, and 0.1/s. These tests were performed on an Instron 3367 Dual Column Testing System equipped with a 30 kN load cell. The compression specimens were prepared according to ASTM D790. The specific energy absorption during initial deformation was taken as the area under the stress-strain curve up to 0.1 strain, normalized by the density of the material. While, the energy absorbed during collapse was calculated as the area below the curve, normalized by the porosity of the material, bounded from 0.1 to 0.4 strain. The porosity of each material was found by analyzing cross-sectional images using the Image-Analyzer software package developed by the Center for Advanced Vehicular Systems (CAVS) at Mississippi State University.

Results and Discussion

Structure-Property Relationships of Porcine Skin

The results in Figure 5 shows a distinct mechanical difference between the scalp composite layer and areolar layer (a) as well as a difference between all four layers of the skin (b). The scalp layer is a lot more stiff than the areolar layer, as expected and the aponeurosis is most stiff.

In comparison with the quasistatic compression test results performed using the Mach1 the aponeurosis and connective tissues appear to reach failure before the other layers. The DMA results correspond with these findings, with respect to the overall storage and loss modulus being the least in these tissues (Figure 6).

Mechanical data was incorporated into an FEA model of skin, with multiple layers of the skin assigned respective properties. The model was based on Thermoplastic parameters and the fit of the model was very close to that of the experimental data. Figure 7 shows the finite element results and the results of the model fitting.

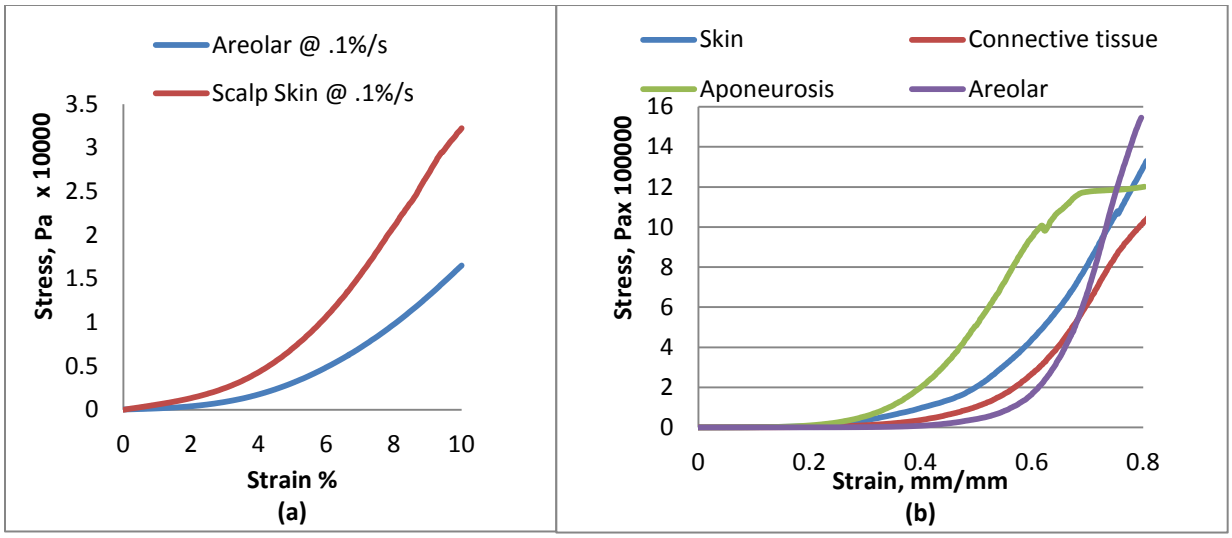

Figure 5. Stress-strain response of skin layers (a) areolar vs. scalp skin composite and (b) comparison of four layers of the skin @.1%/s

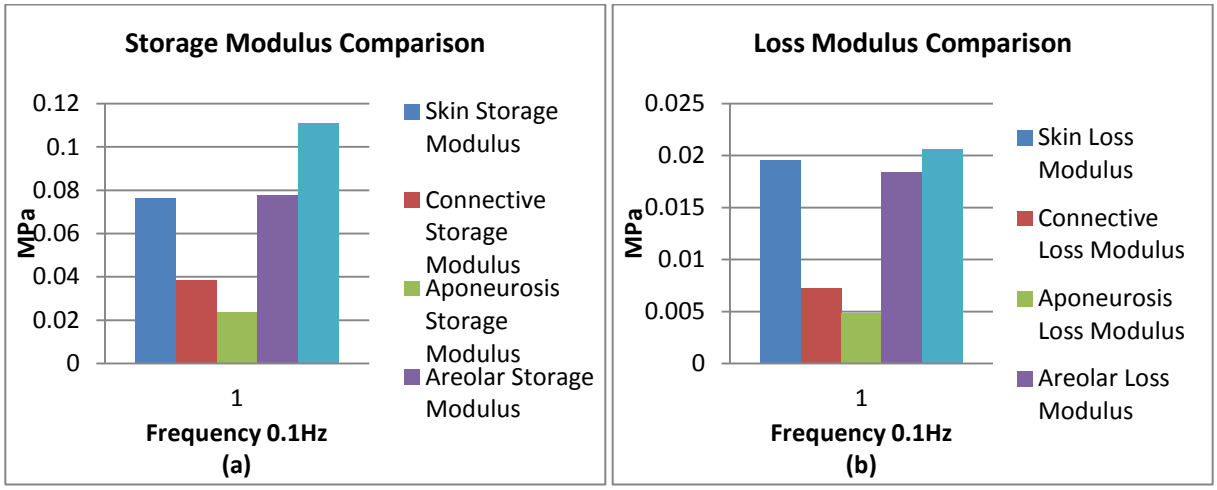

Figure 6. DMA analysis of the multiple layers of the tissue (a) Storage Modulus and (b) Loss Modulus.

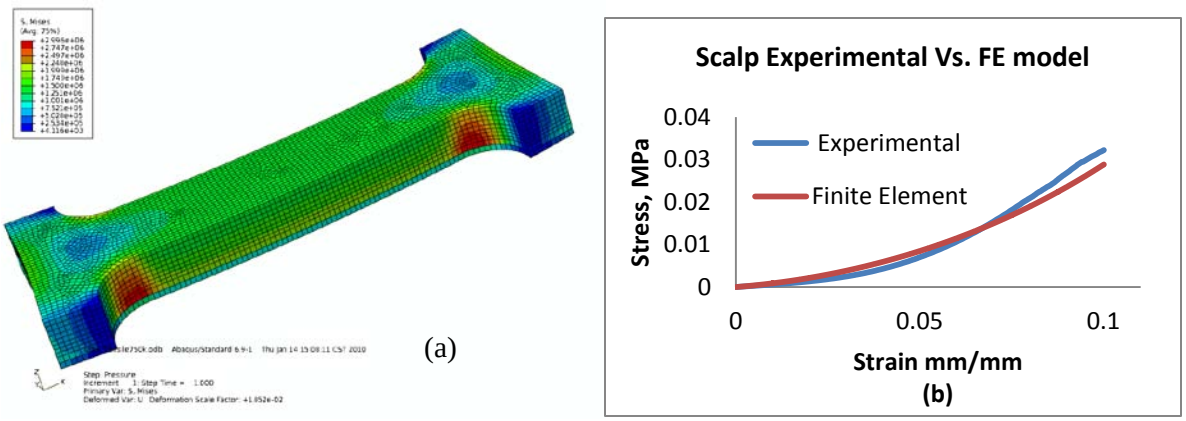

Figure 7. (a) 2 layer finite element model and (b) Model fit of entire scalp experimental test vs. FE model.

Structure-Property Relationships of Porcine Tendon

Porcine patellar tendon samples were tested longitudinally in compression mode and the effect of increasing strain rate was studied. Samples appear to stiffer at a higher strain rate i.e. avg. stress-strain curve of samples rate of 1 per sec appear to be stiffer than 0.1 per sec and 0.01 per sec.

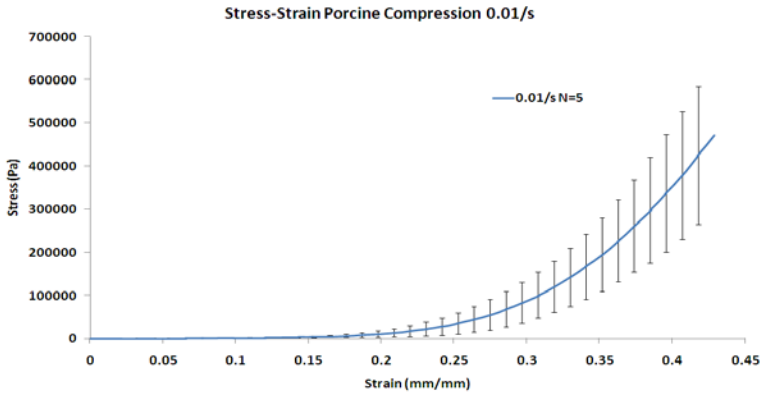

Figure 8. Stress-Strain Curve with strain rate of 0.01/s for porcine under compression with N=5 sample size.

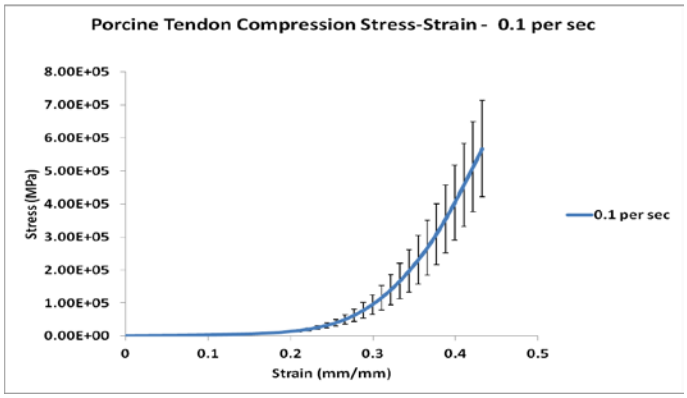

Figure 9. Stress-Strain Curve with strain rate of 0.1/s for porcine under compression with N=6 sample size. A cross-section of the sample is also pictured above.

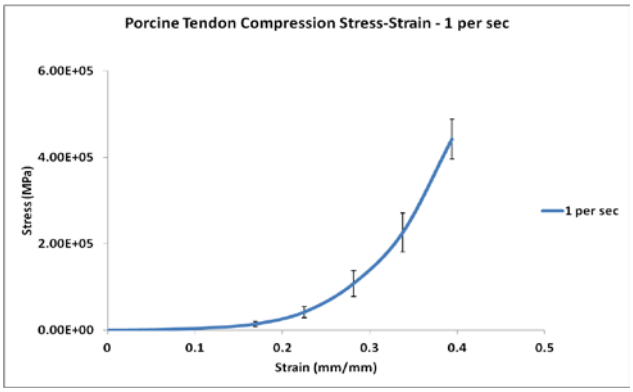

Figure 10. Stress-Strain Curve with strain rate of 1/s for porcine under compression with N=4 sample size

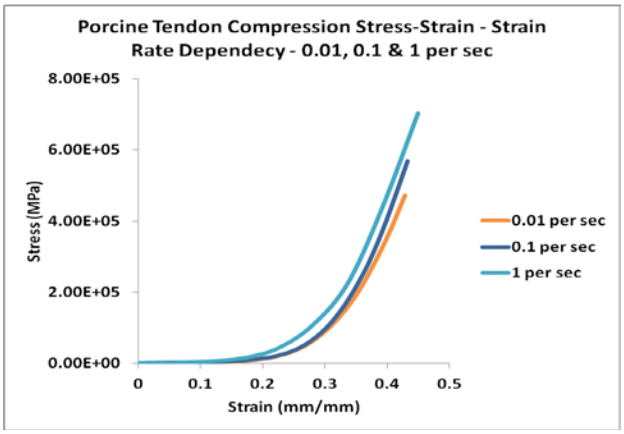

Figure 11. Strain Rate Dependency Graph with strain rates of 0.01/sec, 0.1/sec and 1/sec for porcine under compression loading with sample sizes – N = 5, N = 6 and N = 4 respectively

Split- Hopkinson Pressure Bar (SHPB) Finite Element Simulations of Liver Tissue

For the simulations, strain rate of 550 per sec was selected. Multiple cases were performed to obtain a strain rate closest to experimental setting (Figure 12). In order to capture the elastic and inelastic response of the liver tissue, a novel material model – MSU TP 1.1 (Bouvard, 2010) was used .

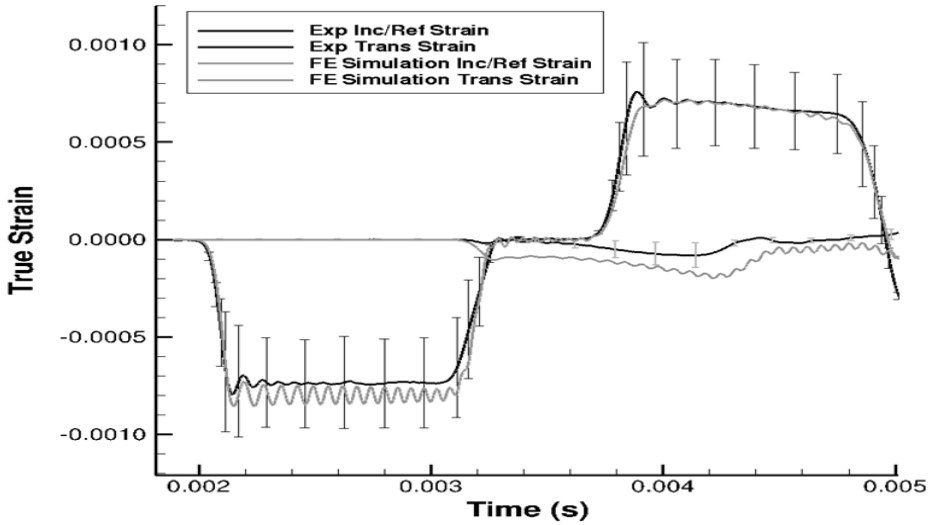

Figure 12. Comparison of L33 from Experimental Data and FE simulation data at 550 s^{-1}.

Comparison of Incident and Reflected strain measurements, from Finite Element Analysis (Sim Inc/Ref), with PSHB experiment data (Exp Inc/Ref) and comparison of Transmitted strain measurements, from Finite Element Analysis (Sim Trans), with PSHB experiment data (Exp Trans) are shown in Figure 12.

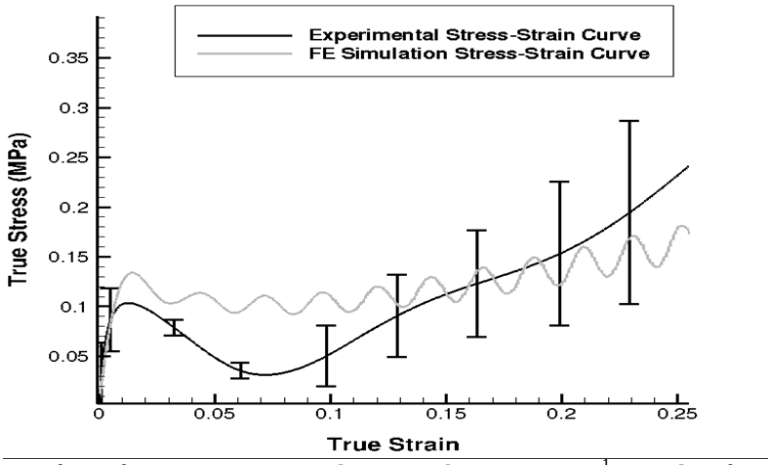

Figure 13 Comparison of S33 from Experiment and FE Simulation at 550 s^{-1}. S33 data from FE simulation was processed in DAVID Viscoelastic software.

Comparison of stress-strain curve of experimental and FE simulation at 550 per sec is shown in Figure 13. Contour plots show the sample deformation with increasing strain level (Figure 14).

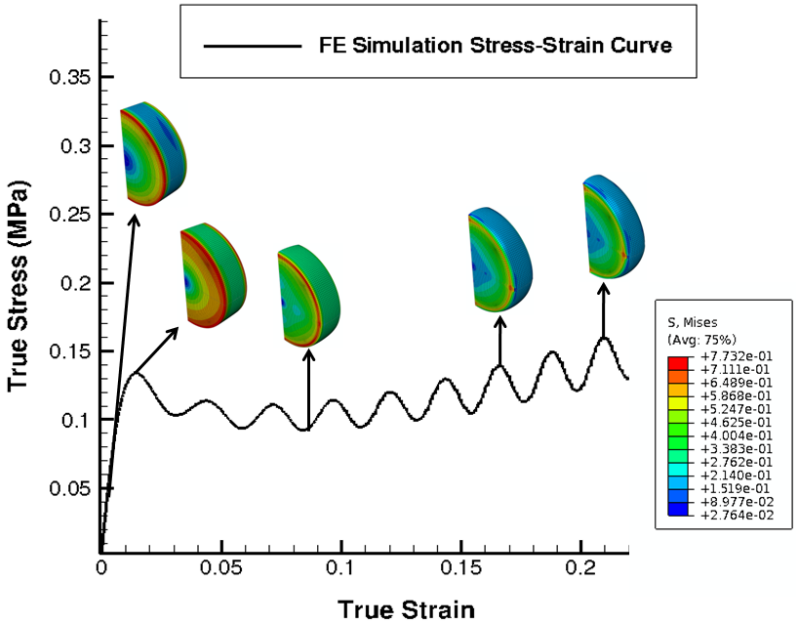

Figure 14. Contour plots of FE Simulation at 550 per sec.

Finite Element Simulations of Blast-Related Traumatic Brain Injury

As discussed earlier, the time period of the shock wave implemented as BC in the FE simulations was 0.040 μs (Mouritz, 2001). Due to the short duration of the time period of the shock wave, much of the results are focused on the earlier part of the duration of the FE simulation (0.100 - 0.360 ms). During the blast simulation, assessment of the head injury was made through the IntraCranial Pressure (ICP), von

mises and maximum principal strain profiles on the brain. Local measurement of ICP, von mises and maximum principal strain values were also made at the coup and countercoup sites.

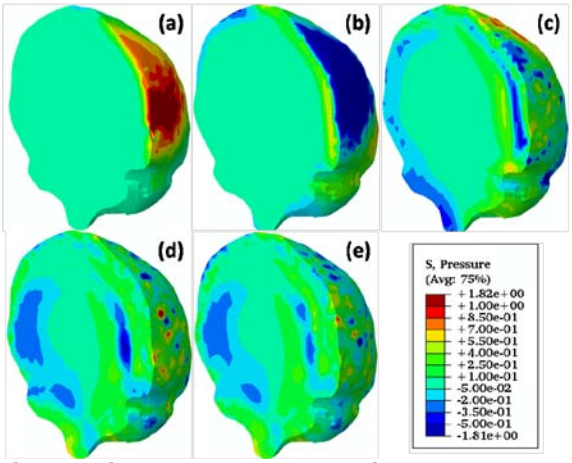

Figure 15. Sagittal view of the brain with pressure contour snapshots at (a) 1.25×10^{-1}, (b) 1.63×10^{-1}, (c) 2.24×10^{-1}, (d) 3.16×10^{-1}, and (e) 3.55×10^{-1} ms.

Figure 15 present the contour plots of pressure on the coronal view of the brain at various points of times ((a) 1.25×10^{-1}, (b) 1.63×10^{-1}, (c) 2.24×10^{-1}, (d) 3.16×10^{-1}, and (e) 3.55×10^{-1} ms). A key aspect to be noted in Figure 15 is that the pressure profile is not uniform at all time points. As observed in a previous study on the modeling blast loads on the human head (Chafi et al., 2010), peak positive pressure was observed at coup site and peak negative pressure was detected at the countercoup site. The fluctuation of the pressure profile from positive to negative values was observed at both coup and countercoup sites over a short duration of time (2.30×10^{-1} ms). Such rapid oscillation of the pressure waves causes the brain parenchyma to undergo compressive and tensile loads locally (coup and countercoup), leading sudden changes in the micro-cellular structures (Mac Donald et al., 2007). The rapid changes in micro-structural structures of the brain have been attributed to neuron degeneration, Diffuse Axonal Injury (DAI) and cerebral contusion (Denny-Brown and Russell, 1941; Ward et al., 1980; Taber, 2006).

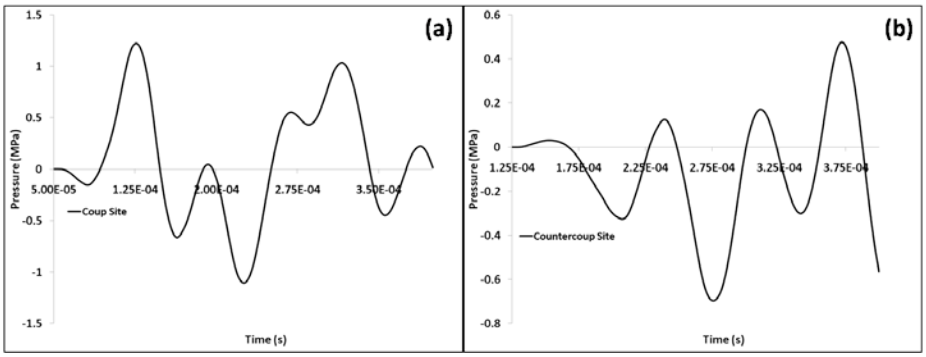

Figure 16. Plots of pressure versus time at (a) coup site and (b) counter coup site of the brain in the human head FE model.

Figure 16 gives the pressure (ICP) plots over time at coup and countercoup sites. Figure 16 brings out the rapid oscillating pattern (~104 s^{-1}) of pressure at coup and countercoup sites more vividly. As noted earlier, the peak positive pressure occurs at the coup site at 1.25×10^{-1} ms (Figure 15(a)). Similar trend of rapid oscillation was observed at the countercoup site (Figure 16(b)). In contrast to the pressure-history at coup site, the pressure-history at countercoup site initially started with a negative pressure. Such oscillatory pressure profile leads to sudden acceleration and deceleration in the local areas (coup and countercoup) of the brain with little movement of the head. This trend of little or no injury to the head or

scalp, but substantial damage to the brain, has been observed in case studies of war fighters encountering bTBI (Elsayed, 1997; Mayorga, 1997).

Mechanics and Modeling of Animal Outer Armor

Similar to turtle and armadillo shell, ram horn is a hierarchical material. The multiscale hierarchical structure of the ram horn is shown in Figure 17. Horn comprises a keratin sheath, surrounding a core of cancellous bone. At the molecular level, a horn comprises helical, α-keratin protofibrils. These protofibrils assemble into rope-like structures called intermediate filaments (Feughelman 1997). The crystalline intermediate filaments are oriented along the growth direction and coil up into hollow, elliptically shaped tubules. These tubules, which resemble hollow reinforcing fibers, are embedded in an amorphous keratin matrix. The matrix is akin to a randomly oriented, chopped fiber composite. There is also a porosity gradient through the thickness of the horn, with the highest porosity being at the outer surface (Tombolato et al. 2010). At the macroscale, a horn takes the shape of a logarithmic spiral. The porosity of the keratin sheath in ram horn was found to be approximately 6%.

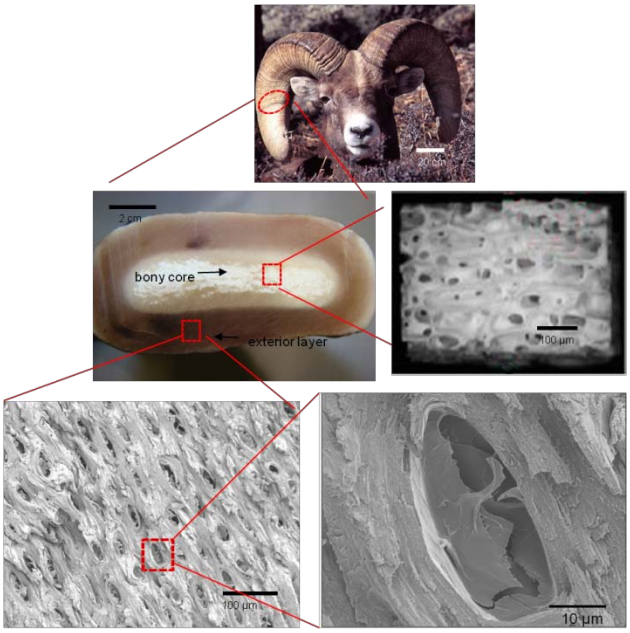

Figure 17. Multiscale hierarchy and structure of the ram horn.

In each of these three materials, keratin surrounds a closed-cell, foam-like core. The porous outer layer of provides toughening mechanisms such crack deflection, crack arrest, and penetration resistance. The central core functions to absorb large amounts of energy during collapse at a low cost in weight.

The compressive stress-strain response for armadillo shell, turtle shell and ram horn at various strain rates is provided in Figure 18. Compression test results revealed a typical deformation behavior of cellular solids showing three distinctive regions: an initial linear elastic deformation, a plateau of deformation, and another period of near linear deformation with a fairly high modulus. The favorable deformation mechanisms of these materials in compressive conditions can be explained by those of synthetic foams found elsewhere (Gibson; Ashby 1988; Rhee et al. 2009).

The three materials showed varying levels of strain rate dependence. The ram horn gave the highest strain rate sensitivity, while the armadillo and turtle shell showed the considerably strain rate dependence. The Young's modulus for each material increased with increasing strain rate, which is a typical phenomenon among polymeric materials. When loaded at a low strain rate, the molecular chains have sufficient time to adjust to the imposed stress and the modulus value is lower than for the case where the same material is loaded at a higher strain rate (Goble; Wolff 1993).

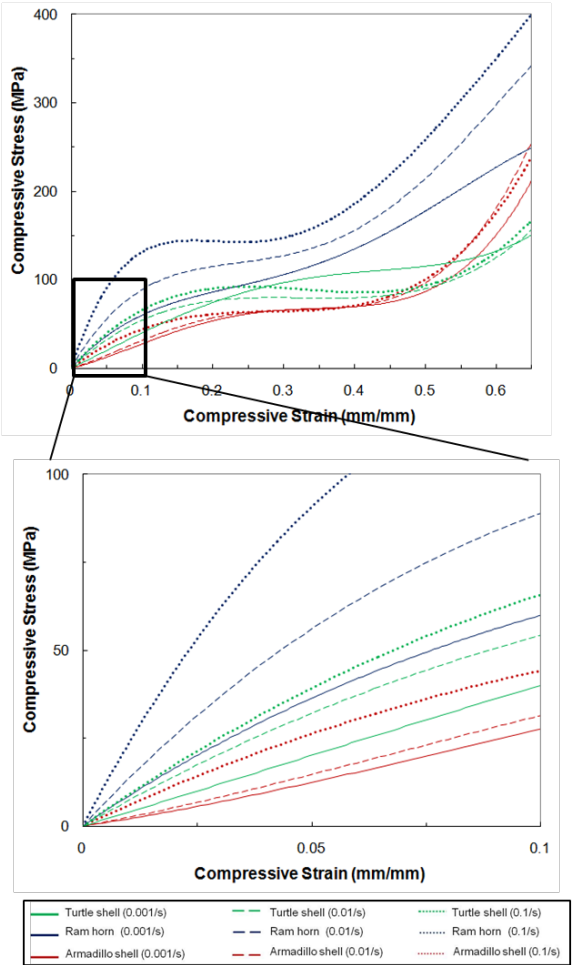

Figure 18. Compressive stress-strain response for turtle shell, armadillo shell, and ram horn for strain rates of 0.001, 0.01, and 0.1/s.

Figure 19 provides a comparison of specific energy absorption obtained from the compression test results. Density and porosity levels of the test specimens are factored into this normalized data. The specific, elastic energy absorption ability of each material increased with increasing strain rate because the Young's modulus increased with strain rate. This yielded more area under the stress-strain curve in the linear elastic regime, which is considered here to be from 0 to 0.1 strain.

Conclusions

A composite skin FE model was developed. Also, all four layers were evaluated to examine the differences in mechanical properties and ultimately correlate the structure and function of the skin tissue. The scalp layer, which consists of the top most 3 layers was compared with the weblike areolar tissue. As expected, scalp tissue was stiffer as it comprises of a more intact and less weblike structure. Also, the data shows that the loss and storage modulus for DMA are less for aponeurosis and connective tissue, which provides and explanation of why these tissues typically reach failure prior to all other layers.

Quasi-static tests of porcine patellar tendon reveal that the tissue is stiffer in compression and stiffness increases with increasing strain rate. A clear difference in the material behavior is seen between the three different strain rates and thus strain rate dependency is achieved. Shear and tensile behavior of tendon will be further investigated to obtain all the material characteristics that will constitute the stress-state behavior of the tendon tissue.

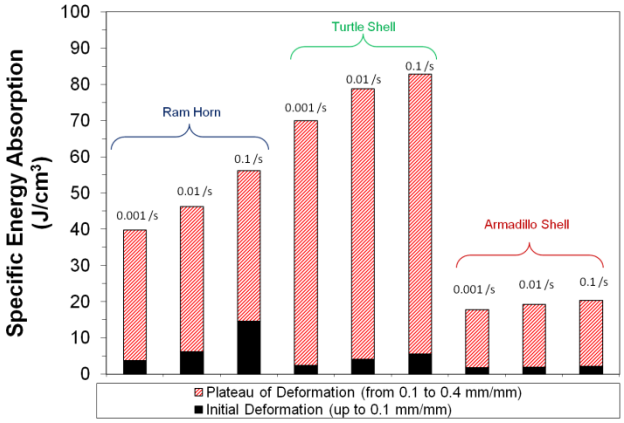

Figure 19. Specific energy absorption for ram horn, turtle shell, and armadillo shell at strain rates of 0.001, 0.01, and 0.1/s.

The SHPB FE simulation of liver tissue results indicate a perfect match up of the experimental and simulation strain rates. Additionally, the stress- strain curve of both experiment and simulation was also matched up (initial bump and overall trend of the data are captured).

The results from our Blast-Related Traumatic Brain Injury FE simulations show that the stress state during a blast was highly non-uniform, with higher stress states around the coup and countercoup sites. The current study is the first one its kind in validating a real world Boundary Value Problem (BVP) in a war fighter's bTBI. FE simulation showed high frequency pressure waves impacting the brain at coup and countercoup sites. The pressure values at these sites vary from positive to negative and vice-versa in short duration of time. Such rapid fluctuation of the pressure wave cause sudden acceleration and deceleration in the brain; leading to neuron degeneration, cerebral contusion and DAI. Finally, the current human head model could be readily used to further study the pathophysiology of the bTBI and analyze by modeling other reported real world cases of bTBI.

Several conclusions can be garnered from this study of the structure-property relations of the energy absorbent, keratinous turtle shell, armadillo shell, and ram horn materials.

- The materials each have a multiscale, hierarchical material structure. Each material also has a sandwich composite structure, with a high porosity, foam-like interior region and denser exterior region.
- Compression test results for the turtle shell, ram horn and armadillo shell showed a typical nonlinear deformation behavior recognizant of synthetic foams.
- Each had an initial nearly linear, elastic regime, followed by a plateau of deformation, which preceded the eventual material densification.
- There is a high degree of interaction and synergism between the protein skin and the foam-like core that strongly enhances the mechanical properties. In fact, the structures are so well organized that biological composites can achieve properties greater than their constituent materials and thus overcome the mixtures law.

We can use these lessons from nature as inspiration for development of lightweight, bio-inspired armor systems. A possible bio-inspired design strategy entails encasing a metallic foam core with a fiber-polymer composite laminate. This sandwich structure mimics the structure found in turtle and armadillo shells, and ram horns. The skin of this design serves to resist penetration whilst the central core functions to absorb large amounts of energy at a low cost in weight. Good adhesion between skin and the metallic core is crucial for this design to succeed and is an excellent opportunity for future research.

Publications/Presentations/Patents

1. Trim, M.W., Horstemeyer, M.F., Rhee, H., Liao, J., Williams, L.N. "The effects of water and microstructure on the mechanical properties of bighorn sheep (Ovis canadensis) horn keratin" *Acta Biomaterialia*, 2011, *7(3)*, pp1228-1240
2. Rhee, H., Horstemeyer, M.F., Ramsay, A. A study on the structure and mechanical behavior of the Dasypus novemcinctus shell, Materials Science and Engineering C. **2011**, *31*, pp.363-369.
3. Prabhu, R., Horstemeyer, M. F., Tucker, M. T., Marin, E. B., Bouvard, J. L., Sherburn, J. A., Liao, J., et al. Coupled experiment/finite element analysis on the mechanical response of porcine brain under high strain rates. *Journal of the Mechanical Behavior of Biomedical Materials*. **2011**, *4*, pp 1067-1080.
4. Clemmer, J., Liao, J., Davis, D., Horstemeyer, M., Williams, L.N., "A Mechanistic Study for Strain Rate Sensitivity of Rabbit Patellar Tendon," *Journal of Biomechanics*. **2010**, 43, pp 2785-2791.
5. Patnaik, S., Weed, B., Young, T., Liao, J., Williams, L. In Dynamic Viscoelastic Properties of Porcine Patellar Tendon: Study of Frequency, Loading, and Regional Dependency, Biomedical Engineering Society (BMES) Annual Conference, Hartford, CT, Hartford, CT, 2011.
6. Rougeau, M., Patnaik, S., Gilbrech, R., Young, T., Prabhu, R., Liao, J., Williams, L., Influence of Water Content on Quasi-static Compressive Properties of Porcine Lungs Tissue. In Biomedical Engineering Society (BMES) Annual Conference, Hartford, CT, 2011.
7. Oje, A., Lee, N., Patnaik, S., Liao, J., Williams, L.N, The Effects of Water Content on the Mechanics and Microstructure of Bone. In Biomedical Engineering Society (BMES) Annual Conference, Hartford, CT, 2011.
8. Weed, B., Borazjani, A., Patnaik, S., Prabhu, R., Horstemeyer, M., Franz, T., Williams, L., Liao, J Stress State Dependence of Human Placenta Mechanical Behavior, ASME Summer Bioengineering Conference, Farmington, PA, Farmington, PA, 2011.
9. Smith, W., Gilbrech, R., Liao J., Weed B., Patnaik, S., Summers RL., Influence of Microgravity on Left Ventricular Sphericity in a Finite Element Model of the Heart. In International Academy of Astronautics "Humans in Space" Symposium, Houston, TX, 2011.
10. Ryland, S., Prabhu, R., Patnaik, S., Horstemeyer, M., Liao, J., Williams, L. , Development of Finite Element Model for Porcine Scalp. In ASME Summer Bioengineering Conference, Farmington, Pa, 2011.
11. Weed, B., Borazjani, A., Patnaik, S., Prabhu, R., Horstemeyer, M., Franz, T., Williams, L., Liao, J., Stress State Dependence of Human Placenta Mechanical Behavior. In Biomedical Engineering Society (BMES) Annual Conference, Austin, TX, 2010.
12. "A comparison study on the structures and mechanical behaviors of sandwich composite biological structural materials", MS&T 2010 Conference & Exhibition, Houston, TX, Oct. 18, 2010.
13. "Structure-Property relationships of the scalp". Biomedical Engineering Society, Austin, TX, October 6, 2010.

References

Ackerman, M.J., (1998), "*The Visible Human Project."* Proc. IEEE, **86**(3), pp. 504-511.

Anderson, R. W. G., C. J. Brown, P. C. Blumbergs, G. Scott, J. W. Finney, N. R. Jones, and A. J. Mclean. (1999) Mechanisms of axonal injury: an experimental and numerical study of a sheep model of head impact. In: Proceedings of the International Conference on the Biomechanics of Impact, pp. 107–120.

Belingardi, G., Chiandussi, G., & Gaviglio, I. (2005). Development and validation of a new finite element model of human head. *International Technical Conference on the Enhanced Safety of Vehicles*.

Bouvard, J.L., Ward, D.K., Hossain, D., Marin, E.B., Bammann, D.J., and Horstemeyer, M.F., 2010, A General Inelastic Internal State Variable Model for Amorphous Glassy Polymers, *Acta. Mech.*, DOI 10.1007/s00707-010-0349-y.

Butler, D. L., E. S. Grood, et al. (1978). "Biomechanics of ligaments and tendons." Exercise and sport sciences reviews 6: 125-181.

Chafi, M., Karami, G., & Ziejewski, M. (2010). Biomechanical Assessment of Brain Dynamic Responses Due to Blast Pressure Waves. *Annals of Biomedical Engineering*, *38*(2), 490-504-504.

Denny-Brown, D., and W. R. Russell.(1941) Experimental cerebral concussion. Brain 64, pp.93–164.

El Sayed, T., Mota, A., Fraternali, F., & Ortiz, M. (2008). Biomechanics of traumatic brain injury. *Computer Methods in Applied Mechanics and Engineering*, *197*(51-52), 4692-4701. Doi:doi: DOI: 10.1016/j.cma.2008.06.006.

Kang, H. S., R. Willimger, B. M. Diaw, and B. Chinn. Modeling of the human head under impact conditions: a parametric study. In: Proceedings of the 41st Stapp Car Crash Conference, SAE Paper No. 973338, 1997.

Mac Donald, C. L., Dikranian, K., Song, S. K., Bayly, P. V., Holtzman, D. M., & Brody, D. L. (2007). Detection of Traumatic Axonal Injury with Diffusion Tensor Imaging in a Mouse Model of Traumatic Brain Injury. *Experimental neurology*, *205*(1), 116-131. doi:10.1016/j.expneurol.2007.01.035.

Mayorga, M. A. (1997). The pathology of primary blast overpressure injury. *Toxicology*, *121*(1), 17-28. doi:doi: DOI: 10.1016/S0300-483X(97)03652-4.

Meyers, M. A., & Taylor Aimone, C. (1983). Dynamic fracture (spalling) of metals. *Progress in Materials Science*, *28*(1), 1-96. Doi:10.1016/0079-6425(83)90003-8

Mouritz, A. P. (2001). Ballistic impact and explosive blast resistance of stitched composites. *Composites Part B: Engineering*, *32*(5), 431-439. Doi:10.1016/S1359-8368(01)00015-4.

Nahum, A. M., Smith, R., & Ward, C. C. (1977). *Intracranial Pressure Dynamics During Head Impact* (No. 770922). Warrendale, PA: SAE International. Retrieved from http://papers.sae.org/770922.

Prabhu, R., Horstemeyer, M. F., Tucker, M. T., Marin, E. B., Bouvard, J. L., Sherburn, J. A., Liao, J., et al. (2011). Coupled experiment/finite element analysis on the mechanical response of porcine brain under high strain rates. *Journal of the Mechanical Behavior of Biomedical Materials*. doi:10.1016/j.jmbbm.2011.03.015.

Simulia Inc., (2009), "ABAQUS/Explicit User's Manual", Version 6.9, Providence, RI, 02909, USA.

Stahura, "An Insidious Enemy: Mild Traumatic Brain Injury", originally published in Veterans Affairs and Military Medicine, 2008-2009 Edition

Taber, K. H., D. L. Warden, and R. A. Hurley.(2006) Blast related traumatic brain injury: what is known? J. Neuropsychiatry Clin. Neurosci. 18:141–145.

Zhang, L., Yang, K. H., Dwarampudi, R., Omori, K., Li, T., Chang, K., Hardy, W. N., et al. (2001). Recent advances in brain injury research: a new human head model development and validation. *Stapp Car Crash Journal*, *45*, 369-394.

Wang, J. H. (2006). "Mechanobiology of tendon." Journal of biomechanics 39(9): 1563-1582.

Ward, C. C., M. Chan, and A. M. Nahum. (1980) Intracranial pressure—a brain injury criterion. In: Proceedings, 24th Stapp Car Crash Conference, SAE Paper No. 801304.

Warden, D. L., French, L. M., Shupenko, L., Fargus, J., Riedy, G., Erickson, M. E., Jaffee, M. S., et al. (2009). Case report of a soldier with primary blast brain injury. *NeuroImage*, *47*(Supplement 2), T152-T153. doi:10.1016/j.neuroimage.2009.01.060.

Feughelman, M., 1997: Mechanical Properties and Structure of Alpha-Keratin Fibres. University of New South Wales Press.

Fraser, R. D. B., and D. A. D. Parry, 1996: The molecular structure of reptilian keratin. International Journal of Biological Macromolecules, 19, 207-211.

Gibson, L. J., and M. F. Ashby, 1988: Cellular Solids: Structure & Properties. Pergamon Press, Inc.

Goble, D. L., and E. G. Wolff, 1993: Strain-rate sensitivity index of thermoplastics. Journal of Materials Science, 28, 5986-5994.

Mayer, G., 2005: Rigid biological systems as models for synthetic composites. Science, 310, 1144-1147.

McKittrick, J., and Coauthors, 2010: Energy absorbent natural materials and bioinspired design strategies: A review. Materials Science and Engineering: C, 30, 331-342.

Meyers, M. A., P.-Y. Chen, A. Lin, and Y. Seki, 2008: Biological Materials: Structure and Mechanical Properties. Progress in Materials Science, 53, 1-206.

Meyers, M. A., A. Y. M. Lin, Y. Seki, P.-Y. Chen, B. K. Kad, and S. Bodde, 2006: Structural Biological Composites: An Overview. JOM.

Munch, E., M. E. Launey, D. H. Alsem, E. Saiz, A. P. Tomsia, and R. O. Ritchie, 2008: Tough, Bio-Inspired Hybrid Materials. Science, 322, 1516-1520.

Rhee, H., M. F. Horstemeyer, Y. Hwang, H. Lim, H. El Kadiri, and W. Trim, 2009: A study on the structure and mechanical behavior of the Terrapene carolina carapace: A pathway to design bio-inspired synthetic composites. Materials Science and Engineering: C, 29, 2333-2339.

Tombolato, L., E. E. Novitskaya, P.-Y. Chen, F. A. Sheppard, and J. McKittrick, 2010: Microstructure, elastic properties and deformation mechanisms of horn keratin. Acta Biomaterialia, 6, 319-330.

MISSISSIPPI STATE UNIVERSITY

Southern Regional Center for Lightweight Innovative Design

Phase III

Final Scientific & Technical Report

October 1, 2009-September 30, 2011

For compliance with contract requirements of Award DE-EE0002323

Task 12

K-12 OUTREACH PROGRAM

Submitted December 27, 2011

TASK 12: K-12 OUTREACH PROGRAM

Table of Contents

TASK 12: K-12 OUTREACH PROGRAM

Principal Investigator: Mark. F. Horstemeyer
Chair Professor, Computational Manufacturing & Design
Center for Advanced Vehicular Systems
Mississippi State University
PO Box 5405, Mississippi State, MS 39762-5405
(662) 325-5449; fax: (662) 325-7223; mfhorst@me.msstate.edu

Participants: R.C. Cuicchi

William Joost: Technology Area Development Manager
e-mail: william.joost@ee.doe.gov

Magda Rivera: Project Manager
e-mail: magda.rivera@netl.doe.gov

Contractor: Mississippi State University (MSST)
Contract No.: DE-EE0002323

Executive Summary

The K-12 Outreach Program is designed to teach the K-12 students the Physics involved in a car crash, the use of safety restraints in a car, and bumper and chassis design for safety in a car. This has been accomplished by creating eight hands-on lessons for the K-12 teachers to use in their classrooms. These eight lessons are explained to the teachers in a hands-on one-day workshop. The teacher then returns to her/his classroom to teach the physics to their students using the lessons and equipment received at the teacher workshop.

Student competitions were designed to afford each student to exhibit the knowledge they learned from the lessons. The competitions are broken into K-2, 3-5, 6-8 and 9-12 grades. The competitions consist of combining physics concepts and engineering principles with the student's problem-solving skills to keep a raw-egg passenger safe in a collision.

The Mission Eggcellence Challenge allows the student to design a bumper from common materials. The Automotive Engineering Challenge allows the student to design a chassis from K'nex (K-5) or balsa wood (6-12). The success of the program is reflected in the number (207) of teachers trained and the number (1086) of students competing in the competitions over the period of the grant.

Accomplishment of Objectives

The objectives of the project (listed below) have been accomplished. The lessons has been illustrated and incorporated into book form. This was presented to the Automotive Engineering Society which has agreed to incorporate into their "A World in Motion" program nationwide. An extra bonus is the fact that the trained students are very aware of the importance of the use to the seat belt and other safety features of a vehicle including air bags and bumper and chassis design. Many parents report that their child makes them buckle up before driving the car.

Objectives

- The Mission Eggcellence Project is designed to develop a commitment from CAVS to the children of Mississippi through curriculum instruction and competitions dealing with the design of a vehicle bumper and/or seatbelt for passenger safety.

- This instruction and student competitions will create an awareness of the importance of design in safety implications and of the real-world applications of mathematics, science, and engineering problem-solving skills.
- Mission Eggcellence will create awareness among the Mississippi school age population of future job opportunities in the State of Mississippi as well as college majors associated with these jobs.

Approach: including industrial partner/collaborator and path to technology transfer and commercialization

- Create a grade appropriate curriculum with experiments and problems associated with the physics of car crashes for grades K-2, 3-5, 6-8, and 9-12. (Objective 1)
- Develop a Teacher Workshop for grades K-2, 3-5, 6-8, 9-12 teachers for training in use of the grade appropriate curriculum in the regular classroom. Equipment necessary to conduct the experiments and compete in the competitions is given to each teacher participant. (Objective 1)
- Design a competition for grades K-2, 3-5, 6-8, and 9-12 incorporating bumper design for passenger safety. (Objective 2)
- Design a competition for grades K-2, 3-5, 6-8, and 9-12 incorporating car design for passenger safety. (Objective 2)
- Publish a book containing the experiments, illustrations, competitions, and safety chapter. An electronic version will be included with the book and will contain videos of the teacher training and competitions. (Objective 3)

Technology/Techniques Used to Accomplish Goals

A website has been maintained for information about the program and its successes as well as workshop and competition dates. A program created CD consisting of an explanation with animation and illustrations of the physics concepts is provided to each teacher along with two purchased DVDs (Understanding Car Crashes: It's Basic Physics and Understanding Car Crashes: When Physics Meets Biology).

Mission Eggcellence provides students with a hands-on introduction into vehicular crashworthiness through applying basic concepts of physics (students are provided with simple definitions from physics such as mass, velocity, momentum, and energy, and how they are used during a crash), explanations of what actually happens during a crash (using the physics terms and defining what is necessary to enable passengers to survive a crash), and examples of safety devices (explanations and examples of some devices such as bumpers, seatbelts, airbags, and safety cages, used in cars and trucks, with simulations to demonstrate how they work). Other explanations provided will include manufacturer goals (creating a vehicle that is lightweight for the cheapest price possible, creating a vehicle that demonstrates good fuel efficiency, creating a vehicle that is aesthetically pleasing in appearance) versus consumer goals (a vehicle that is strong enough to protect passengers from impact, a vehicle that is light enough to provide economical fuel consumption, a vehicle that has a pleasing appearance, a vehicle that has a memory of its shape and can be repaired faster, cheaper, and easier) and the difficulties involved in balancing these requirements.

Vehicles, materials, eggs, workbooks/worksheets, and instructions will be provided to the students with which they must design a safety barrier for each team's vehicle that will prevent the egg from breaking upon impact during an impact competition. The vehicles are released upon a ramp, which is elevated to a higher degree of angle, from 15 degrees to 70 degrees, at each step of the impact competition, and the vehicle(s) in which the eggs do not break can win. The winners are determined by the lightweight designs. Competitions are expected to be state wide. Undergraduates and graduate

students will play a large role in communicating the principles and overseeing the activities. They will also be used to help monitor the tournaments and mentor some of the K-12 students

Each curriculum consists of eight grade-appropriate experiments for the physics concepts of velocity, acceleration, Newton's Third Law, momentum, impulse, elastic, and inelastic collisions. These experiments include a bumper design and a car design. In the bumper design competitions for grades K-2, 3-5, 6-8, and 9-12, the bumper is tested by rolling a wooden car, with the bumper attached, down a ramp using a raw egg as the passenger. The winner is the one that can endure the steepest incline without cracking the egg. The tie breaker is the lightest mass. In the K-2 and 3-5 car design competitions, a car is designed using K' NEX pieces from a kit. The 6-8 and 9-12 car design competitions use a car designed from balsa wood. Winner is steepest incline with egg intact. The tie breaker again is the lightest mass.

Conclusions

The Mission Eggcellence Program has been developed for the grades K-2, 3-5, 6-8, and 9-12. The Teacher Workshop for these grades has been very successful. Forty-two school districts in 35 counties have had 207 teachers participate in the teacher workshops. One thousand eighty-six students have competed in the student competitions. Seventy-five percent of the teachers who attended the workshop had students compete in both the bumper design and car design competitions. Feedback was excellent.